

SURFACE STUDIES OF POTENTIALLY CORROSION RESISTANT THIN FILM
COATINGS ON CHROMIUM AND TYPE 316L STAINLESS STEEL

by

STEPHANIE LEE JOHNSON

B. S., Cameron University, 1998

AN ABSTRACT OF A DISSERTATION

submitted in partial fulfillment of the requirements for the degree

DOCTOR OF PHILOSOPHY

Department of Chemistry
College of Arts and Sciences

KANSAS STATE UNIVERSITY
Manhattan, Kansas

2006

Abstract

This work is a detailed study of the interaction between two phosphorous-containing acids and the metals chromium and 316L stainless steel. The objective of this work is to investigate the formation of unique thin films on the two metals and to probe the surface chemistry of these films through the use of core level and valence band X-ray photoelectron spectroscopy (XPS).

Chromium forms a wide array of oxides and can exist at several valencies. Valence band XPS is used in conjunction with band structure and multiple scattered wave $X-\alpha$ calculations to distinguish which states are present in the resultant films. Both 99.99% chromium and 316L stainless steel foils were treated with orthophosphoric acid and 1-hydroxyethylidene-1,1-diphosphonic acid, otherwise known as etidronic acid. Two methods developed in the Sherwood research laboratory for forming oxide-free films on metal surfaces are utilized in this work.

Core level XPS results did not provide sufficient information to draw conclusions regarding the products formed in the reactions. The valence band results showed clear evidence of multiple forms of phosphates forming on the metal surfaces as evidenced by the subtle differences in separation between the phosphorous 3p and 3s peaks as well as differences in separation between the O2s and phosphorous 3s peaks. The Valence Band XPS results were interpreted by $X-\alpha$ cluster and band structure calculations.

Films formed on chromium foil from the orthophosphoric acid were found to be condensed phosphates that are stable in air. Etidronic acid formed very thin phosphate films on chromium with both treatment methods as well as on 316L stainless steel when the bench top method was applied. Treatment in the anaerobic cell of etched 316L steel generated an etidronate film. This sample was the only etidronate film formed, all other etidronate-based films were generated from disassembled portions of the etidronate ion to form phosphate films.

SURFACE STUDIES OF POTENTIALLY CORROSION RESISTANT THIN FILM
COATINGS ON CHROMIUM AND TYPE 316L STAINLESS STEEL

by

STEPHANIE LEE JOHNSON

B. S., Cameron University, 1998

A DISSERTATION

submitted in partial fulfillment of the requirements for the degree

DOCTOR OF PHILOSOPHY

Department of Chemistry
College of Arts and Sciences

KANSAS STATE UNIVERSITY
Manhattan, Kansas

2006

Approved by:

Major Professor
Dr. Peter M. A. Sherwood

Abstract

This work is a detailed study of the interaction between two phosphorous-containing acids and the metals chromium and 316L stainless steel. The objective of this work is to investigate the formation of unique thin films on the two metals and to probe the surface chemistry of these films through the use of core level and valence band X-ray photoelectron spectroscopy (XPS).

Chromium forms a wide array of oxides and can exist at several valencies. Valence band XPS is used in conjunction with band structure and multiple scattered wave $X-\alpha$ calculations to distinguish which states are present in the resultant films. Both 99.99% chromium and 316L stainless steel foils were treated with orthophosphoric acid and 1-hydroxyethylidene-1,1-diphosphonic acid, otherwise known as etidronic acid. Two methods developed in the Sherwood research laboratory for forming oxide-free films on metal surfaces are utilized in this work.

Core level XPS results did not provide sufficient information to draw conclusions regarding the products formed in the reactions. The valence band results showed clear evidence of multiple forms of phosphates forming on the metal surfaces as evidenced by the subtle differences in separation between the phosphorous 3p and 3s peaks as well as differences in separation between the O2s and phosphorous 3s peaks. The Valence Band XPS results were interpreted by $X-\alpha$ cluster and band structure calculations.

Films formed on chromium foil from the orthophosphoric acid were found to be condensed phosphates that are stable in air. Etidronic acid formed very thin phosphate films on chromium with both treatment methods as well as on 316L stainless steel when the bench top method was applied. Treatment of etched 316L steel in the anaerobic cell generated an etidronate film. This sample was the only etidronate film formed, all other etidronate-based films were generated from disassembled portions of the etidronate ion to form phosphate films.

Table of Contents

List of Figures.....	xi
List of Tables.....	xviii
Acknowledgements.....	xx
Dedication.....	xxi
Preface.....	xxii
CHAPTER 1 - Surface Analysis.....	1
1.1 Introduction.....	1
1.2 X-ray photoelectron spectroscopy.....	2
1.2.1 The Nature of X-ray Photoelectron Spectra.....	2
1.2.1.1 The Excitation Process.....	2
1.2.1.2 The Three Step Model.....	3
1.2.1.3 Inelastic Mean Free Path and Sampling Depth.....	4
1.2.1.4 Chemical shifts In Core Levels.....	4
1.2.1.5 Theoretical Models for Binding Energies.....	5
1.2.1.5.1 Koopman's Theorem.....	5
1.2.1.5.2 Ground State Potential Model (GPM).....	5
1.2.1.5.3 Relaxation Potential Model (RPM).....	6
1.2.2 XPS Spectral Features.....	6
1.2.2.1 Primary Peak Attributes.....	6
1.2.2.1.1 Peak Position.....	7
1.2.2.1.2 Peak Intensity.....	8
1.2.2.1.3 Peak Width.....	9
1.2.2.1.4 Peak Shape.....	9
1.2.2.1.5 Spin Orbit Splitting.....	9
1.2.2.2 Secondary Peak Structural Features.....	10
1.2.2.2.1 Multiplet Splitting.....	10
1.2.2.2.2 X-ray Source Satellites and Ghost Features.....	10
1.2.2.2.3 Plasmon Features.....	11

1.2.2.2.4 Shake-up and Shake-off Satellites	11
1.2.3 Auger Features	11
1.3 Data analysis techniques	12
1.3.1 Curve Fitting	12
1.3.2 Atomic Ratio Calculations	12
1.4 Acknowledgements	13
1.5 References	14
1.6 Figures	15
1.7 Tables	23
CHAPTER 2 - Instrumentation Utilized In XPS	24
2.1 The Vacuum System	24
2.2 General XPS Instrumentation Arrangement	24
2.4 The Lens System	26
2.5 The Analyzer	26
2.6 Electronic Detector Systems	27
2.6.1 Single channel detection	27
2.6.2 Multichannel detection	28
2.7 Techniques Utilized in XPS Experiments	28
2.7.1 Charge Compensation	28
2.7.2 The Anaerobic Cell	28
2.8 References	30
2.9 Figures	31
CHAPTER 3 - Corrosion and Inhibition of Corrosion	39
3.1 Introduction	39
3.2 Process of corrosion	40
3.2.1 Chemical Corrosion	40
3.2.2 Electrochemical Corrosion	41
3.2.2.1 Mixed Potential Theory	41
3.2.2.2 Passivity	42
3.3 Corrosion protection	42
3.3.1 Inhibition	43

3.3.2 Electrochemical Protection	43
3.3.3. Protective Coatings	43
3.4 References	45
3.5 Figures	46
CHAPTER 4 - Chromium and Stainless Steels	50
4.1 Introduction	50
4.2 Chromium	50
4.2.1 Occurrence, Abundance and Utility of Chromium	50
4.2.2 Physical Properties	51
4.2.3 Chemical Properties	51
4.3 Stainless steel	53
4.3.1 Manufacture and Utility of Steels	53
4.3.2 Alloying Elements	55
4.3.2.1 Chromium	55
4.3.2.2 Molybdenum	55
4.3.2.3 Manganese	55
4.3.2.4 Nickel	56
4.3.2.5 Trace Alloying Elements	56
4.3.3 Classification of Stainless Steels	56
4.3.3.1 Austenitic Grades of Stainless Steel	57
4.3.3.2 Martensitic Grades of Stainless Steel	57
4.3.3.3 Ferritic Grades of Stainless Steels	57
4.3.3.4 Duplex Stainless Steels	58
4.4 References	59
4.6 Figures	61
4.7 Tables	62
CHAPTER 5 - Phosphorous-Containing Compounds	64
5.1 Introduction	64
5.2 Nomenclature of phosphates	64
5.3 Phosphates and corrosion protection	66
5.3.1 Conversion Coatings	66

5.3.2 Conversion Coatings in Biomedical Applications.....	66
5.3.3 Conversion Coating Thickness	67
5.3.4 Creating Ultra Thin Phosphate Films	67
5.4 Application	68
5.5 References	70
5.6 Figures	72
CHAPTER 6 - Core and Valence Band X-ray Photoelectron Spectroscopy Studies of Chromium	
Oxide Standards and Chromium Aqueous Oxidation	77
6.1 Abstract.....	77
6.2 Introduction	78
6.3 The Nature of Chromium Oxides	79
6.4 Experimental.....	80
6.4.1 Instrumentation	80
6.4.2. XPS Measurement of Standard Compounds	80
6.4.3 The Anaerobic Cell Procedure.....	81
6.5 Data analysis.....	82
6.5.1 Curve Fitting.....	82
6.5.2 Calculations	83
6.5.3 Atomic Ratio Calculations.....	83
6.6 Results and discussion	84
6.6.1 Analysis of chromium oxide standards.....	84
6.6.1.1 O 1s Region	85
6.6.1.2 Cr 2p Region.....	86
6.6.1.3 Valence Band Region	87
6.6.2 Analysis of Oxide Film on Chromium Foil in 4D H ₂ O.....	89
6.6.2.1 O 1s and Cr 2p Core Regions	89
6.6.2.2 Valence Band XPS Results.....	90
6.7 Conclusions	93
6.8 Acknowledgements	93
6.9 References	94
6.10 Figures	96

6.11 Tables.....	112
CHAPTER 7 - Formation of Ultrathin Film Oxide-free Protective Coatings on Chromium Utilizing Orthophosphoric Acid	
7.1 Abstract.....	115
7.2 Introduction	116
7.3 Data Analysis.....	117
7.4 Experimental.....	118
7.4.1 Instrumentation	118
7.4.2 The Anaerobic Cell Procedure.....	118
7.4.3 The Bench Top Procedure	120
7.4.4 XPS Measurement of Standard Compounds	120
7.5 Results and Discussion	121
7.5.1 Types of Experiments Performed	121
7.5.2 Analysis of phosphate films formed	122
7.5.2.1 O 1s core region.....	123
7.5.2.2 Cr 2p Core Region	124
7.5.2.3 P 2p Core level.....	125
7.5.2.4 Valence Band Analysis.....	126
7.5.2.4.1 Valence Band of CPBno.....	128
7.5.2.4.2 Valence Band of CPB	129
7.5.2.4.3 Valence Band of CPA1H.....	131
7.6 Conclusions	133
7.7 Acknowledgements	134
7.8 References.....	135
7.9 Figures	137
7.10 Tables.....	154
CHAPTER 8 - Formation of Ultra Thin Oxide-free Protective Coatings on Chromium and 316 L Stainless Steel from 3M Etidronic Acid.	
8.1 Abstract.....	157
8.2 Introduction	158
8.3 Experimental.....	160

8.3.1 Instrumentation	160
8.3.2 Materials and Preparation	160
8.3.2.1 Anaerobic Cell Procedure	161
8.3.2.2 Bench top Procedure	161
8.3.2.3 Calculations	162
8.4 Results and discussion	162
8.4.1 Discussion of Chromium and Stainless Steel States.....	163
8.4.2 The Etidronate Ion	164
8.4.3 Chromium Treatment.....	165
8.4.3.1 Core Level Spectra	166
8.4.3.2 Valence band XPS results.....	167
8.4.4 316L Stainless Steel Treatment	169
8.4.4.1 Core level XPS results	170
8.4.4.2 Valence Band XPS Spectra	171
8.5 Conclusion	173
8.6 References.....	174
8.7 Figures	176
8.8 Tables.....	193
CHAPTER 9 - Concluding Remarks	195
9.1 Conclusion	195
9.2 References	197

List of Figures

Figure 1.1 2-D Representation of Surface layers compared with probe method depth.	15
Figure 1.2 Illustration of the concept of escape depth of photoelectrons. Incoming electromagnetic radiation is represented by $h\nu$, an elastically ejected electron is represented by e and an electron which has lost energy due to a collision and is inelastically ejected is represented as e'	16
Figure 1.3 A wide energy range scan of Ar+ etched 99.99% chromium foil.	17
Figure 1.4 The excitation and photoemission process. On the left incident X-radiation excites electrons which are emitted; electrons A and B have undergone a collision resulting in loss of kinetic energy. On the right is a diagram of the emission of a 1s core level electron.	18
Figure 1.5 The dependence of attenuation length, which is approximately 10% less than the IMFP, on the emitted electron energy. The energy dependency is the same for the IMFP. (After Seah and Dench ¹³)	19
Figure 1.6 The Cr2p core level spectra of a series of chromium oxides. CrO ₃ is Cr(VI), CrO ₂ is Cr(IV) and Cr ₂ O ₃ is Cr(III).	20
Figure 1.7 Intensity of emitted photoelectrons as a function of depth. The dashed line represents a distance from the surface above which 95% of the observed photoelectron signal originates. This escape depth is a function of the IMFP or attenuation length. This is what makes XPS a surface sensitive technique.	20
Figure 1.8 Coupling between the magnetic fields of spin angular momentum (s) and orbital angular momentum produces the spin orbit splitting observed in core levels p, d and f.	21
Figure 1.9 Cr2p core level spectra of chromium sesquioxide (Cr ₂ O ₃) obtained using monochromatic Al K $\alpha_{1,2}$ X-rays. Note the spin orbit split Cr2p _{1/2} and Cr2p _{3/2} (lower BE) features and the satellite caused by multiplet splitting at 598.6 eV.	21
Figure 1.10 Ag3d core level spectrum obtained using achromatic MgK $\alpha_{1,2}$ incident X-radiation. The dominant features are the Ag3d _{3/2} and Ag3d _{5/2} spin orbit split components. The labeled features are satellites.	22

Figure 1.11 The three possible events following excitation of an electron by soft X-ray light. The top process represents photoelectron emission, the bottom left is the Auger process and the bottom right represents the occurrence of X-ray emission (not covered here).....	22
Figure 2.1 XPS Spectrometer Set-up. Photoelectrons generated by the X-ray light travel through the lens system and the analyzer before striking the multi-channel detector.	31
Figure 2.2 The Roland circle.	31
Figure 2.3 Diagram of the application of Bragg's Law: $n\lambda = 2d\sin\theta$	32
Figure 2.4 Spectral distribution of the Al $K\alpha_{1,2}$ emission line and the effect of monochromatization.	32
Figure 2.5 Lens System – photoelectrons travel left to right.	33
Figure 2.6 Concentric Hemispherical Analyzer (CHA).	34
Figure 2.7 Channeltron detector (top) and Multichannel Detector.	35
Figure 2.8 Sherwood Surface Science Lab HA 150 Photoelectron Spectrometer.	36
Figure 2.9 Comparison of the effects from use of a flood gun. Without flood gun (a) and using flood gun (b) show there is no change in peak width. The kinetic energy shifts and the line resolution is improved when sample charging is compensated for with a flood gun.	37
Figure 2.10 Schematic diagram of the Anaerobic Cell modification.	38
Figure 3.1 Structural failure of Aloha Airlines Boeing 737.	46
Figure 3.2 Rivet heads popped on Boeing 737 belly.	46
Figure 3.3 Detailed view of the corrosion process occurring beneath a drop of water. Oxygen is readily available at the perimeter of the drop which forms the cathodic region. Oxidation of iron occurs in the center of the drop then the positive ion migrates toward the cathode, where it is reduced and forms Fe_2O_3 which separates into a separate phase from the metal.	47
Figure 3.4 Potential–current density plot for Zn and H, showing the mixed potential (i_{corr}) for the two in electrochemical reaction.	48
Figure 3.5 Polarization curve showing the passive potential range.	49
Figure 4.1 Schaeffler diagram. % Ni Equivalent = %Ni + %Co + 30(%C) + 25(%N) + 0.5(%Mn) + 0.3(%Cu). % Cr Equivalent = %Cr + 2(%Si) + 1.5(%Mo) + 5(%V) + 5.5(%Al) + 1.75(%Nb) + 1.5(%Ti) + 0.75(%W).	61

Figure 4.2 Austenitic grain in Stainless Steel Type NF709. The two arrows indicate <i>annealing twins</i> , which are identical in composition but oriented differently.....	61
Figure 5.1 Forms of Phosphorus. Figure on the left is white phosphorus, P ₄ . When heated the bonding structure reorganizes to form the long chains of P ₄ in the isomorphous red phosphorus shown on the right.	72
Figure 5.2 Orthophosphoric acid (left) and Phosphorous acid (right).	72
Figure 5.3 Formation of a diphosphate ion via condensation, or loss of H ₂ O. Note the end groups are each at the 2- oxidation state and the product is at 4-.	72
Figure 5.4 Types of phosphate tetrahedral referenced in discussion of condensed and metaphosphate arrangements. Arrows indicate bonding location.	73
Figure 5.5 Condensed PO ₄ tetrahedra. Top left: corner sharing, top right: edge sharing, bottom: face sharing.	73
Figure 5.6 C-type Cr(PO ₃) ₃ , chromium (III) tris(metaphosphate) shown in (a) ; B-type Cr(PO ₃) ₃ ; reported as Cr ₂ P ₆ O ₁₈ , chromium (III) hexametaphosphate (b). White structures are CrO ₆ octahedra.....	74
Figure 5.7 Several Ultraphosphate Networks in the phosphate MP ₄ O ₁₁	75
Figure 5.8 Scanning electron micrographs of conversion coatings on Al ₂ CuMg (a), Al ₃ (FeCu) (b) and Mg ₂ Si (c). The areas where the film is discontinuous are associated with the intermetallic particles.....	76
Figure 6.1 O 1s core region XPS spectra for etched 99.9% pure chromium foil treated in deaerated quadruply distilled H ₂ O in the anaerobic cell (a), 99.9% pure chromium metal, as received (b), 99.9% pure chromium metal, polished (c) and 99.9% pure chromium metal, etched (d).	96
Figure 6.2 Diagram representation of the overlayers of oxy-hydroxide (a) on the Cr ₂ O ₃ (b) oxide layer formed on the chromium bulk.....	97
Figure 6.3 Core and Valence Band Spectra for Cr ^{II} Acetate (a), Cr ₂ O ₃ (b), CrO ₂ (c) and 98	98
Figure 6.4 O 1s Core Data. Curve fitted O 1s peaks for Cr ^{II} Acetate (a), Cr ₂ O ₃ (b), CrO ₂ (c) and CrO ₃ (d).....	99
Figure 6.5 Core level XPS results for the Cr 2p region of the chromium oxide standards. Shown in order of increasing formal oxidation state are (a) Cr ^{II} acetate, (b) Cr ^{III} ₂ O ₃ , (c) Cr ^{IV} O ₂ and (d) Cr ^{VI} O ₃	100

Figure 6.6 Comparison of the effects from use of a flood gun. Without flood gun (a) and using flood gun (b) show there is no change in peak width. The kinetic energy shifts and the line resolution is improved when sample charging is compensated for with a flood gun.	101
Figure 6.7 Valence band XPS spectra of Cr ^{II} acetate (a), Cr ₂ O ₃ (b), CrO ₂ (c) and CrO ₃ (d).	102
Figure 6.8 Band structure calculations of the valence bands of (a) Cr ₂ O ₃ , (b) CrO ₂ and (c) CrO ₃	103
Figure 6.9 Comparison of experimental spectra (top) to spectra synthesized from band structure calculations (bottom).	104
Figure 6.10 Core level XPS spectra for the 4D H ₂ O oxide (a) and chromium etched foil (b). ..	105
Figure 6.11 Experimental VBXPS spectra for 99.9% Cr foil Ar ⁺ etched for 30 min. (a), the same Cr foil sample Ar ⁺ etched for another 90 min. (b) and the constructed theoretical spectrum of the valence band region of pure argon (c).	106
Figure 6.12 Valence band of chromium metal generated from band structure calculations.	107
Figure 6.13 Carbon 1s core region XPS data for the as-received 99.9% Cr foil (a), the Ar ⁺ etched 99.9% Cr foil (b) and Cr ₂₃ C ₆ chromium carbide powder (c).	108
Figure 6.14 VBXPS spectra for Ar ⁺ etched 99.9% Cr Foil (a), Cr ₂₃ C ₆ chromium carbide powder (b) and Cr ₃ C ₂ chromium carbide powder (c).	109
Figure 6.15 Valence band spectra of chromium oxides and etched, oxide-free 99.9% pure chromium foil treated in quadruply distilled water (a), Cr ^{II} Acetate (b), Cr ₂ O ₃ (c), CrO ₂ (d) and CrO ₃ (e).	110
Figure 6.16 Comparison of normal angle XPS spectra (a) and surface sensitive angle core and valence band (b) spectra of Ar ⁺ etched 99.99% pure chromium foil exposed to deaerated 4D water in the anaerobic cell.	111
Figure 7.1 Chromium foil O 1s core XPS data which has been curve fitted. CPBno sample (a), CPB sample (b), CPA1H (c) and CPA10 (d).	137
Figure 7.2 Core region XPS spectra for (a) etched chromium, (b) CPB, (c) CPA1H and (d) CPA10.	139
Figure 7.3 Core region XPS spectra for (a) etched chromium, (b) CPB, (c) CPA1H and	140
Figure 7.4 Valence band XPS spectra of (a) as-received 99.99% chromium foil, (b) polished 99.99% chromium foil and (c) 99.99% chromium foil which has been Argon ion etched for 90 minutes.	141

Figure 7.5 Valence band spectra generated from band structure calculations of the chromium phosphate compounds shown in Table 7.4.	142
Figure 7.6 Experimental Valence Band XPS spectra of (a) etched chromium foil, (b) CPBno, (c) CPB, (d) CPA10, (e) CPA1H and CrPO ₄ powder.	143
Figure 7.7 Valence Band XPS spectra of (a) 4D H ₂ O sample, (b) 99.99% polished chromium foil and (c) CPBno sample.	144
Figure 7.8 Multiple scattered wave X-alpha calculation of the [PO ₄ ³⁻] ion.....	145
Figure 7.9 Comparison of metaphosphate features and orthophosphate features. A valence band spectrum of chromium tripolyphosphate generated from a band structure calculation is shown in (a), while the orthophosphate CrPO ₄ is shown in an experimental VBXPS spectrum (b) and a calculated valence band of the PO ₄ ³⁻ ion generated from multiple scattered wave X-alpha calculations is shown in (c).	146
Figure 7.10 Overlay of condensed phosphate band structure calculations on VBXPS spectrum of CPB sample. Generated spectra of (a) Cr ₇ (PO ₄) ₆ , (b) Cr ₃ (PO ₄) ₂ and (c) Cr ₆ (P ₂ O ₇) ₄	147
Figure 7.11 Topographical comparison of XPS valence band spectrum of the CPB sample below the predicted dichromium(II) tetrachromium tetrakis(diphosphate) [Cr ₆ (P ₂ O ₇) ₄] spectrum generated from band structure calculations.	148
Figure 7.12 Valence Band XPS spectra of (a) chromium foil exposed to 4-D H ₂ O in the anaerobic cell for 10 min., (b) polished chromium foil and (c) chromium foil treated with 5M o-H ₃ PO ₄ in the anaerobic cell for 1 hour.	149
Figure 7.13 X-ray photoelectron valence band spectra of O 1s curve fitted peaks of CPA1H at normal angle and surface sensitive angle shown one on top of the other.....	150
Figure 7.14 Comparison of CPA1H sample (a) to the valence band spectra generated from band structure calculations of (b) dichromium(II) tetrachromium tetrakis(diphosphate) [Cr ₆ (P ₂ O ₇) ₄] and (c) tripolyphosphate [Cr ₃ (PO ₄) ₂].	151
Figure 7.15 Topographical comparison of XPS valence band spectrum of the CPA1H sample beneath the predicted valence band spectrum of chromium cyclo-hexaphosphate [Cr ₂ P ₆ O ₁₈] spectrum generated from band structure calculations.....	152
Figure 7.16 Experimental Valence Band XPS spectra of (a) CPA1H, (b) CPA1H recorded at a surface sensitive angle and (c) the same sample after exposure to ambient air for one week.	153

Figure 8.1 Outer valence band XPS results for 99.99% chromium foil and 99.9% iron foil. Experimental VBXPS results (a) and outer valence band of spectra generated from band structure calculations (b) of the metals are shown.....	176
Figure 8.2 Valence band XPS results of 99.99% chromium foil and 99.9% 316L stainless steel foil in the (a) as-received state, (b) polished with 600 grit silicon carbide emery paper and (c) 99.999% argon ion etched.	177
Figure 8.3 Valence band XPS spectra of argon ion etched (a) 99.9% 316L stainless steel foil and (b) 99.9% iron foil.....	178
Figure 8.4 Atomic configuration within the idealized etidronate ion.....	179
Figure 8.5 Experimental outer valence band region XPS spectra for the iron-phosphorous containing compounds (a) iron etidronate and (b) iron phosphate.	179
Figure 8.6 X-ray photoelectron spectroscopy valence band spectra of (a) calcium etidronate (achromatic), (b) multiple scattered wave X-alpha calculation of etidronate ion, (c) lab prep calcium etidronate (2:1 molar ratio), (d) lab prep calcium etidronate (1:1 molar ratio) and (e) aged etidronic acid on 99.99% chromium foil.	180
Figure 8.7 Core level X-ray photoelectron spectroscopy spectra for (a) CEB sample, 99.99% chromium foil treated using bench top method, (b) CEA sample, 99.99% chromium foil treated using the anaerobic cell method and (c) argon ion etched 99.99% chromium foil.	181
Figure 8.8 Core level x-ray photoelectron spectroscopy spectra for (a) curve fitted spectra of as-received chromium foil, (b) curve fitted spectra argon ion etched 99.99% chromium foil, (c) chromium foil treated in etidronic acid using bench top method and (d) using anaerobic cell method.....	182
Figure 8.9 Valence band X-ray photoelectron spectra for (a) CEB sample, (b) CEA sample and (c) argon ion etched chromium foil.	183
Figure 8.10 Comparison of VBXPS of outer valence band of calcium etidronate (lower overlain spectra) to VBXPS spectra of (a) CEB sample and (b) CEA sample.	184
Figure 8.11 Corrosion study of CEA sample results. VBXPS spectra of (a) chromium foil treated using bench top method (CEA), (b) same sample after exposure to ambient air for one week and (c) same as for (b) after two hour immersion in 1M NaCl solution.	185
Figure 8.12 Valence band XPS spectra for (a) polished chromium foil immersed in 5 M H ₃ PO ₄ 11 min. with no treatment, (b) chromium in 3 M etidronic acid using bench top method, (c)	

chromium foil treated in anaerobic cell with 3 M etidronic acid and (d) etched chromium foil.....	186
Figure 8.13 Core level XPS spectra of (a) 316L stainless steel treated using bench top method (316EB), (b) 316L stainless steel treated using anaerobic cell method (316EA) and argon ion etched of 99.99% 316L stainless steel.....	187
Figure 8.14 Core level XPS curve fitted spectra of the O 1s region of (a) 316EB, (b) 316EA and (c) calcium etidronate.....	188
Figure 8.15 Valence band XPS results for 316L stainless steel: 316EB sample (a), 316EA sample and (c) 99.99% 316L stainless steel polished with 600 grit silicon carbide emery paper.....	189
Figure 8.16 Comparison of VBXPS of outer valence band of calcium etidronate (lower overlain spectra) to VBXPS spectra of (a) 316EB sample and (b) 316EA sample.....	190
Figure 8.17 Corrosion study of 316EA sample results. VBXPS spectra of (a) chromium foil treated using the anaerobic cell method (316EA), (b) same sample after exposure to ambient air for one week and (c) same as for (b) after two hour immersion in 1M NaCl solution..	191
Figure 8.18 Valence band XPS spectra for 316EA sample (a) treated in anaerobic cell, (b) sample in (a) after being exposed to air for one week, (c) same as in (a) and (b) after immersion in 1 M NaCl solution for two hours compared with chromium phosphate powder (d).....	192

List of Tables

Table 1.1	Total angular momentum $j = l \pm s $; l =quantum number for electron orbital angular momentum; s =quantum number for the electron spin (either up or down).	23
Table 4.1	Rate of Corrosion of Chromium	62
Table 6.1	Crystal structure data for the band structure calculations	112
Table 6.2	Parameters used to calculate atomic ratios of the chromium standard powders. Intensities are normalized (Area/# scans). Additional parameters used: $\alpha_{Cr2p} = 11.67$, $\alpha_{O1s} = 2.93$, $\lambda_{Cr} = 13.5283$, $\lambda_{Cr2O3} = 21.8731$	112
Table 6.3	Parameters used to calculate atomic ratios of the oxide films on 99.99% pure chromium foil. Intensities are normalized (Area/# scans). Additional parameters used: $\alpha_{Cr2p} = 11.67$, $\alpha_{O1s} = 2.93$, $\lambda_{Cr} = 13.5283$, $\lambda_{Cr2O3} = 21.8731$	113
Table 6.4	Curve fitting parameters for the chromium oxide standards O 1s region	113
Table 6.5	Binding energy (eV) for Cr 2p (left) and O 1s (right) core level regions	114
Table 6.6	Comparison of the Cr 2p region of the four powder standards, listed in the far left column. Data listed from left to right: Binding energy of the Cr 2p _{3/2} peak center at half-maximum, The full peak width at half-maximum, the configuration of the d-orbital electrons, the separation between the metallic and oxide peaks and the separation between the spin-orbit split components.	114
Table 7.1	Summary of Experiments	154
Table 7.2	Core level peaks widths at half maximum (FWHM) and atomic ratios listed by sample.	154
Table 7.3	Data for Chromium Foil Atomic Ratio Calculations	155
Table 7.4	Binding energy (eV) for Cr 2p (left) and O 1s (right) core level regions. *PO ₄ ³⁻ peak in CrPO ₄ O 1s at 534.1 BE	155
Table 7.5	Crystal structure data for calculated chromium phosphate compounds.	156
Table 8.1	Summary of Experiments	193
Table 8.2	Core level atomic ratios per sample	193
Table 8.3	Normalized Peak Areas (counts*step size) eV	194

Table 8.4 Experimental Binding Energies 194

Acknowledgements

I would like to thank Dr. Peter M. A. Sherwood, an excellent research director and teacher as well as a stalwart friend. I extend heartfelt thanks to my committee members for enduring the trials and tribulations of a long distance research project. Thanks also to the faculty and staff in the KSU Department of Chemistry for their help and support.

Dedication

This work is dedicated to Beth, John Paul and Wren who have added a sparkling effervescence to my life that is now filled with joy and laughter. This dissertation is also dedicated to my clan, especially John John and Patsy, the best substitute parents a sister could hope for. Lastly this is dedicated to Paul, whose passion for excellence and years of friendship have always inspired me

Preface

This research has been conducted as a continuation of projects within this research group directed at increasing the scientific community's understanding of the complex corrosion systems between metals and phosphates. Novel phosphate films bonded directly to the metal substrate have been generated from phosphoric acid in an anaerobic environment designed by members of this research group.^{1,2} These oxide-free phosphate films have been successfully formed on copper⁴, aluminium^{1,3}, titanium⁵ and iron.^{1,3} These films are potentially corrosion inhibiting, biocompatible films which can also provide an interface on which other materials may adhere to.

The choice of materials used in the systems studied in this research is based on the fact that corrosion is a serious challenge, especially in the biomedical field. One area where it is most critical involves catastrophic implant failure resulting in great suffering and expense. 316L stainless steel is the most prevalent material used in fabrication of implants. It is a steel alloy which has on the order of 18% chromium as its second largest component with the largest being iron. It is established that the oxide-free phosphate films can form on iron, and so the chromium phosphate system is the next logical step in the ongoing project.

In addition to the investigation of thin films generated from phosphoric acid there has been previous work done in this group examining the corrosion inhibiting effects of an organophosphonic acid, 1-hydroxyethylidene-1, 1-diphosphonic acid (HEDP), otherwise known as etidronic acid, on iron and mild steel.^{6,7} The work in this dissertation continues the investigation of thin films generated from these two phosphorous-containing acids on chromium and 316L stainless steel in anaerobic environments using the two methods developed in this group.

The organization of this dissertation is designed to acquaint the reader with a background in the analytical methods employed to characterize the results as well as providing a brief description of the theories upon which X-ray photoelectron spectroscopy is based.

Chapter one is a brief overview of the nature of X-ray photoelectron spectroscopy, or XPS, and methods of data analysis techniques used to extract information from the spectral

results of XPS studies. The instrumentation used in XPS spectrometer systems is reviewed in Chapter two. Methods of managing potential difficulties which may arise during the course of an investigation are also addressed and a description of the chamber modification which allows wet chemistry to be performed under an inert anaerobic environment on an oxide-free metal surface is given.

The phenomena of corrosion are addressed in Chapter three. The process of corrosion is explained and a discussion of current methods used in industry to inhibit and prevent corrosion is provided. There is also a brief discussion of the problems faced with the use of these current anti-corrosive measures. Chapter four provides an overview of the properties, occurrence and utility of chromium along with the history of the development of steels, their fabrication, alloying components and classification are also addressed.

Chapter five is a brief introduction to the complex nature and nomenclature of phosphates and phosphate-containing compounds. This chapter will address phosphate “conversion” coatings and biomedical applications of phosphate films. The chapter concludes with a brief review of several chromium phosphate compounds

Four chromium oxides are studied in Chapter six to provide a reference for comparison with experimental results of the studies of films derived from phosphoric and etidronic acids. The formal oxidation state of chromium is different in each of the four compounds studied. An argon ion etched oxide-free chromium foil is exposed to quadruply distilled water while in an inert, anaerobic environment. The results are characterized by core and valence band XPS, providing a baseline for an ultra thin oxide film bonded directly to chromium metal. The oxidation of chromium metal has been studied in depth by other workers, but, to the investigator’s knowledge, this is the first study of the oxidation process occurring on an oxide-free chromium surface. This work provides high resolution detailed information on a set of chromium oxide standards providing a framework on which to construct valid conclusions of the chromium and 316L steel studies using phosphorous-containing acids. The results of the chromium oxide studies are interpreted through the use of band structure calculations.

Chapter seven is a detailed study of the reactions of oxide-free argon ion etched chromium and 316L stainless steel foils with deareated orthophosphoric acid. The systems are created using the anaerobic cell and a new method developed by members of this research group,

referred to as the “bench top” method. These results are evaluated using the oxide standards, band structure and multiple scattered wave X-alpha cluster calculations.

Chapter eight also utilizes the two methods for treating the oxide-free metal surfaces in an anaerobic environment. Both the chromium and 316L steel foils are stripped of their native oxide and reacted with deaerated etidronic acid. Evaluation of the experimental outcome makes use of the previous results from chapters six and seven as well as results from prior studies of etidronate films formed on iron and mild steel. Calcium etidronate was synthesized in order to characterize the etidronate ion using high resolution monochromatic x-rays. The resulting valence band XPS spectra are used as a standard reference for the evaluation of the films generated from deaerated etidronic acid. All but one of the films formed was oxide-free and each method produced films unique to the others.

References

1. J. Rotole and P. M. A. Sherwood, U.S. Patent No. 6,066,403, (23 May 2000).
2. Y. Liand, D. Paul, Y. Xie and P. M. A. Sherwood, *Anal. Chem.*, **65**, 2276, (1993).
3. . J. Rotole and P. M. A. Sherwood, *Chem. Mater.*, **13**, 3933, (2001).
4. J. A. Rotole and P. M. A. Sherwood, *J. Vac. Sci. Technol. A*, **18**, 1066, (2000).
5. J. A. Rotole, K. Gaskell, A. Comte and P. M. A. Sherwood, *J. Vac. Sci. Technol. A*, **19**, 1176, (2001).
6. I.D. Welsh and P.M.A. Sherwood, *Chem. Mater.*, **4**, 133, 1992.
7. I.D. Welsh and P.M.A. Sherwood, *Proceedings Electrochemical Society*, **89-13**
(*Advances in Corrosion Protection by Organic Coatings*: Edited by D. Scantlebury and M. Kendig), 417, (1989).

CHAPTER 1 - Surface Analysis

1.1 Introduction

The surface of a material is, by definition, the interface between phases. In mathematics a surface is defined as the outermost portion of a three dimensional object. On an atomic scale the surface is not an evenly distributed layer of atoms and differs from the inner material due to the two-dimensionality of the forces which act on it. Since the surface is geometrically unconstrained in one dimension there is a shifting of the atoms or molecules into a lowest energy configuration. This relaxation interrupts the periodicity which is maintained in the bulk of the material and creates an environment which is unique to the bulk environment. Since the surface experiences forces different than, and is physically and chemically different from the bulk material, it is the surface which determines the outcome of any interaction with other moieties. While it is often straightforward to predict the results of an interaction between the bulk material and a given reactant, the surface often possesses properties different from the bulk which dictate reaction, corrosion and catalytic rates and outcomes. Accurate analysis of the surface physical and chemical properties is critical for successful materials development and engineering.

Techniques for analyzing surfaces must be very sensitive since the region of interest is less than 100 angstroms. The method of analysis must also be very efficient at delineating between bulk and surface analyte signals. The analysis depth must penetrate beneath the outer few angstroms of ubiquitous surface contaminants but shallow enough to provide robust information about the structure and properties of the interface region. X-ray photoelectron spectroscopy (XPS) has the capacity to determine elemental composition, the chemical states of the elements present, the atomic ratios of the elements, and the thickness of surface films present. Ultraviolet photoelectron spectroscopy (UPS) is another popular surface analytical technique, however due to the much lower energy of the incident radiation the information provided by UPS only elucidates the composition and properties of the outer 1.5 angstroms (\AA) of the surface interface. Considering the ionic radius of oxygen is 1.4 \AA it becomes evident that the information provided by UPS can not reveal much below the first layer of contamination, which is most often in the form of hydrocarbons. As illustrated in Figure 1.1, very little is revealed about the actual chemical nature of the surface interactions.

1.2 X-ray photoelectron spectroscopy

X-ray photoelectron spectroscopy, henceforth referred to as XPS, is based on the photoelectric effect described by Albert Einstein in 1905. The photoelectric effect is the emission of electrons from matter upon the absorption of electromagnetic radiation as a result of the current produced by the absorption of the radiation. This effect was initially referred to as the Hertz effect since Heinrich Hertz published observations of the photoelectric effect in 1887.¹ Einstein's analysis provided firm evidence of the particle nature of light. Kai Siegbahn and his research group developed a spectrometer which measured the first high energy XPS spectrum in 1954. In 1969 Hewlett-Packard, in cooperation with Dr. Siegbahn, produced the first commercial monochromatic XPS instrument. Dr. Siegbahn received the Nobel Prize in Physics in 1981 for his work in XPS.

1.2.1 The Nature of X-ray Photoelectron Spectra

XPS provides information about the binding energy of electrons in the sample material under examination. The sample surface is irradiated with soft x-rays of a characteristic energy dependent upon the wavelength of the incident radiation multiplied by Planck's constant ($h\lambda$). These photons can penetrate to a significant depth, but the electrons only have enough energy to escape inelastically from, at the most, 100Å into the material as depicted in Figure 1.2. The flux of emitted electrons is measured at pre-determined energy intervals across a range of energies. Peaks in the intensity (counts per second) of the ejected electrons correspond to energy characteristic of elemental core and valence binding energies. Figure 1.3 is an example of a wide range energy spectrum. The resulting peaks are from both the photoelectric effect and emission due to the Auger process.

1.2.1.1 The Excitation Process

Photoemission results from an electron within the sample absorbing the energy of an incident photon leading to ionization and ejection from the material. The kinetic energy of the emitted photoelectron is expressed in the equation Einstein derived through the use of quantum mechanics:

$$KE = h\nu - BE \quad (1.1)$$

Where,

KE = kinetic energy of the photoelectron

h = Planck's constant

ν = frequency of the incident radiation

And BE = binding energy of the orbital shell which the photoelectron was ejected (with respect to the vacuum level).

This equation is accurately applied to a gaseous sample but with a solid sample the situation becomes more complex. When two materials come into contact, such as when a sample is mounted on a sample holder, their Fermi edges will equilibrate which results in a contact potential developing from the difference in the two work functions (ϕ) of the materials. When a sample is mounted on a sample arm the contact potential becomes: $\Delta\phi = \phi_{\text{sample}} - \phi_{\text{spectrometer}}$. Additionally, the binding energy reported in Equation 1.1 is the binding energy with reference to the vacuum level. In solids the convention is to report binding energies with reference to the Fermi level which is:

$$BE_{\text{Fermi}} = BE_{\text{vacuum}} + \phi_{\text{sample}} \quad (1.2)$$

Equation 1.1 then becomes :

$$KE = h\nu - BE_{\text{Fermi}} + \phi_{\text{sample}} - \phi_{\text{spectrometer}} \quad (1.3)$$

for solid conducting samples. Insulating samples require an additional term subtracted to account for the sample charging (S). Sample charging is most often treated by flooding the sample with electrons of sufficient energy to offset the positive charge built up by the holes left by the ejected electrons.²

$$KE = h\nu - BE_{\text{Fermi}} + \phi_{\text{sample}} - \phi_{\text{spectrometer}} - S \quad (1.4)$$

1.2.1.2 The Three Step Model

Photoemission is most readily understood through the Three Step Model, which incorporates both intrinsic and extrinsic processes involved in photoemission.³ The entire excitation process is represented in Figure 1.3. The first step occurs as the X-rays excite a ground state electron to a higher (final) energy state as it absorbs the energy of an incident

photon and moves into a conduction band of energy. This is an intrinsic process, which simply means it is connected with the photoemission process. The electron is transported from the conduction band state to the surface in the second step. In the third step the electron escapes into the vacuum when the excited state matches the energy level at the vacuum interface. For X-ray light there are no selection rules to follow in XPS since there is a continuum of final states which an electron can be excited into.

1.2.1.3 Inelastic Mean Free Path and Sampling Depth

Once an electron is excited the average distance the ejected electron will travel within the material before it loses sufficient energy to escape because of interaction with other particles within the sample. The inelastically scattered electrons contribute to the background of a spectrum. This is usually a result of electron-electron interaction but may also result from electron-phonon and electron-plasmon interaction processes. The depth or distance from which photoelectrons can escape freely without suffering any inelastic collisions is referred to as the Inelastic Mean Free Path (IMFP). The value of this IMFP is dependent on the KE of the electron as shown in Figure 1.4. At low energies the IMFP is large due to the magnitude of electron-electron repulsion within the material. The IMFP is also dependent on the nature of the material being traveled through.^{4,5} It is found that 95% of the signal in the XPS spectrum is derived from a depth of 3x IMFP into the sample. Since photoelectrons generated from soft X-rays have a low IMFP the sampling depth is on the order of 100Å making XPS a surface sensitive analytical technique.

1.2.1.4 Chemical shifts In Core Levels

Each core atomic orbital of each element has its own characteristic binding energy, which is to say that each element has its own characteristic set of peaks in a wide energy range spectrum. An electron's exact binding energy is determined by the atomic orbital it was ejected from, the formal oxidation state of the atom and the chemical environment surrounding the atom. Chemical shifts, or changes in binding energy of an ejected electron, result from changes in oxidation state and local chemical environment. A more positive oxidation state atom will have a higher binding energy as a result of extra coulombic interaction between the photoelectron and

the ion core. A metal oxide will have a higher binding energy than its corresponding metal peak. Figure 1.5 shows the Cr2p region of a series of chromium oxides with different oxidation states. Note that Cr₂O₃, a Cr^(III) species, has a lower binding energy than CrO₃ which is in a Cr^(VI) oxidation state. Additionally, an increase in binding energy results with an increasing electro-negativity of the attached groups.

1.2.1.5 Theoretical Models for Binding Energies

1.2.1.5.1 Koopman's Theorem

Equation 1.3 will yield a reasonably accurate estimation of the binding energy value. The simplest binding energy calculation is based on Koopman's Theorem⁶ which assumes that the ionization energy of an electron in a given molecular orbital is approximately that of the Hartree-Fock orbital energy of that molecular orbital. While this approach of only considering the ground state effects simplifies the evaluation of chemical shift information the assumption neglects the relaxation within the orbital after an electron is ejected during the photoemission process.

1.2.1.5.2 Ground State Potential Model (GPM)

In 1967 Siegbahn and coworkers developed an electrostatic model whereby the atom of interest is considered to be a hollow conducting sphere of charge and radius q_i and r_i , respectively.⁷ The difference between nuclear charge and electronic charge for an ion is q_i . For an isolated, neutral atom this equals zero but becomes a positive or negative charge when bonding occurs in a molecule as a result of the effect of neighboring atoms on the valence electrons. Surrounding atoms are considered point charges of charge q_j with distance r_j from the hollow sphere, i.e. the positively charged nucleus is surrounded by a cloud of negatively charged electrons. The potential at the hollow sphere is the sum of the sphere charge and the potential from all the surrounding point charges:

$$\Delta E = q_i/r_i + \sum_{i \neq j} (q_j/r_{ij}) \quad (1.5)$$

The chemical shift, and hence the resulting binding energy, can be predicted by calculating the potential energy difference between an atom of zero charge and an atom of the

same type with q_i charge in the chemical environment with other atoms of charge q_j . When the atom participates in bonding its valence electrons bonding, nonbonding and antibonding relationships develop within the molecular orbitals of the resulting compound. Even though the core electrons do not participate in bonding the perturbation in the valence level is still experienced in the core levels to an extent since the potential within the sphere is constant and the change in charge density is distributed throughout the sphere.

1.2.1.5.3 Relaxation Potential Model (RPM)

Neither the GPM nor Koopman's Theorem take relaxation effects into account. Another model proposed by Siegbahn and coworkers is the RPM.⁷ When an electron is removed from a solid the remaining electrons experience a lessened electron-electron repulsive force and so shift to a lower energy configuration which is nearer to the positively charged nucleus. The redistribution of the remaining electrons shields the departing electron from the nuclear charge which imparts a higher kinetic energy than the electron would have in the absence of this shielding. Usually this relaxation energy (R_k) is fairly substantial and can be as high as 10% of the binding energy of the electrons involved. With the relaxation energy term the binding energy equation then becomes:

$$\Delta E = \frac{q_i}{r_i} + \sum_{i \neq j} \frac{q_j}{r_{ij}} + \Delta R \quad (1.6), \text{ and}$$

$$\Delta R = R_s - R_c \quad (1.7)$$

Where R_s is the standard relaxation energy and R_c is the relaxation energy of the compound.

1.2.2 XPS Spectral Features

1.2.2.1 Primary Peak Attributes

The information provided in XPS is derived from the characteristic features that comprise the peaks appearing in a spectrum. These features result not only from subtle differences in the chemical and physical environment of the sample, but also by instrumental

processes. Familiarity with the various features which can appear in the spectra in an experiment is essential for accurate analysis of the data.

There are several data bases that catalog the results of the studies of elemental core regions. Chemical shifts have also been studied and many attempts to create a definitive library of the results have been made, but uncertainties in the calibration of an insulating sample, differential sample charging and differences in instrument resolution present challenges when comparing data from different instruments. Each experiment yields results which must be interpreted through consideration of the primary peak attributes.

Following in this section are the features that yield information about the chemical environment of the sample surface under investigation.

1.2.2.1.1 Peak Position

Each core atomic orbital of element has its own unique binding energy. As the sample is irradiated with soft X-ray light photoelectrons which have escaped the solid with no energy loss are detected and their kinetic energies measured. Typical XPS spectra are presented as Intensity versus Binding Energy plot (see Figure 1.3). By convention the binding energy is usually presented decreasing from left to right. The binding energies of the elements and their corresponding atomic orbitals have been studied and reported and are now cataloged in several databases such as that found at The National Institute of Standards and Technology (NIST).⁸

Generally the determination of the peak binding energy through use of Equation 1.2 is used in the laboratory to calculate binding energies. While being a simple approximation based on Koopman's theorem the results are sufficient for identification of elemental composition based on peak location on the binding energy scale. The peak position identifies the element and the core level that the photoelectron was ejected from. Peak positions may also reveal the chemical shift resulting from the interaction of the ejected photoelectron with the surrounding and the valence electrons.

1.2.2.1.2 Peak Intensity

The peak intensity is calculated after removal of the spectral background created by inelastic loss processes and is proportional to the number of the elemental atoms present. Figure 1.4 shows both elastic and inelastic scattering. The electrons labeled A and B collide and suffer energy loss yet still have sufficient energy to escape from the solid. The unlabeled electrons contribute to the area under the peak and the labeled ones contribute to the background on the spectrum. The inelastic scattering effectively limits the sampling depth to tens of angstroms which is why XPS is a surface sensitive method.

Once the background is removed from the spectrum the peak intensity for a homogeneous gas phase sample can be represented as:

$$I = I_0 \alpha C k x \quad (1.8)$$

Where,

I_0 = The intensity of the incident photon (photon flux);

α = The photoelectron cross section, which is the probability of putting a photoelectron into the system and getting a photoelectron out and is unique for each elemental orbital energy level.⁹

C = The concentration of the sample (gas phase units of atoms/volume);

k = instrumental efficiency factor;

x = depth through which the photoelectron travels.

Solid samples change the situation since the photoelectrons are emitted from a packed crystalline lattice which increases the probability of inelastic collisions and reduces the IMFP. Modification of Equation 1.8 to account for this includes λ , which in this case is the attenuation length and is associated with the IMFP. Seah and Dench¹⁰ related this variable to electron energy and the material properties by use of the equation:

$$\lambda = 538 a_A / E_A^2 + 0.41 a_A (a_A E_A)^{0.5} \quad (1.9)$$

where,

a_A = the atomic volume in nm³

E_A = the energy of the electron in electron volts (eV)

And λ is in nm.

The intensity of electron emitted from depths larger than d in a surface normal direction is specified by the equation:

$$I = I_0 e^{(-d/\lambda)} \quad (1.10)$$

Where I_0 is from a uniform, infinitely thick substrate. Calculations performed have revealed that 98% of peak intensity comes from a depth of 3 times the IMFP, as shown in Figure 1.6.¹¹

1.2.2.1.3 Peak Width

When experimental data is reported peak widths are given at the full width of the peak at half the maximum intensity (FWHM), given in eV. The factors which impact the peak width are the inherent line width of the core level (E_a), the natural line width of the source radiation (E_b), and the resolution of the analyzer (E_c) which is affected by the type of analyzer used as well as the mode the analyzer is operated in during data collection.¹² The relationship is represented by the equation:

$$E_{FWHM} = (E_a^2 + E_b^2 + E_c^2)^{1/2} \quad (1.11)$$

1.2.2.1.4 Peak Shape

The factors affecting peak width yield a Gaussian shape to the resultant peak, however other factors such as the emission of the photoelectron lend a Lorentzian character as well. In addition to the Gaussian/Lorentzian character of the peak conducting samples have a tail toward the higher binding energy side. When the photoelectron is ejected it leaves behind a positive hole which interacts with the conduction band electrons causing this tailing of the peak.

1.2.2.1.5 Spin Orbit Splitting

When an electron is emitted from any orbital other than an s orbital coupling occurs between the spin of the electron remaining and the orbital angular momentum in which it resides. Two final states are possible: spin up or spin down as illustrated in Figure 1.8. This results in the peak for that core level being spin orbit split into two peak components with some separation in eV. The relative areas of the spin orbit peaks have a definite ratio dependent on the degeneracies of these states, given by $2j+1$. Table 1.1 shows the notation for angular momentum at each core level that has spin orbit splitting.

1.2.2.2 Secondary Peak Structural Features

Other features present in peaks appear under certain circumstances and must be defined and recognized for accurate interpretation of data.

1.2.2.2.1 Multiplet Splitting

Figure 1.6 is a Cr2p spectrum which shows the Cr2p_{1/2} and Cr2p_{3/2} spin orbit split peaks as well as the multiplet splitting satellite feature occurring at the higher binding energy side of the spectrum. Multiplet splitting occurs when there is photoemission of a closed shell in the presence of an open shell (unpaired electrons) and results in a satellite feature. The unpaired electron left in the core level which the photoelectron was ejected interacts with an unpaired valence electron. The chromium trioxide (Cr₂O₃) shown in Figure 1.8 is a Cr^(III) compound having three unpaired electrons in the 3d orbital. In this spectrum the effect of the multiplet splitting is clearly seen about 597.6 eV.

1.2.2.2.2 X-ray Source Satellites and Ghost Features

Often the electromagnetic spectrum generated by the source X-ray tube has more than one line of intensity that may be close enough in intensity to create additional features in a spectrum. In example, the K_{α3,4} satellites appear approximately 10 eV lower in binding energy than the main K_{α1,2} excited peak. Figure 1.9 shows a Ag 3d core level spectrum acquired via an achromatic MgK_α radiation source. Not only are there the Ag3d_{3/2} and Ag3d_{5/2} spin orbit split components, but there are also plasmon features (denoted by p), but there are satellite features from the Ag3d_{3/2} (indicated by 3 and 4) as well as four additional satellite peaks from the Ag3d_{5/2} region (marked 3', 4', 5' and 6').¹² These features are not present with the use of monochromatic radiation.

The magnesium or aluminum metal used to provide the characteristic X-rays is sputtered onto a copper X-ray target. Over a period of time the coating degrades and underlying copper may be exposed. The resulting X-rays from copper will also produces peaks of a different binding energy (recall Equation 1.3). These peaks are referred to as *ghosts* and usually

appear at 556.9 and 323.9 eV lower kinetic energy than the respective Al $K\alpha_{1,2}$ and Mg $K\alpha_{1,2}$ lines.

1.2.2.2.3 Plasmon Features

During the collision of an ejected electron with surrounding environment collective oscillations may occur within the metallic sea of valence electrons. These quantized oscillations are referred to as plasmons and appear on the low kinetic energy side of the peak from which the electron was emitted. If the oscillation originated during step 2 of the 3-step emission process the plasmon is labeled as a bulk plasmon. Surface plasmons are created during the third step as the ejected photoelectron leaves the solid and moves into the vacuum level.

1.2.2.2.4 Shake-up and Shake-off Satellites

The perturbation of the valence electrons resulting from the reorganization (or relaxation) in response to the effective increase in nuclear charge can excite one of the valence electrons such that it may be ejected (shake-off) or be promoted into an unoccupied level (shake-up). The kinetic energy of the initial ejected photoelectron is reduced as the perturbation takes energy from the incident photon. The discrete structure appears on the high binding energy side of the $K_{\alpha_{1,2}}$ peak. These so-called shake-up and shake-off satellites are also referred to as configuration interaction satellites.

1.2.3 Auger Features

Another process that occurs concurrently with photoelectron emission is the Auger process which is illustrated in Figure 1.11. After a core level electron is ejected it is possible for an electron from a higher energy level to fill the hole left by the emitted electron and transfer the difference in energy between the two levels to another electron from the same higher energy level. When this occurs the electron which is the recipient of the energy transfer (still in the higher energy level) is ejected as well. The resulting peaks differ from peaks generated by the photoelectron emission process in that they represent a two-electron process. The Auger peaks

also appear in XPS spectrum but interpretation of the data presented by them is much more involved than those of the one-electron photoemission process.

1.3 Data analysis techniques

1.3.1 Curve Fitting

Core level spectra contain data about the chemical state of an analyzed element. A photoelectron peak most often contains several overlapping peaks resulting in electrons originating from the same element in different chemical environments. It is advantageous to resolve the different components of a peak. Having a good understanding of the chemistry involved with the experiment allows for reliable interpretation of the component peaks.

In Figure 6.1 three spectra from the O1s region are shown. The chromium foil as-received O1s region has three features associated with three different forms of oxygen which are not obvious at first glance without the deconvoluted peaks being curve fit. The chromium oxide appears at 530.8 eV, hydroxide is at 532.3 eV and oxygen associated with water shows at 533.7 eV.

Professor Sherwood has designed the GAMET program to perform non-linear least squares analysis on the spectrum. There are seven parameters for the characteristic features of a peak. A peak can be described by its position, intensity, and width. It is further described by the peak shape which are dictated by the percent Gaussian/Lorentzian mixing ratio, the height of the constant tail (if present), the slope of the exponential tail and the tail mixing ratio. The background slope and intercept are also taken into account. Each peak curve fit consists of $7n+2$ variable parameters, where n equals the number of component peaks in the spectrum.

1.3.2 Atomic Ratio Calculations

Core level peaks are proportional to the number of atoms originating from a given chemical environment. The peaks are described in two dimensions by their area which is the number of counts multiplied by the step size in eV. The peak intensity may therefore be

expressed as the measurement of the peak area. The area, or intensity, may be used to calculate atomic ratios if it is assumed that the peak is being described by data arising from a uniform surface (usually not the case). The accurate determination of peak intensity necessitates removal of the background. There are several approaches that can be used but our group uses the Proctor-Shirley background removal method. This method is based on the Shirley iterative method which assumes that the background intensity at a given point is proportional to the intensity of the total peak area above the background and to a higher energy than the data point.

Once peak intensities are obtained the atomic ratios can be determined by employing the following equation¹³:

$$n_x/n_{ref} = (A_x/A_{ref})(\alpha_{ref}/\alpha_x)(\sqrt{KE_x}/\sqrt{KE_{ref}})(\lambda_{ref}/\lambda_x) \quad (1.12)$$

where,

n_x = number of atoms in core level of interest, x refers to core level of interest

n_{ref} = number of atoms in the reference core level, ref refers to the reference core level

A = experimentally derived area of the core peak (A=(peak area x step size)/number of scans)

α = the photoelectron cross section of the core level

KE = the kinetic energy of the core level peak

λ = the inelastic mean free path of the electrons from the level. This value is usually determined from the Seah and Dench equations¹³. Atomic ratios are usually referenced to the core level of the substrate material, but other species of interest in the sample may be used.

When interpreting atomic ratios from core level data, one must bear in mind that the contributions from a given spectral area are usually not from a single component. The results may be misleading if the ratio doesn't match the empirical formula of the species assumed present, as often happens with the O1s core data which not only includes the oxide data but also oxygen counts from adsorbed water or CO common in UHV environments.

1.4 Acknowledgements

Grateful acknowledgement is given to Dr. Peter M. A. Sherwood, Dr. M. P. Seah and Dr. D. Briggs for the figures and data reprinted from their book.

1.5 References

1. Heinrich Hertz, *Ann. Phys.*, **33**, 983, (1887).
2. D. Briggs, M. P. Seah, *Practical Surface Analysis Vol 1: Auger and X-ray Photoelectron Spectroscopy*, 2nd ed., Wiley and Sons, Inc.: New York, (1990).
3. C. N. Berglund and W. E. Spicer, *Phys. Rev.*, **136**, (1984).
4. C. J. Powell, *Surf. Sci.*, **44**, 29, (1974).
5. I. Lindau and W. E. Spicer, *J. Electron Spectr. Relat. Phenom.*, **3**, 409, (1974).
6. T. A. Koopman, *Physika I*, **104**, (1933).
7. K. Siegbahn, et al., *ESCA: Atomic, Molecular and Solid State Studied by Means of Electron Spectroscopy*, *Nova Acta Regia. Sci.*, Ups. Ser. IV 20, (1967).
8. <http://www.nist.gov>
9. A. Einstein, *Ann. Physik*, **17**, 132, (1907).
10. M. P. Seah and W. A. Dench, *Surf. Interf. Analy.*, **1**, 2, (1979).
11. J. F. Watts and J. Wolstenholme, *An Introduction to Surface Analysis by XPS and UPS*, John Wiley and Sons, Ltd.: Chichester, West Sussex, England, (2003).
12. G. K. Wertheim and P. H. Citrin, *Photoemission in Solids I*, Topics in Applied Physics Vol 26, M. Cardona and L. Ley, ed., Springer-Verlag, Berlin, (1978).
13. M. Seah and W. Dench, *Surf. Interface Anal.*, **1**, 2, (1979).

1.6 Figures

Figure 1.1 2-D Representation of Surface layers compared with probe method depth.

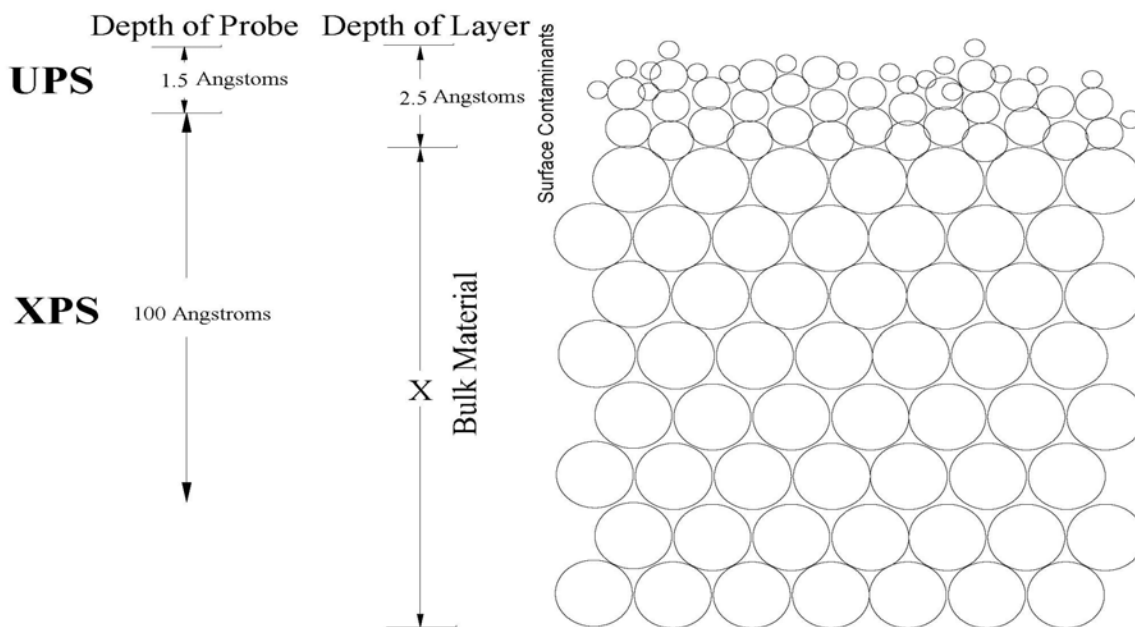


Figure 1.2 Illustration of the concept of escape depth of photoelectrons. Incoming electromagnetic radiation is represented by $h\nu$, an elastically ejected electron is represented by e and an electron which has lost energy due to a collision and is inelastically ejected is represented as e' .

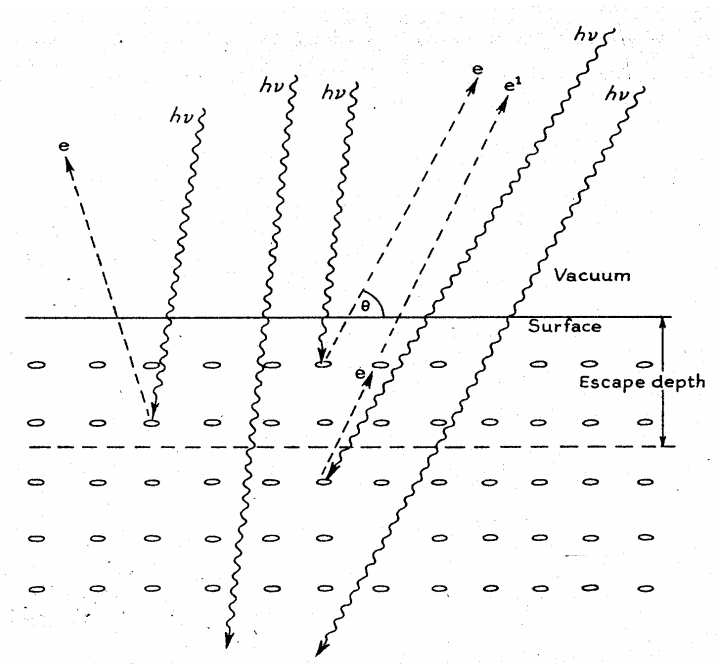


Figure 1.3 A wide energy range scan of Ar+ etched 99.99% chromium foil.

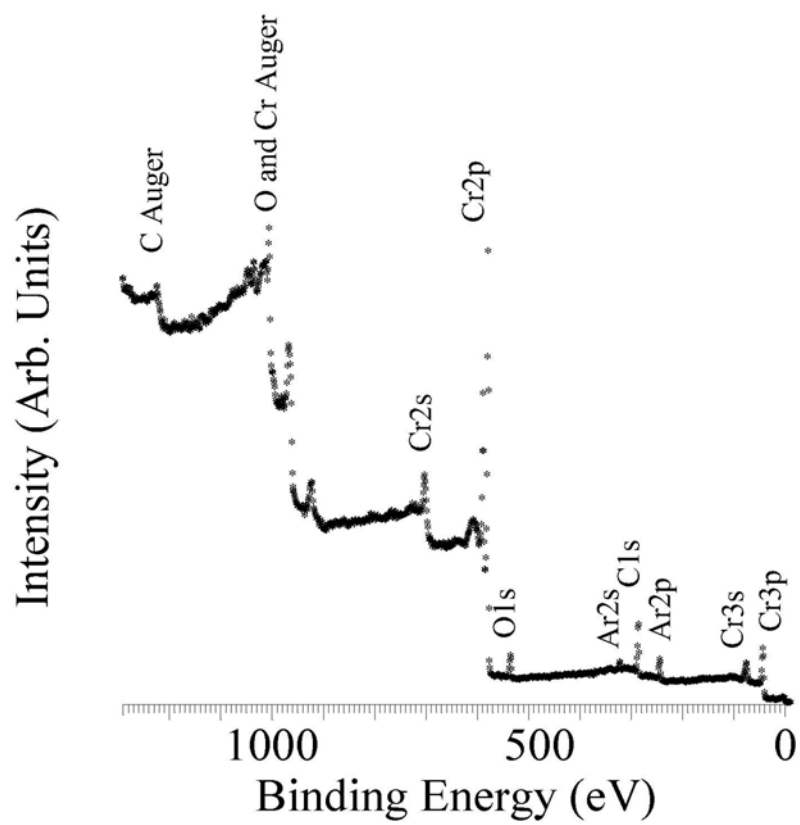


Figure 1.4 The excitation and photoemission process. On the left incident X-radiation excites electrons which are emitted; electrons A and B have undergone a collision resulting in loss of kinetic energy. On the right is a diagram of the emission of a 1s core level electron.

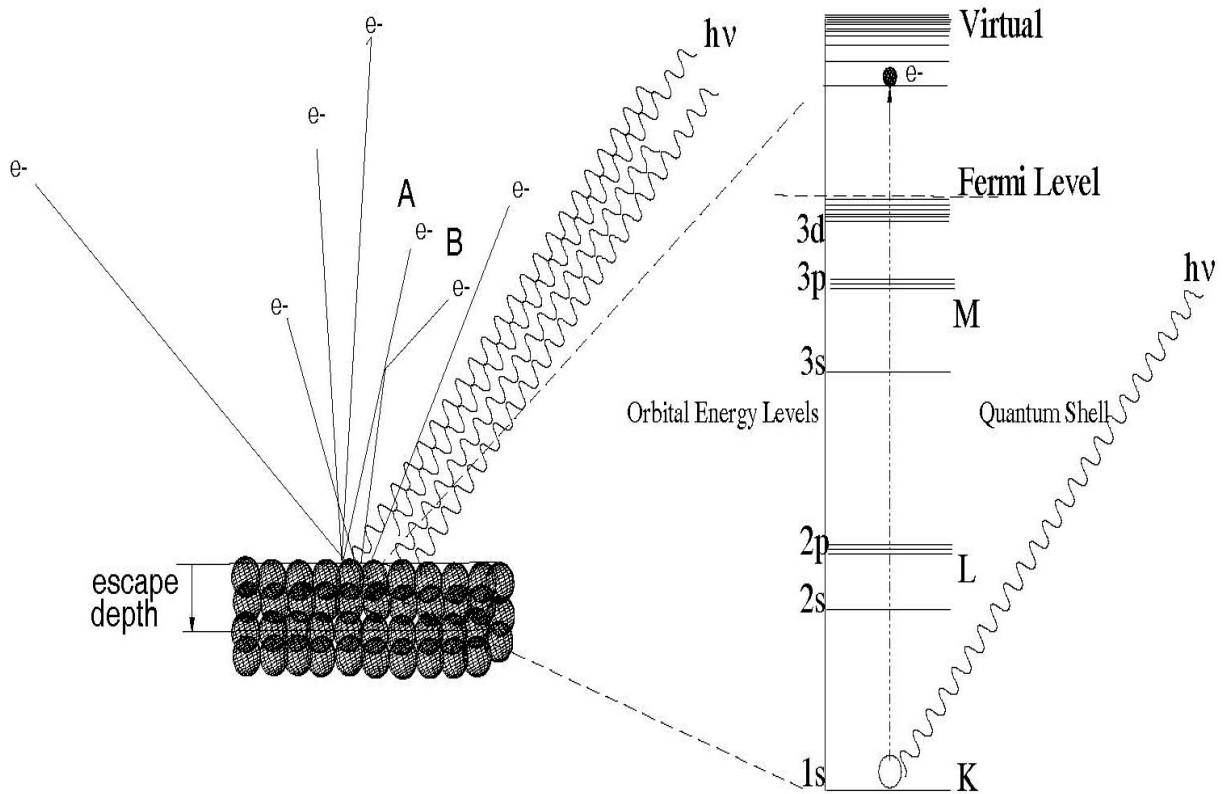


Figure 1.5 The dependence of attenuation length, which is approximately 10% less than the IMFP, on the emitted electron energy. The energy dependency is the same for the IMFP. (After Seah and Dench ¹³)

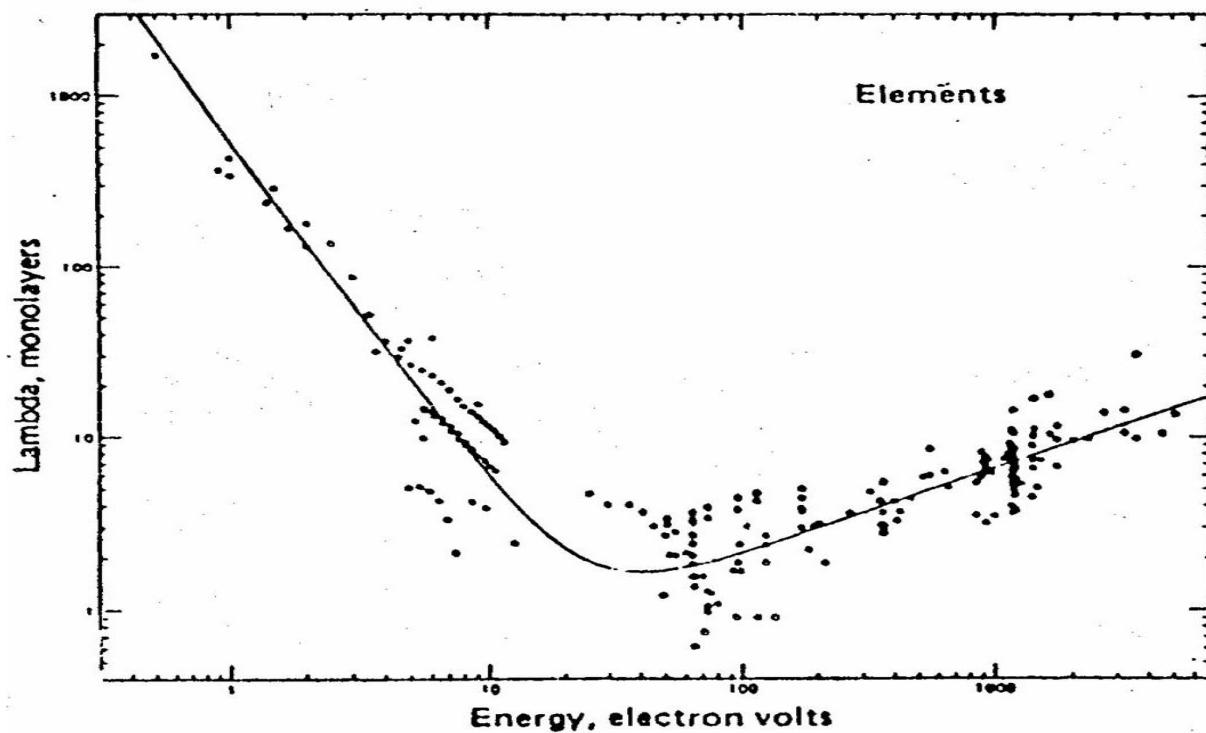


Figure 1.6 The Cr2p core level spectra of a series of chromium oxides. CrO3 is Cr(VI), CrO2 is Cr(IV) and Cr2O3 is Cr(III).

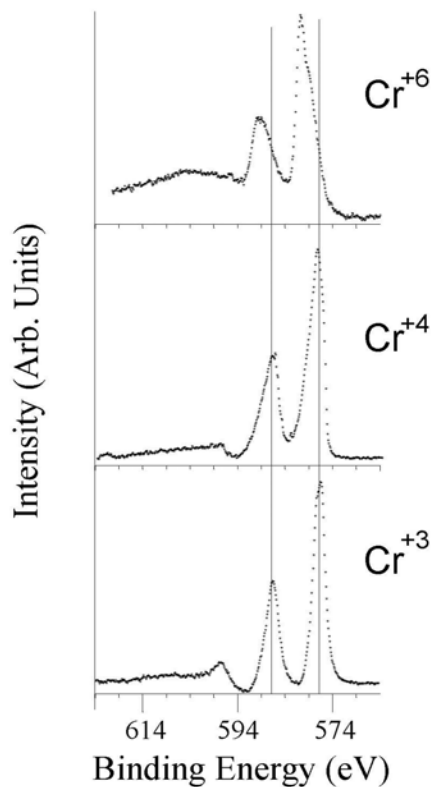


Figure 1.7 Intensity of emitted photoelectrons as a function of depth. The dashed line represents a distance from the surface above which 95% of the observed photoelectron signal originates. This escape depth is a function of the IMFP or attenuation length. This is what makes XPS a surface sensitive technique.

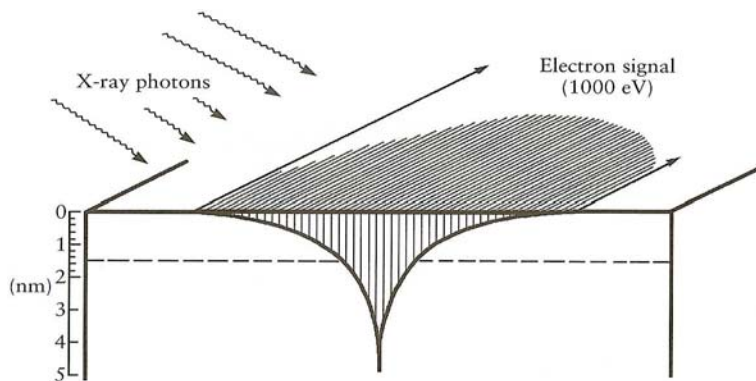


Figure 1.8 Coupling between the magnetic fields of spin angular momentum (s) and orbital angular momentum produces the spin orbit splitting observed in core levels p, d and f.

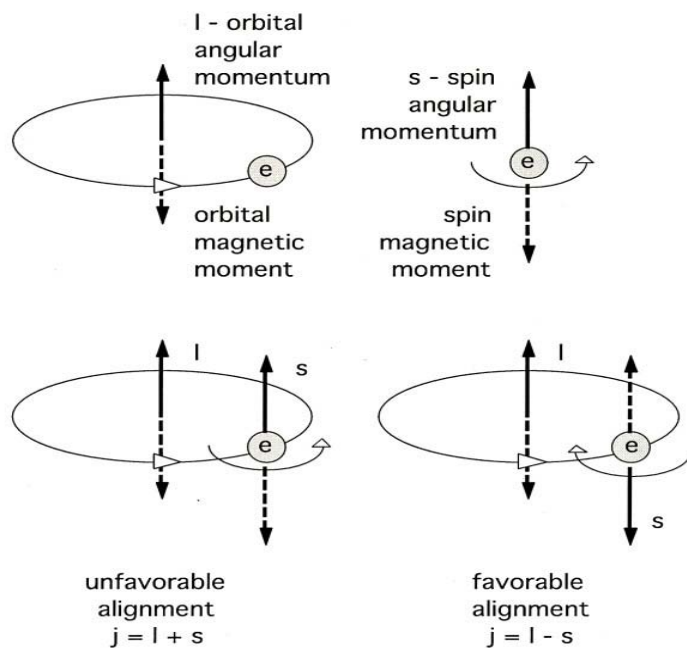


Figure 1.9 Cr2p core level spectra of chromium sesquioxide (Cr_2O_3) obtained using monochromatic Al $\text{K}\alpha_{1,2}$ X-rays. Note the spin orbit split Cr2p_{1/2} and Cr2p_{3/2} (lower BE) features and the satellite caused by multiplet splitting at 598.6 eV.

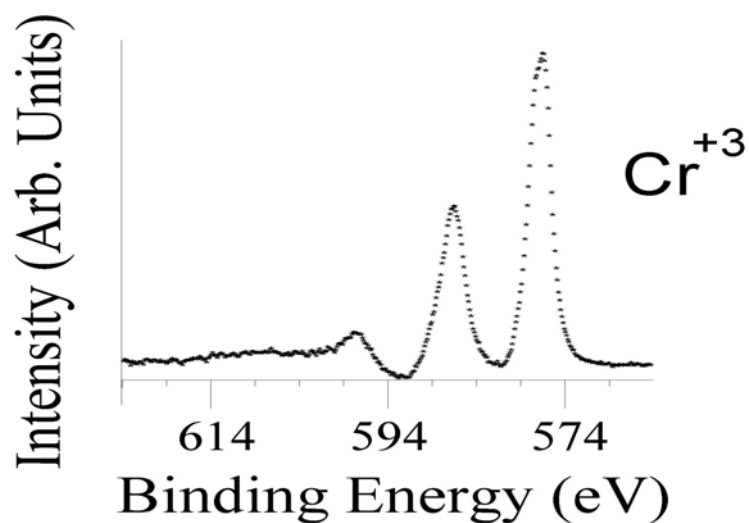


Figure 1.10 Ag3d core level spectrum obtained using achromatic MgK $\alpha_{1,2}$ incident X-radiation. The dominant features are the Ag3d $_{3/2}$ and Ag3d $_{5/2}$ spin orbit split components. The labeled features are satellites.

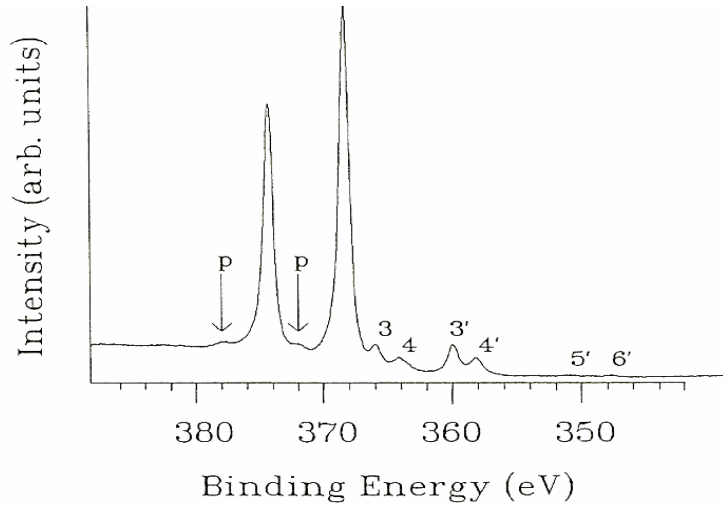
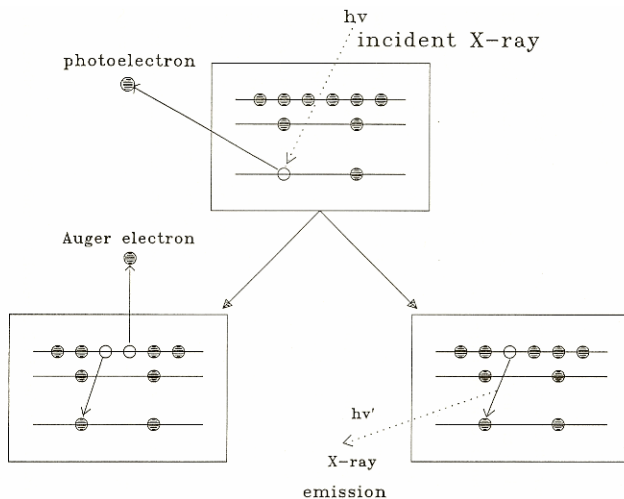


Figure 1.11 The three possible events following excitation of an electron by soft X-ray light. The top process represents photoelectron emission, the bottom left is the Auger process and the bottom right represents the occurrence of X-ray emission (not covered here).



1.7 Tables

Table 1.1 Total angular momentum $j = |l \pm s|$; l =quantum number for electron orbital angular momentum; s =quantum number for the electron spin (either up or down).

N	Quantum numbers			Atomic notation	X-ray notation
	l	s	j	$n l_j$	
1	0	$\pm 1/2$	1/2	1s _{1/2}	K ₁
2	0	$\pm 1/2$	1/2	2s _{1/2}	L ₁
2	1	+ 1/2	3/2	2p _{3/2}	L ₂
2	1	- 1/2	1/2	2p _{1/2}	L ₃
3	0	$\pm 1/2$	1/2	3s _{1/2}	M ₁
3	1	- 1/2	1/2	3p _{1/2}	M ₂
3	1	+ 1/2	3/2	3p _{3/2}	M ₃
3	2	-1/2	3/2	3d _{3/2}	M ₄
3	2	+ 1/2	5/2	3d _{5/2}	M ₅

Degeneracy = $2j + 1$		
Subshell	j values	Degeneracy
s	1/2	
p	1/2, 3/2	2, 4 = 1, 2
d	3/2, 5/2	4, 6 = 2, 3
f	5/2, 7/2	6, 8 = 3, 4

CHAPTER 2 - Instrumentation Utilized In XPS

2.1 The Vacuum System

Any surface analysis requires a surface which is free from contamination. Surfaces exposed to atmosphere will attract contaminating molecules which can cover it, thereby obscuring the substrate and interface. To facilitate the collection of data representative of the actual well-ordered surface layers vacuum systems are employed. A vacuum must be maintained throughout the data collection timeframe in order to maintain the contamination-free state.

Another reason for the use of vacuum systems is to allow relatively low energy electrons to travel from surface to detector without colliding with gas molecules which would cause loss of kinetic energy. To avoid gas phase scattering the level of vacuum can be estimated by determining the length of time for the surface to be covered with a monolayer of adsorbants. The precise values for the flux of gas molecules impinging on the surface, the actual sticking coefficient and the actual coverage corresponding to a monolayer are not necessarily required. An estimate which would suffice can be made by assuming a sticking probability of 1 (unity) and noting that the average monolayer is on the order of 10^{15} cm^{-2} . When time/monolayer is considered, pressures at 10^{-10} Torr (considered ultra-high vacuum) allow for a monolayer to form in 10^4 seconds. At the high vacuum level of 10^{-6} Torr the monolayer will form in 1 second and 10^{-9} seconds is required for monolayer formation at atmosphere. Generally a vacuum of 10^{-4} Torr is sufficient to provide collision free conditions and 10^{-9} Torr will maintain a clean surface. ¹

2.2 General XPS Instrumentation Arrangement.

The vacuum system consists of chambers into which a sample can be moved for treatment and/or examination. Once the sample is placed on a sample holder it is attached to a device which can position the sample where needed while maintaining vacuum conditions. The sample is loaded then the chamber is pumped down to ultrahigh vacuum (UHV) conditions.

The general layout for a spectrometer used in XPS is shown in Figure 2.1. The sequence of steps which occur during XPS analysis follow the path along the components of the spectrometer beginning with the generation of X-rays.

Once UHV is attained the sample is moved to a position on what is known as the Rowland circle. Henry Rowland showed that if a grating, in this case a monochromator, is placed at a tangent to a circle of diameter equal to the radius of curvature of the concave grating and the entrance of the radiation lies on the same circle, then a focused spectrum will be produced on that circle.² Figure 2.2 is a schematic of the Rowland circle as utilized in XPS. The X-ray source, monochromator and the sample are all carefully positioned tangent to this circle.

2.3 Generation of X-rays and Use of a Monochromator

The X-ray source consists of a water-cooled anode which has the target region(s) coated with the metal which will produce the characteristic X-rays. A current is applied to a thorium coated filament which emits electrons that are accelerated onto the anode at very high potential (12kV for Mg and Al $K\alpha$). The twin anode style of target has two target regions usually coated with magnesium on one side and aluminum on the other. When the accelerated electrons from the target reach the anode soft X-rays characteristic of the anode metal coating are generated.

All X-ray light produced is achromatic in nature. Anode materials are selected which have sufficient X-ray energy to produce excitation in most core electrons and have a natural line width to allow for sufficient resolution of spectral features. Mg $K\alpha_{1,2}$ has a radiant energy of 1253.6 eV and a line width of 0.7 eV while Al $K\alpha_{1,2}$ light is produced at 1486.6 eV and has a natural linewidth of 0.85 eV. Selecting the higher energy X-rays allows for deeper penetration of the sample which is useful with samples composed of layers of composition. An additional benefit to using Al $K\alpha_{1,2}$ light is that its wavelength is the same as that required for optimum diffraction in a quartz crystal grating in a monochromator.

High resolution spectra can be achieved by narrowing the line width of the incident light. An X-ray monochromator narrows the range of energies produced by the achromatic radiation source. This is accomplished by directing the X-rays to a quartz crystal grating which diffracts the light and focuses a selected monochromatic light onto the sample located on the Rowland circle. The quartz crystals are precisely ground along the 1010 plane and toroidally bent to satisfy the Bragg angle condition for diffraction of radiation which is given in the equation:

$$n\lambda = 2d\sin\theta \quad (2.1)$$

Where,

n = some positive integer; for these purposes $n=1$

λ = wavelength of the light used

d = the distance between planes in the crystal unit cell

and θ = the angle of incidence/reflection as shown in Figure 2.3. For Al $K\alpha_{1,2}$ radiation this angle is 78.5° .³ This allows for the incident Al $K\alpha_{1,2}$ linewidth to be reduced to approximately 0.2 eV. Not only does the monochromatic radiation provide greater resolution, interfering satellite features are eliminated and Bremsstrahlung radiation which raises the spectral background and degrades samples is eliminated as well. The improvement in resolution and spectral quality are represented in Figure 2.4.⁴

2.4 The Lens System

Photoelectrons ejected from the sample travel through vacuum to the lens system. The lens system is an electrostatic configuration of two concentric cylinders or apertures held at differing potentials. Figure 2.5 is a schematic of the Omni Focus Lens produced by Physical Electronics of Eden Prairie, MN. As the photoelectrons enter the lens they are steered and focused onto an entrance slit into the next stage of the system which retards the electron beam in order to obtain adequate resolution since the resolving power of the analyzer decreases with increasing electron energy. A much larger hemispherical analyzer would be required without this retarding of energy to produce the same resolution.⁵

2.5 The Analyzer

The beam of photoelectrons focused in the lens system enter through an extremely small source slit into a kinetic energy analyzer. Most XPS instruments employ either a concentric hemispherical analyzer (CHA) or a cylindrical mirror analyzer (CMA).⁶ In the CHA utilized in this laboratory a voltage bias is applied to both the inner and outer plates of the analyzer, shown in Figure 2.6, producing an electrostatic field between the two concentric hemispherical plates. The applied voltage to the inner hemisphere is positive with respect to the outer hemisphere. The pass energy, or the energy required for an electron entering at the source

slit (S) to pass through the CHA, focused and exit through the focus slit (F) and pass to the detector, is determined by the electrostatic field between the two hemispheres. Electrons of energy differing from the pass energy travel in a circular trajectory causing them to collide with some other point in the analyzer.

Two modes of operation are used in the analyzer, fixed analyzer transmission mode (FAT) or Fixed Analyzer Resolution (FRR) mode. In FAT mode the analyzer maintains a constant pass energy through out the scan. This limits the electrons passing through the analyzer to a selected range of kinetic energy. The resolution of the analyzer is best at the lowest possible pass energy because the spread of energies across the entrance slit is reduced. Operating the analyzer in the FAT mode produces a spectrum with higher counts at low kinetic energies and lower counts at high kinetic energies. At the FRR setting the incoming electrons are retarded prior to entering slit S of the analyzer governed by a set ratio of their original energy. In this manner only electrons of an appropriate ratio possess kinetic energy sufficient to reach the detector. This results in a spectrum with a constant background.⁷

2.6 Electronic Detector Systems

The photoelectron detector is located at the F slit in the analyzer. Electrons entering the detector are of a narrow range of energies as a result of the pass energy in the analyzer and the size of the exit slit. A channel electron multiplier is mounted behind the exit slit of the analyzer and amplifies the incoming photoelectron event into a measurable signal. In achromatic sources the flux of electrons is large enough to produce intense spectral features with a single channel detector.

2.6.1 Single channel detection

When a photoelectron enters the channeltron, as shown in Figure 2.7, it strikes the side of the internal wall (channel) which is coated with emissive material that ejects additional electrons which are accelerated down the tube. These in turn strike the wall further into the tube producing still more electrons. This process continues creating an electron avalanche. One entering electron produces a 10^{-9} second charge pulse containing up to 108 electrons.⁸

2.6.2 Multichannel detection

Alternatively, a multichannel detection system may be employed for photoelectron detection. This arrangement allows for a spread of kinetic energies to be detected simultaneously. The whole electron image is focused onto several detector channels rather than part of the image focusing on one channel. This has two results: the signal to noise ratio is improved for the given collection time and the collection time is reduced. The HA 150 multichannel detector has 16 channels as diagramed in Figure 2.7. A series of capillary tubes of diameter 10-20 μm and arrayed in a thin microchannel plate amplify the incoming signal. Each capillary tube operates on the same principle as the channeltron and is positioned at a 13° angle away from the surface normal. Two channel plates are placed in a chevron configuration to ensure entering electrons strike the walls of the capillaries. The electrons are accelerated by creating a positive bias gradient from 400V at the electron entrance end to 2kV where the charge pulse is detected by 16 gold anode wires equally spaced in energy. The resulting signal is fed to the data handling system. This laboratory's HA 150 X-ray photoelectron spectrometer is pictured in Figure 2.8.

2.7 Techniques Utilized in XPS Experiments

2.7.1 Charge Compensation

During the photoemission process electrons are ejected from the sample, which presents no problem for conducting samples as electrons within it are free to move in the "sea" of electrons characteristic of metallic bonding. In a sample which has insulating properties sample charging occurs as the sample develops a more positive charge with each ejected electron. A low energy flood gun is employed to supply low energy electrons to the sample to replace those which have been ejected in the photoemission process. The effects of flood gun usage are demonstrated in Figure 2.9.

2.7.2 The Anaerobic Cell

An oxide-free metal surface is required for the formation of ultra thin phosphate films.⁹ An adaptation to the HA150 spectrometer was developed in this research group which provides a

means of creating an oxide-free metal surface.¹⁰ The instrumentation of the vacuum system is modified by fitting it with an anaerobic cell, or chamber that allows for sample treatment in an inert anaerobic environment. This chamber is isolated from the main vacuum chamber by a gate valve so that the sample, once moved into the anaerobic cell, can be placed in an inert anaerobic environment in which wet chemistry can be performed without ever exposing the experiment to ambient oxygen or contaminants until the resulting chemical system has been characterized. The anaerobic cell allows for the metal surface to be monitored during the etching process as well as after the surface chemistry has been altered.

Once etching has removed the native oxide and surface adsorbants, as determined by monitoring the metal and oxygen core regions, the sample is moved into the cell using a motorized sample arm. The anaerobic cell is then isolated from the main chamber of the vacuum system by a gate valve and brought up to a slightly positive pressure using an ultra pure inert gas such as argon creating an inert anaerobic atmosphere in which to conduct the experiment. Performing an experiment in this fashion prevents any ambient air or contaminants from entering the chamber during the procedure.

The deaerated liquid reagent is introduced into the electrochemical cell via the luggin capillary. An electrochemical apparatus adaptation may also be used to perform electrochemistry. The sample is then immersed into the solution for the duration of the reaction time. Once the reaction has progressed for the prescribed amount of time the acid solution is drained from the cell and deaerated 4-D H₂O is utilized in rinsing the sample. The water is drained from the cell, the reaction vessel is removed and the sample is returned to high vacuum and allowed to dry before analysis begins.

2.8 References

1. P. E. J. Flewitt and R. K. Wild, Physical Methods For Materials Characterization, 2nd Edition, Institute of Physics Publishing: Bristol, UK (2003).
2. C. Palmer, Diffraction Grating Handbook, 4th Edition, Richardson Grating Laboratory, Rochester, NY, (2000)
3. J. F. Watts, An Introduction to Surface Analysis by Electron Spectroscopy, Oxford, NY, (1990).
4. G. K. Wertheim and P. H. Citrin, Photoemission in Solids I, Topics in Applied Physics Vol 26, M. Cardona and L. Ley, ed., Springer-Verlag, Berlin, (1978).
5. A. Barrie, Handbook of X-ray and Ultraviolet Photoelectron Spectroscopy, D. Briggs, ed., Heydon and Sons, London, (1977).
6. K. Siegbahn, et al., ESCA: Atomic, Molecular and Solid State Structure Studied by Means of Electron Spectroscopy, Almqvist and Wiksells, Uppsala, (1967).
7. VSW Instruction Manual for the Class Analyzer, VSW, Ltd., Surrey, UK.
8. Galileo Electro-optics Corp., Channeltron Electron Multiplier Handbook for Mass Spectrometry Applications, Galileo Electro-optics Corp., Sturbridge, MA
9. J. Rotole and P. Sherwood, U.S. Patent No. 6,066,403, (23 May 2000).
10. P.M.A. Sherwood, Journal de microscopie et de spectroscopie electroniques, 5 ,475, (1980).

2.9 Figures

Figure 2.1 XPS Spectrometer Set-up. Photoelectrons generated by the X-ray light travel through the lens system and the analyzer before striking the multi-channel detector.

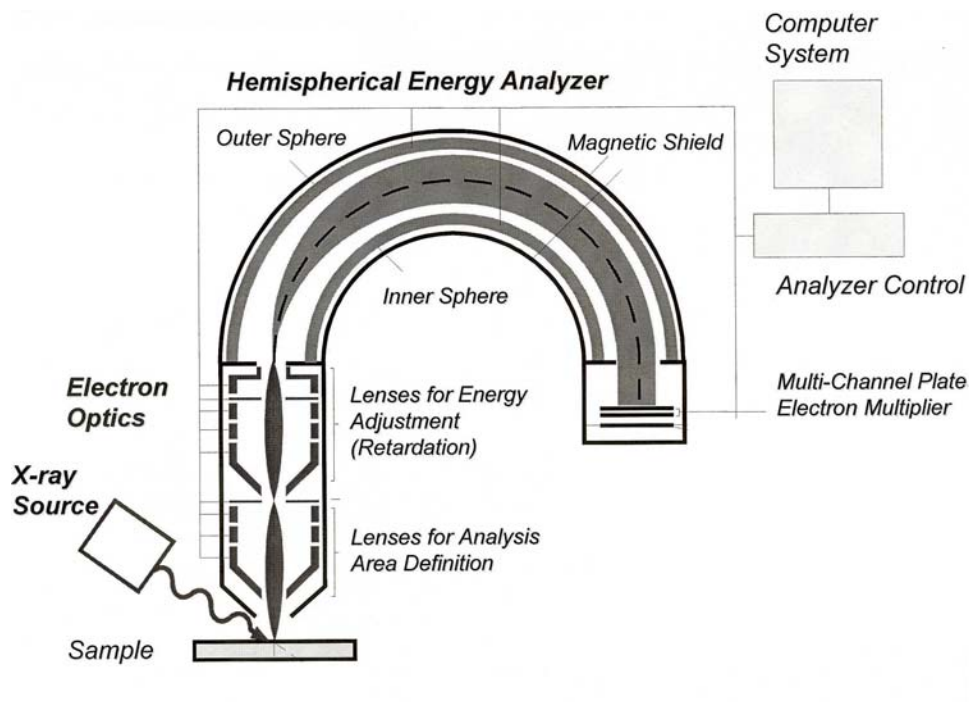


Figure 2.2 The Roland circle.

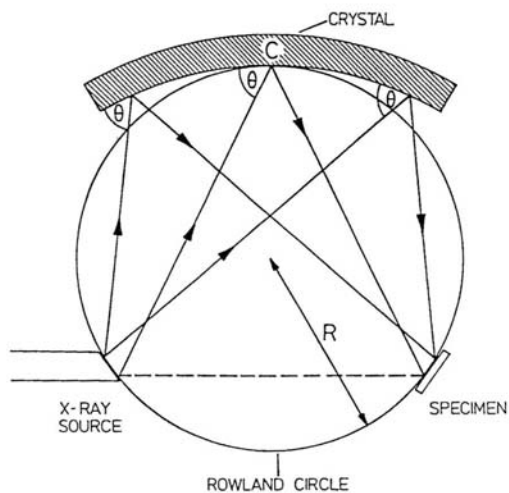


Figure 2.3 Diagram of the application of Bragg's Law: $n\lambda = 2d\sin\theta$.

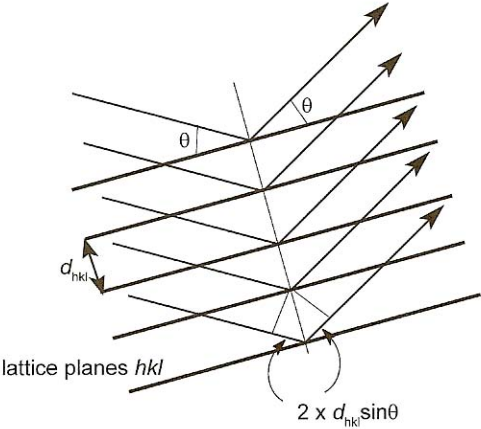


Figure 2.4 Spectral distribution of the Al $K\alpha_{1,2}$ emission line and the effect of monochromatization.

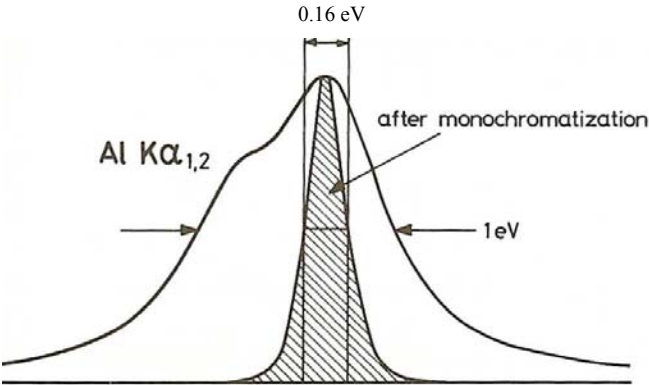


Figure 2.5 Lens System – photoelectrons travel left to right.

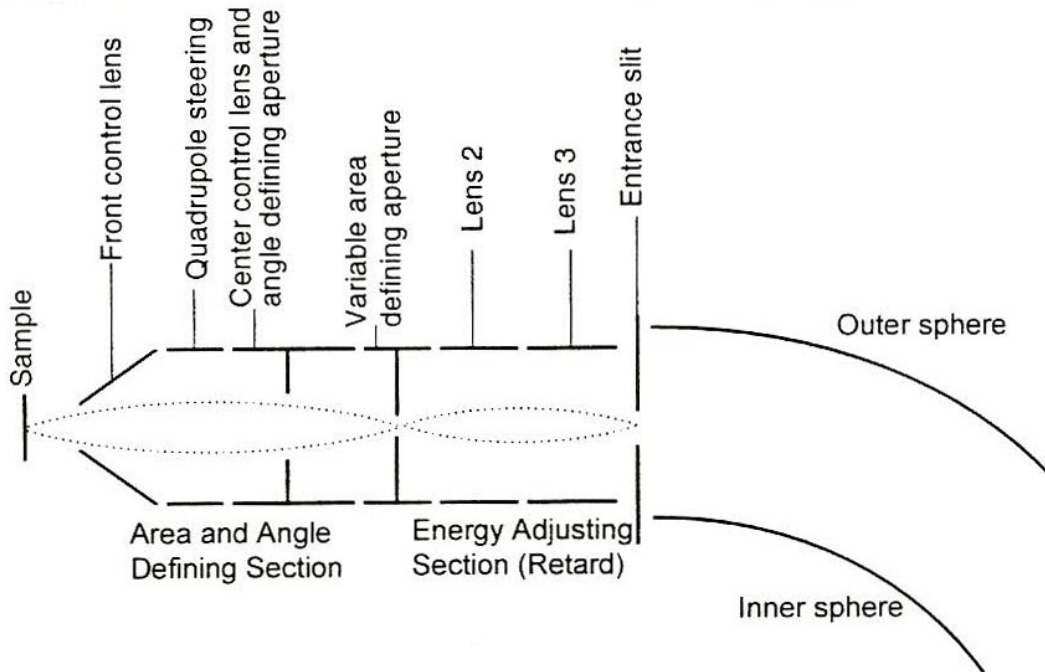


Figure 2.6 Concentric Hemispherical Analyzer (CHA).

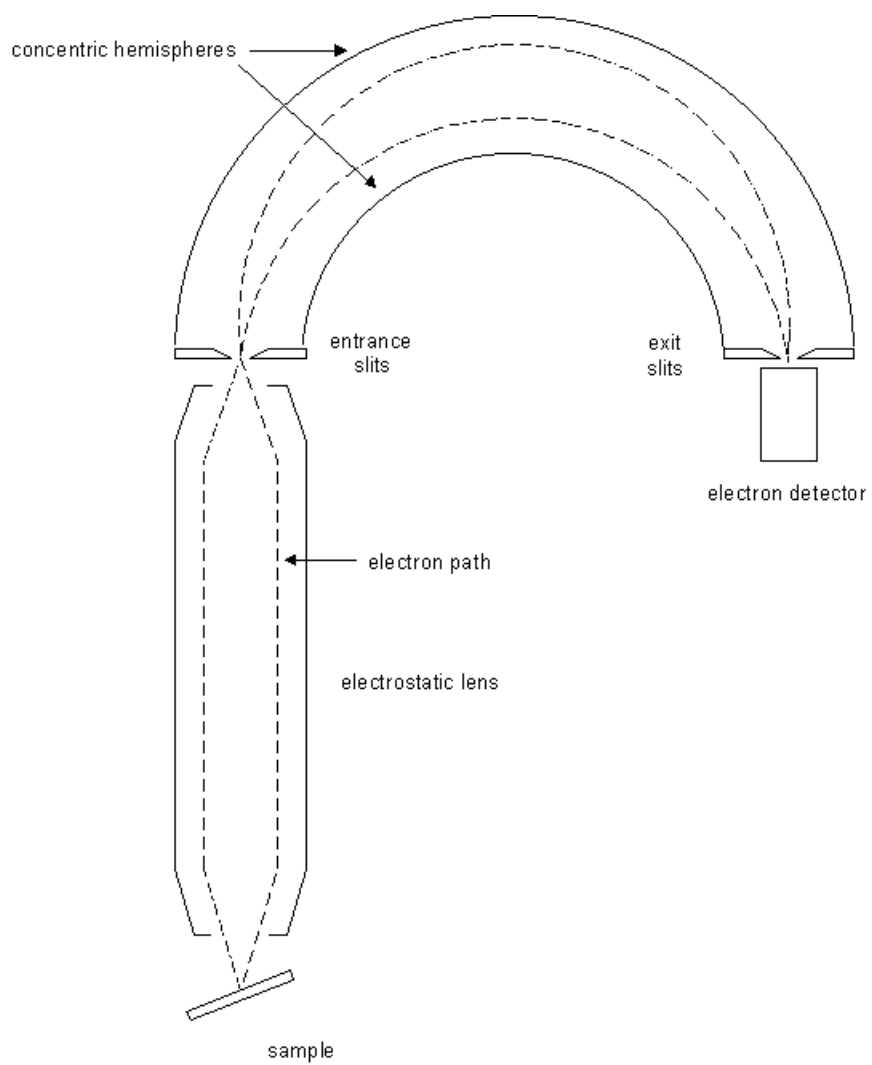


Figure 2.7 Channeltron detector (top) and Multichannel Detector.

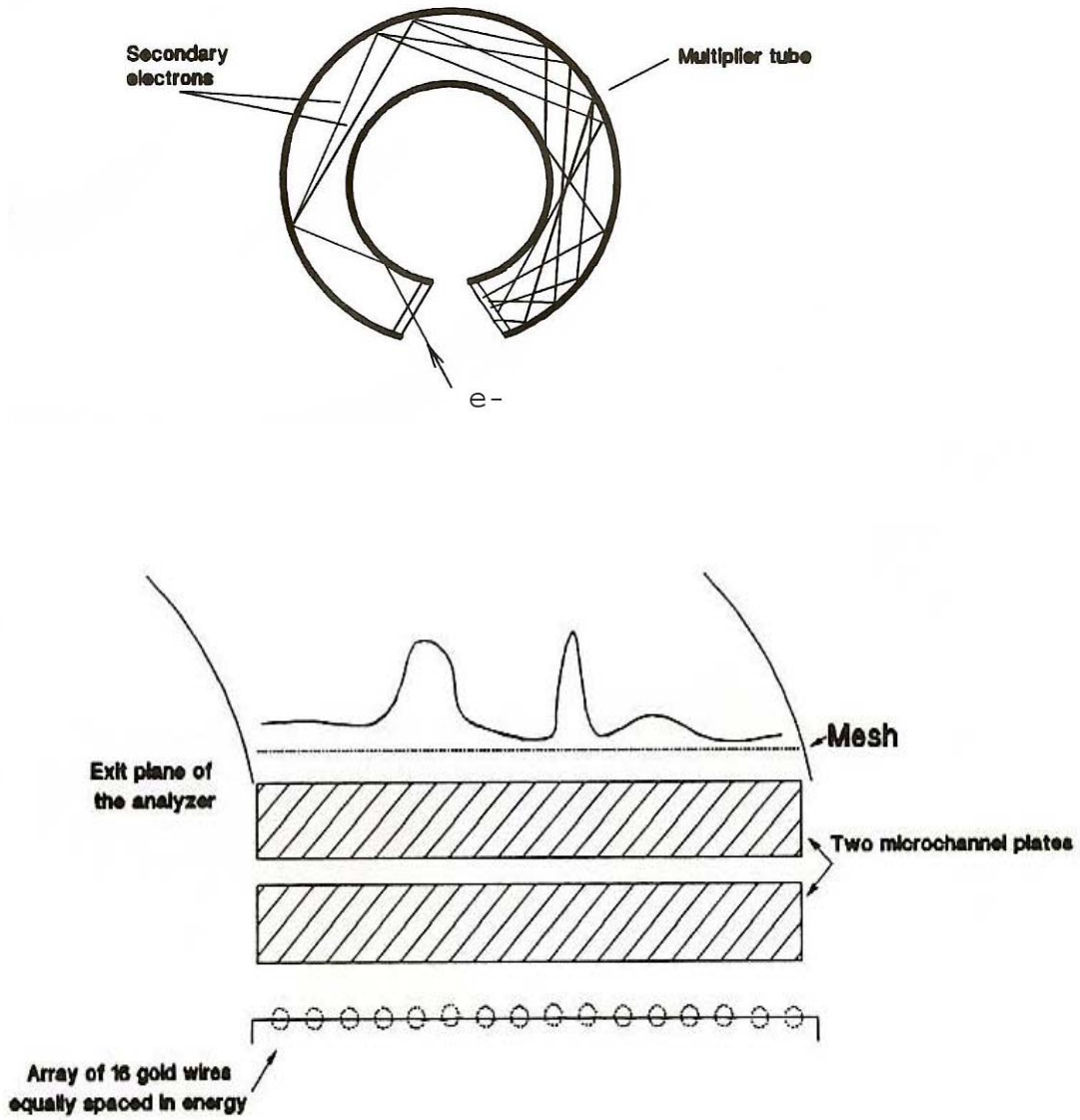


Figure 2.8 Sherwood Surface Science Lab HA 150 Photoelectron Spectrometer.

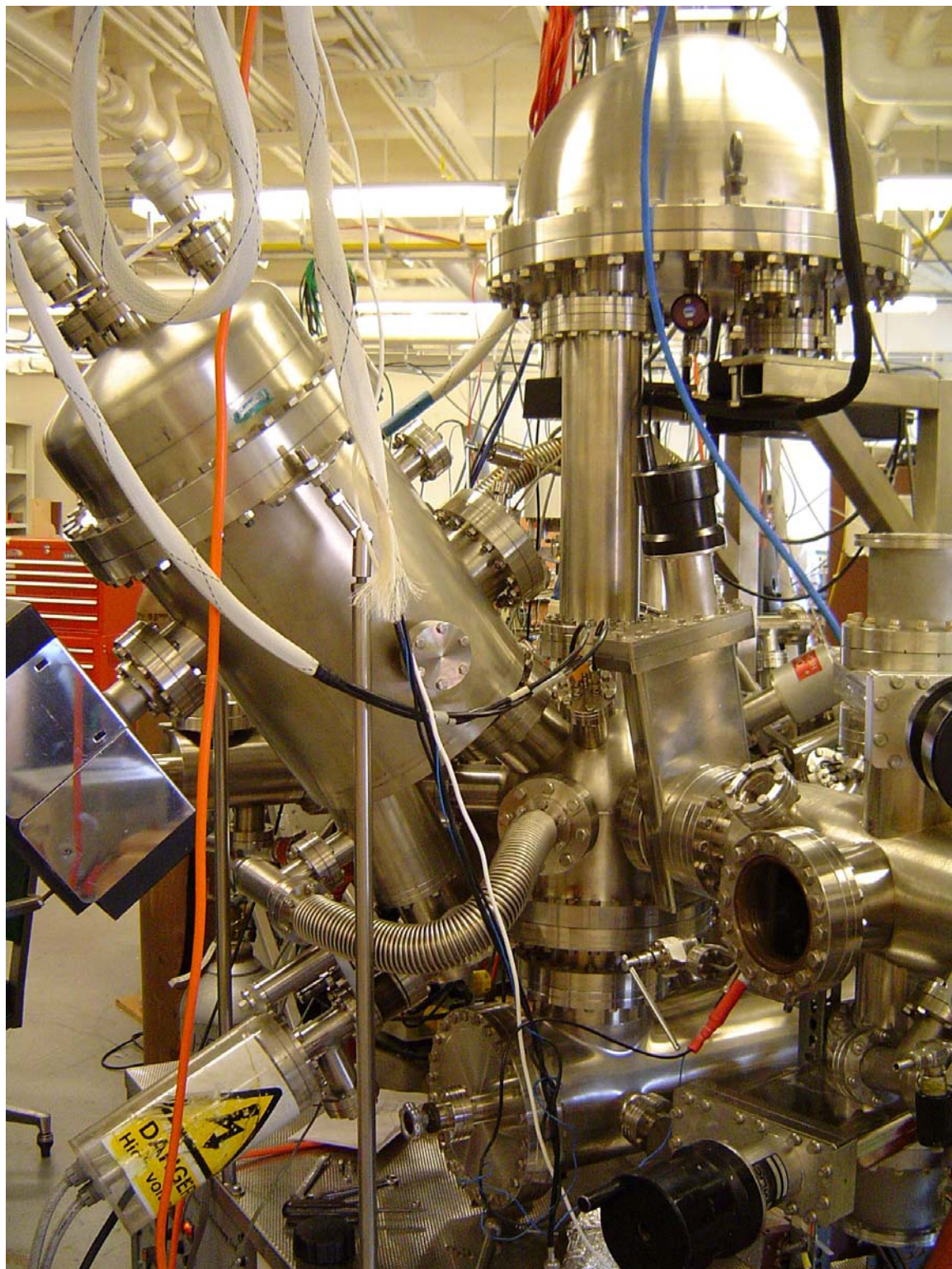


Figure 2.9 Comparison of the effects from use of a flood gun. Without flood gun (a) and using flood gun (b) show there is no change in peak width. The kinetic energy shifts and the line resolution is improved when sample charging is compensated for with a flood gun.

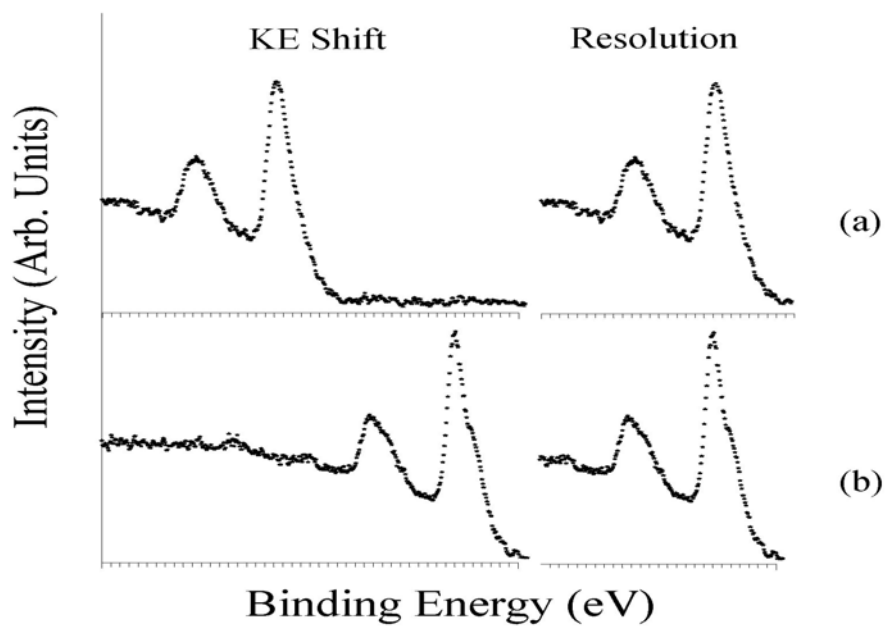
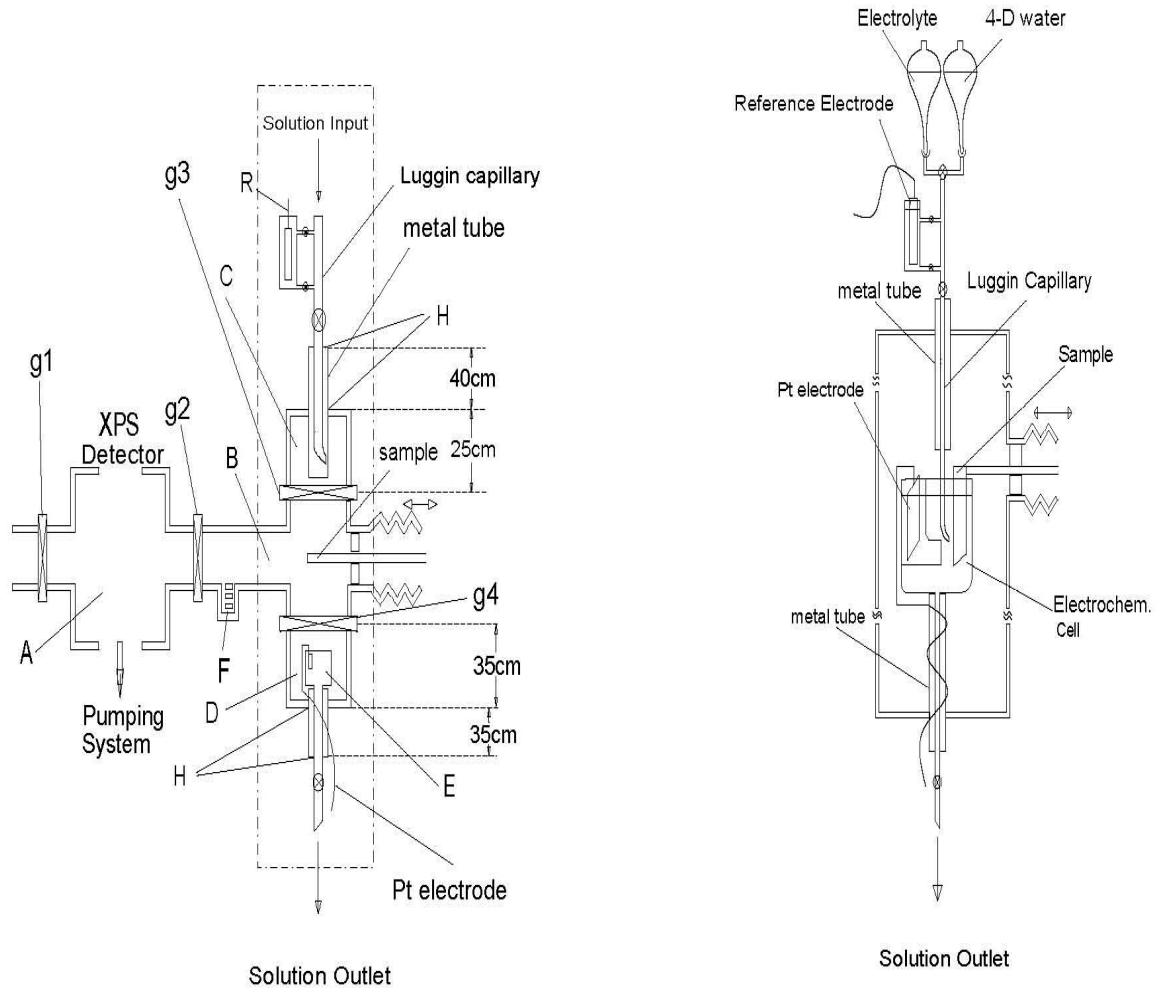


Figure 2.10 Schematic diagram of the Anaerobic Cell modification.



CHAPTER 3 - Corrosion and Inhibition of Corrosion

3.1 Introduction

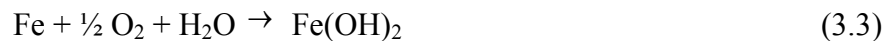
The National Association of Corrosion Engineers (NACE) has defined corrosion as "**the deterioration of a material, usually a metal, that results from a reaction with its environment**". Corrosion is an electrochemical process that is facilitated by the metallic sharing of electrons creating a "sea" of electrons within a metal. Since the electrons are free to move throughout the lattice, metal atoms at the surface are periodically left ionized and can bond with negatively charged ions from the surrounding environment. Once this occurs the new molecular material, having different properties from the substrate metal, becomes a separate phase of the material. The most familiar example is that of iron oxidizing or "rusting". This is chemically represented with the equations:



and



which are combined to produce:



The iron can be further oxidized to Fe^{3+} :



which is insoluble in water and relatively inert. Other "rust" products that can form are FeO , Fe_2O_3 , FeOOH and Fe_3O_4 , to which different equations apply. This example reflects ambient water and oxygen as the "causes" of the corrosion but metals can corrode on contact with acids, bases, salts or even oils.

Corrosion can be obvious, as in the hulls of ships, or insidious and undetected. In Figure 3.1 is a photograph of the results of an incident which occurred in 1988 where a Boeing 737 in the Aloha Airlines fleet had a catastrophic failure of the upper fuselage at 24,000 feet. Corrosion accelerated fatigue at the lap joints of the fuselage skin panels was determined to be the precipitating cause. Additional fatigue cracks were found in the remaining structure and

pillowing of flocculent corrosion material was seen beneath the metal around the rivets.¹ Note in Figure 3.2 how the rivets appear to be sunken into the metal.

The chemistry of corrosion is, in reality, quite complex and has many factors which affect rates of corrosion as well as degrees of deterioration. During the manufacture of the above-mentioned aircraft in 1969 the fuselage skin was attached by an epoxy cold-bonding process at the overlap joints then the rivets were drilled in. It was determined three years later that the surface preparation prior to application of the adhesive strip created an uneven oxide surface that compromised the integrity of the adhesive bond. Compounding the problem was the cold bonding process which attracted condensation before curing.² The need for a deeper understanding of the surface chemistry of the corrosion process has been recognized for many years. Recent surface science investigations have yielded substantial improvements in materials fabrication and design, however many corrosion systems are still not readily understood. Surgical implant failure and materials degradation in the electronic components are but two corrosion issues under investigation.

3.2 Process of corrosion

The corrosion process is classified by whether or not a current is produced. If there is no resultant current the process is referred to as chemical corrosion. Gaseous corrosion and corrosion occurring in nonconducting liquids (non-electrolytes) are chemical corrosion processes. Electrochemical corrosion does produce a current in that the process is accompanied by the flow of electrons between cathodic and anodic areas on a metallic surface. Atmospheric corrosion, which occurs in the presence of a moist gas (e.g. in air), soil corrosion, corrosion in molten salts and corrosion occurring in electrolytic solutions are electrochemical corrosion processes.

3.2.1 Chemical Corrosion

Chemical corrosion is a purely chemical process. It occurs in a nonconductive environment. Examples of chemical corrosion are gaseous corrosion and corrosion occurring in nonelectrolyte solutions.

Also referred to as dry corrosion, gaseous corrosion is often found on parts of internal combustion engines, furnace armatures and other industrial components used in high temperature/high pressure environments. Protection from gaseous corrosion is usually realized through the use of alloys designed for high temperature and pressure oxidation resistance.

The same can be said of protection from corrosion occurring in nonelectrolyte solutions such as organic solvents and alcohols. The gas and oil industries have experienced significant losses as a result of this type of corrosion. The corrosion damage occurs as a result of chemical reactions between the metal components and impurities in the organics such as H₂S or catalytic reactants used in the refining and purification process.

3.2.2 Electrochemical Corrosion

Electrochemical corrosion occurs via two processes involving the migration or flow of electrons creating a current. Oxidation, or the loss of electrons, occurs at an anode and the reverse process whereby the material gains or consumes an electron, which is known as reduction, occurs at the cathode. The electrochemical process is driven by the voltage between the anode and cathode. This potential arises because of differences on the metal surface such as differences in access to oxygen, dissimilar phases or the alteration of local chemistry due to a contaminant. The corrosion process is represented in detail in the illustration in Figure 3.3.

3.2.2.1 Mixed Potential Theory

Modern electrochemical corrosion theory is derived from the mixed potential theory developed in 1938.³ In this theory Wagner and Traud postulate that the total rates of oxidation reactions equal the total rates of reduction on a corroding surface.⁴ The mixed potential theory proposes that the electron liberated during oxidation is consumed in a corresponding reduction process, therefore the total rates of the oxidation reactions will equal the total rates of the reductions.

The cause of the entire process is based on two factors. The oxidation and reduction reactions each have a unique half-cell electrode potential and exchange current density. The half-cell potentials cannot coexist separately in the same conductive environment. There must be a polarization or change in potential to a common intermediate value referred to as the mixed

potential. This is illustrated in the Figure 3.4 diagram illustrating the two half-cell reactions occurring when zinc is placed in an acid. These are represented as:



The two half-cell potentials are plotted with respect to the corresponding current density of the half-cell reactions (i_o). An increase in current density is required for the equilibrium mixed potential (i_{corr}) to be reached.

3.2.2.2 Passivity

Passivation is the spontaneous formation of a surface film on a metal which inhibits further corrosion. A metal is passive when it behaves nobler than it is in a given solution as a result of the protective surface film, usually an oxide. As the name indicates, the metal is then said to be passive to corrosion.

Application of a potentiostat enables the potential to be controlled and the current density as a function of the applied potential to be monitored and a curve of the type shown in Figure 3.5 can be generated. Between point A and B the metal is active, with anodic dissolution of the metal occurring. In the transition region the metal reaches the passivation potential at the maximum current and oxidation quickly begins to subside. As potential is increased the current drops dramatically and remains extremely low. This indicates there is little, if any, flow of electrons at that potential range. At increased potential oxygen evolution will begin as the water in the solution begins to be oxidized.

Metals can be made passive by application of oxidizing agents such as warm dilute nitric acid or dilute hydrogen peroxide. Treatment of the metal in this manner generally results in the formation of an oxide that is insoluble in the electrolyte solution.

3.3 Corrosion protection

While passivation is an effective method to control corrosion, other methods include the addition of corrosion inhibitors, anodic or cathodic protection and the application of coatings.

3.3.1 Inhibition

Inhibition of corrosion can be achieved by either removing corrosive reagents from the surrounding environment or adding compounds that suppress either or both of the half-cell reactions. Anodic inhibitors suppress the oxidation process while cathodic inhibitors prevent reduction of water to hydrogen. Chromate, used in conversion coatings, and nitrite are anodic inhibitors. The use of amine in steam increases the pH in the pipes making proton reduction less favorable.⁵

3.3.2 Electrochemical Protection

Anodic protection raises the corrosion potential to a value within the passive range by applying a current density. Once this is accomplished a much smaller current density is passed to maintain the passivity. The current to maintain the passivity may be on the order of two orders of magnitude smaller.⁴

Galvanic corrosion, the degradation of one metal by contact with another in the presence of an electrolyte as a result of the difference in their electrode potentials, can be employed to inhibit corrosion.⁵⁻¹⁰ A less noble metal is wired to the metal component which needs to be protected from corrosion. This less noble metal is referred to as the sacrificial anode, as it supplies electrons to the metal component forcing it to become cathodic. This can also be achieved by connecting a direct current power source, such as a solar panel to the metal component to supply electrons. This is referred to as an Impressed Current Cathodic Protection (ICCP) system.

3.3.3. Protective Coatings

Protective coatings applied to the metal shield the surface from the corrosive medium. Coatings can be metallic, such as a zinc coating on (galvanized) steel, non-metallic, such as paints, polymers or enamels, or chemical, such as oxides and phosphates. Bluing-type oxidations are done by heating the metals, generally steels, at 370°C in a steam atmosphere. Oiled gun bluing provides protection from atmospheric corrosion.

Chemical coatings are referred to as conversion coatings. Application of phosphate coatings, called phosphating, is one of the most useful conversion coatings as they often provide

protection from wear as well as from corrosion. The resulting surface of the phosphate crystals provides a receptive surface for other coatings. Calcium phosphate coatings have been applied to metallic implants^{11,12}.

3.4 References

1. M. Asbury, Bureau of Air Safety Investigation Journal, June, (1992). Accessed via www.avstop.com/Stories/3.html.
2. PB89-910404, *National Transportation and Safety Board Aircraft Accident Reports*, NTSB/AAR-89/03, National Transportation and Safety Board, Washington, D.C., (1989).
3. A. Sedriks, *Corrosion of Stainless Steels*, John Wiley and Sons, Inc.: New York, (1996).
4. C. Wagner and W. Traud, *Zeitschrift fur Electrochemie*, **44**, 391, (1938).
5. C. P. Dillon, *Corrosion Resistance of Stainless Steels*, Marcel Dekker, Inc.: New York, (1995).
6. R. Hart, *Trans. Faraday Soc.*, **53**, 1020, (1957).
7. H. Raether, *C.R.*, **227**, 1247, (1949).
8. J. Keller and F. Edwards, *Mater. Progr.*, **54**, 35, (1948).
9. D. Altenpohl, *Aluminum*, **33**, 78, (1958).
10. D. Altenpohl, *Aluminum*, **31**, 62, (1955).
11. C. Du, et al., *J. Biomed. Mater. Res.*, **59**, 535, (2002).
12. ASTM F 1609, *Standard Specification for Calcium Phosphate Coatings for Implantable Materials*, ASTM International: West Conshohocken, PA, (2003).

3.5 Figures

Figure 3.1 Structural failure of Aloha Airlines Boeing 737.



Figure 3.2 Rivet heads popped on Boeing 737 belly.



Figure 3.3 Detailed view of the corrosion process occurring beneath a drop of water.
Oxygen is readily available at the perimeter of the drop which forms the cathodic region. Oxidation of iron occurs in the center of the drop then the positive ion migrates toward the cathode, where it is reduced and forms Fe_2O_3 which separates into a separate phase from the metal.

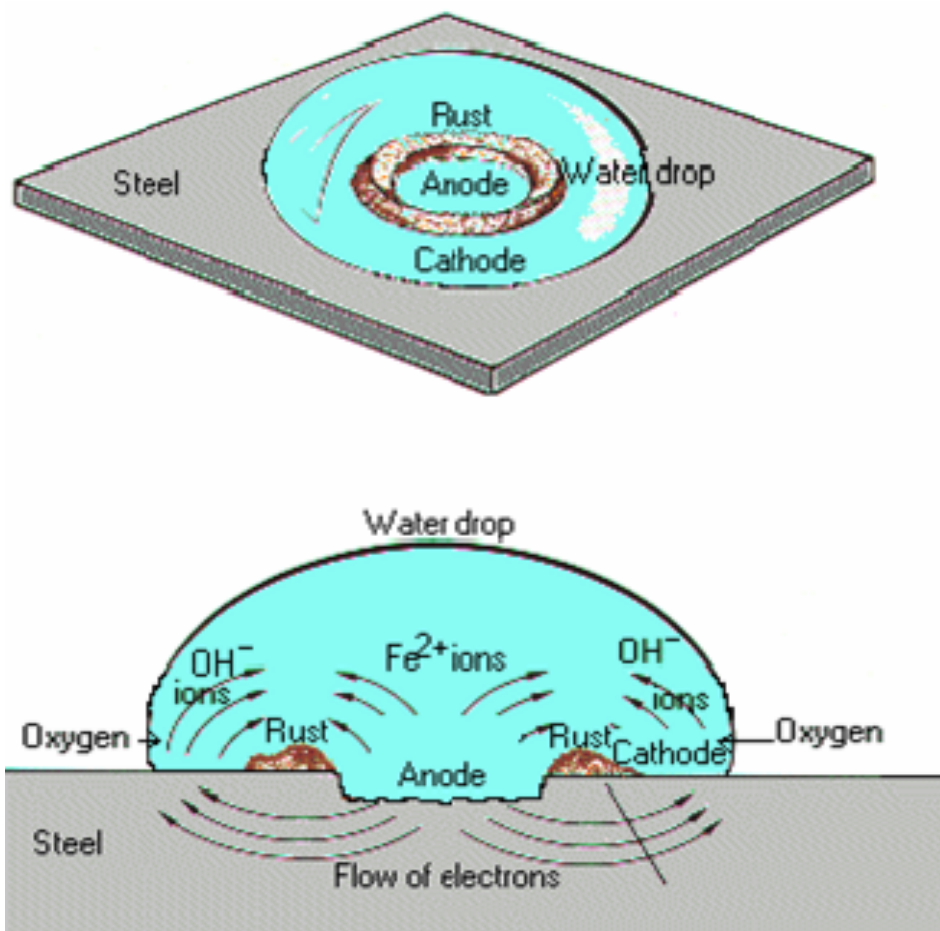


Figure 3.4 Potential–current density plot for Zn and H, showing the mixed potential (i_{corr}) for the two in electrochemical reaction.

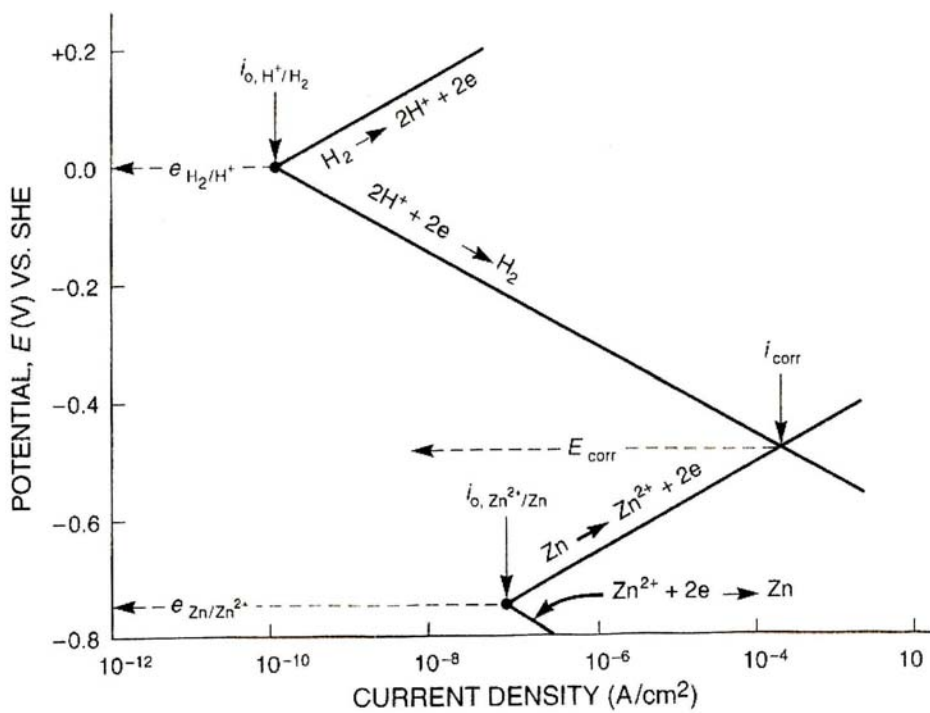
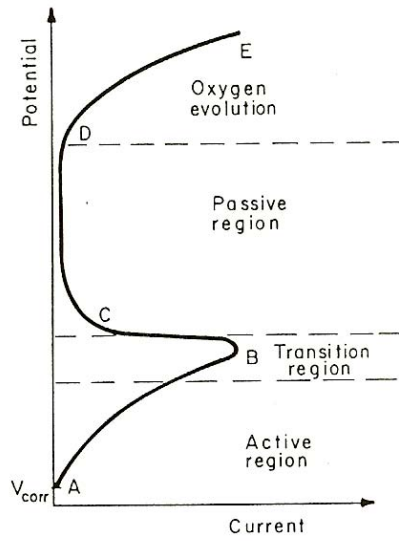


Figure 3.5 Polarization curve showing the passive potential range.



CHAPTER 4 - Chromium and Stainless Steels

4.1 Introduction

The utility and prevalence of stainless steel is evident in nearly all walks of life. The properties of corrosion resistance and hardness make this alloy invaluable in modern society. Stainless steel owes its “stainless” nature to the inclusion of chromium in the alloy. Chromium forms an invisible corrosion resistant oxide immediately on exposure to any oxygen and imparts this quality to the steel alloy. Chromium and stainless steel are interesting to corrosion scientists and have been studied extensively in this aspect.¹⁻³ and references therein

4.2 Chromium

Discovered in 1797 by Nicholas-Louis Vauquelin, it was isolated from crocoite (PbCrO_4) in 1798. It was found that same year by Tobias Lowitz and Martin Heinrich Klaproth independently in chromite ($\text{Fe}(\text{CrO}_2)_2$) samples from Russia, and found in French chromite a year later by a German chemist by the name of Tassart. The chromite ore is the only commercial source of chromium available.⁴

4.2.1 Occurrence, Abundance and Utility of Chromium

A Group VIb element of the periodic table, chromium exists in several valencies. With the acetate ion chromium is in the 2+ state (chromous), with oxides and phosphates it exists in the innocuous 3+ valency (chromic).⁵ In the trivalent form chromium is an essential trace element in mammals, necessary for glucose metabolism. It also is found to reduce the levels of LDLs (low density lipoproteins) and cholesterol in the blood. Chromium also assists in transport of amino acids. Hexavalent chromium (chromic and chromate) is not found naturally, but it is a by-product of industrial uses.⁶ Exposures to $\text{Cr}^{(\text{VI})}$ occur during the production of stainless steel, chromate chemicals, and chromate pigments and also during other work activities such as stainless steel welding, thermal cutting, chrome plating, painting, and coating processes. $\text{Cr}^{(\text{VI})}$ causes oxidative stress *in vivo*. Renal failure, anemia, hemolysis (reduction and impairment of

red blood corpuscles), liver failure and lung cancer result from long term exposure to hexavalent chromium.⁶

Chromium is used as a catalyst in ammonia synthesis and in the production of stainless steels and chromium alloys and for electroplating. Organic chromium complexes are used as development dyes in color photography. Inorganic chromium compounds are used as paint pigments. Industrial wood preservation and leather tannery use $\text{Cr}^{(\text{VI})}$ salts. Chromate coatings have been applied to other metals to provide a protective coating from corrosion. Recent findings regarding chromate toxicity have almost eliminated this process in industry. Trivalent compounds of chromium are insoluble in the natural environment and so only trace amounts have been detected in sea water, yet it is found to be relatively abundant in the earth's crust (21st most abundant element).

4.2.2 Physical Properties

Chromium has remarkable physical properties. Ordinary chromium metal has a hardness of 9 (Mohs scale) which is inferior only to diamond. It cannot be scratched by other metals, which makes it useful in a wide range of industries. Chromium's hardness is also responsible for its brittleness which renders it unsuitable unalloyed as a material of construction. For this investigation the hardness of chromium metal is a benefit since abrading the oxide from the surface will not leave contaminants from the abrasive imbedded in the metal.

Chromium is antiferromagnetic below 311K (99.5⁰ F), but the chromium oxide CrO_2 is ferromagnetic and is utilized in data storage applications. It has a heat of fusion of 16.9kJ/mol, a boiling point of 2642⁰ C and a bulk modulus of 160 GPa which lends strength and heat resistance to alloys of which it is a component.⁷ Chromium crystallizes in the body centered cubic crystal structure, International space group #229 (Im3m) with a lattice constant of 2.88Å.⁸

4.2.3 Chemical Properties

Chromium metal is very stable in air due to the presence of the tough oxide film that forms on the surface. It is resistant to attack by a wide array of chemicals at standard

temperature. Rates of corrosion by O₂, H₂O, SO₂, and CO are shown in Table 4.1.⁹ Chromium dissolves in aqueous halide acids (HCl, HF, HBr, HI) forming the Cr²⁺ species, and reacts slowly in H₂SO₄.¹⁰ Phosphoric acid does not attack it and it is insoluble in nitric acid and aqua regia. Chromium is also resistant to attack by organic acids such as formic, citric and tartaric acids but will slowly dissolve in glacial acetic acid.^{10, 11} The organic acids as well as phosphoric acid make chromium passive. It can be made active in a reducing process such as treatment with hydrogen or immersion in dilute H₂SO₄ and touching it with zinc below the surface of the acid.¹¹ In the active state chromium is very reactive and can displace copper, tin and nickel ions from their salts in aqueous solutions.¹²

Transition states in chromium have been documented for 2-, 1-, 0, 1+, 2+, 3+, 4+, 5+ and 6+ valencies. The hexavalent chromium is devoid of valence electrons. The most common (and stable) oxidation states are 2+, 3+ and 6+. The 1+ and lower valencies are found in complexes such as the carbonyls, nitrosyls and organometallic complexes. It is strongly reducing in these lower oxidation states with 2+ being the lowest aqueous oxidation state for chromium. Chromium carbides are metallic in nature and are interstitial phases.¹¹ Chromium carbides are formed by reaction of carbon with the zero-valent metal or with Cr₂O₃ *in vacuo* or in a hydrogen atmosphere.

The nitrides of chromium, also interstitial, have metallic properties such as high thermal and electrical conductivity. Most of the nitrides of chromium satisfy Hägg's rule ($r_{\text{covalent}}/r_{\text{metallic}} < 0.59$) maintaining a higher symmetry. CrN is stable towards water but Cr₂N is not. Chromium phosphides have a high value of Hägg's ratio and are usually in the form of pairs or chains of phosphorous atoms. Only one sulfide of chromium, CrS, or daubrelite, is found in nature (Mexico) and is meteoric in origin.¹¹

As with most d-block elements, chromium forms complexes with neutral compounds that stabilize a low oxidation state. The low oxidation state indicates high electron density around the metal atom which can be delocalized into vacant orbitals on the ligands. π -acceptor ligands associated with chromium are nitric oxide, carbon monoxide, isocyanides, phosphines, arsines, 1,2-dithioketone containing ligands, 1,2 dithiolene groups and aromatic amines.^{13,14}

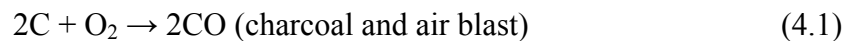
4.3 Stainless steel

The first record of steel dates back to the about 1400 B.C. when the Hittites developed a material the ancient records referred to as *good iron*. Good iron was produced by cycles of heating an iron bloom in a charcoal furnace near 1200°C and hammering the hot metal to remove the slag and compact it. The charcoal in the furnace supplied carbon monoxide gas as it burned allowing the carbon to be diffused into the surface of the iron. India began producing and trading a so-called *wootz* steel, which is now referred to as Damascus steel. This steel was wrought by small pieces of sponge, or wrought, iron together with wood chips and leaves into a ceramic crucible which was sealed and heated in air-blast enhanced fires. This enabled the carbon from the organic material to evenly penetrate the iron creating an essentially homogenous iron carbide steel.¹⁵

The process was kept secret until the middle ages when, as legend has it, a Germanic weapon-smith named Wieland was famed for his superior swords that were unsurpassed in strength and held a fine edge. Allegedly he filed a forged piece of iron and fed the iron filings to his chickens. After collecting the feces he separated the iron out with a magnet. After seven passes the material was forged into a sword. Another German metallurgist recreated the process in the 1930's and found that the biological processes reduced the carbon content and enriched the iron with nitrogen which made the steel stronger.¹⁶

4.3.1 Manufacture and Utility of Steels

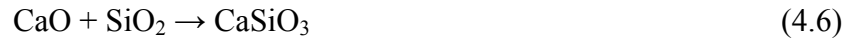
Modern steel production utilizes massive blast furnaces (as tall as 30 meters), so called because preheated air is blast-injected near the bottom of the furnace to obtain the high temperatures necessary for separation the iron metal from the ore. The fuel for the furnace is supplied in the form of coke which is obtained by heating soft coal powder in an airtight oven to drive off impurities. As the coke burns it gives off carbon monoxide which combines with the iron oxides in the ore, producing metallic iron in the series of reactions:



Limestone (also referred to as flux in the industry) is included in the heating process to produce calcium silicate from the silica in the ore:



Δ



Δ

If the silica were not removed iron silicate would form and reduce the amount of metallic iron produced. The resulting molten iron/carbon alloy is poured into molds or casts and cooled. The *pig iron*, as it is called, is cooled and removed from the mold. If left in this form it is brittle enough to be shattered if dropped. The cast iron is reheated in the presence of oxygen. The oxygen combines with carbon and other impurities and reduces the amount of carbon in the steel thereby improving ductility.

The different alloy components are added to the reheated pig iron. The new mixture is poured into molds and quenched by spraying with water until it becomes solid throughout. This refined steel is heated another time and sent through several roughing stands that flatten it into sheets, where it is washed, cooled and coiled. The steel is then referred to as *cold rolled* steel. This is a most elementary description of steel production. Many variations exist which are designed to enhance preferred properties of the resulting steel alloy. In example, re-melting can be performed in a vacuum induction melting, a consumable electrode vacuum arc re-melting process or via electroslag refining. Each process is designed to remove certain impurities to control uniformity of properties.

The utility of steels drives the tailoring of the fabrication process and creates the wide array of steel materials in existence today. The varieties of stainless steel are diverse and their list of applications is extensive. The focus of information conveyed in this dissertation pertains to Type 316L stainless steel. Type 316 is second only to Type 304 in commercial importance¹⁷ and is the most widely utilized metal in the health industry. Additionally only Types 316 and 310 remain non-magnetic among the stainless steels. For these reasons Type 316L was selected for this investigation. The “L” indicates low carbon content ($\leq 0.03\%$ by weight) and was chosen in hopes of minimizing the effects of Ar^+ etching-induced carbide formation.

4.3.2 Alloying Elements

The predominant elements found in stainless steels, other than iron, are chromium, molybdenum, manganese and nickel. Trace amounts of calcium, carbon, cobalt, copper, niobium, nitrogen, phosphorous, selenium, silicon, sulfur, and titanium are also utilized. Each alloying element serves a specific purpose and defines added or enhanced properties.

4.3.2.1 Chromium

Chromium is the largest percentage component in stainless steels other than iron. By definition steels must contain at least 10.5% chromium to be classified as “stainless”. The “stainless” nature of these types of steel is derived from the protective layer of chromium oxide (Cr_2O_3) that forms on the surface of the steel. If damaged the oxide layer reforms almost instantly; this is referred to as "self-healing". Increasing the percentage of chromium also increases the resistance to corrosion. But, increasing the amount of chromium eventually reaches a point where the steel begins to lose ductility and becomes impractically brittle. The highest percentage of chromium found in stainless steel is 27.5% and is usually on the order of 18%.¹⁸

4.3.2.2 Molybdenum

Molybdenum increases the steel material's resistance to pitting and crevice corrosion. Both of these forms of corrosion are frequently found in biomedical implants. Pitting corrosion is a localized chemical attack which produces a cavity in the metal surface. The mechanism in pitting corrosion centers around inclusions of sulfur in the steel which create a significant reduction of chromium in the immediate vicinity of the inclusion.¹⁹ Inclusion of molybdenum raises the potential at which pitting is initiated.²

4.3.2.3 Manganese

Manganese in steel improves the strength, toughness and hardenability of the material. The steel's hot working properties are improved making it easier to forge and weld.

4.3.2.4 Nickel

Nickel is included in stainless in fairly high amounts, usually between 8% and 10% but can go as high as 35.5%. It increases high temperature resilience and resistance to attack from acids. It also increases impact strength at temperature extremes as well as improving ductility.

4.3.2.5 Trace Alloying Elements

As previously discussed, carbon increases the hardness of steel, but relatively small amounts will make steel too brittle to be useful. Nitrogen will increase yield strength and pitting corrosion resistance while sulfur can improve machinability of the material. Sulfur can prove detrimental to the material's corrosion and high temperature resistance, as well as weldability and so should be kept to extremely small percentages. Phosphorous increases strength and will also improve machinability, but can cause the material to crack during welding. Calcium and selenium have been used to improve machinability as well. Titanium and niobium are both used as carbide stabilizers. The carbides of these metals are very stable and minimize intergranular corrosion. These metals will form carbides preferentially over chromium and so allow chromium at grain boundaries not to be depleted and so remain available for protection. Additionally niobium increases the strength of steels used in high temperature environments. Cobalt and silicon are found in residual amounts from the refining process of iron and nickel. Cobalt can become radioactive in nuclear reactors and so is restricted in steels fabricated for use in the nuclear industry.

4.3.3 Classification of Stainless Steels

It is customary to divide stainless steels into five groups according to their metallurgical structure. Face-centered cubic structured steel is referred to as *austenite*, named for the English metallurgist Sir W. C. Roberts-Austen, who devoted his life to its study. Likewise, the German engineer A. Martens had the body-centered tetragonal or cubic structure *martensite* named in his honor. A third family of stainless steels which is strictly body-centered cubic in structure is called ferrite. Another class of stainless steels, known as duplex steels contains roughly equal amounts of austenite and ferrite. The Schaeffler diagram shown in Figure 4.1 roughly illustrates which structure is obtained after rapid cooling to room temperature from

1050°C. The diagram is an approximation, not a phase diagram²⁰ and is expressed in terms of weight percent of chromium and nickel due to their respective roles as a ferric stabilizer and an austenitic stabilizer.

4.3.3.1 Austenitic Grades of Stainless Steel

These stainless steels are generally nonmagnetic and retain their *fcc* crystal structure over a very wide range of temperature extremes. An example of an austenitic crystal is shown in the TEM image in Figure 4.2.²¹ Heat treatment will not harden these steels, but they may be cold hardened. Cold hardening is a process of plastically deforming the material at ambient temperature. Cold working also makes the material more brittle. The physical properties include corrosion resistance, high-temperature strength, good ductility and weldability and good impact resistance to -183°C. Type 316L is an austenitic grade stainless steel; its properties are listed in Table 4.2.^{1,2,18}

4.3.3.2 Martensitic Grades of Stainless Steel

These steels are from 11-13% chromium and can be hardened in heat treatment. They have a lower corrosion resistance as a result of the lower chromium content, but still provide sufficient protection to be used where a stainless nature and a hard metal are needed, such as with turbine blades and high temperature parts. Cutlery blades are frequently fabricated from martensitic grade stainless steel.^{1,2}

4.3.3.3 Ferritic Grades of Stainless Steels

Ferritic grades have varying chromium content, from as low as 11.5% to as high as 30%. The corrosion resistance of any given ferritic steel is directly proportional to the chromium content, but generally they have better corrosion resistance than the martensitic grades. They are not hardened by heat treatment. Their high temperature oxidation resistance is also good, but they suffer from poor impact resistance and weldability. They also suffer stress-corrosion cracking in caustic environments and with chlorides. They are most often used in water and food processing, as auto trim and in architectural applications.¹

4.3.3.4 Duplex Stainless Steels

The properties of duplex steels are intermediate between austenite and ferrite. They are about twice as strong as austenitic grades but lower than martensitic grades. Their toughness is superior to the ferritic stainless steels and lower than austenitic steels. Their corrosion resistance is higher than many of the austenitic 18/8 steels (so called because of the 18% Cr, 8% Ni content). These steels are usually used in temperatures below 300°C, as are ferritic steels, due to their becoming very brittle at 475°C.²

4.4 References

1. C. P. Dillon, *Corrosion Resistance of Stainless Steels*. Marcel Dekker, Inc.: New York. (1995).
2. A. Sedriks, *Corrosion of Stainless Steels*, John Wiley and Sons, Inc.: New York. (1996).
3. NMAB-480, *High-Purity Chromium Metal: Supply Issues for Gas-Turbine Superalloys*, Committee on High-Purity Electrolytic Chromium Metal, National Materials Advisory Board. National Academy Press: Washington, D. C..(1995).
4. M. Udy, "History of Chromium", in *Chromium*, 2. Reinhold: New York. (1956).
5. C. Rollinson, *Comprehensive Inorganic Chemistry*, Vol. 21. Pergamon Press: Oxford. (1975).
6. S.Katz and H. Salem. *The Biological and Environmental Chemistry of Chromium*. John Wiley and Sons: Hoboken, NJ. (1994).
7. *CRC Handbook of Chemistry and Physics*, 85th ed.. CRC Press: Boca Raton. (2005).
8. R. Wyckoff, *Crystal Structures*, 2nd ed.. Interscience Publishers: New York. (1963).
9. R. Keller, *Basic Tables in Chemistry*. McGraw-Hill: New York. (1967).
10. J. Amiel, in *Nouveau Traité de Chimie Minérale*, 14. Masson et Cie: Paris. (1959).
11. G. Samsonov, ed., *Handbook of the Physicochemical Properties of the Elements*. Plenum Press: New York. (1968).
12. D. Shriver, P. Atkins and C. Langford, *Inorganic Chemistry*, 2nd ed.. W.H. Freeman and Company: New : New York. (1994).
13. T. Manuel, in *Advances in Organometallic Chemistry*, 2. Academic Press: New York. (1965).
14. F. Calderazzo, R. Ercoli and G. Natta, in *Organic Synthesis via Metal Carbonyls*. Interscience: New York. (1968).
15. J. Macqueen, *The Hittites and Their Contemporaries in Asia Minor*. Thames and Hudson: London. (1986).
16. R. Tylecote, *A History of Metallurgy*. The Metals Society: London. (1976).

17. Aalco Stainless Steel Grade 316 Data Sheet. Aalco Metals, Ltd.: Surrey, UK
18. *Source Book on Industrial Alloy and Engineering Data*. American Society For Metals: Metals Park, OH. (1978).
19. M. Ryan, et al., *Nature*, **80**, 7, 11, (2002).
20. F. Pickering, *Intl. Metals Rev.*, **21**, 227, (1976).
21. T. Sourmail, et al., at
<http://www.msm.cam.ac.uk/phase-trans/abstracts/annealing.twin.html>

4.6 Figures

Figure 4.1 Schaeffler diagram. % Ni Equivalent = %Ni + %Co + 30(%C) + 25(%N) + 0.5(%Mn) + 0.3(%Cu). % Cr Equivalent = %Cr + 2(%Si) + 1.5(%Mo) + 5(%V) + 5.5(%Al) + 1.75(%Nb) + 1.5(%Ti) + 0.75(%W)

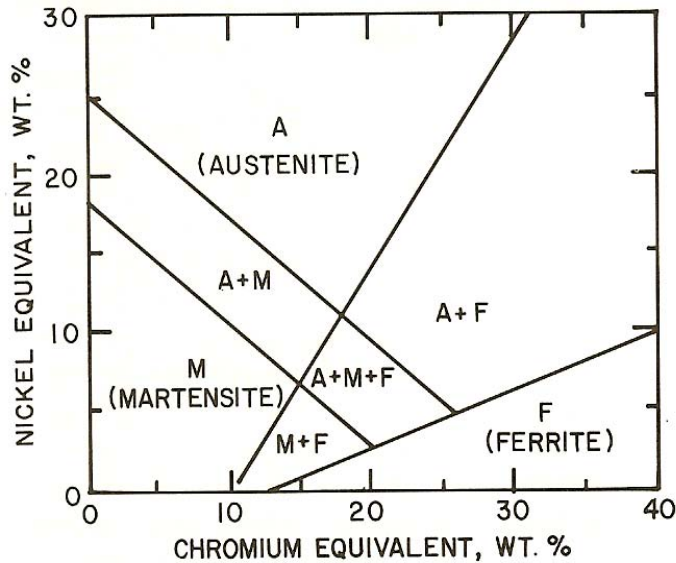
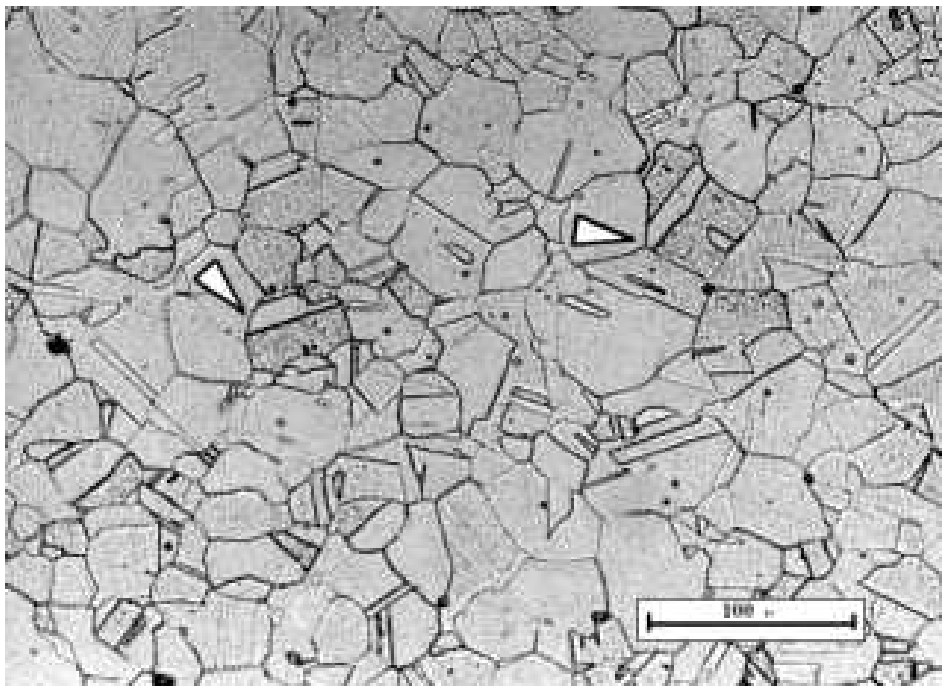


Figure 4.2 Austenitic grain in Stainless Steel Type NF709. The two arrows indicate *annealing twins*, which are identical in composition but oriented differently.



4.7 Tables

Table 4.1 Rate of Corrosion of Chromium

Temperature °C	Corrosion Rate (mg/cm ² /hr) in:			
	O ₂	H ₂ O	SO ₂	CO
700	0.019	0.002	0.007	0.011
800	0.040	0.015	0.016	0.014
900	0.093	0.048	0.135	0.056
1000	0.265	0.090	0.149	0.128

Table 4.2 Properties of 316L Stainless Steel

Composition: 16-18% Cr, 10-14% Ni, 0.03% C, 3% Mo, 2% Mn, 1% Si, .045% P, 0.03% S

Melting Range: 2500°F - 2550°F

Density: 0.29 lbs/in³

Specific Heat: (32-212°F) 0.12 Btu/lb/ °F

Coefficient of Thermal Expansion: (in/in/ °F)

32-212°F 8.9 x 10⁻⁶

32-600°F 9.0 x 10⁻⁶

32-1000°F 9.7 x 10⁻⁶

32-1200°F 10.3 x 10⁻⁶

32-1500°F 11.1 x 10⁻⁶

Thermal Conductivity: (Btu/ft²/hr/ °F/ft)

212°F 9.4

932°F 12.4

Electrical Resistivity: (μohm-cm)

68°F 74

Magnetic Permeability: (H=200Oersteds)

Annealed 102 max

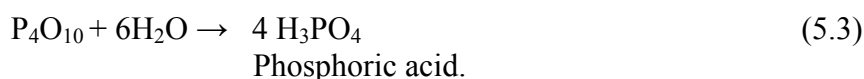
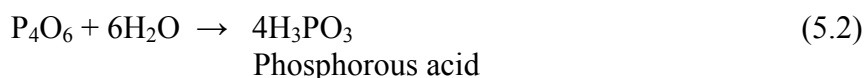
CHAPTER 5 - Phosphorous-Containing Compounds

5.1 Introduction

Phosphorus was first isolated by the German physician Hennig Brand in 1669 in his quest to discover the fabled Philosopher's Stone. He found a glowing white residual after the distillation of urine, but kept the discovery secret until after Robert Boyle isolated it in 1680 during his own alchemical studies. It occurs naturally in phosphate rock, referred to as apatite, and is the 11th most abundant element in the earth's crust. It can be isolated by heating phosphate rock, silica and coke to 250°C:



Once isolated and condensed to a solid the white phosphorous, as it is called, is very reactive and must be stored under water. If heated to 300°C it transforms into red phosphorus which is in the form of long chains of the P₄ fragment, as shown in Figure 5.1.¹ There are two important forms of phosphorous oxides: tetraphosphorus hexoxide, P₄O₆, and tetraphosphorus decoxide, P₄O₁₀. These oxides are acid anhydrides of phosphorus and phosphoric acids:



Phosphoric acid can react to produce pyrophosphoric acid:



The salt of pyrophosphoric acid is called pyrophosphate, or more accurately diphosphate.^{2,3} The product of such a condensation reaction, represented in Fig. 5.3, is referred to as a condensed phosphate.

5.2 Nomenclature of phosphates

Though commonly referred to as phosphoric acid, phosphate nomenclature distinguishes H₃PO₄ as orthophosphoric acid, with the ion being referred to as the orthophosphate ion, [PO₄]³⁻. Since orthophosphate has three hydrogen atoms it can form mono-, di- or tri-metal orthophosphates. As shown in Figure 5.2, it has a tetrahedral configuration which allows for the sharing of any of the oxygen atoms with neighboring phosphate ions. This ability

to share tetrahedral oxygens and form unlimited P-O-P bonds leads to a wide and varied array of phosphate forms as well as sophisticated nomenclature to distinguish these forms from each other. When discussing structural formulas for the various types of phosphate structures a general formula for the anion can be used for each structure of a given class.

Figure 5.4 shows the three types of “building blocks” of phosphate structures. Phosphate ions that only share one oxygen atom are referred to as end groups in phosphate chemistry. Two end groups joined together become the condensed phosphate shown in Equation 5.4 and Figure 5.3. Two trans-shared oxygen atoms are called a middle group which characteristically has an ester-type linkage: -O-P-O-. A branching group has three shared oxygen atoms.

There are many possible combinations of joining the phosphate tetrahedra in a given compound. Although it is possible to use the ball-and-stick, ortep or space-filling visual models most visual representations of 3-dimensional phosphate molecules represent the $[P_nO_n]$ as shaded tetrahedral. The possible combinations of oxygen sharing represented as such are shown in Figure 5.5.

Essentially there are only two categories of phosphates: monophosphates, called orthophosphates and the condensed phosphates, of which there are three subgroups. Polyphosphates are condensed phosphates with the anionic formula $[P_nO_{3n+1}]^{(n+2)-}$. For example, in diphosphate, $n=2$ in the anionic formula as evidenced by the condensed phosphate $[P_2O_7]^{4-}$.

The cyclic forms have the anionic formula $[P_nO_{3n}]^{n-}$, i.e. chromium cyclotetraphosphate, $Cr_4(P_4O_{12})_3$. Another cyclophosphate, $Cr(PO_3)_3$ shown in Figure 5.6(a), is a long-chain polyphosphate referred to as a cyclononaphosphate. A deceptively simple chemical formula is a very complicated structure in three dimensions. The phosphate salt in Figure 5.6(b) is chromium(III) hexametaphosphate $Cr_2P_6O_{18}$. These are two of six reported polymorphs of the same compound.⁶ The third group of condensed phosphates are the ultraphosphates. The anionic formula for these complicated structures is $n[PO_3]^- + mP_2O_5$, which becomes $[P_{(2m+n)}O_{(5m+3n)}]^{n-}$. To date there is only one known ultraphosphate anion: $P_4O_{11}^{2-}$ ($m=1, n=2$). The cation associated with it is M^{2+} ($M = Mn, Fe, Co, Ni, Cu, Zn$ or Cd).⁷

5.3 Phosphates and corrosion protection

5.3.1 Conversion Coatings

As mentioned in Chapter 4, passivating a metal surface provides protection from corrosion by creating an insoluble oxide on the surface that protects it from further corrosion. Another method of corrosion protection is called a conversion coating. Chromium phosphate powder is frequently used in materials fabrication as a preparation of metal surfaces to increase adhesion of primers and paints as well as reduce corrosion before these are applied. These coatings are referred to as conversion coatings because the surface of the metal being coated undergoes a chemical “conversion” with the metal phosphate. The substrate metal is chemically modified during the process producing a porous film that is structurally as well as chemically enhanced. The porosity of the film allows for additional coatings to bond more securely, as well as create pockets for lubricants to fill thereby improving lubrication properties as well as adhesion properties. Other metal phosphates utilized in conversion coatings are zinc, manganese and iron phosphates.

5.3.2 Conversion Coatings in Biomedical Applications

Calcium phosphates have been used as coatings on biomedical implants. Not only do they provide corrosion protection, but they are also designed to mimic phosphate-containing biomaterials so as to promote biocompatibility. The process of bioadhesion is also promoted by the implant coatings as well as providing the benefits of enhanced lubrication with the joint. The calcium phosphate coating gradually is dissolved and reformed as hydroxyapatite. This process is not a problem, but the rate at which it occurs is an uncontrolled variable. The adhesion to the implant could be compromised if the dissolution rate is higher than that in which the replacement layer forms.⁸

A major drawback with the current coating processes is a lack of mechanical ductility. Research has shown that two major factors affect formation of particulate debris in the region surrounding a biomedical implant. Mechanical abrasion resulting from normal wear may cause the surface coating damage and fracture if the coating is applied unevenly. Additionally, the actual preparation of the surface to receive the coating often leaves aluminum oxide or silicon

dioxide (depending on which material was used to blast the surface prior to coating) particles imbedded in the metal.⁹

5.3.3 Conversion Coating Thickness

The conversion coatings in use currently are on the order of 1-5 μm thick, for the more precise applications 0.25 μm can be attained commercially.^{12,13} The initial coating is gelatinous and hardens as it cures, much like a sol-gel.^{10,11} There are problems associated with significant variations in thickness of these films which are associated with the ferri/ferrocyanides and fluorides used in the conversion coating process. The metal to be coated is first etched with HF acid solution, then the conversion coating solution is applied. These coating solutions frequently contain the ferri/ferrocyanide as an accelerator. Not only does the accelerator add to the molecular weight of the coating film, it also attacks the surface at the grain boundaries of intermetallic islands, as does the fluoride. The result is a conversion coating ranging in thickness from about 150-400 \AA thick. Although very thin the variations in the film thickness posed potential problems in mechanical properties as shown in Figure 5.7.¹⁴ Areas which are topographically different in the SEM image shown are concurrently analyzed using the energy dispersive spectrometer (EDS) fitted onto the SEM tool. The composition beneath the thinner-appearing regions was identified as intermetallic islands.¹⁴

5.3.4 Creating Ultra Thin Phosphate Films

The examples above – TiN and CrO^3 containing solutions – are not phosphate-containing compounds but are examples of the thinnest films commercially available at present. The phosphate-based coatings are much thicker, on the order of 0.008 inches (20 μm) and up. Obviously, problems associated with the thinner films are amplified in the thicker phosphate conversion coatings. Fracture of the non-pliant film creates particle debris which grinds around with mechanical use and creates more destruction of the coating as well as damage to the immediate physiological surroundings. It is advantageous to develop a pliant biocompatible thin film coating which possesses the desirable properties of the current films in use without the complications associated with the mechanical rigidity of the thicker coatings.

5.4 Application

Research in this group has shown that oxide-free phosphate films can be created that are bonded directly to the metal surface.¹⁵⁻¹⁷ These films are ultrathin films, on the order of 100Å or less, and are stable in air for extended periods of time. They are created in an inert anaerobic environment allowing the phosphate solution to chemically react directly with the metal substrate. They are potentially corrosion resistant as well as potentially biocompatible and could address all of the problematic issues posed above. In the next two chapters the formation of these phosphate-containing films on 99.9% pure chromium and 316L stainless steel are examined in depth.

This research is a continuation of a series of projects in this research group that focuses on formation and characterization of oxide-free phosphate films on clean metal surfaces. This research is important in furthering insight into the chemistry of complex corrosion systems and the fabrication of corrosion inhibiting materials.

Recently biomaterial research has been done on developing protective coatings on implant materials. The bisphosphonate salts of organophosphoric acids, such as etidronate, alendronate and zolendronate have been utilized as therapeutic interventions in inhibiting the body's osteoclastic response to irritation in bones of joints that have been replaced with artificial joints. This process causes periprosthetic osteolysis, or bone resorption that initiates aseptic loosening and failure in hip implants. Bisphosphonate drugs have been administered orally or via intravenous injection and are distributed throughout the body. Side effects of this method cause a reduction in bone turnover rate throughout the entire skeletal system and accumulative renal toxicity.¹⁸ If a coating of a bisphosphonate were successfully applied to an implant this could not only provide corrosion inhibition of the metallic portion of the implant, but it could also provide *local delivery* of the osteoclast activity-reducing drug thereby avoiding the negative effects of the orally or intravenously administered drug therapy.¹⁸

Early research into the application of films generated from etidronic acid to iron and mild steel has provided insight into this chemical system.^{19,20} A goal of this research is to pursue

the possibility of producing an etidronate film on Type 316L stainless steel, which is the most widely used material in the manufacture of implants. It has been shown that an etidronate-rich surface film could be generated on both iron and mild steel surfaces.²⁰ Depth profiling the film revealed increasing amounts of iron oxide (Fe_2O_3 and FeOOH) with increasing removal of the film using an argon ion beam.

Laboratory techniques developed within this lab enable the investigator to create clean surfaces to which phosphate films can bond to directly. In the prior work with etidronic acid the film bonded to the oxide on the surface of the samples. In time the film would likely become unstable as the substrate continued to interact with the oxide intermediate between the metal substrate and the etidronate outer film. This would be prevented by generating the film on an oxide-free surface producing a stable bisphosphonic thin film bonded directly to the metal substrate.

5.5 References

1. J. Hill and R. Petrucci, *General Chemistry: An Integrated Approach*. Prentice Hall: Upper Saddle River, NJ. (1999).
2. D. Schriver, P. Atkins and C. Langford, *Inorganic Chemistry*, 2nd ed. W. H. Freeman and Company: New York. (1994).
3. D. Corbridge, *The Structural Chemistry of Phosphorus*. Elsevier Scientific Publishing Company, London. (1974).
4. M. Gruss and R. Glaum, *Acta Cryst.*, **C52**, 2647 (1996).
5. M. Bagieu-Beucher and J. Guitel, *Acta Cryst.*, **B33**, 2529 (1977).
6. J. M. Rojo, J.L. Pizarro, L. M. Rodriguez-Martinez, et al, *J. Mater. Chem.*, **14**, 992 (2004).
7. R. Glaum, Postdoc Treatise “New Investigations of the Waterfree Phosphates of the Transition Metals”. Posted at <http://bibd.uni-giessen.de/ghtm/1999/uni/h990001.htm#Volltext>.
8. G. Davis, et al, *Journal Mat. Chem.*, **17**, 1807, (1982).
9. K. St John, ed., *Particulate Debris From Medical Implants: Mechanisms of Formation and Biological Consequences*. ASTM, Philadelphia. (1992).
10. G. Frankel and R. McCreery, *Interface*, **10**, 34, (2001).
11. J. Osborne, *Prog. Org. Coat.*, **41**, 280, (2001).
12. <http://www.brycoat.com/thickns.html>.
13. http://www.atotech.com/start.php3?cl_my_id=845515.
14. Q. Meng and G. Frankel, *Surf. Interface Anal.*, **36**, 30, (2004).
15. J. Rotole and P. M. A. Sherwood, *J. Vac. Sci. Tech.*, **A18**, 1066, (2000).
16. J. Rotole, K. Gaskell, A. Comte and P. M.A. Sherwood, *J. Vac. Sci. Tech.*, **A19**, 1176, (2001).
17. J. Rotole and P. Sherwood, *Chem. Mat.*, **13**, 3933, (2001).
18. H. Fleisch, *Bisphosphonates in Bone Disease: From the Laboratory to the Patient*, 4th ed., Academic Press, San Diego, (2000).
19. I.D. Welsh and P.M.A. Sherwood, *Chemistry of Materials*, **4**, 133, (1992).
20. I.D. Welsh and P.M.A. Sherwood, *Proceedings Electrochemical Society*, **89-13**

(Advances in Corrosion Protection by Organic Coatings: Edited by D. Scantlebury and M. Kendig), 417, (1989).

5.6 Figures

Figure 5.1 Forms of Phosphorus. Figure on the left is white phosphorus, P₄. When heated the bonding structure reorganizes to form the long chains of P₄ in the isomorphous red phosphorus shown on the right.

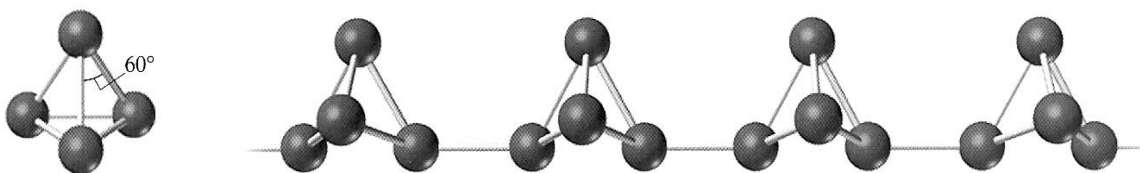


Figure 5.2 Orthophosphoric acid (left) and Phosphorous acid (right).

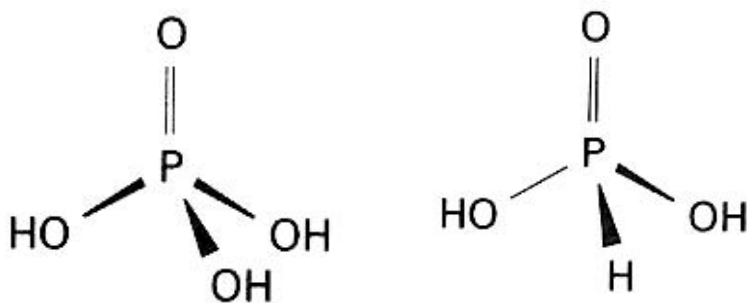


Figure 5.3 Formation of a diphosphate ion via condensation, or loss of H₂O. Note the end groups are each at the 2- oxidation state and the product is at 4-.

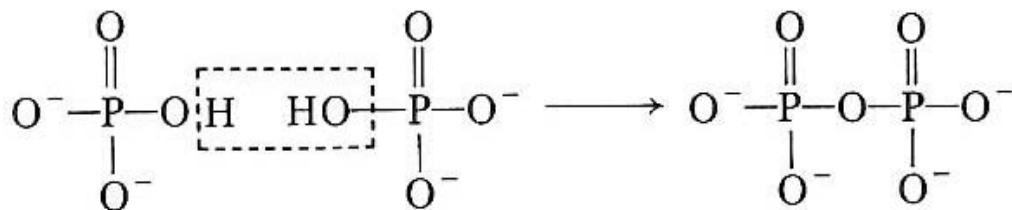


Figure 5.4 Types of phosphate tetrahedral referenced in discussion of condensed and metaphosphate arrangements. Arrows indicate bonding location.

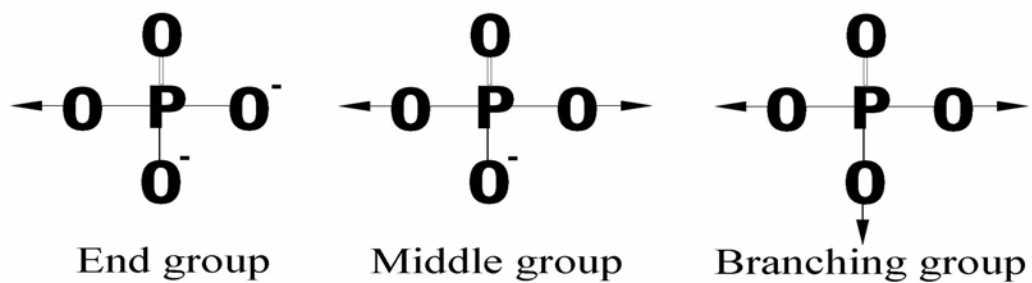


Figure 5.5 Condensed PO_4 tetrahedra. Top left: corner sharing, top right: edge sharing, bottom: face sharing.

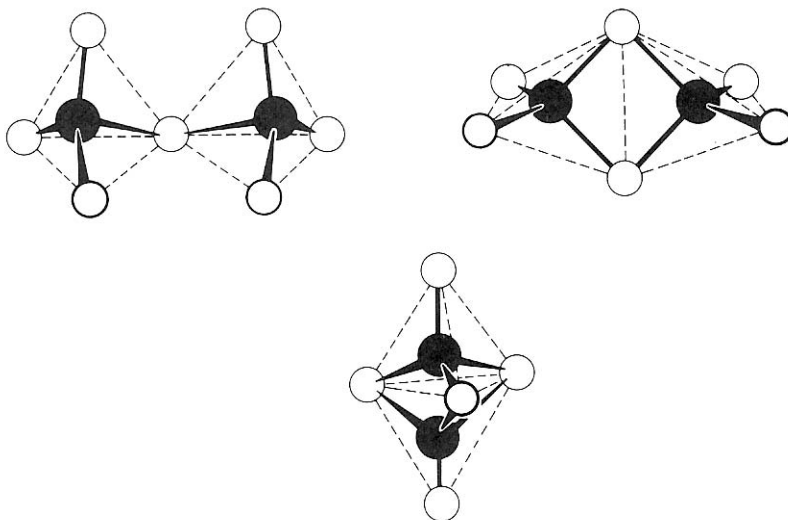


Figure 5.6 C-type $\text{Cr}(\text{PO}_3)_3$, chromium (III) tris(metaphosphate) shown in (a) ; B-type $\text{Cr}(\text{PO}_3)_3$; reported as $\text{Cr}_2\text{P}_6\text{O}_{18}$, chromium (III) hexametaphosphate (b). White structures are CrO_6 octahedra.

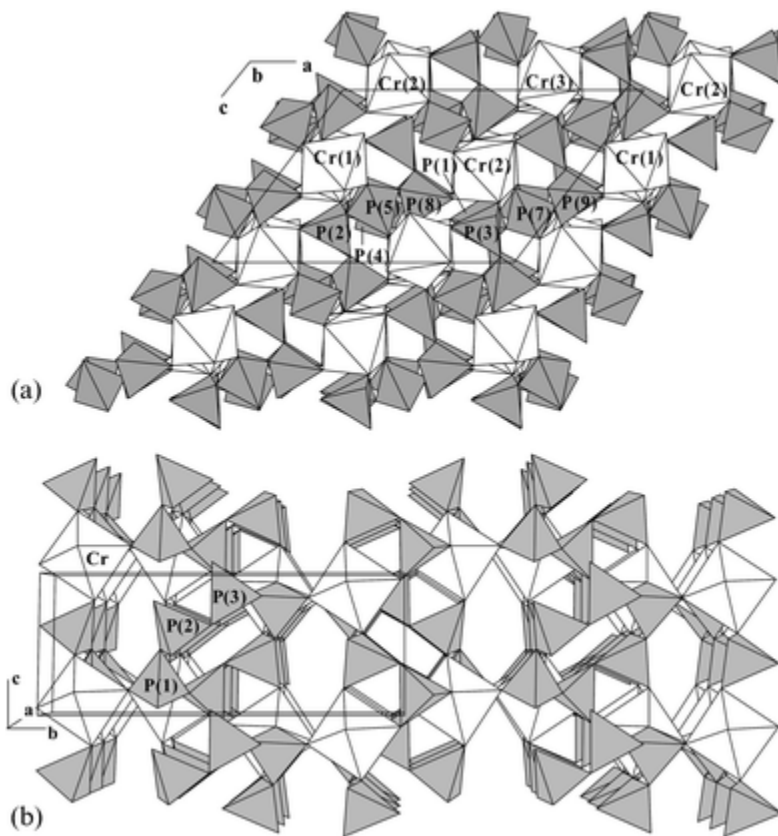


Figure 5.7 Several Ultraphosphate Networks in the phosphate MP_4O_{11} .

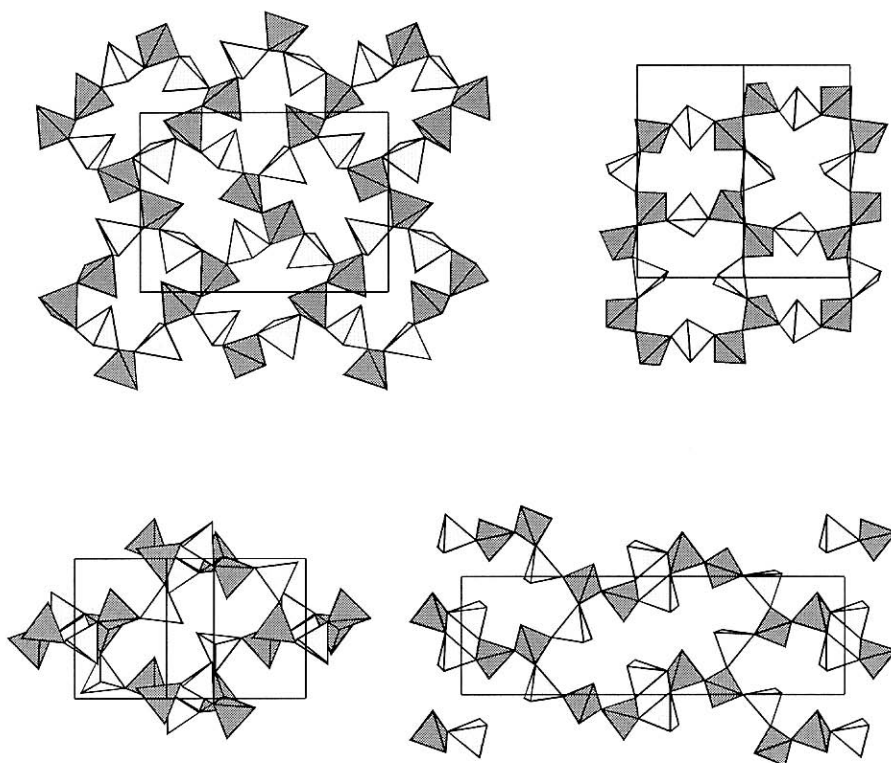
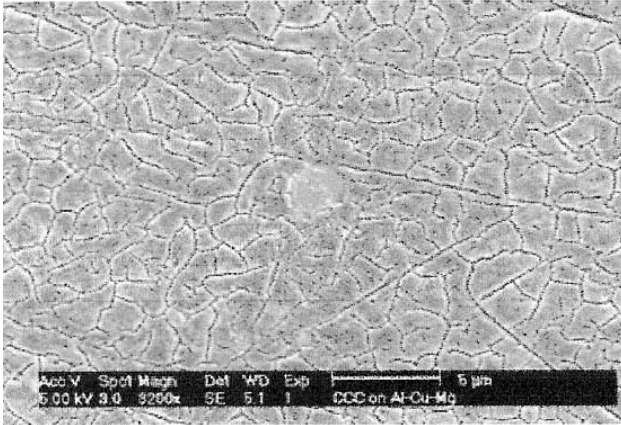
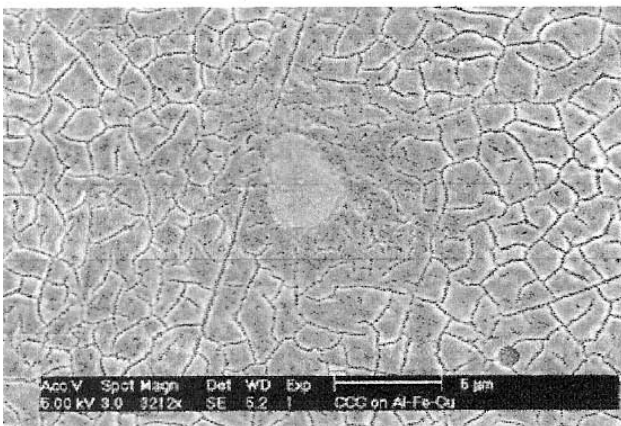


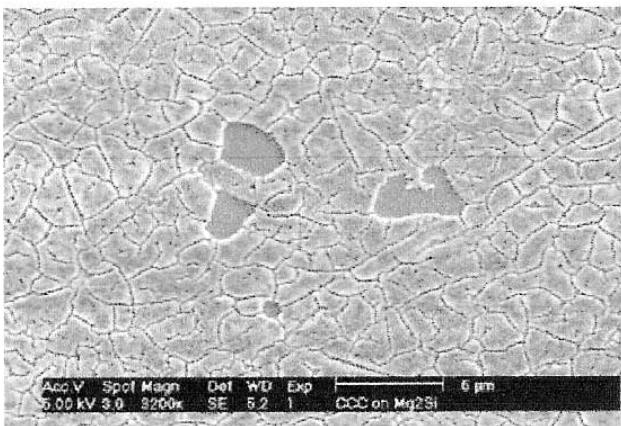
Figure 5.8 Scanning electron micrographs of conversion coatings on Al_2CuMg (a), $\text{Al}_3(\text{FeCu})$ (b) and Mg_2Si (c). The areas where the film is discontinuous are associated with the intermetallic particles.



(a)



(b)



(c)

CHAPTER 6 - Core and Valence Band X-ray Photoelectron Spectroscopy Studies of Chromium Oxide Standards and Chromium Aqueous Oxidation

6.1 Abstract

The systematic X-ray photoelectron spectroscopic study of four chromium oxides and the investigation of the oxidation of oxide-free chromium metal immersed in deaerated, quadruply distilled water under an anaerobic inert atmosphere is reported. The chromium oxides are a series of increasing chromium cation oxidation states in stable compound form. Three are strictly inorganic oxides and one is an organic based chromium compound which is included to provide comparison with carbon-containing compounds of chromium. The data obtained provide a homogeneous, consistent set of spectral parameters to serve as standards with which to compare more complicated spectra of other chromium compounds. Core level results show differences in Cr 2p and O 1s peak binding energies and chemical shifts that provide some indication of formal oxidation state, but do not provide enough information to unambiguously identify forms of chromium oxide present in chromium corrosion systems. Valence band studies show clear differences in the oxides and can be utilized in further investigations of chromium systems to identify species present in surface films on chromium and chromium-containing metals. The investigation of the surface film formed during the oxidation of chromium in deaerated, quadruply distilled water provides keen insight on the response of oxide-free etched chromium metal to an aqueous environment without other species present in a controlled environment.

6.2 Introduction

The oxidation behavior of chromium and its compounds has been extensively studied in the past.¹⁻¹⁰ Chromium is not only highly functional in today's society it also provides a ready substrate on which to study chemisorption processes and oxidation mechanisms. The data have been produced with multiple forms of X-ray light, some monochromatized, some not, under varying chemical, vacuum and temperature constraints and the very large majority of the data is only of core level spectra. There are precious few studies which include the valence band region of the chromium oxides. In order to have a consistent, detailed set of data to use in determining oxide structures and metal/oxide ratios in more complicated chromium systems four chromium oxide powders were studied. In order to provide predictive information on the oxidation behavior of chromium foil 99.99% chromium foil was treated in the anaerobic cell by removing the native oxide via argon ion etching, then exposing the oxide-free chromium foil to deaerated quadruply distilled (4D) water in an inert anaerobic environment and investigating the results without ever exposing the foil to atmosphere.

Corrosion behavior of chromium continues to present challenges to current industry. Nuclear fuel processing plants expose essential steel components to extreme conditions such as nitric acid vapor attack. Steel samples were studied after being treated with aqueous concentrated boiling acid and examined using X-ray photoelectron spectroscopy (XPS). The focus of the data was the identification of the Cr^{III} and Cr^{VI} species resulting from the oxidizing conditions.¹³ Biomedical applications of stainless steels still undergo pitting corrosion and degradation that often results in failure of the implant. Developments in surface coating technology have yet to produce a solution to the problem.

The focus of our research group has been on understanding corrosion systems and, recently, the formation of oxide-free thin films on metal surfaces.^{11, 13-17} The application of corrosion inhibitors in surface modifications to provide protection from corrosion has long been utilized in industry. The protection is usually in the form of a coating or film which chemically interacts with a pre-existing oxide layer on the metal substrate. Our group has developed two novel approaches to surface modification designed to form stable ultrathin oxide-free films which chemically bind with the surface of the metal substrate.^{11, 15} An ongoing effort to investigate the formation of these films on various metals chromium will be the focus of the current studies. In order to identify the features in the valence bands for the chromium

phosphate experiments, and identify them as an oxide or a phosphate, a clear picture of the oxides of chromium needs to be established.

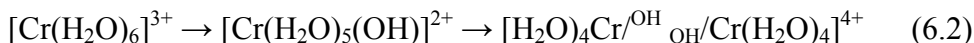
6.3 The Nature of Chromium Oxides

The three main chromium species reported in controlled oxidation experiments are Cr⁰ bulk metal, Cr^{III}₂O₃ oxide, and Cr^{III}O(OH) oxy-hydroxide.¹⁻¹² The oxy-hydroxide is a result of the presence of water vapor which reacts with the Cr₂O₃:



There is also a hydrated form of Cr₂O₃ present in the films as well (Cr₂O₃·nH₂O). Figure 6.2 illustrates the concept of the oxide layers forming on the chromium metal surface.

Cr^{III} has a tendency to hydrolyze and form polynuclear complexes with OH⁻ bridges as shown by Equation 6.2:



Given the fact that water vapor is present in most environments it is clear to see how a hydroxide film forms on the oxide film bonded to the clean metal substrate (Eq. 6.1), and is followed by the formation of the oxyhydroxide film (Eq. 6.2), which we see in the XPS spectra of the chromium oxides.

There is some disagreement regarding the reaction kinetics of the oxide formation. Sakisaka, Kato and Onchi⁵ concluded the process occurred in four stages: (1) dissociative chemisorption, (2) incorporation of the O adatoms into the Cr selvedge, (3) rapid oxidation occurring between 6-15 L (Langmuir) leading to the formation of the initial thin film of Cr₂O₃ and (4) slow thickening beyond 15L. The Palacio, Mathieu and Landolt⁶ results indicated the process occurs in *three* stages: (1) dissociative chemisorption, (2) nucleation of Cr₂O₃ islands which coalesce at about 10L, and (3) the oxide slowly thickens above 10L. Stage 2 is marked by abrupt changes in the AES, XPS and EELS spectra of these researchers. However, another group of researchers⁷ deduced no initial adsorption occurred as their results showed no change in the work function measurements at that stage. One fact is agreed upon: the oxide formation is a *self-limiting* process in that chromium metal oxide films slow to a logarithmic growth scale at about 20L⁴⁻⁷. This property of chromium metal lends high corrosion protection to alloys it is

incorporated into. The chromium oxide films are very hard and mechanically stable as well as self-healing when the oxide film becomes structurally compromised.

Naturally occurring chromium compounds are found in the Cr^{III} oxidation state. Only when exposed to highly oxidating environments, such as in the nitric acid steams occurring in spent nuclear fuel processing plants, will Cr^{III} oxidize into a stable Cr^{VI} formal oxidation state. The hexavalent form of chromium, CrO₃ and related species, pose a clear health risk in the environment and must be removed at appreciable expense²⁷.

6.4 Experimental

6.4.1 Instrumentation

Monochromatic Al K α (240 W) X-radiation was used with a VSW HA150 spectrometer (150mm hemispherical analyzer) utilizing a 16-plate multi-channel detector system. The monochromatic X-radiation was produced with a 32 quartz crystal VSW monochromator. The resulting line width is better than 0.2 eV. The base pressure of the ultrahigh vacuum system is better than 10⁻⁹ Torr. The system is fitted with a modification that allows for sample treatment in an inert anaerobic environment, referred to as the *anaerobic cell*. This chamber is isolated from the main vacuum chamber by a gate valve.

The spectrometer was operated in the fixed analyzer transmission mode with a pass energy of 50 eV for survey and valence band scans, and a pass energy of 20 eV for the core region sampling. The spectrometer was calibrated using copper and silver¹⁸ with spectra referenced to the adventitious hydrocarbon peak at a binding energy of 284.6 eV, or the Fermi edge if a distinct metal edge was present. Backgrounds were subtracted using the Proctor-Sherwood method previously described.¹⁹ Charge correction for the powder samples experiencing charging was achieved by using a low energy flood gun operated at about 2.24 mA and 280eV during collection of spectra.

6.4.2. XPS Measurement of Standard Compounds

XPS core and valence band spectra of pure chromium oxide and chromium phosphate powders were measured on the VSW HA150 instrument using monochromatic Al K α X-radiation with

the spectrometer parameters described above. The chromium sesquioxide, chromium dioxide, chromium trioxide, chromium acetate and chromium phosphate research grade powders were all obtained from Sigma-Aldrich Chemicals. The powders were evenly distributed on a double-sided carbon tape and mounted on a copper sample holder. Sample charging was present in several of the powders. This was corrected through the use of a low energy electron flood gun which continuously supplied the sample with electrons to replace those that have been lost in the photoemission process. The flood gun was operated at 2.23 mA and 280eV kinetic energy during spectral collection. Survey regions collected in this manner are 100eV narrower than survey spectra for conducting samples collected without the use of a flood gun in order to avoid the large spike at 280eV.

6.4.3 The Anaerobic Cell Procedure

The purpose of this experiment is to study the results of exposing a chromium metal surface, which has had the native oxide layer removed, to deaerated quadruply distilled (4D) water utilizing the anaerobic treatment previously described. This approach facilitates reaction of a clean, oxide-free metal surface directly with the deaerated aqueous reagent. An oxide-free metal surface is required for the formation of ultra thin phosphate films and this experiment provides information on the chromium-water system reacting concurrently with phosphate film formation on chromium.

The anaerobic cell allows for the metal surface to be monitored during the etching process as well as after the surface chemistry has been altered without ever exposing the experiment to ambient oxygen or contaminants until the resulting chemical system has been characterized. Chemistry performed in the anaerobic cell was done at a positive pressure (above 1 atm or >760 Torr) to prevent any ambient air or contaminants from entering the chamber during the procedure.

High purity (99.99%) research metal was obtained from Goodfellow. The sample was degreased with acetone and polished with 600 grit silicon carbide emery paper to remove the contaminant and native surface oxide layers. An Ion Tech saddle field ion etcher was used with ultrahigh purity (99.999%) argon gas and operated at 2 mA and 5kV backed by a pressure on the order of 10^{-4} Torr, providing an estimated etch rate of 2-5 Å min⁻¹. The chromium metal was

etched for 120 minutes. Once etching has removed the native oxide and surface adsorbants, as determined by monitoring the Cr2p and O1s core regions, the sample was moved to the anaerobic cell which was isolated from the main chamber of the vacuum system by a gate valve. The cell was filled with 99.999% pure argon gas, obtained from Matheson Gas, to a positive pressure to create an inert anaerobic atmosphere in which to conduct the experiment.

4-D H₂O was deaerated for four hours by bubbling pure nitrogen gas through the solution immediately prior to the experiment. The deaerated 4D H₂O was introduced into the anaerobic cell via the luggin capillary. In this experiment the electrochemical apparatus was not needed as the rest potential of chromium is -0.76 which is conducive to a spontaneous reaction occurring. The sample is then immersed into the acid solution for the duration of the reaction time of 10 minutes. This time period has proven effective in treatment of other metals in our research group.^{15,17} Once the reaction time has passed the 4-D H₂O is drained from the cell and the sample is allowed to dry *in vacuo* while UHV conditions are restored.

6.5 Data analysis

Data analysis is performed using software programs designed and written by Professor Sherwood. Spectral analysis is performed in the ESCA program and includes functions that allow the researcher to remove background, add and remove channels, spectral smoothing, differentiation and integration of spectra, synthetic spectral generation and Fourier deconvolution, among other features. Curve fitting is done using the GAMET program. Backgrounds were subtracted from some spectra using the Proctor-Sherwood method.²⁰

6.5.1 Curve Fitting

Core level spectra contain data about the chemical state of an analyzed element. A photoelectron peak most often contains several overlapping peaks resulting in electrons originating from the same element in different chemical environments. It is advantageous to resolve the different components of a peak. Having a good understanding of the chemistry involved with the experiment allows for reliable interpretation of the component peaks.

In Figure 6.1 four spectra from the O1s region are shown. The chromium foil as-received O1s region has three features associated with three different forms of oxygen which are

not obvious at first glance without the peaks being curve fit. The chromium oxide appears at 530.3 eV, hydroxide is at 531.8 eV and oxygen associated with water shows at 533.6 eV.

Professor Sherwood has designed the GAMET program to perform non-linear least squares analysis on the spectrum. There are seven parameters for the characteristic features of a peak. A peak can be described by its position, intensity, and width. It is further described by the peak shape which are dictated by the percent Gaussian/Lorentzian mixing ratio, the height of the constant tail (if present), the slope of the exponential tail and the tail mixing ratio. The background slope and intercept are also taken into account. Each peak curve fit consists of $7n+2$ variable parameters, where n equals the number of component peaks in the spectrum.

6.5.2 Calculations

The valence band spectra of the standard oxides were interpreted using data obtained from band structure calculations using the Hartree-Fock approach. Band structure calculations were carried out using an extended version of the software program CRYSTAL.^{23,24} Crystal structure data used for the calculations are supplied in Table 6.1. The Wachters STO-3G basis sets²⁵ were used for all structures. The data for chromium sesquioxide²⁸, chromium dioxide²⁹ and chromium trioxide³⁰ can be found in the listed references. The calculations are all unrestricted Hartree-Fock (UHF) calculations. Spectra were generated from the band structure calculations by adjusting the density of states in the valence band for each orbital symmetry type (O2s and O2p, P3s and P3p, Cr 4s and Cr 3d) by the appropriate Scofield atomic photoelectron cross section.²⁶ The density of states was then convoluted with a 50% mixed Gaussian-Lorentzian product function with a full width at half maximum (fwhm) of 1.5 eV.¹⁴

6.5.3 Atomic Ratio Calculations

Core level peaks are proportional to the number of atoms originating from a given chemical environment. The peaks are described in two dimensions by their area which is the number of counts multiplied by the step size in eV. The peak intensity may therefore be expressed as the measurement of the peak area. The area, or intensity, may be used to calculate atomic ratios if it is assumed that the peak is being described by data arising from a uniform surface (usually not the case). The accurate determination of peak intensity necessitates removal

of the background. There are several approaches that can be used, but our group uses the Proctor-Shirley background removal method. This method is based on the Shirley iterative method which assumes that the background intensity at a given point is proportional to the intensity of the total peak area above the background and to a higher energy than the data point.

Once peak intensities are obtained the atomic ratios can be determined by employing the following equation²¹:

$$n_x/n_{ref} = (A_x/A_{ref})(\alpha_{ref}/\alpha_x)(\sqrt{KE_x}/\sqrt{KE_{ref}})(\lambda_{ref}/\lambda_x) \quad (6.2)$$

where,

n_x = number of atoms in core level of interest, x refers to core level of interest

n_{ref} = number of atoms in the reference core level, ref refers to the reference core level

A = experimentally derived area of the core peak ($A=(\text{peak area} \times \text{step size})/\text{number of scans}$)

α = the photoelectron cross section of the core level

KE = the kinetic energy of the core level peak

λ = the inelastic mean free path of the electrons from the level. This value is usually determined from the Seah and Dench equations.²¹ Atomic ratios are usually referenced to the core level of the substrate material, but other species of interest in the sample may be used.

When interpreting atomic ratios from core level data, one must bear in mind that the contributions from a given spectral area are usually not from a single component. The results may be misleading if the ratio does not match the empirical formula of the species assumed present. This often happens with the O1s core data which not only includes the oxide data but also oxygen counts from adsorbed H₂O or CO common in UHV environments.

6.6 Results and discussion

6.6.1 Analysis of chromium oxide standards

Overall survey, Cr 2p, Cr 3p, Cr 3s, O 1s, C 1s and valence band spectra were measured and recorded. Only the Cr 2p, O 1s and valence band regions will be presented and discussed as the other core regions do not add significantly to the information provided by these

regions. Table 6.2 gives a rough approximation of the atomic ratios of the standard powders. The assumption is made in the calculation of the ratios that 100% of the signal from the core region is from a homogeneous mixture of Cr-O. Signal from the O 1s region can also contain contributions from water and other contaminants present in the sample as stated above.

The atomic ratios are adjusted for the differences in the photoelectric cross-section of each component and the analyzer transmission function is accounted for during the intensity normalization process. XPS spectra were collected at an emission angle normal to the sample surface. O 1s core region peaks were fitted as described in section 6.4.1, above and are shown in Fig. 6.4. Figure 6.3 shows core level and valence band results for the study of the chromium oxide standards.

6.6.1.1 O 1s Region

The curve fit data shown in Figure 6.4 reveal significant differences in the chromium oxides. Parameters for the curve fitting of the O 1s regions for the chromium standards are shown in Table 6.4. All of the fitting was done using a 50% Gaussian/Lorentzian shape. The exponential tail, tail mix ratios or exponential tail height information were all entered as zero.

The O 1s core region of chromium acetate is dominated by oxygen from the acetate (O-C=O) ion. There are very minor contributions from the hydroxide and water oxygens. The fitted peaks show hydroxide at 530.8 eV, the ester group in the acetate ion is at a binding energy of 532.0 eV and the oxygen from H₂O shows at 533.2 eV.

Chromium sesquioxide (Cr₂O₃) is predominantly composed of hydroxide. If Equations 6.1 and 6.2 are considered then this result is not unexpected. The O²⁻ feature has a full width at half maximum of the peak area (FWHM) nearly as wide as the hydroxide component. There is nearly three times the amount of water as contained in the chromium acetate. While the three inorganic chromium oxides were opened immediately beside the sample loading area and the powders were mounted with due haste there was still quite an affinity for water in all three compounds.

Chromium dioxide (CrO₂) was the only powder that did not require correction for charging. This compound is unique among the group of standards assembled for this study in that it is ferromagnetic. One of the uses of CrO₂ is for data storage. Before the music industry began using CD media for music and vocal recordings, cassette tapes used chromium oxide to

improve the quality of the sound recorded on the tape. The CrO₂ O 1s core region is dominated by the O²⁻ species. Almost equally represented, though not as high in intensity, is the hydroxide portion of the photoelectrons generated by oxygen. This compound shows the greatest affinity for water among the chromium oxides studied. The chromium trioxide has no discernable feature for the O²⁻ species. This may mean that the surface is largely hydroxide.

6.6.1.2 Cr 2p Region

The Cr 2p region has two main spin orbit split features. A higher binding energy peak at about 590 eV corresponds to the 2p_{1/2} electrons. A more intense peak occurs at a binding energy of about 575 eV, are measured which correspond to the 2p_{3/2} electrons. The spin orbit split doublets result from there being two possible final states, one for the spin-up electrons and one for the spin-down. The coupling occurs between the angular momentum of the orbital and the spin of the electron still remaining in that orbital after photoemission has occurred. When a vectorial sum of the solitary electron's angular momentum (quantum number *l*) and the electron spin (quantum number *s*) is taken spin-orbit coupling is described. The relative areas of the two peaks are governed by the degeneracy of the two states, as discussed in Chapter 1. The Cr 2p_{1/2} lies at a binding energy generally 9.8 ± 0.3 eV higher than the 2p_{3/2}.

Table 6.5 lists the binding energies for the core level peaks discussed in this dissertation. Table 6.6 addresses the four powder standards studied here by comparing the binding energies of the 2p_{3/2} metal peaks, the FWHM of those peaks, the difference between the metal and oxide features within the peak, and the separation between the 2p_{3/2} metal and 2p_{1/2} peaks. The four chromium oxide Cr 2p peaks are shown in Figure 6.5.

The general trend of chemical shift within a set of similar compounds indicates that the higher the formal oxidation state of an atom the higher the binding energy of electrons in that core level, as discussed in Chapter 1. When comparing the binding energy at the peak center at FWHM of the four compounds this trend holds true until the Cr 2p_{3/2} binding energy of the chromium acetate is compared with the other four compounds. The chromium in this compound has a formal oxidation state of +2 which, if the trend held true, would appear below 576.7 eV. As previously stated chromium acetate is an organo-metallic compound. The molecular formula for chromium acetate is Cr₂(O₂CCH₃)₄(H₂O)₂. Each chromium atom has a coordination number of 5 (ignoring the Cr-Cr bond). The chromium atoms have a quadruple bond between them

(bond distance of 2.362 Å).³¹ There is a σ component from the overlap of the d_z^2 orbitals of the two atoms, two π bonds from the d_{xz} d_{yz} orbitals and a δ bond from the xy overlap.³² Even though there are four d-orbital electrons the compound is diamagnetic because of the quadruple Cr-Cr bond. As a result of the compound having a more covalent nature than the other three chromium compounds studied the Cr2p peaks appear at a slightly higher binding energy than would be expected. In fact the relationship between increasing binding energy and increasing oxidation state is not always observed. The actual chemical shift can be explained by calculations based upon the relaxation potential model.

The chromium acetate Cr 2p_{3/2} peak center at FWHM appears at the same binding energy as CrO₂; however there is a difference of over 1 eV in their widths. CrO₂ is more metallic in nature, having a metallic peak feature in the Cr 2p_{3/2} region 1.7 eV lower binding energy than the oxide feature in the peak. There is also a contribution to the peak width from lifetime broadening as discussed in the previous section. The lifetime broadening effect is greatest in CrO₂. The peak widths are the same for Cr₂O₃ and CrO₃ at 2.96 eV. An argument could be made that the use of the flood gun, or lack thereof, might account for the difference in peak width. However, comparing the CrO₃ spectra in Figure 6.6 it becomes evident that the main impact of the flood gun is on the kinetic energy of the ejected photoelectrons. Also shown in Figure 6.6 is the refinement of the resolution as a result of the charge compensation.

6.6.1.3 Valence Band Region

While the core regions yield relevant chemical information about the compounds studied the chemical information provided is not enough to be able to readily identify which type of oxide might be present in the study of an unknown compound. The overall chemical composition could certainly be deduced, but given an unknown O 1s or Cr 2p region of a chromium phosphate there would still be many of the features discussed above, but all chromium phosphates contain chromium and oxygen and would likely also have water and/or hydroxide present. Through analysis of the valence band region, especially the outer valence band (from 0-15 eV binding energy), one is able to see straight away the subtle differences which are not evident in core region data. Information from valence band XPS reflects the levels involved in chemical bonding because the valence electrons are molecular in nature with binding energies

characteristic of the molecular orbitals they came from. These energies reflect the ground state density of states and can therefore be correlated to calculated energy levels.

In Figure 6.7 the experimental valence band spectra of the four chromium oxide powders are shown. Though there are obvious differences between the four, there are features they all have in common. The dominant feature in all four is the peak appearing at a binding energy of about 21 eV. The major component of this peak is contributed by the O 2s electrons, but it also contains contributions from C 2s C 2p and O 2p. In the Cr₂O₃ spectrum the shoulder on the most intense peak at 18eV indicates that there is carbon present in the sample, either from the carbon tape used to mount the sample or from the adventitious carbon vapor present in the vacuum system from the pump oil. This peak is predominantly C 2s in character, but obviously has a great deal of O 2s influence as well as minor contributions from O 2p, C 2p and possibly some Cr 3d interaction. The second peak common to all four oxides is in the region of 4-5 eV. This peak is predominantly O 2p in character, but has features arising from the C 2s, C 2p, O 2s and Cr 3d. The CrO₃ peak is lower in intensity and narrower than the other three since there are no d-level electrons present in the Cr⁶⁺ state. Both the Cr₂O₃ (Cr³⁺) and the CrO₂ (Cr⁴⁺) valence band spectra have a clear peak at about 1.5 eV that is mostly representative of the Cr 3d electrons. This feature is less intense in the CrO₂ spectrum since it is in the 3d² configuration. Again, as in the previous cases, there is contribution from oxygen in this region from the O 2p electrons and from the C 2p as well, although there is less carbon present in the CrO₂ sample than the Cr₂O₃, judging by the much lower intensity of the predominantly C 2s region at 17-18 eV.

The valence band spectrum of the Cr^{II} acetate has very obvious features resulting from the 8 carbon atoms in the molecule (recall the molecular formula of chromium acetate is Cr₂(O₂CCH₃)₄(H₂O)). The least intense of the four peaks present in the spectrum at 17eV is fairly broad since there are carbon atoms in two slightly different environments. There is a carbon chemically bonded to two oxygen atoms, one of which is a carbonyl, and a carbon bonded to another carbon and four hydrogen atoms. This region has strong contributions from the oxygen 2s and 2p and influence from hydrogen atoms as well. The π-bonding in the carbonyl generally appears at about 8-9 eV.³³ Indeed, the Cr^{II} acetate valence band spectrum has a strong feature at about 11eV. The peak appears at a higher binding energy than referenced because of the O 2s and O 2p electrons participating in covalent bonding with carbon. The peak

at 4.7 eV has a great deal of O 2p, C 2p and Cr 3d representation, yet still is somewhat influenced by the O 2s and C 2s electrons as well.

Band structure calculations were done for the inorganic chromium oxides and the spectra resulting from the calculations are shown in Figure 6.8. These are aligned such that it becomes clear that there are very distinct differences that allow for greater confidence in identifying which oxide might be present. The CrO₃ calculated spectra has no visible contribution from the Cr 3d electrons as indicated by the absence of any feature below 4 eV. The CrO₂ outer valence band indicates a broader region than the Cr₂O₃ band structure calculation has where the O 2p and Cr 3d electrons are the major contributors. The Cr₂O₃ band structure calculation shows a greater amount of mixing between the Cr 3d and O 2p orbitals than the CrO₂. When the experimental spectra are compared to the calculated results, as shown in Figure 6.9, there are variations in relative peak intensities between the two but the features in the experimental spectra are present in the calculated results confirming the experimental results can indeed be used as standards with which to compare any phosphate films formed on chromium in other experiments to confirm the absence, or presence, of an oxide in the film formed.

6.6.2 Analysis of Oxide Film on Chromium Foil in 4D H₂O

6.6.2.1 O 1s and Cr 2p Core Regions

The core region XPS spectra of the 99.99% pure chromium foil, which was etched and exposed to 4D H₂O in the anaerobic environment provided by following the protocol discussed above for the anaerobic cell, are shown in Figure 6.10 compared to XPS spectra of the same regions of the etched foil immediately prior to the anaerobic cell treatment. The O 1s regions shown are also shown in Figure 6.1 curve fitted. The 4D H₂O oxide is mainly composed of hydroxide (indicated by the strong feature around 532 eV but has a strong portion which is O²⁻. The feature around 533 eV shows that oxygen from water is a relatively small percentage of the O 1s region. The parameters used in curve fitting the peaks are included in Table 6.4. The binding energies for the regions are listed in Table 6.5. Both tables include data for all the experimental results. The O 1s spectrum for the etched chromium foil has almost equal amounts of hydroxide and water with slightly more O²⁻ contributing to the spectrum. While the spectra in

Figure 6.1 are comparable in relative intensity, one must bear in mind that the intensity scale for the etched foil O 1s spectra was not meant to imply there are comparable electron counts for the spectra. The etched chromium foil had very low oxygen counts since there was so little present on the sample, which is why the statistics in the spectra are not as good as the others in the figure.

The 4D H₂O oxide appears on the Cr 2p peak 3 eV higher binding energy than the metal peak, which still dominates the spectrum. While the Cr 2p data indicates that a thin oxide film was formed there is no additional information that can be useful in determining what that oxide film consists of. The results of the study of the chromium standards Cr 2p region indicate that the chemical shift of CrO₃ is 5.1 eV and Cr₂O₃ is about 2.8 eV. This indicates the oxide *might* be Cr₂O₃ but further information is required.

6.6.2.2 Valence Band XPS Results

The information provided by valence band XPS is complimentary to that acquired in the core level XPS studies. The O 1s and Cr 2p core region spectra do not provide enough detail to clearly indicate the chemical environment of the etched chromium foil sample exposed to 4D H₂O. Further information is provided in the comparison and contrasting of the VBXPS spectra of the experimental sample and the reference chromium oxides. However, the reference chromium oxides are in the form of a powder and the surface oxides on the experimental samples are formed on a hard chromium foil which has been argon ion etched. There are two chemical events that occur when chromium is etched and both have a pronounced impact on the valence band spectra. Before analyzing the oxide valence band the features resulting from the argon-ion etching process must be addressed.

The argon-ion etching process results in argon being embedded in the substrate. The chromium metal valence bands shown in Fig. 6.11(a) and (b) show the Ar 3s peak at 22 eV and Ar 3p at about 9 eV, which are then compared to the constructed theoretical argon valence band with the Ar 3s and 3p features. The theoretical spectrum was created by incorporating the FWHM and peak separation from the experimental data. Additionally, the peak areas were synthesized according to the photoelectron cross sections as predicted by Scofield which is substantial, especially when one considers the fact that a portion of the Ar 3s directly overlaps the O 2s region and has a photoelectric cross section that is nearly twice as large as O 2s (0.1405

units for O 2s -vs- 0.227 units for Ar 3s).²⁶ The valence band shown in Fig 6.11(a) is after 30 minutes of etching and shows both argon features clearly. Figure 6.11(b) is the same sample after an additional 90 minutes of etching and indicates that the amount of argon imbedded in the sample has greatly increased, disproportionately to the other features, implying that the amount of argon present in the sample has increased to the point that it is beginning to obscure the other features. The argon present in the sample hinders the interpretation of the valence band spectra if not accounted for. In the case of the etched metal it would appear that there is an oxide layer still remaining on the metal indicating that the oxide layer was not removed prior to the experiment, which is not the case here. The chromium metal valence band generated from band structure calculations is shown in Figure 6.12 and demonstrates what the spectrum would look like if the argon were not present.

Further complicating the valence band interpretation is the presence of chromium carbide which formed during the etching process. There is also the likelihood of the presence of carbon monoxide which would have formed during the etching process by the liberated oxygen reacting with the adventitious hydrocarbon present in the vacuum system and originating in the diffing pump oil. The carbide is most noticeable in the etched valence band spectra at around 12 eV, which is more predominant in the 30 minute etched sample and is beginning to be overshadowed by the Ar 3p peak as the argon layer begins to deepen and obscure the chromium metal/carbide beneath it. The presence of the chromium is confirmed when the C 1s core region of the etched metal sample is compared with the as-received metal sample and the chromium carbide powder in Fig. 6.13. The C 1s core region spectrum of the etched sample has a large carbide feature appearing 2.1 eV lower in binding energy than the hydrocarbon at 284.6 eV. The chromium carbide powder also has the carbide feature appearing 2.1 eV lower than the hydrocarbon. It is important to note that the powder sample was fresh and exposed to air only for the time required to load onto the sample holder and transfer it into the analysis chamber, or approximately 2-3 minutes, and the carbide powders are reactive in air. Additionally, the carbide powders were mounted with carbon tape which was probably somewhat present in the spectrum, as evidenced by the larger hydrocarbon feature in Fig. 6.13(c). The C 2s generally appears at approximately 18-19 eV which would lie in the region of the Ar 3s peak and shows as a low binding energy shoulder on the said peak in the chromium metal sample etched for 30 minutes

shown in Fig. 6.11(a). The sigma bonding in the C 2p region appears around 8 eV and the pi-bond is from 3-4 eV.³³

Two forms of chromium carbide were run in order to better identify the type of chromium carbide resulting from the etching process and are shown in the comparison in Fig. 6.14. The Cr₂₃C₆ form of chromium carbide is the most common form found. The Cr₃C₂ powder was studied for comparison purposes (Fig. 6.14(c)) and has a much different valence band spectra, as shown in 6.14(c), than that of Cr₂₃C₆, which is shown in Fig. 6.14(c). Both valence band spectra indicate the carbon influence in the etched metal sample spectra shown in Fig. 6.14(a). While both powder samples show a great deal of C 2p character only the Cr₂₃C₆ sample has pronounced chromium 3d character as indicated by the peak at 1.5 eV in Fig. 6.14(b). Given this information and the prevalence of this particular form of chromium carbide formation it is reasonable to conclude that the metallic chromium carbide on the etched sample is in the form of Cr₂₃C₆.

The valence bands of the chromium oxides show pronounced differences in the “fingerprint” region in the outer valence band spectra at binding energies below 15 eV. Examination of this region in the valence band spectrum of 99.9% Cr foil exposed to quadruply distilled water reveals features leading to the conclusion that the oxide formed in the metal surface is Cr₂O₃. The 4D H₂O oxide seen in the O 1s core region shown in Fig. 6.10(a) has a predominant hydroxide component present, as do the Cr₂O₃ and CrO₃ standards. However the chemical shift of 2.8 eV demonstrated in the Cr 2p core region shown in Fig. 6.3(b) corresponds to the shift in the Cr 2p core region of the 4D H₂O oxide shown in Figure 6.10(a) indicates the presence of trivalent chromium, as does the broadened peak at 4.8 eV in the valence band XPS spectrum of the 4D H₂O sample shown in Fig. 6.15(a) when compared with the Cr^(III) form shown in Fig. 6.15(c).

An angle resolved study was done to extract information regarding the composition of the outer layer of the surface film. The take off angle of the ejected photoelectrons was changed from 90° to 60°. This method of sampling increases the path length that the photoelectrons travel through the outer surface making the spectral results more surface sensitive. The curve fitted O 1s results are shown in Figure 6.16(b) indicating the change in relative amounts of the three forms of oxygen bonding in the sample when the sampling conditions were altered. The O²⁻ region decreased in intensity and the hydroxide component essentially remained the same. The

highest binding energy peak corresponding to oxygen associated with water decreased dramatically. The angle resolved Cr 2p spectrum shows an intensity increase in the chemically shifted oxide region on both spin orbit split peaks. The valence band spectrum taken at the surface sensitive angle has an increase in intensity for all the peaks except the Cr 3d metal peak at 1.5 eV. The fact that the intensity increased at peaks at 9 and 12 eV could be the result of a very small amount of phosphate contamination from incorrectly cleaned anaerobic cell glassware. The C2s and C 2p regions at 18 and 8 eV, respectively, showed a relatively large increase indicating some hydrocarbon is present on the surface, which is common for UHV systems using diff pumps. The peak at 4 eV is O 2p and Cr 3d in character. The increase in this peak's intensity and width may indicate a multilayered film where the immediate surface of the chromium foil is bonded with the water and changes to a layer of mixed Cr₂O₃, CrOOH and water which lies beneath the outer layer of hydroxide and contaminants. The O 2s region at 24 eV did not change peak shape but also shows an increase in intensity indicating an increase in the amount of oxygen present in the outer layers of the film.

6.7 Conclusions

The valence band spectra of the chromium oxide standards were essential in the interpretation of the oxide shown in the valence band spectrum of the etched 99.9% chromium foil exposed to deaerated, quadruply distilled water in the inert atmosphere of the anaerobic cell designed by this research group. It was determined that the oxide film generated from quadruply distilled water was Cr^(III) in composition. Additional data provided by an angle resolved study yielded data indicating a multi-layered film exists on the chromium foil. Theoretical spectra created by band structure calculations and peak synthesis yielded critical information for valence band interpretation and supported the conclusions drawn.

6.8 Acknowledgements

Acknowledgement is gratefully given to Professor Sherwood for his assistance with the band structure calculations and the construction of the argon valence band.

6.9 References

1. E. Desimoni, C. Malitesta, P. G. Zambonin and Rivière, *Surf. Interface Anal.*, **13**, 173, (1988).
2. Z. M. Hanafi, F. M. Ismail, A. K. Mohamed, *Zeit. für Physik. Chem.*, **194**, 61, (1996).
3. M. C. Biesinger, C. Brown, J. R. Mycroft, R. D. Davidson and N. S. McIntyre, *Surf. Interface Anal.*, **36**, 1550, (2004).
4. P. Dolle, M. Alnot, J. J. Ehrhardt and A. Cassuto, *J. Electron Spectroscopy Rel. Phenom.*, **17**, 299, (1979). (Printed in the Netherlands)
5. Y. Sakisaka, H. Kato, M. Onchi, *Surf. Sci.*, **120**, 150, (1982).
6. C. Palacio, H. J. Mathieu, and D. Landolt, *Surf. Sci.*, **182**, 41, (1987).
7. G. Gewinner, J. C. Peruchetti, A. Jaegle, A. Kalt, *Surf. Sci.*, **78**, 439, (1978).
8. J. C. Carver and G. K. Schweitzer, *J. Chem. Phys.*, **57**, 973, (1972).
9. E. McCafferty and J. P. Wightman, *Surf. Interface Anal.*, **26**, 549, (1998).
10. S. F. Ho, S. Contarini and J. W. Rabalais, *J. Phys. Chem.*, **91**, 4779, (1987).
11. Y. Liang, D. K. Paul, Y. Xie and P. M. A. Sherwood, *Anal. Chem.*, **65**, 2276, (1993).
12. J. A. Beavers, R. R. White, W. E. Berry and J. C. Griess, *Oak Ridge Natnl. Lab. Report ORNL/Sub-7327/13*, Oak Ridge, TN, USA.
13. J. A. Rotole and P. M. A. Sherwood, *Fresenius J. Anal. Chem.*, **369**, 342, (2001).
14. H. G. Hixon and P. M. A. Sherwood, *J. Phys. Chem.*, **105**, 3957, (2001).
15. J. A. Rotole and P. M. A. Sherwood, *Chem. Mater.*, **13**, 3933, (2001).
16. H. Hixon and P. M. A. Sherwood, *J. Chem. Soc. Faraday Trans.*, **91**, 3593, (1995).
17. D. J. Asunskis and P. M. A. Sherwood, *J. Vac. Sci. Technol. A*, **21**, 1133, (2003).
18. M. P. Seah, I. S. Gilmore and G. Beamson, *Surf. Interface Anal.*, **26**, 642, (1998).
19. A. Proctor and P. M. A. Sherwood, *Anal. Chem.*, **54**, 13, (1982).
20. M. Seah and W. Dench, *Surf. Interface Anal.*, **1**, 2, (1979).
21. Y. Liang, D. Paul and P. M. A. Sherwood, *Vac. Sci. Technol. A*, **5**, 1554, (1993).
22. C. Pisani, R. Dovesi and C. Roetti, *Hartree-Fock ab Initio Treatment of Crystalline Systems: Lecture Notes in Chemistry*, 48. Springer: Berlin. (1988).

23. V. Saunders, et al., *CRYSTAL 98 User's Manual*. University of Torino: Turin, Italy. (1998).
24. A. Wachters, *J. Chem Phys.*, **52**, 1033, (1970).
25. J. Scofield, *Electron Spectr. Relat. Phenom.*, **8**, 129, (1976).
26. M. Trnovsky, J. P. Ozer, R. J. Rudy, M. J. Hanchak and B. Hartsfield, *Hazard. Waste: Detect., Control, Treat., Proc. World Conf.*. R. Abbou, Ed., Elsevier: Amsterdam, Neth. (1988).
27. R.E. Newnham, and Y. M. de Haan, *Zeit. Für Kristall.*, **117**, 235, (1962).
28. P. Porta, M. Marezio, J. P. Remeika and P. D. Dernier, *Mat. Research Bulliten*, **7**, 157, (1972).
29. J. S. Stephens and D. W. J. Cruickshank, *Acta Crystall. B*, **26**, 222, (1970).
30. L. R. Ocone and B. P. Block, *Inorg Syn.*, **8**, 71, (1966).
31. S.F. Rice, *Inorg. Chem*, **19**, 3425, (1980).
32. H. Viswanathan, M. A. Rooke and P. M. A. Sherwood, *Surf. Interface Anal.*, **25**, 409, (1997).
33. J. Rotole, K. Gaskell, A. Comte and P. M. A. Sherwood, *J. Vac. Sci. Technol. A*, **19**, 1176, (2001).

6.10 Figures

Figure 6.1 O 1s core region XPS spectra for etched 99.9% pure chromium foil treated in deaerated quadruply distilled H₂O in the anaerobic cell (a), 99.9% pure chromium metal, as received (b), 99.9% pure chromium metal, polished (c) and 99.9% pure chromium metal, etched (d).

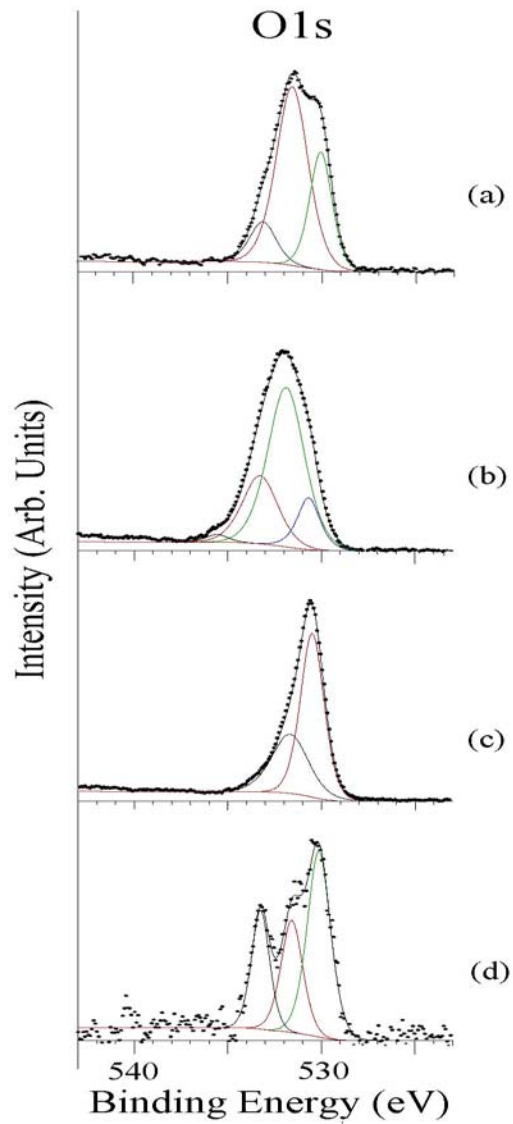


Figure 6.2 Diagram representation of the overlayers of oxy-hydroxide (a) on the Cr_2O_3 (b) oxide layer formed on the chromium bulk.

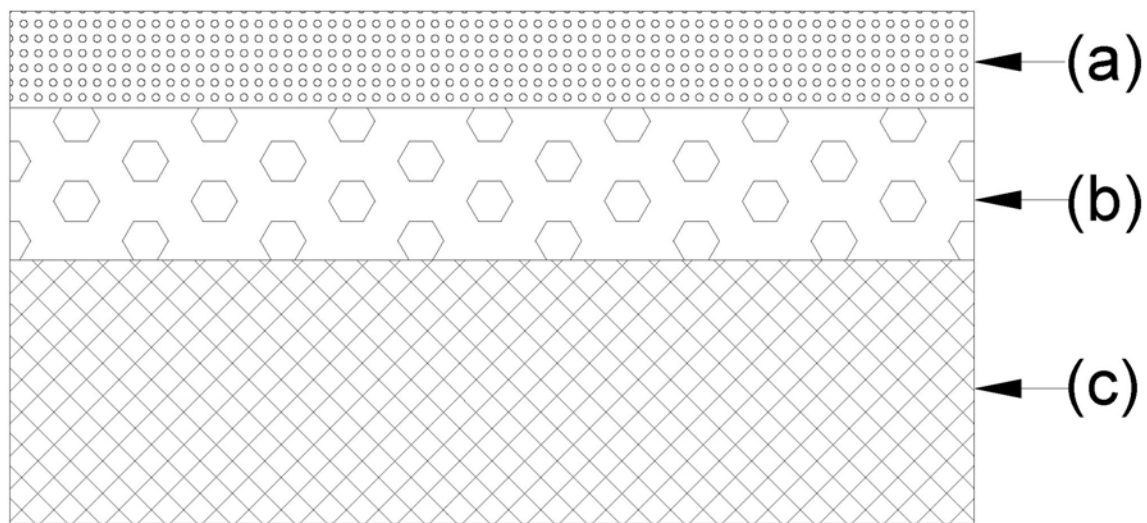


Figure 6.3 Core and Valence Band Spectra for Cr^{II} Acetate (a), Cr₂O₃ (b), CrO₂ (c) and CrO₃ (d).

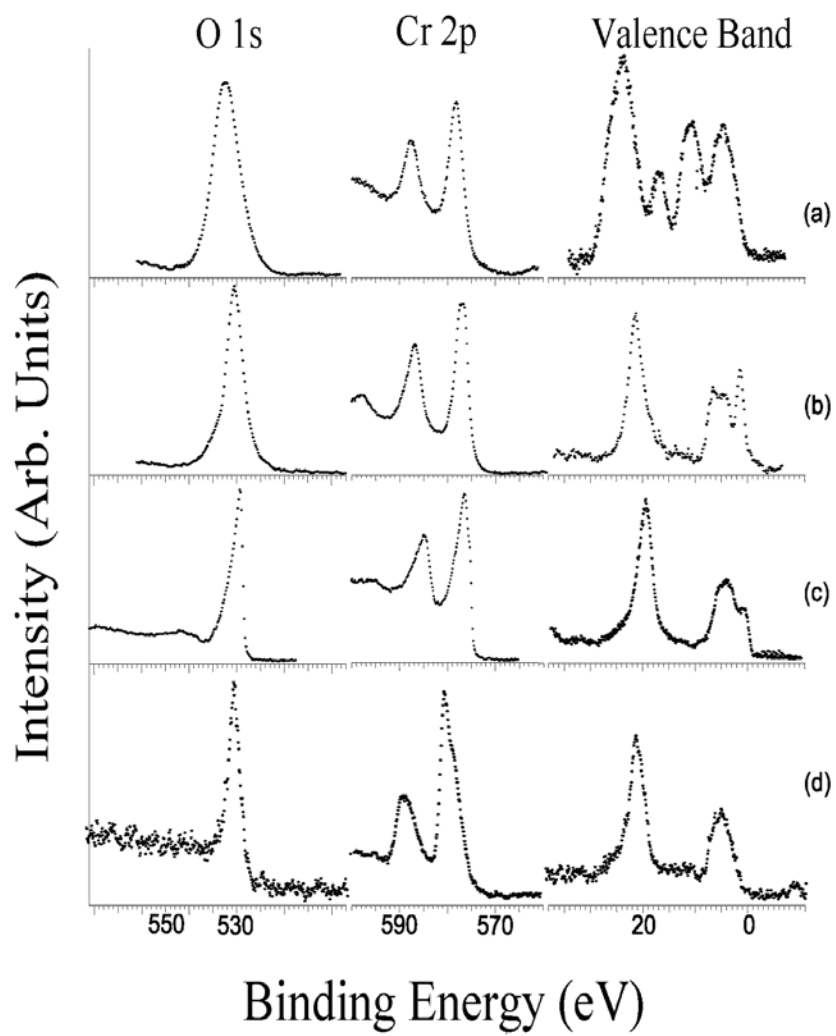


Figure 6.4 O 1s Core Data. Curve fitted O 1s peaks for Cr^{II} Acetate (a), Cr₂O₃ (b), CrO₂ (c) and CrO₃ (d).

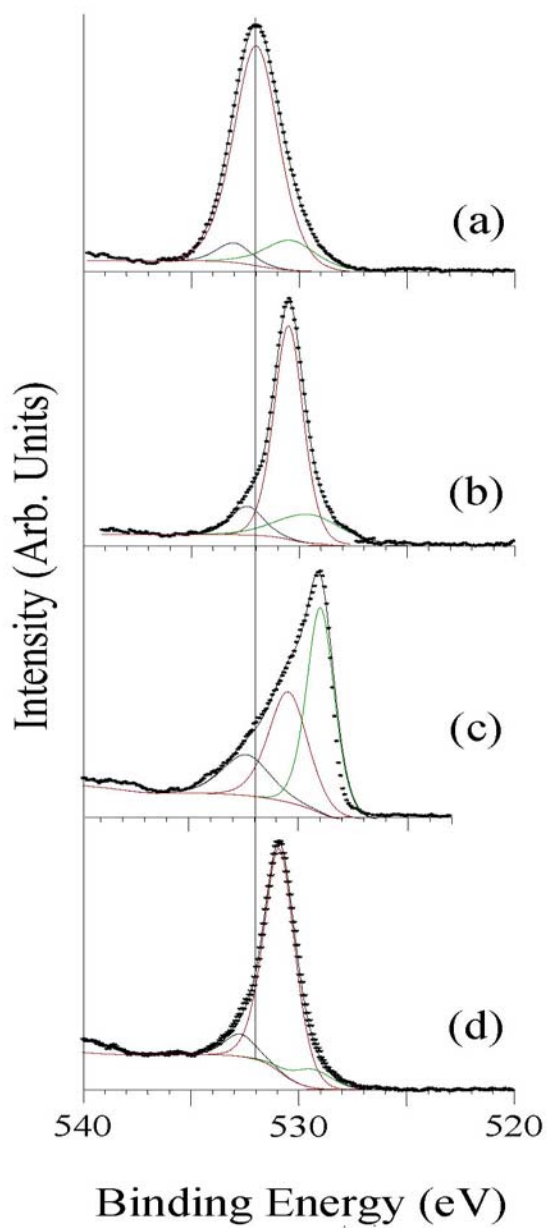


Figure 6.5 Core level XPS results for the Cr 2p region of the chromium oxide standards. Shown in order of increasing formal oxidation state are (a) Cr^{II} acetate, (b) Cr^{III}₂O₃, (c) Cr^{IV}O₂ and (d) Cr^{VI}O₃.

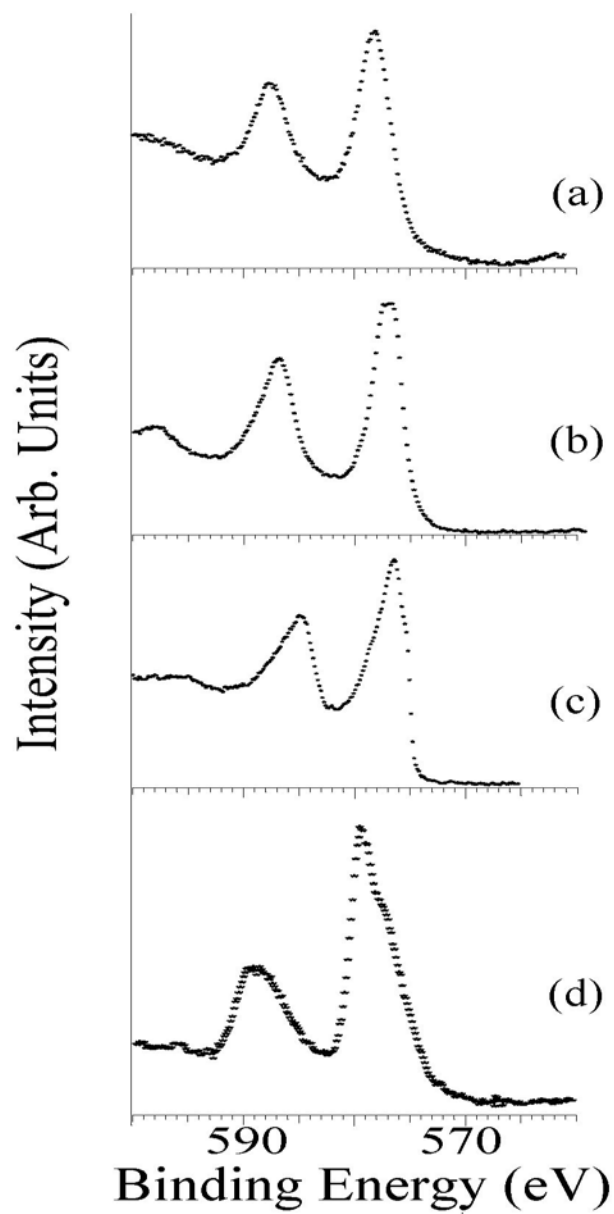


Figure 6.6 Comparison of the effects from use of a flood gun. Without flood gun (a) and using flood gun (b) show there is no change in peak width. The kinetic energy shifts and the line resolution is improved when sample charging is compensated for with a flood gun.

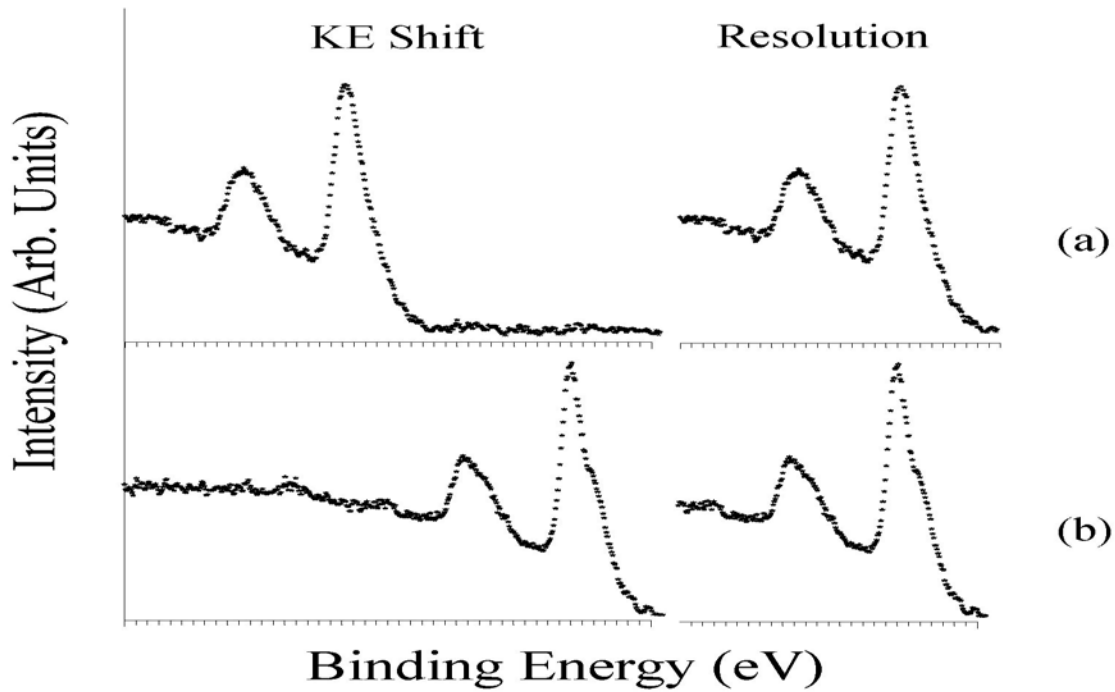


Figure 6.7 Valence band XPS spectra of Cr^{II} acetate (a), Cr_2O_3 (b), CrO_2 (c) and CrO_3 (d).

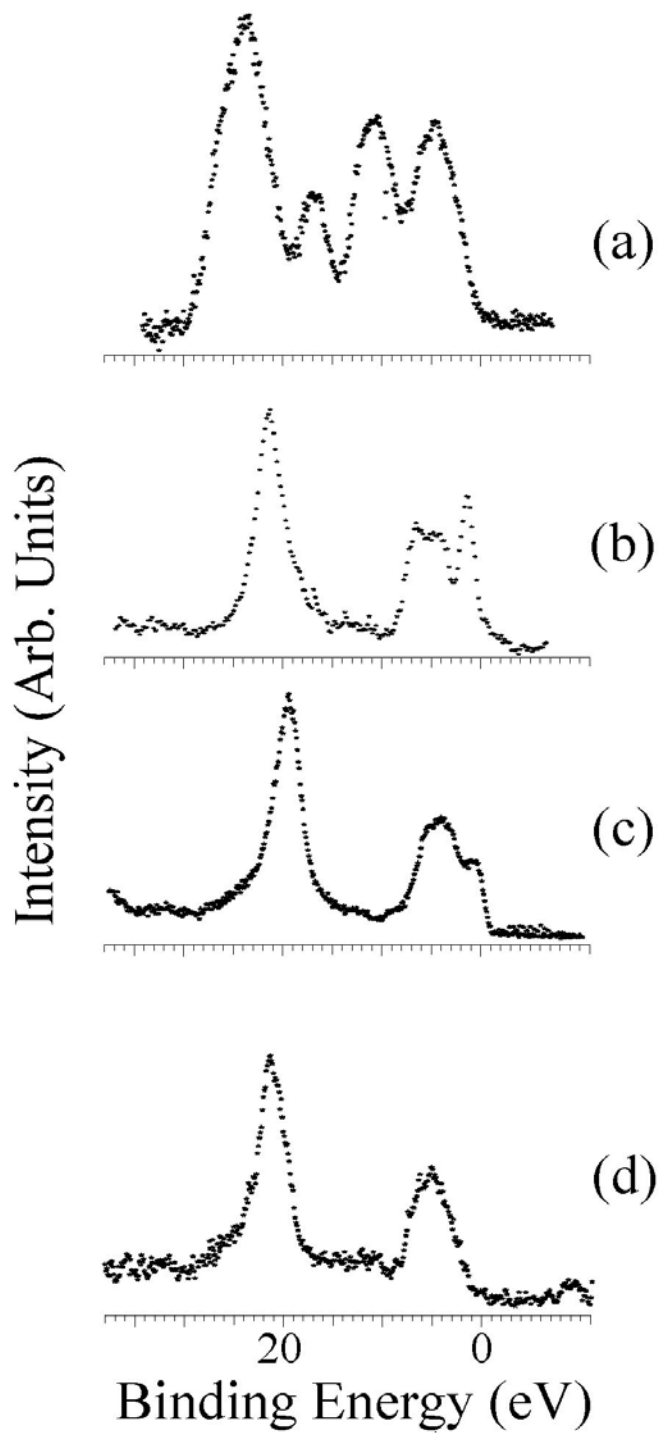


Figure 6.8 Band structure calculations of the valance bands of (a) Cr_2O_3 , (b) CrO_2 and (c) CrO_3 .

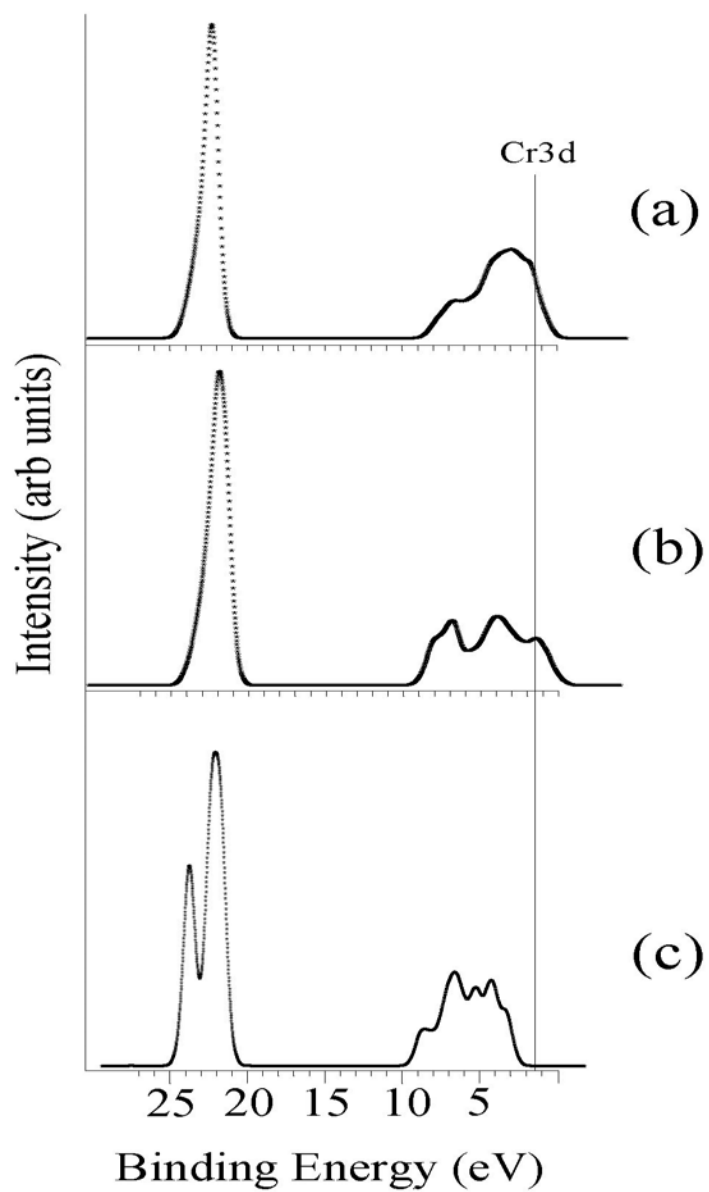


Figure 6.9 Comparison of experimental spectra (top) to spectra synthesized from band structure calculations (bottom).

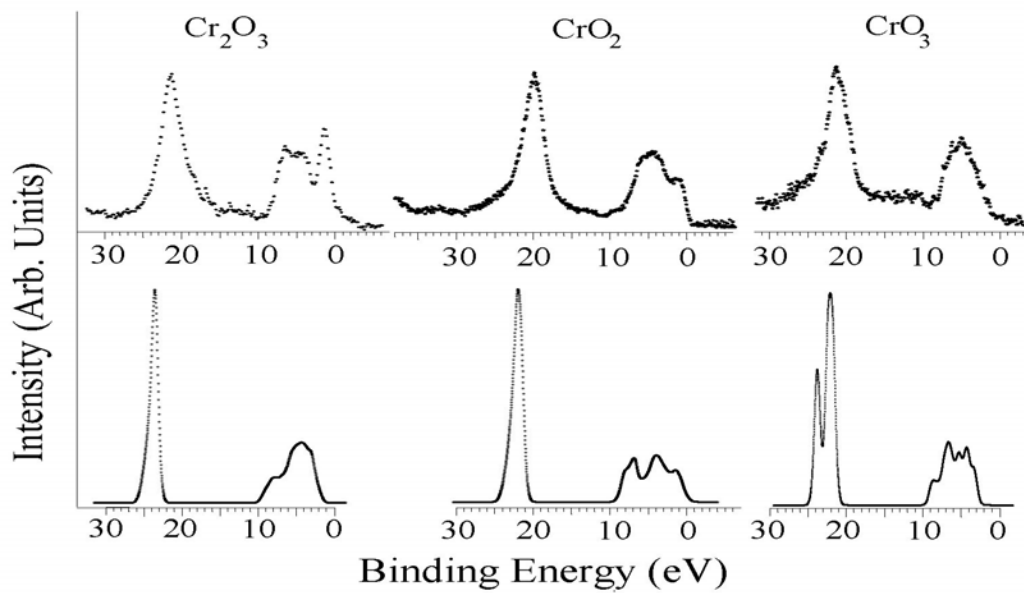


Figure 6.10 Core level XPS spectra for the 4D H₂O oxide (a) and chromium etched foil (b).

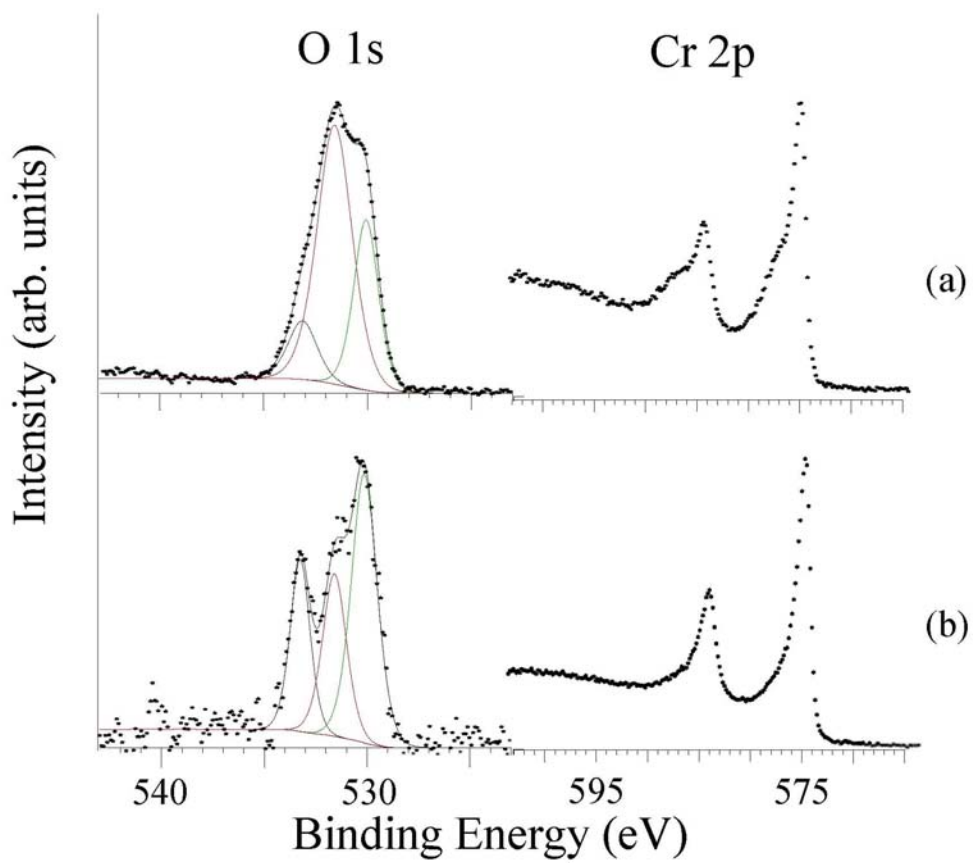


Figure 6.11 Experimental VBXPS spectra for 99.9% Cr foil Ar⁺ etched for 30 min. (a), the same Cr foil sample Ar⁺ etched for another 90 min. (b) and the constructed theoretical spectrum of the valence band region of pure argon (c).

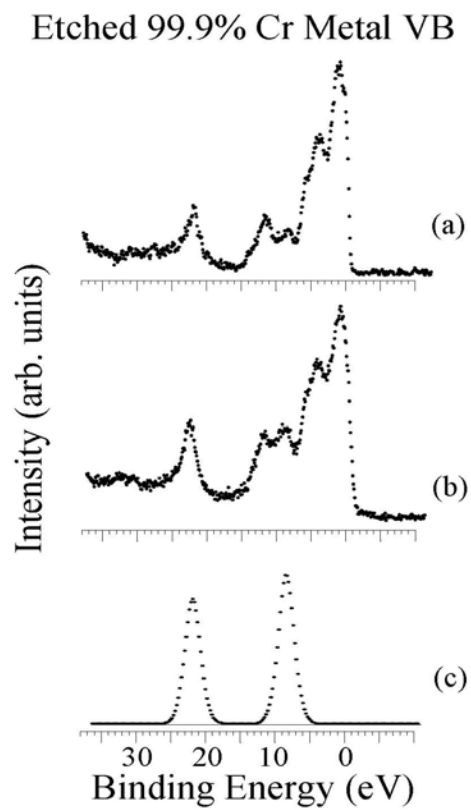


Figure 6.12 Valence band of chromium metal generated from band structure calculations.

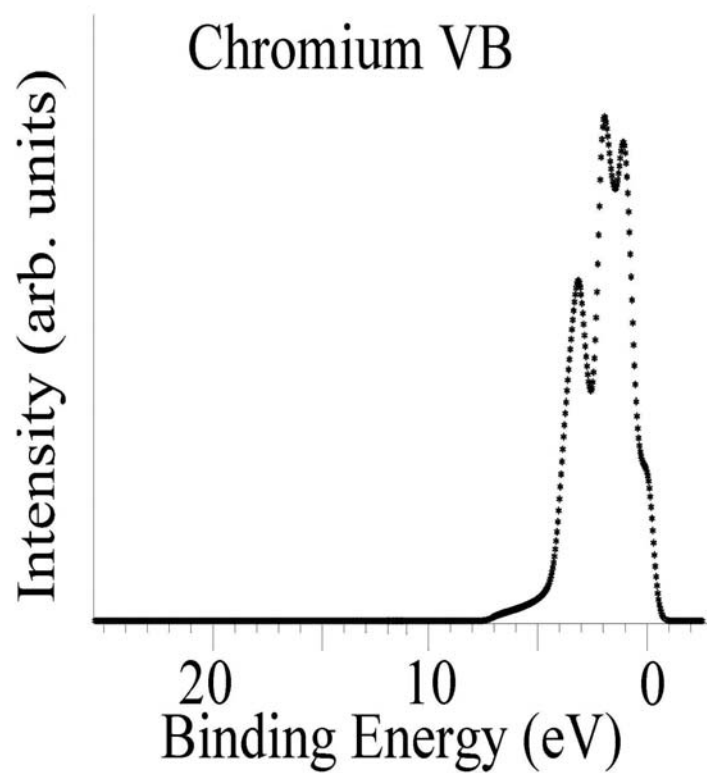


Figure 6.13 Carbon 1s core region XPS data for the as-received 99.9% Cr foil (a), the Ar⁺ etched 99.9% Cr foil (b) and Cr₂₃C₆ chromium carbide powder (c).

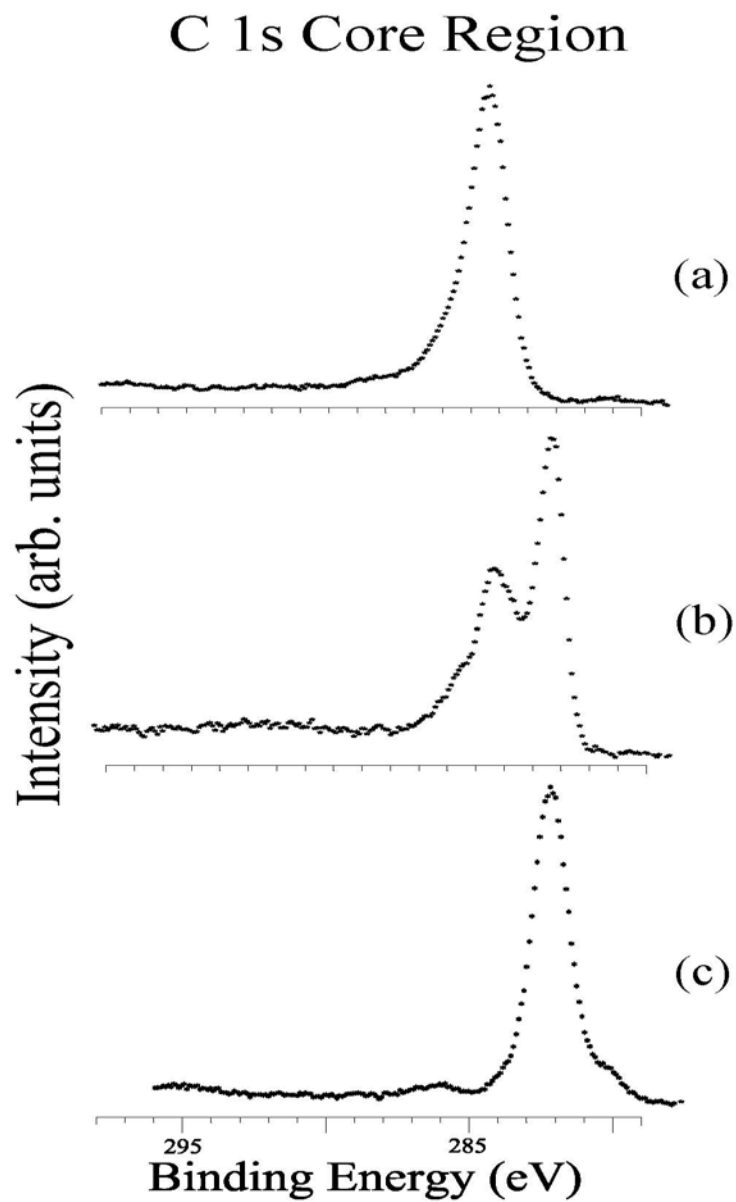


Figure 6.14 VBXPS spectra for Ar⁺ etched 99.9% Cr Foil (a), Cr₂₃C₆ chromium carbide powder (b) and Cr₃C₂ chromium carbide powder (c).

Etched Cr Foil -vs Cr Carbides VBXPS

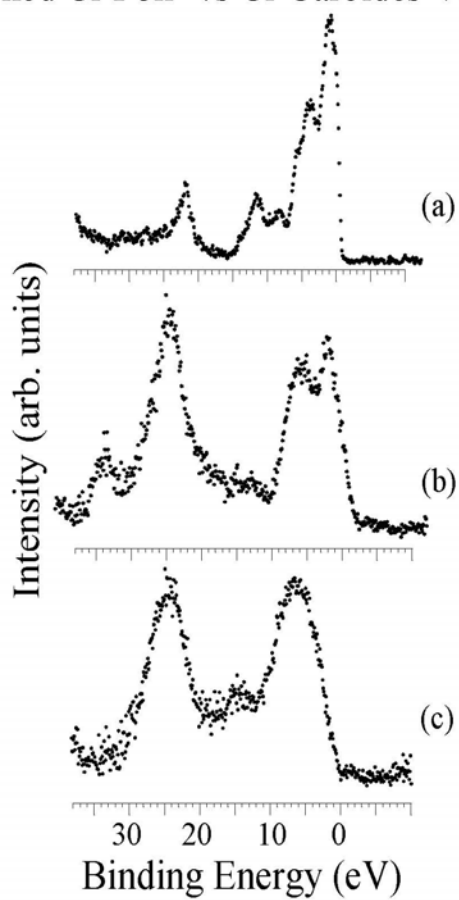


Figure 6.15 Valence band spectra of chromium oxides and etched, oxide-free 99.9% pure chromium foil treated in quadruply distilled water (a), Cr^{II} Acetate (b), Cr_2O_3 (c), CrO_2 (d) and CrO_3 (e).

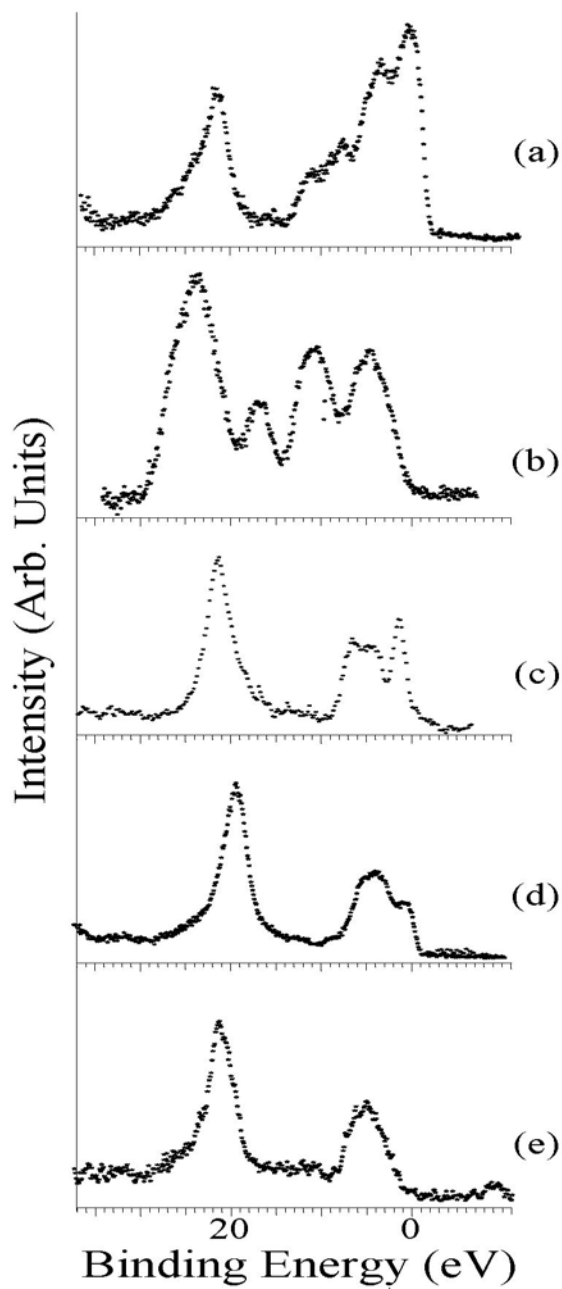
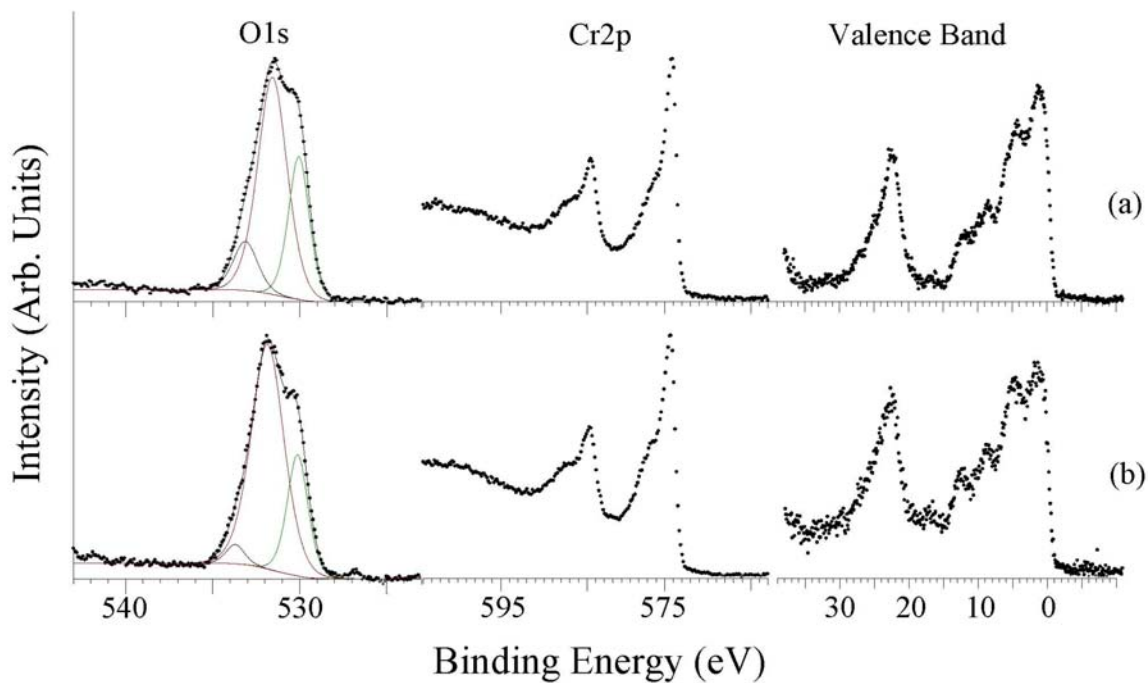


Figure 6.16 Comparison of normal angle XPS spectra (a) and surface sensitive angle core and valence band (b) spectra of Ar⁺ etched 99.99% pure chromium foil exposed to deaerated 4D water in the anaerobic cell.



6.11 Tables

Table 6.1 Crystal structure data for the band structure calculations.

Oxide	Symmetry	Space Group	International Tables Number
Chromium sesquioxide Cr ₂ O ₃	Trigonal	R -3 c H	167
Chromium dioxide CrO ₂	Tetragonal	P 42/m n m	136
Chromium trioxide CrO ₃	Orthorhombic	C 2 c m	40

Table 6.2 Parameters used to calculate atomic ratios of the chromium standard powders.

Intensities are normalized (Area/# scans). Additional parameters used: $\alpha_{Cr2p} = 11.67$,

$\alpha_{O1s} = 2.93$, $\lambda_{Cr} = 13.5283$, $\lambda_{Cr2O3} = 21.8731$

	Cr ^{II} Acetate	Cr ₂ O ₃	CrO ₂	CrO ₃
Intensity Cr2p	6422	1339.5	5787	797
Intensity O1s	2170	830.2	2760	592
$\frac{I_{Cr2p}}{I_{O1s}}$	0.3	0.6	0.5	0.7
$\frac{O}{Cr}$	0.8	1.5	1.2	1.8

Table 6.3 Parameters used to calculate atomic ratios of the oxide films on 99.99% pure chromium foil. Intensities are normalized (Area/# scans). Additional parameters used:

$\alpha_{Cr2p} = 11.67$, $\alpha_{O1s} = 2.93$, $\lambda_{Cr} = 13.5283$, $\lambda_{Cr2O3} = 21.8731$.

	Cr ⁰ As Rcvd	Cr ⁰ Polished	Cr ⁰ Etched	Cr + 4D H ₂ O
Intensity Cr2p	794.5	4469.2	3302.1	6790
Intensity O1s	1752.7	942.3	362.6	2383
$\frac{I_{Cr2p}}{I_{O1s}}$	2.2	0.2	0.1	0.3
$\frac{O}{Cr}$	5.4	0.5	0.3	0.8

Table 6.4 Curve fitting parameters for the chromium oxide standards O 1s region.

	H ₂ O	-O-C=O	OH-	O ²⁻
Binding Energy (eV)	533.2	532.0	530.8	–
FWHM	6.0	13.0	8.0	–
Binding Energy (eV)	532.6	–	529.8	529.8
FWHM	6.0	–	8.0	7.0
Binding Energy (eV)	532.5	–	530.5	529.4
FWHM	14.5	–	12.0	8.5
Binding Energy (eV)	532.6	–	530.7	529.6
FWHM	5.0	–	11.0	10.0

Table 6.5 Binding energy (eV) for Cr 2p (left) and O 1s (right) core level regions.

Sample	Chromium				Oxygen		
	2p _{3/2} met	2p _{3/2} ox	2p _{1/2} met	2p _{1/2} ox	H ₂ O	OH ⁻	O ²⁻
Cr Acetate	577.7	-	587.5	-	533.2	532.0	530.4
Cr ₂ O ₃	576.7	-	586.6	-	532.4	530.4	529.8
CrO ₂	575.2	576.9	586.6	585.2	532.4	530.4	529.0
CrO ₃	577.9	579.6	587.3	589.2	532.8	530.9	529.2
Cr + H ₂ O	574.7	577.5	584.8	587.8	533.2	531.8	530.1
Cr Etched	574.5	-	584.8	-	533.9	532.0	530.8
Cr Polish	574.3	576.9	574.3	586.5	-	531.8	530.5
Cr As Rcv	574.4	577.8	583.6	587.6	533.6	531.9	530.8

Table 6.6 Comparison of the Cr 2p region of the four powder standards, listed in the far left column. Data listed from left to right: Binding energy of the Cr 2p_{3/2} peak center at half-maximum, The full peak width at half-maximum, the configuration of the d-orbital electrons, the separation between the metallic and oxide peaks and the separation between the spin-orbit split components.

	Cr 2p _{3/2} BE	FWHM (eV)	Electron Configuration	Δ oxide-metal (eV)	Δ 2p _{3/2} - 2p _{1/2} (eV)
Cr Acetate	577.7	3.40	3d ⁴	-	9.8
Cr ₂ O ₃	576.9	3.0	3d ³	-	9.9
CrO ₂	577.7	4.03	3d ²	1.7	9.7
CrO ₃	579.1	3.0	3d ⁰	1.7	9.4

CHAPTER 7 - Formation of Ultrathin Film Oxide-free Protective Coatings on Chromium Utilizing Orthophosphoric Acid

7.1 Abstract

This study reports the results from a continuing investigation focused on the surface chemistries of metal surfaces and the results of treating those surfaces with phosphate containing compounds. This study reports the results of the exposure of oxide-free chromium foil to deaerated orthophosphoric acid which produced thin films ($< 100\text{\AA}$) containing different forms of phosphates. The results are examined by comparison with valence band spectra constructed from band structure and multiple scattered wave X-alpha calculations of different crystal structures of phosphorous-oxygen containing chromium compounds. The use of valence band X-ray photoelectron spectroscopy (VBXPS) proves especially effective in identifying subtle differences between the surface chemistries of similar compounds.

Core level and valence band XPS investigations of the film formed by treatment with deaerated 5 molar aqueous orthophosphoric acid solution under an inert anaerobic environment utilizing two methods developed by our research group are presented. The acid treatments were performed on 99.99% pure chromium metal surfaces, both methods entail removing the native oxide from the foil substrate in oxygen-free environments to ensure the phosphate films formed are oxide-free. A bench top method involves immersing the polished metal in a deaerated orthophosphoric solution and abrading the surface continuously for five minutes then allowing the metal to remain in the solution for another five minutes while the reaction of the phosphate with the metal goes to completion. A previously described anaerobic chamber¹ attached to the main vacuum chamber is utilized for the second treatment process. First the metal is argon ion etched to remove the native oxide from the surface then the sample is moved to the anaerobic cell which is brought up to a positive pressure with 99.999% pure argon gas to provide an

inert anaerobic environment in the reaction chamber and also ensure no air leaks in during the treatment. The clean metal foil surface is then exposed to deaerated orthophosphoric solution for a total of ten minutes for one study and one hour for the other study. The ten minute bench top and the one hour anaerobic cell methods produced condensed metaphosphates. The ten minute anaerobic cell treatment produced a phosphate film on the metal surface that was too thin to characterize clearly. All films formed using the two methods were oxide free.

7.2 Introduction

Oxide-free thin films ($<100\text{\AA}$) have been successfully generated in a reaction between an oxide-free metal surface and five molar (5M) orthophosphoric acid [H_3PO_4] on aluminum, iron, titanium, and vanadium previously in our research group.²⁻⁵ The phosphoric acid solutions most likely contain the one of the deprotonated forms of the acid [H_2PO_4^-] or [HPO_4^{2-}] ($\text{pK}_a = 2.15$ and 7.20 , respectively). Calculations were performed on seven unique forms of chromium phosphate: the alpha form of chromium orthophosphate [CrPO_4], chromium cyclo-hexaphosphate [$\text{Cr}_2\text{P}_6\text{O}_{18}$], chromium tetraphosphate [$\text{Cr}_2\text{P}_4\text{O}_{13}$], dichromium (II) tetrachromium tetrakis(diphosphate) [$\text{Cr}_2\text{Cr}_4(\text{P}_2\text{O}_7)_4$], trichromium(II) tetrachromium hexaphosphate [$\text{Cr}_7(\text{PO}_4)_6$], chromium catena-tris (phosphate(V)) [$\text{Cr}(\text{PO}_3)_3$] and trichromium(II) bis(phosphate(V)) [$\text{Cr}_3(\text{PO}_4)_2$]. Crystallographic data was taken from Wyckoff⁶ and from other crystal structure determination references listed herein. All were unrestricted Hartree-Fock calculations using Slater-type orbital (STO-3G) basis sets. Valence band spectra were generated from the calculated band structures by adjusting the density of states for each orbital type (Cr 4s, Cr 4p, Cr 3d, O 2s, O 2p, P 3s and P 3p) using the appropriate Scofield atomic photoelectric cross section²³. The density of states were then convoluted with a 50% Gaussian-Lorentzian product function with a full peak width at half maximum (FWHM) of 1 eV. Cluster calculations used multiple scattered wave X-alpha calculations performed previously in this research group, the details of which are described elsewhere.^{7,8}

Phosphate films on metal surfaces are used extensively to inhibit corrosion but these films are thick, on the order of thousands of angstroms, and consist of metal phosphate particles embedded into a native oxide coating on the metal.⁹ The ultra thin phosphate films formed by this research group have shown to be stable in air for extended periods of time. The fact that they are oxide-free translates to enhanced corrosion protection properties since the phosphate films are bonded directly to the metal surface and not residing on top of a potentially unstable oxide film. The films formed are thin enough that deformation of the metal substrate would not cause rupture of the film.

The films are studied through the use of core level and valence band XPS. The valence band spectra are interpreted by comparison of the experimental spectra with spectra derived from band structure calculations and multiple scattered wave X- α cluster calculations as well as by comparison with a previously established group of chromium oxide reference spectra. It has been found that valence band XPS is very sensitive to the subtle differences in molecular bonding between oxides and phosphates as well as between the different forms of phosphates.⁸ VBXPS is an important tool in the interpretation of the phosphate film valence band spectra obtained in this study.

7.3 Data Analysis

Data analysis is performed using software programs designed and written by Professor Sherwood. Spectral analysis is performed in the ESCA program and includes functions that provide the researcher opportunity for background removal, channel addition or subtraction, remove background, channel addition or removal, spectral smoothing, spectral differentiation and integration, synthetic spectral generation and Fourier deconvolution, among other features. Curve fitting is done using the GAMET program. Backgrounds were subtracted from some spectra using the Proctor-Sherwood method.

The valence band spectra of the phosphates resulting from the treatments in deaerated 5 M orthophosphoric acid were interpreted using data obtained from band structure calculations and cluster calculations using the Hartree-Fock approach. Band structure calculations were carried out using an extended version of the software program

CRYSTAL.^{10, 11} Crystal structure data used for the calculations are supplied in Table 7.5. The Wachters STO-3G basis sets¹² were used for all structures.

7.4 Experimental

7.4.1 Instrumentation

All reported spectra were collected on a VSW HA150 spectrometer (150mm hemispherical analyzer) operated in fixed analyzer transmission mode with the overall spectrum and the valence band data being collected at a pass energy of 50eV and the core regions being collected at 20eV pass energy. The system is equipped with a 16-plate multichannel detector system and Al K α X-radiation (240 W) produced from a 32 quartz crystal VSW monochromator providing an X-ray linewidth of better than 0.2 eV. Base pressure of the system is 10⁻⁹ Torr or better. The spectrometer energy scales were calibrated using an argon ion etched copper plate.²⁵ All spectra were referenced to the adventitious hydrocarbon 1s peak at 284.6 eV binding energy except for valence band data which was calibrated to the Fermi edge.

An additional chamber for solid-liquid interface studies is attached to the main UHV chamber and separated by a gate valve.

Argon ion etching was done with an Ion Tech B21 saddle field ion etcher to remove any native surface oxide. 99.99% ultrahigh purity argon gas from Matheson was operated at 2 mA and 5 KV and an argon gas pressure lower than 10⁻³ Torr. This yielded an etch rate of approximately 2-5 Å min⁻¹. The chromium foil was etched for 120 minutes and the 316L stainless steel was etched for 45 minutes. Both of these etch times were determined by monitoring the Cr2p and O1s core regions until surface oxide was not detected.

7.4.2 The Anaerobic Cell Procedure

The purpose of this experiment is to study the results of exposing chromium metal surfaces, which have had the native oxide layer removed, to deareated orthophosphoric

acid utilizing two anaerobic treatments developed in this lab group.^{13, 14} This approach facilitates reaction of a clean, oxide-free metal surface directly with the deaerated aqueous orthophosphoric acid. An oxide-free metal surface is required for the formation of ultrathin phosphate films.

The anaerobic cell allows for a sample to be cleaned in an ultrahigh vacuum environment and have its surface chemistry monitored during removal of the native oxide. The resulting oxide-free surface can then be treated with the deaerated phosphoric acid solution without ever exposing the experiment to ambient oxygen or contaminants until the resulting chemical system has been characterized.

Chemistry performed in the anaerobic cell was done at a positive pressure (above 1 atm or >760 Torr) to prevent any ambient air or contaminants from entering the chamber during the procedure. Once etching had removed the native oxide and surface adsorbants, as determined by monitoring the Cr 2p and O 1s core regions, the anaerobic cell was isolated from the main chamber of the vacuum system by a gate valve. The cell was filled with 99.999% pure argon gas, to a positive pressure, to create an inert anaerobic atmosphere in which to conduct the experiment.

Freshly prepared 5M ortho-H₃PO₄ and quadruply distilled (4-D) H₂O were deaerated for four hours by bubbling pure nitrogen or argon gas through the solution immediately prior to the experiment. The deaerated 5M ortho-H₃PO₄ was introduced into the electrochemical cell via the luggin capillary. In this experiment the electrochemical apparatus was not needed as the rest potential of chromium is -0.76 which is conducive to a spontaneous reaction occurring. The sample is then immersed into the acid solution for the duration of the reaction time. Once the reaction has progressed for the prescribed amount of time the acid solution is drained from the cell and the deaerated 4-D H₂O is utilized in rinsing the sample for five minutes.

The water is drained from the cell, the reaction vessel is removed and the sample is returned to high vacuum and allowed to dry before analysis begins. Two time periods were used in the study. A ten minute reaction time was performed initially to coincide with the total reaction time required for the bench top procedure. A second experiment was done in the anaerobic cell allowing one hour for reaction time in the acid solution but following all other prescribed protocol.

7.4.3 The Bench Top Procedure

The bench top method of treatment has previously been reported.¹⁴ In this treatment method the native oxide on the metal surface is removed while submerged in the freshly prepared, deaerated 5M orthophosphate solution. This was accomplished by abrading the metal surface with 3M brand 600 grit waterproof silicon carbide emery paper continuously for five minutes while keeping the foil and emery paper completely submerged in the phosphate solution. The metal sample was left in the solution for an additional five minutes in order for the metal surface to completely react with the 5M orthophosphoric acid. The metal sample was then removed from the aqueous acid solution and rinsed continuously for five minutes with deaerated 4-D H₂O. Excess water was removed from the sample surface by placing a Kem Wipe against the side of the sample while holding it vertically. The treated sample was placed in vacuum to dry overnight then transferred in air to the analysis chamber, which took less than three minutes.

7.4.4 XPS Measurement of Standard Compounds

XPS core and valence band spectra of pure chromium oxide and chromium phosphate powders were measured on the VSW HA150 spectrometer using monochromatic Al K α X-radiation using the spectrometer parameters described above. The chromium sesquioxide, chromium dioxide, chromium trioxide, chromium acetate and chromium phosphate research grade powders were all obtained from Sigma-Aldrich Chemicals. The powders were evenly distributed on a double-sided carbon tape and mounted on a copper sample holder. Sample charging was present on several of the powders and was corrected through the use of a low energy electron flood gun which continuously supplied the sample with electrons to replace those that have been lost in the photoemission process. The flood gun was operated at 2.23 A and 280 eV kinetic energy during spectral collection. Survey regions collected in this manner are 100 eV narrower than survey spectra for conducting samples collected without the use of a flood gun in order to avoid the large spike at 280 eV KE.

7.5 Results and Discussion

7.5.1 Types of Experiments Performed

This investigation focused on chromium foil as the metal substrate being mindful of the fact that the greater portion of biocompatible alloys utilized in the medical industry contains chromium as the second greatest component of the alloys utilized. The anaerobic methods of phosphate film generation were utilized to ensure that no native oxide was present to affect the properties of the resulting compounds.

The degree of chromium foil reactivity toward deaerated 5M orthophosphoric was established by placing a chromium foil sample, polished using 600 grit silicon carbide emery paper, into the aqueous phosphoric acid solution which had been deaerated with 99.999% pure argon gas for two hours immediately prior to the experiment. The polished foil remained undisturbed in solution for eleven minutes. The sample was removed and rinsed with deaerated quadruply distilled water for two minutes then dried under vacuum overnight.

The bench top method of treatment was performed as described above and compared with the anaerobic cell method results from exposure of the oxide-free chromium foil to the deaerated 5M orthophosphoric solution for ten minutes followed by immersion into deaerated 4-D H₂O for an additional five minutes. The results indicate an extremely thin phosphate film formed on the foil surface that was oxide-free. The experiment was repeated using an exposure time to the orthophosphoric solution of one hour followed by the same rinsing and drying procedure. The resulting film was examined after being exposed to the ambient laboratory atmosphere for one week to determine if the film would decompose upon exposure. After an additional two weeks in ambient atmosphere the sample was placed in distilled water for twenty four hours and dried overnight under vacuum and studied.

The following scheme will be used for the sake of brevity and is outlined in Table 7.1. There are two methods of treatment employed in this study as described above and will be represented with the letters "B", referring to the *bench top* approach, and "A" which refers to the *anaerobic cell* process. Both methods are used with 5M *phosphoric acid*, and

so the letter P will precede the method reference letter, and all will refer to the sample substrate which, in this experiment, is *chromium* by using the designator "C". Following this logic the chromium foil treated in 5 M H₃PO₄ via the bench top method is abbreviated as "CPB", and the anaerobic cell treatment become "CPA". Variations within the treatment approach are referenced after the three letter designator with "no", or no mechanical manipulation of the substrate (such as abrasion), "10", which refers to the sample being exposed to the phosphate solution for ten minutes, or "1H" meaning one hour of exposure time.

7.5.2 Analysis of phosphate films formed

Overall survey, Cr 2p, Cr 3p, Cr 3s, O 1s, C 1s, P 2s, P 2p core region and valence band XPS data were measured and recorded. The discussion will focus only on the Cr 2p, O 1s, P 2p and valence band results as the results of the data from the remaining core regions do not contribute any significant additional information not shown in the three regions discussed herein. Angle resolved XPS was conducted on the same regions by adjusting the take off angle of the photons from the sample surface to increase the path length that the photoelectrons travel from the substrate through the thin phosphate film and into the vacuum level. This technique provides a larger photoelectron yield from the atoms present in the film formed on the foil substrate. A take off angle of 60° was employed and the information is reported in the atomic ratio calculation results listed in Table 7.3.

The atomic ratios are presented based on an assumption that the data obtained is representative of an homogeneous arrangement of Cr-P-O within the entire film generated on the metal surface and does not take into account any waters of crystallization, CO formed during etching or surface restructuring which may occur during the etching process. Differences in atomic photoelectric cross section and differences in the analyzer transmission function are addressed and accounted for by normalization of the intensities by taking into account spectral collection step size and the number of scans done for each spectral region reported.

The O 1s and P 2p core level regions are curve fitted as previously described in order to elucidate differences in the differing forms of oxide and phosphate environments present in each sample.

7.5.2.1 *O 1s core region*

The spectra of oxygen 1s core region of the samples prepared in the anaerobic environment all show two features revealed in the curve fit spectra. The polished chromium foil placed in deaerated 5M orthophosphoric acid for eleven minutes without abrasion has a third peak around 530 eV due to oxide (O^{2-}) as shown in Fig. 7.1 (a). The two features appearing at 532 eV and 534 eV are produced by oxygen atoms in two different bonding configurations with phosphorous. The higher binding energy feature corresponds to a P-O-P linkage found in condensed phosphates and the peak at 532 eV is due to terminal P-O bonding.¹⁵ The argument could be made that the peaks correspond to water and hydroxide as these chemical moieties appear very close to these binding energies (533 eV and 531 eV, respectively). If this were the case the curve fitting of the peaks would not be as clean since they would complicate the spectra, requiring at least three peaks, if not four. Given the chemical environment which gave rise to these peaks it is certain that there would have to be at least one P-O feature, which would have to eliminate either the water or hydroxide peak from the spectral fit. The spectrum shown in Fig. 7.1(a) shows a separation of 1.9 eV between the two peaks in question while the three other spectra each have a separation of 1.7 eV. Another consideration is the fact that the three treated samples all have good agreement in the peak positions of the P-O peak component and the higher binding energy P-O-P component. The two phosphate peak components of the O 1s spectra are slightly shifted in the CPBno sample, appearing at slightly higher binding energies than the treated samples.

While it is clear that the O 1s core region fails to provide enough information to clearly ascertain if there is any water or hydroxide present or provide any indication of the presence and type of phosphate formed in the thin film, there are several indications of the different chemical environments which can be noted. The CPB O 1s peak has nearly equal amounts of terminal P-O and bridging P-O-P contributions. The two anaerobic cell O 1s spectra have large differences in peak shape resulting from a much

lower contribution of terminal P-O groups in the CPA1H spectrum than the CPA10 sample. The terminal P-O peak is much broader in the CPA10 sample and implies a much higher ratio of P-O to P-O-P molecular components such as would be found in $\text{Cr}_2\text{P}_6\text{O}_{18}$ and $\text{Cr}_2\text{P}_4\text{O}_{13}$.

When other peak properties are examined a trend is noted in peak width (FWHM) when compared to the atomic ratios which are listed in Table 7.2. The O 1s peak widths for the CPB and the CPA1H samples are 2.9 eV and 2.4 eV, respectively while the CPBno and the CPA10 samples had a FWHM of 3.6 eV. The oxygen to chromium atomic ratio is 1.14 for CPBno and 1.0 for CPA10 which have the same FWHM while the atomic ratio for CPB is 4.7 and 18.5 for CPA1H. It is difficult to reliably determine from this additional information whether there is any non-phosphate component in the samples based solely on the information provided in the O 1s core level XPS data. This information is revealed in the valence band data.

7.5.2.2 Cr 2p Core Region

The chromium 2p core level XPS spectra are shown in Fig. 7.2 along with the P 2p and O 1s core level spectra from the three treatment methods employed in this study. The Cr 2p spectrum for the etched chromium foil has two spin orbit split components at 574.6 eV and 584.1 eV corresponding to the Cr 2p_{3/2} and Cr 2p_{1/2}, respectively. These spin orbit split peaks are very prominent in the other three Cr 2p core level spectra shown in the figure indicating the film on metal foil is less than 100Å thick. The phosphate interaction on the chromium foil is present in the peaks around 578 eV and 588 eV. This set of peaks representing the phosphate layer on the surface is unique for each sample.

The peak shape and intensity for the Cr 2p phosphate features are similar for the two anaerobic cell treatments while the binding energies of the peaks are similar for the CPB and CPA1H samples. The CPA10 phosphate peaks appear at 586.6 eV and 577.7 eV (8.9 eV separation) while the CPA1H and CPB sample peaks appear at 588.2 eV and 578.4 eV (9.8 eV separation). The Cr 2p core level region of the foil placed in solution without treatment, CPBno, has the same shape and chemical shift as the trivalent chromium oxide found in the treated chromium foils shown in Figure 7.2. This difference in binding energies points to a difference in phosphate composition, as demonstrated by the different binding energies of the oxide portion of the Cr 2p core level region in the chromium

oxides study. Also shown with the Cr 2p region in Figure 7.2 is the O 1s core level XPS spectrum for the three treated foils further indicating the presence of the Cr₂O₃ oxide. A Cr^(VI) valency had a chemical shift of 2.8 eV while Cr^(III) only had a shift of 1.7 eV. A chemical shift also occurs with changes in the electronegativity of the atom or functional group interacting with the metal. The chromium phosphate compounds which have been characterized are almost exclusively in the Cr^(II) or Cr^(III) state therefore the differences noted in the phosphate features in the Cr 2p core level region are most likely due to variation in the phosphate films formed.

7.5.2.3 P 2p Core level

All three curve-fitted P 2p core level spectra shown are made up of two peak components, most likely from the terminal P-O groups and the bridging P-O-P linkages in the phosphate films generated. This would further support the conclusion that the generated phosphate films are indeed oxide-free. Since there are two types of phosphorous bonding possibilities in the chromium phosphate compounds and both involve oxygen atoms the conclusion drawn is that the two types of phosphorous-oxygen bonds discussed in the O 1s core level spectra and the two types of phosphorous peaks appearing in the P 2p curve fitted spectra must be derived from the same types of chemical environments surrounding phosphorous atoms in the films. The presence of two unique phosphate environments, however, does not give any indication of the type of phosphate present in the sample.

Figure 7.3 has the core level XPS spectra of the etched chromium foil, CPB, CPA1H and CPBno. The P 2p region of the CPBno sample indicates a very slight presence of phosphorous but it is important to note that there is very little present as indicated by the low intensity (485 units -vs- 9226 units in CPB P 2p) which, combined with the resulting low statistics in the spectrum, indicates the only reasonable conclusion that can be made regarding the phosphate from this spectrum is that there is a trace amount of phosphate present in the sample. This agrees with the atomic ratio of phosphorous to chromium at 0.02.

It is interesting to note the FWHM of the P 2p peaks are the same for the CPB sample and the CrPO₄ powder sample which could indicate an orthophosphate film formed on the chromium foil treated on the bench. There is a difference reported between the P 2p

peak widths of orthophosphates and metaphosphates with the ortho form being wider than the metaphosphate which would support this conjecture¹⁵, but to form a reliable conclusion the valence band spectra must be analyzed.

7.5.2.4 *Valence Band Analysis*

Valence band XPS employed for the study of oxide-free chromium foils exposed to deaerated orthophosphoric acid has proven to be a vital tool in the analysis of the generated phosphate films. The core level XPS spectra all indicate that there are differences in the films formed but do not provide sufficient evidence to confidently make assertions regarding the properties of the films. It will be found that there are very distinctive variations in the outer valence band region of the VBXPS spectra which, when combined with calculated spectra to predict the experimental results, allow for greater certainty in the chemical analysis. When considering the nature of the phosphate films it is necessary to distinguish between oxides and phosphates. Chapter six described a series of four chromium oxide standards and evaluated the results of exposing etched chromium foil to deaerated quadruply distilled water to determine the form of oxide in the resulting thin film on the foil. These oxide standards each have features characteristic of their unique chemical identity which provide the means of discriminating between phosphates and oxides.

Valence band spectra of seven crystalline forms of ortho- and metaphosphate forms of chromium phosphate were generated from band structure calculations performed using an extended version of the CRYSTAL program.^{10,11} Cluster calculations provide an approach unique to that of band structure calculations in that the cluster calculation uses a well defined small cluster of atoms to represent the bulk layers of the material under investigation. Band structure calculations are based on an infinite model and have shown good agreement with phosphate compounds having relatively limited dispersion in energy through the different directions within the crystal.^{7,8} Generally the bands of phosphates are found to have very little dispersion and are rather flat. Spectral features have been shown to arise from even a slight amount of dispersion in energy so there is a good probability that the valence bands of the chromium phosphates calculated using band structure calculations can be predicted with relatively good accuracy using this

approach. Cluster model calculations have shown good agreement with compounds which have very little dispersion, or flat, energy bands as well.

Calculations were executed for chromium phosphate (CrPO_4), an orthophosphate with an orthorhombic crystal structure,¹⁶ the other six chromium phosphates are all condensed phosphate structures.¹⁶⁻²³ In order to ascertain the relative changes within the experimental valence band spectra and to determine if the film is formed on an oxide-free surface it is essential to be familiar with the valence band spectra of the substrate metal and its behavior within the native oxide system. Figure 7.4 illustrates the dramatic differences between three stages of oxide removal within the chromium oxide system. The film on the as-received sample in Fig. 7.4(a) is thick enough to obscure the chromium metal peaks (therefore greater than 100\AA) of the foil, indicating the film is approaching the range beyond the capacity to detect in photoelectron spectroscopy. The native oxide on chromium is revealed in Fig. 7.4(b) as the $\text{Cr}^{(\text{III})}$ form found in the chromium trioxide (Cr_2O_3) oxide film remaining after polishing the foil sample. In Fig. 7.4(c) the spectrum of the etched chromium foil is shown but is somewhat complicated by the unavoidable presence of both the argon 3s and 3p peaks from imbedded argon as well as the prominent carbon 2s and carbon 3p peaks which result from the formation of chromium carbide during the etching process. During the process of interpreting the experimental valence band spectra of the chromium phosphate systems the interfering peaks from the etching process will contribute to the spectrum at 9 eV from argon 3p, at 12 eV where chromium carbide appears, another carbon feature is around 18 eV due to the C 2s contribution, and another argon feature arising from the Ar 3s peak is in the vicinity of 22 eV. Regions where oxide features will be present are the O 2s peak, which is usually prominent, as seen in Figure 7.4(b) around 22 eV and a broad O 2p peak shows up near 5-7 eV. The phosphate spectrum will have peaks in the O 2s and 2p regions as well due to the P-O bonding. This demonstrates why the predicted valence band spectrum is so essential to successful interpretation of the spectra from the valence band region. The most obvious features of a phosphate will show in the outer valence band region at binding energies below 15 eV where the P 3s will be found around 14eV while the P3p shows in the 9-10 eV range. When evaluating experimental valence band spectra greater confidence in determining the chemical identity of the surface films is gained by

comparison with spectra generated from calculations. Valence band calculations used to predict and confirm the chemical identity of the species present have proven to be extremely useful with phosphates. Band structure calculations were performed as previously described on the seven chromium phosphates shown in Figure 7.5. Generally the structures of the condensed phosphates were constructed from isolated CrO_6 octahedra and one dimensional infinite metaphosphate chains of PO_4 tetrahedra. The octahedron participates in both edge sharing and apical sharing with the tetrahedral PO_4 units.¹⁶⁻²³ Trichromium(II) tetrachromium hexaphosphate, $[\text{Cr}_7(\text{PO}_4)_6]$, is a mixed chromium(II) chromium (III) structure that exhibits Jahn-Teller effects within the metal octahedra²⁰ while the metal octahedra do not participate in oxygen sharing in the cyclohexametaphosphate, $\text{Cr}_2\text{P}_6\text{O}_{18}$.¹⁷ The only orthophosphate calculated was chromium phosphate, CrPO_4 , shown in both Fig. 7.5 resulting from band structure calculations, and in Fig. 7.10 as the spectrum from VBXPS of the powder. Shown below in Fig. 7.8 is the multiple scattered wave X-alpha calculation of the $[\text{PO}_4]^{3-}$ orthophosphate ion.⁷ The chromium orthophosphate has CrO_6 metal octahedra connected by two edge sharing PO_4 tetrahedra at opposite edges. The crystal structure has channels extending throughout parallel to the a- and b-axis.¹⁶ A condensed polyphosphate showing antiferromagnetic behavior, $\text{Cr}(\text{PO}_3)_3$, is the calculated spectrum in Fig. 7.9(a), shown for comparison purposes. This phosphate has each metal octahedra sharing its six apices with six different PO_4 tetrahedra that further connect to other PO_4 tetrahedra forming infinite chains of $[\text{PO}_3]_\infty$.²¹

7.5.2.4.1 Valence Band of CPBno

Valence band XPS spectral results for each experiment conducted here are shown in Fig. 7.6. The Ar^+ etched chromium foil valence band in Fig. 7.6(a) is shown for the purpose of establishing a baseline for comparison of features to the CPA valence bands in Figs. 7.6(d) and (e) of which the surfaces were prepared by argon ion etching.

When polished chromium foil (shown in 7.7(b)) was placed in deaerated 5M orthophosphoric acid solution without further treatment the results, shown in Figure 7.7, provide very little indication of a reaction occurring between the phosphate and the chromium. The CPBno sample shows a dominant Cr 3d peak at 1.3 eV which is nearly

two times as intense as the next most prominent feature at the O 2s region above 25 eV. There is some evidence of phosphorous being present at the 14 eV region which is confirmed by the low intensity P 2p peak in the core level, however this is not readily visible as it is nearly overshadowed by the C 2s peak at 8.87 eV from hydrocarbon. What can be stated regarding this experiment is the oxide layer has been eroded by the orthophosphoric acid indicated by the diminished intensity in the O 2s region around 23eV and the O 2p peak appearing as a higher binding energy shoulder on the very prominent Cr 3d peak at 5.28 eV

7.5.2.4.2 Valence Band of CPB

The chromium foil treated using the bench top method readily shows that the process produced a reaction between the chromium and the orthophosphate. When the outer valence band region is focused on one observes four prominent features. The metal edge is slightly visible and the Cr 3d peak is barely seen near 1eV. The feature at 2 eV is most likely the phosphate chemical shift of the Cr 3d orbital.

There is a broad feature spanning from 5 -10 eV which contains the O 2p and P 3p contributions. The oxygen is, as previously stated, from the P-O bonding occurring within the phosphate. This feature at 6 eV is somewhat lower in intensity than the peak at 9 eV which is mostly O 2p in nature. These two distinct peaks are separated by 3.7 eV. The intensity of the P 3p peak near 9 eV likely has some Ar 3p character as well which could increase the intensity, however based on the degree to which the Cr 3d feature has been obscured the thickness of the surface film is likely sufficient to minimize the impact that the implanted argon has on this spectrum. The highest binding energy feature at 14eV is lower in intensity than the other two phosphate peaks and slightly narrower. This feature stands 4.9 eV from the neighboring lower binding energy phosphate peak.

The cluster calculation of the $[\text{PO}_4]^{3-}$ ion is shown in Fig. 7.8 indicates the percentage contribution made by each component of the phosphate. The feature appearing at 9 eV, while assigned to P 2p, is mostly oxygen in composition and is similar in relative intensity to the experimental CPB valence band results. There is a mainly O 2s peak at 24 eV which contains two overlapping peaks, one has O 2s, O 2p and P 2s contributions, the other has O 2s, O 2p and P 2p character. When this region is compared to the CPBno

valence band shown in Fig. 7.7 the impact of having an oxide present in the surface film becomes evident. The CPBno sample has two distinct features which make up the very broad O 2s region feature. There is no evidence of any oxide present in the CPB film formed in an anaerobic environment as evidenced by the differences in the O 2s region as well as the O 2p region which is remarkably lower in intensity than the corresponding regions shown in Fig. 7.7. Additionally, the CPB sample O 2p region is nearly 60% lower in intensity than the O 2s region in the spectrum. Clearly the bench top method of treatment produces a phosphate film which is directly bonded to the chromium surface.

The form of phosphate in the surface film is determined through evaluation of the separation, binding energy and relative intensity of the distinct features in the outer valence band. Phosphate valence bands characteristically have three peaks appearing at binding energies of 5 – 15 eV. The separation between these peaks is an important factor in determining whether the film is an orthophosphate or a form of condensed phosphate. Figure 7.9 illustrates the differences between a metaphosphate [Fig. 7.9(a)], an VBXPS spectrum of the orthophosphate CrPO_4 [Fig. 7.9(b)] and a multiple scattered wave X-alpha calculation of the $[\text{PO}_4]^{3-}$ ion [Fig. 7.9(c)]. The orthophosphates in the illustration have the peaks fairly evenly spaced 3 eV apart and the region is symmetrical. Intensities are relatively equal among the three peaks. The metaphosphate has a much wider separation between the first and second of the three peaks (6.2 eV) as well as between the second and third peaks (5.8 eV), in this case. The peaks are of differing widths and intensities which is also typical of condensed phosphates.

The predicted valence band spectra produced from band structure calculations shown in Fig. 7.10 are used for comparison purposes with the experimental data. Band structure calculations of phosphates based on divalent or mixed divalent chromium are shown overlain on the CPB x-ray photoelectron valence band spectrum. Frequently the intensities of experimental valence band spectra do not match the intensities of the phosphate peaks, but the binding energies must align. Based on the data in the predicted spectrum, the phosphate form in the generated surface film is likely $\text{Cr}_6(\text{P}_2\text{O}_7)_4$, dichromium(II) tetrachromium tetrakis(diphosphate). A different perspective of the predicted spectrum and the experimental valence band spectrum is shown in Fig. 7.11.

Dichromium(II) tetrachromium tetrakis(diphosphate) $[\text{Cr}_6(\text{P}_2\text{O}_7)_4]$ exists in crystal form as transparent brown pinacoidal crystals. The structure has two different metal polyhedra within, a compacted metal octahedral and a distorted trigonal bipyramid.¹⁹ There are 40 atoms in the unit cell which has triclinic symmetry. The $\text{Cr}^{(\text{II})}$ is surrounded by six oxygens occupying the corners on an elongated octahedron, four P-O bonds are 2.04Å and two are 22% longer at 2.62Å while the $\text{Cr}^{(\text{III})}$ octahedral have bond lengths of 1.930Å and 2.061Å in length with the bridging angles at 136.5° and 138.9°, respectively.

7.5.2.4.3 Valence Band of CPA1H

The film formed on the chromium foil in the anaerobic cell treatment after a ten minute exposure [Fig. 7.6(d)] was of insufficient thickness to characterize the possible phosphate structure. The experiment was repeated leaving the oxide-free chromium foil exposed to the deaerated 5M H_3PO_4 for one hour. The resulting film, shown in Fig. 7.12(c) was substantial in comparison to the ten minute exposure time. The valence band spectrum is distinctive from the thin film generated during the anaerobic bench top treatment.

The metal edge is still visible, but very low in intensity indicating the surface film is thicker than that residing on the CPB sample. The region between 5 – 10 eV is narrower than the CPB valence band. This feature has two peaks, one at 10 eV and the other as a lower binding energy shoulder at 7 eV. The phosphate peaks in the bench top sample occur 1-2 eV lower binding energy. The highest binding energy phosphate peak in the outer valence band is nearly the same intensity as the peak at 10 eV and is narrower, though there is a slight shoulder 2 eV lower binding energy or 1 eV closer than the much more prominent shoulder on the 10 eV peak. This higher BE peak, at about 15 eV is sharper and more broad than the highest BE peak on the CPB sample. Overall the outer valence band on the CPA1H sample is much narrower with far less influence from the Cr 3d region than the CPB sample.

The O 2s region, occurring at 25.5 eV is wider than the same region on the bench top sample, but still is not indicative of an oxide as these have produced very broad peaks around 22-23 eV in the chromium oxide samples. Additional evidence that the surface film of the CPA1H sample is directly bonded to the chromium surface is the absence of

any oxide features in the O 2p region. The fact that the O 1s region only has the two peaks is further support for this conclusion.

The angle resolved study indicated insignificant changes in both the outer valence band and the O 2s region. When the O 1s region was evaluated it was found the only difference between the normal and surface sensitive angles was a very slight rise in intensity in the 533 eV peak in the curve fitted spectra shown one overlaying the other in Fig. 7.13.

The shape and definition of the phosphate peaks in the CPA1H valence band region possibly indicates that there is one valence state among the chromium atoms, and that there is a regular array within the phosphate structure since the features are also ordered and proportional. Comparing the chromium phosphate forms which are all Cr^(III) [Fig. 7.14 and 7.15] the best agreement was from the chromium cyclo-hexaphosphate band structure calculated spectrum, shown in Fig. 7.15 where the synthesized spectrum is once again shown alongside the experimental valence band spectrum. There is good agreement in peak location, if not in relative intensities, which is common for spectra generated from band structure calculations.

Finally, a study was performed to evaluate the stability of the surface when exposed to ambient air in the laboratory environment. The sample was removed from UHV after the initial XPS studies were complete and placed in a watch glass evaporating dish. The dish was then placed on the bench top and a Kem Wipe was lightly placed over the dish to minimize dust or debris contamination from the HVAC system and regular lab activities. The sample was allowed to remain on the bench for ten days and placed in the sample chamber of the HA150 for further study. It was noted that the Kem Wipe had been dislodged and the sample was exposed over the weekend to circulating air within the lab.

Fig. 7.16(c) shows the valence band spectra after being exposed to ambient air and shows the film to be stable under these conditions. There is evidence of an oxide film forming on top of the phosphate film exhibited by the increase in intensity and broadening of the features of the O 2p region at 7 eV and 2 eV. There is also a similar, but slight change in the O 2s region at 25 eV.

7.6 Conclusions

This study examines the effects on 99.99% chromium foil when treated by various methods in 5M orthophosphoric acid. Placing a polished chromium foil sample into deaerated 5M H_3PO_4 solution and allowing it to remain in solution undisturbed for eleven minutes on the bench top produced no evidence of a chemical reaction with the foil itself, but most likely with the native oxide on the foil when it was placed in the solution. The experiment was repeated using a method developed in our laboratory for removing the native oxide while the sample is submerged in the 5M orthophosphoric acid solution by abrading it with waterproof 600 grit emery paper while keeping the sample immersed. This method produced what is believed to be a mixed valency ($\text{Cr}^{\text{III}}/\text{Cr}^{\text{II}}$) condensed chromium metaphosphate, $\text{Cr}_6(\text{P}_2\text{O}_7)_4$. The chromium foil was then treated in a chamber within the UHV system which can be isolated to provide an inert anaerobic atmosphere in which to expose the etched oxide-free metal surface to an electrolyte solution for the purpose of forming oxide-free surface films which can provide valuable insight into metal phosphate chemical systems. The initial approach was to expose the etched foil to the 5M H_3PO_4 solution for the same amount of time as the bench top treatment. The 10 minute exposure did not produce the expected results so the experiment was repeated extending the exposure time to 1 hour. This approach was successful in producing a phosphate surface film bonded directly to the chromium that was substantial in thickness, but still considered an ultra thin film ($<100\text{\AA}$). The film appeared to remain consistent in composition when an angle resolved study was done which revealed almost no shifting in peak features at the surface sensitive angle. The film was exposed to ambient lab atmosphere on the bench top for approximately one week and was found to be extremely stable in air. The peak characteristics in the valence band region showed good agreement with the predicted valence band generated from band structure calculations for the cyclic hexametaphosphate $\text{Cr}_2\text{P}_6\text{O}_{18}$. Although this method of data interpretation produces confidence in the conclusions, the possibility that the surface phosphate films could be of a different phosphate structure cannot be ruled out.

These conclusions could not have been drawn based solely on the XPS data from the core regions alone. Although the core level spectra yielded supporting information for the conclusions drawn in this study, it is self-evident that the information provided by the VBXPS spectra was substantial and provided vital information not available in the core level data.

7.7 Acknowledgements

Appreciation is extended to Dr. Peter M. A. Sherwood for the multiple scattered wave X-alpha calculations of the phosphate ion PO_4^{3-} . The information provided in the calculation was invaluable. Along with Dr. Sherwood, Dr. Yu Qing Wang and Dr. Daniel Asunskis are also extended grateful thanks for their assistance and instruction in the execution of band structure calculations.

7.8 References

1. J. Rotole and P. Sherwood, *Chem. Mater.*, **13**, 3933, (2001).
2. J. Rotole, et al., *J. Vac. Sci. Technol. A*, **19**, 1176, (2001).
3. D. Asunskis and P. Sherwood, *J. Vac. Sci. Technol. A*, **21**, 1133, (2003).
4. P. M. A. Sherwood, "Data Analysis in X-ray Photoelectron Spectroscopy" chapter in *Practical Surface Analysis*, D. Briggs and M. Seah, eds.. J. Wiley and Sons: New York. (1990).
5. A. Proctor and P. M. A. Sherwood, *Anal. Chem.*, **54**, 13, (1982).
6. R. W. G. Wyckoff, *Crystal Structures, Vol. 1*, Second edition. Interscience Publishers: New York, New York, (1963).
7. A. L. Asunskis, K.J. Gaskell, D.J. Asunskis and P.M.A. Sherwood, *Journal of Vacuum Science and Technology A*, **21**, 1126, (2003).
8. P. M.A. Sherwood, "Introduction to Studies of Phosphorus-Oxygen Compounds by XPS, *Surface Science Spectra*, **9**, 62-66, 2002 (published 2003).
9. K. St John, ed., *Particulate Debris From Medical Implants: Mechanisms of Formation and Biological Consequences*. ASTM, Philadelphia. (1992).
10. V. Saunders, et al., *CRYSTAL 98 User's Manual*. University of Torino: Turin, Italy. (1998).
11. C. Pisani, R. Dovesi and C. Roetti, *Hartree-Fock ab Initio Treatment of Crystalline Systems: Lecture Notes in Chemistry*, 48. Springer: Berlin. (1988).
12. A. Wachters, *J. Chem Phys.*, **52**, 1033, (1970).
13. J. Rotole and P. Sherwood, U.S. Patent No. 6,066,403, (23 May 2000).
14. Y-Q Wang and P.M.A. Sherwood, *J. Vac. Sci. Technol. A*, **21**, 11 (2003).
15. J. A. Rotole and P. M.A. Sherwood, *Chemistry of Materials*, **13**, 3933-3942, 2001
16. R. Glaum, R. Gruehn and M. Moeller, *Zeitsch. Anorgan. und Allgemeine Chemi.*, **543**, 111, (1986).

17. M. Bagieu-Beucher and J.C. Guitel, *Acta Crystall. B*, **33**, 2529, (1977).
18. K. H. Lii, Y. B. Chen, C. C. Su and S. L. Wang, *J. Solid State Chem.*, **82**, 156, (1989).
19. R. Glaum, *Zeitsch. Anorgan. und Allgemeine Chemi.*, **616**, 46, (1992).
20. R. Glaum, *Zeit. Krystall.*, **205**, 69, (1993).
21. M. Gruss and R. Glaum, *Acta Crystall.*, **52**, 2647, (1996).
22. R. Glaum and A. Schmidt, *Zeitsch. Anorgan. und Allgemeine Chemi.*, **623**, 1672, (1997).
23. J. Scofield, *Electron Spectr. Relat. Phenom.*, **8**, 129, (1976).
24. M. Seah and W. Dench, *Surf. Interface Anal.*, **1**, 2, (1979).
25. ASTM, E902-93, (1994), 1994 Annual book of ASTM Standards, Vol. 09.06. American Society for Testing and Materials, Philadelphia.

7.9 Figures

Figure 7.1 Chromium foil O 1s core XPS data which has been curve fitted. CPBno sample (a), CPB sample (b), CPA1H (c) and CPA10 (d).

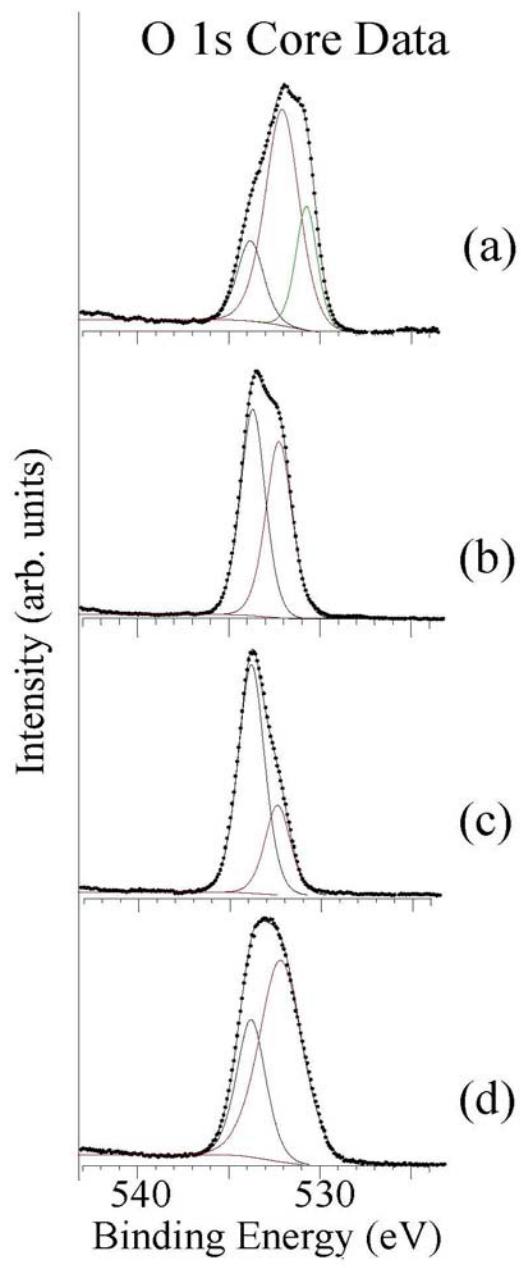


Figure 7.2 Core region XPS spectra for (a) etched chromium, (b) CPB, (c) CPA1H and (d) CPA10.

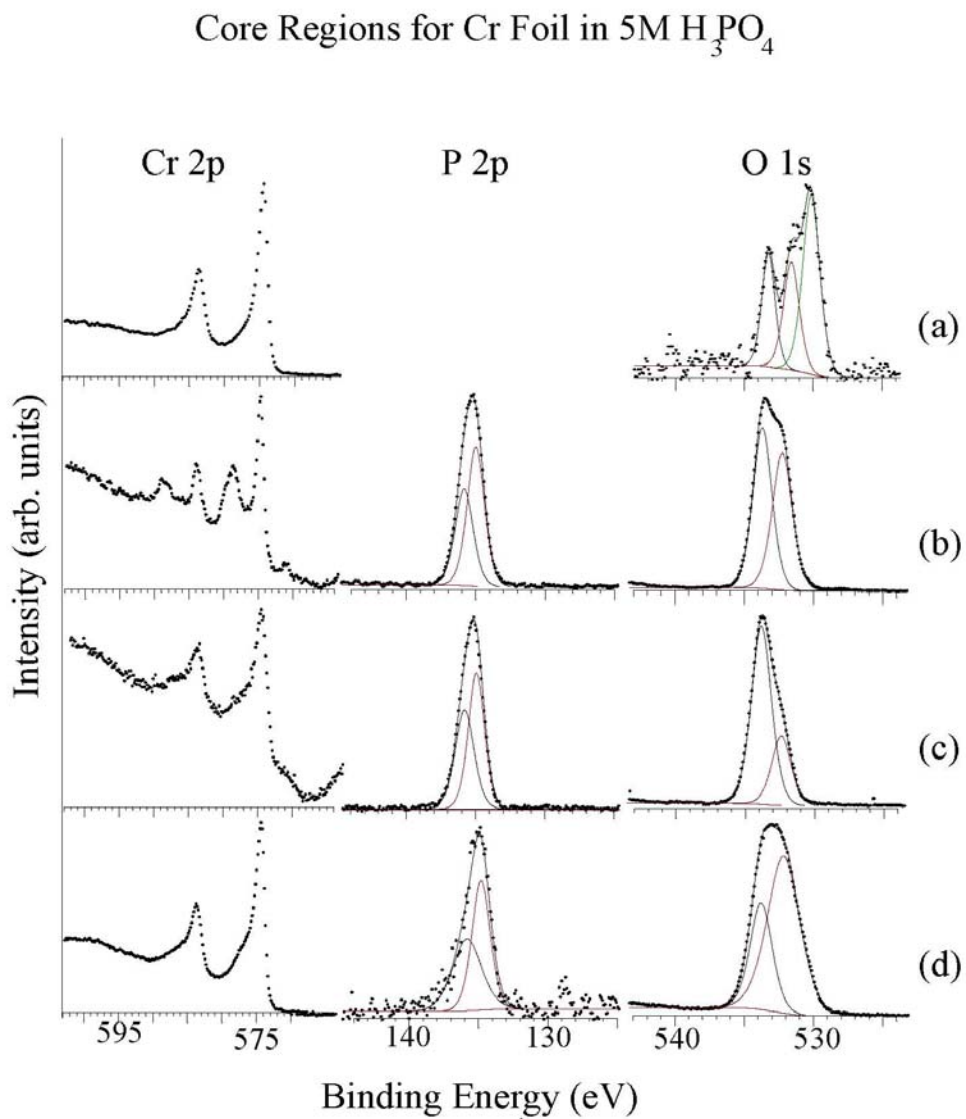


Figure 7.3 Core region XPS spectra for (a) etched chromium, (b) CPB, (c) CPA1H and (d) CPBno.

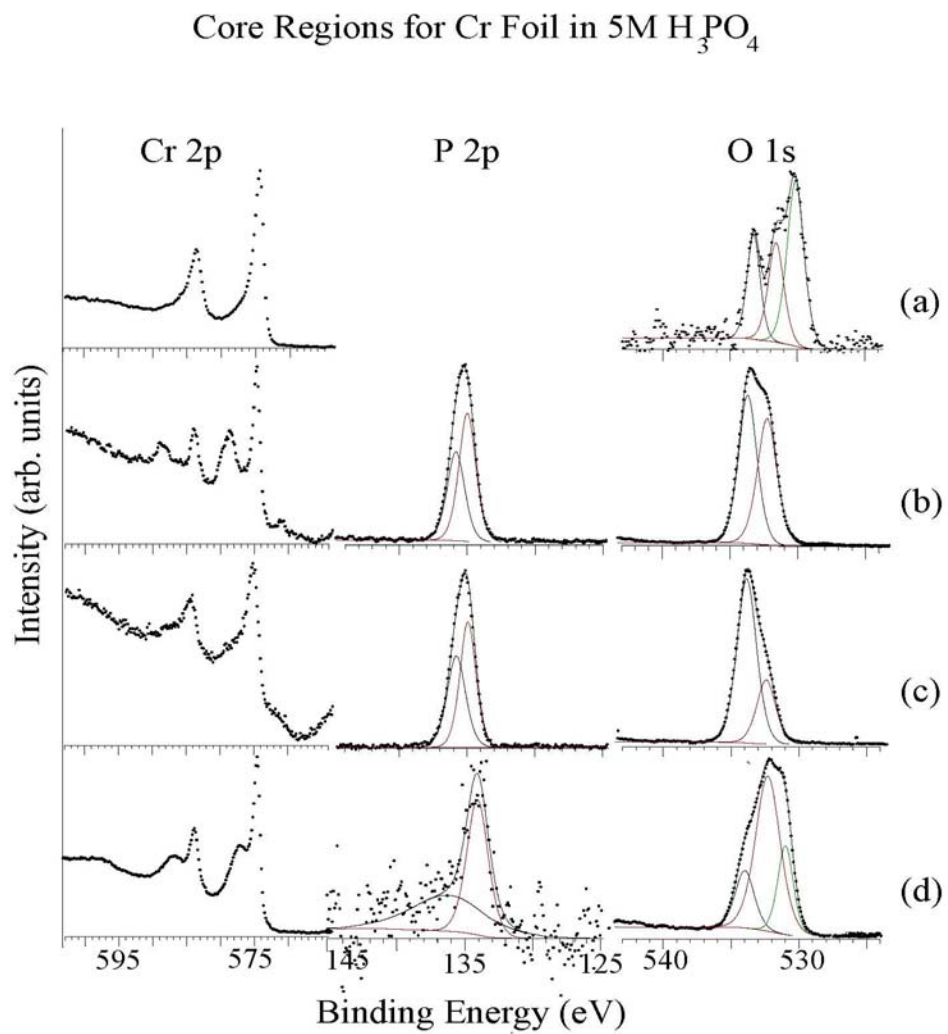


Figure 7.4 Valence band XPS spectra of (a) as-received 99.99% chromium foil, (b) polished 99.99% chromium foil and (c) 99.99% chromium foil which has been Argon ion etched for 90 minutes.

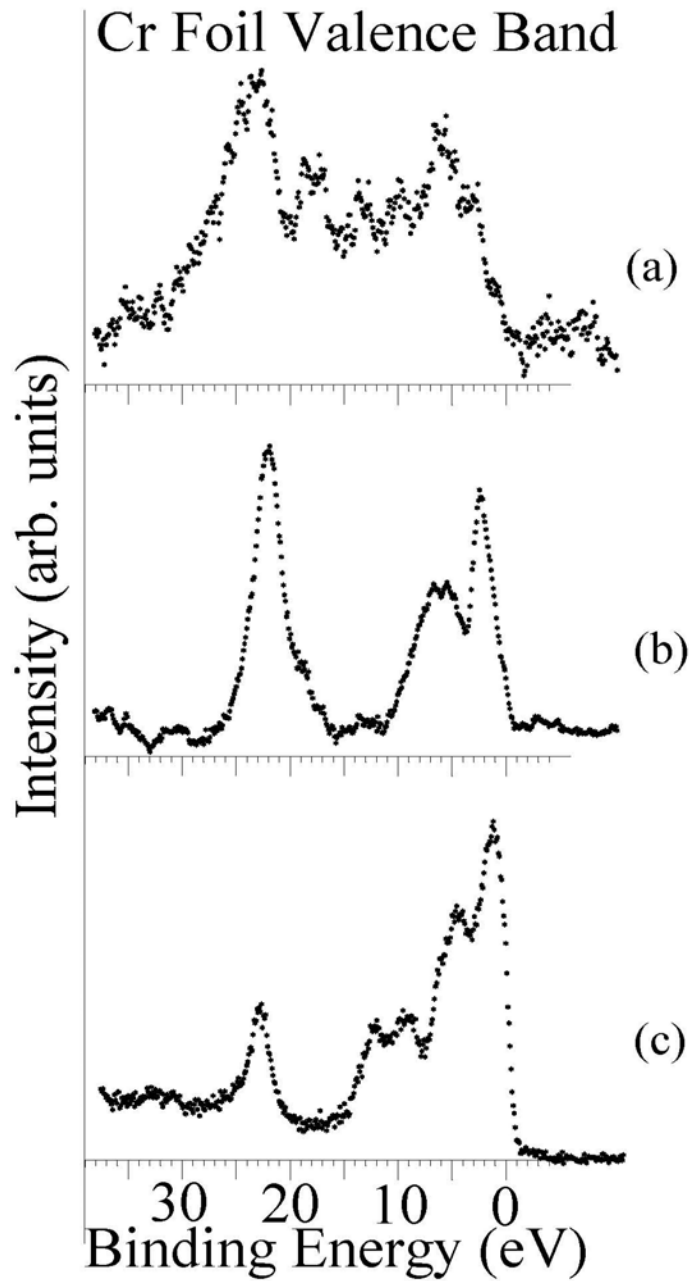


Figure 7.5 Valence band spectra generated from band structure calculations of the chromium phosphate compounds shown in Table 7.4.

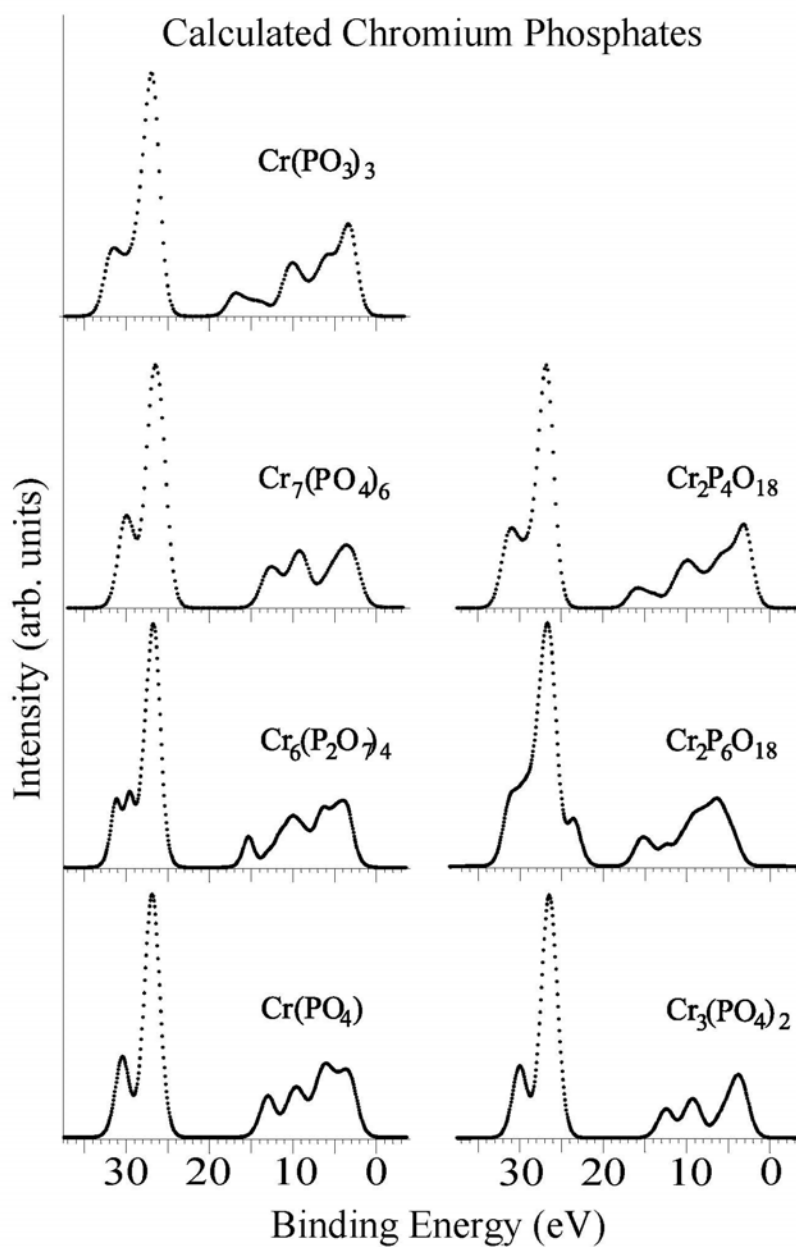


Figure 7.6 Experimental Valence Band XPS spectra of (a) etched chromium foil, (b) CPBno, (c) CPB, (d) CPA10, (e) CPA1H and CrPO₄ powder.

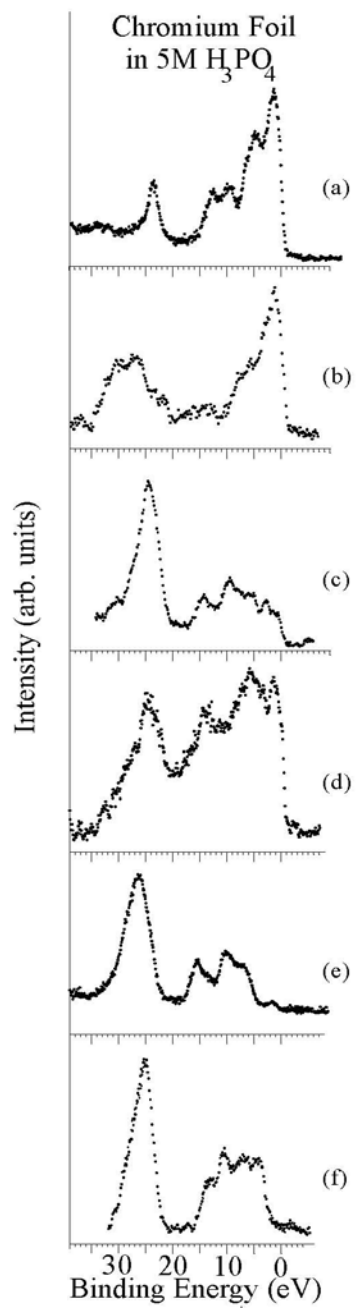


Figure 7.7 Valence Band XPS spectra of (a) 4D H₂O sample, (b) 99.99% polished chromium foil and (c) CPBno sample.

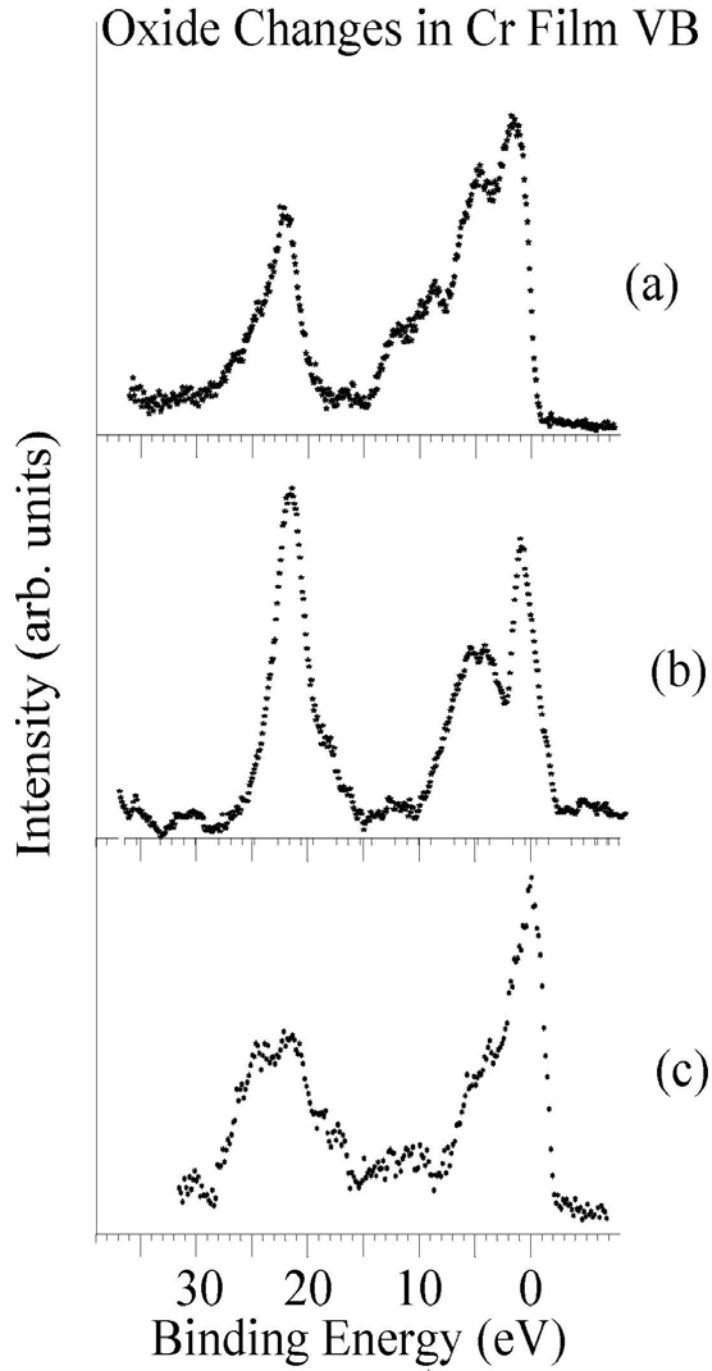


Figure 7.8 Multiple scattered wave X-alpha calculation of the $[\text{PO}_4^{3-}]$ ion.

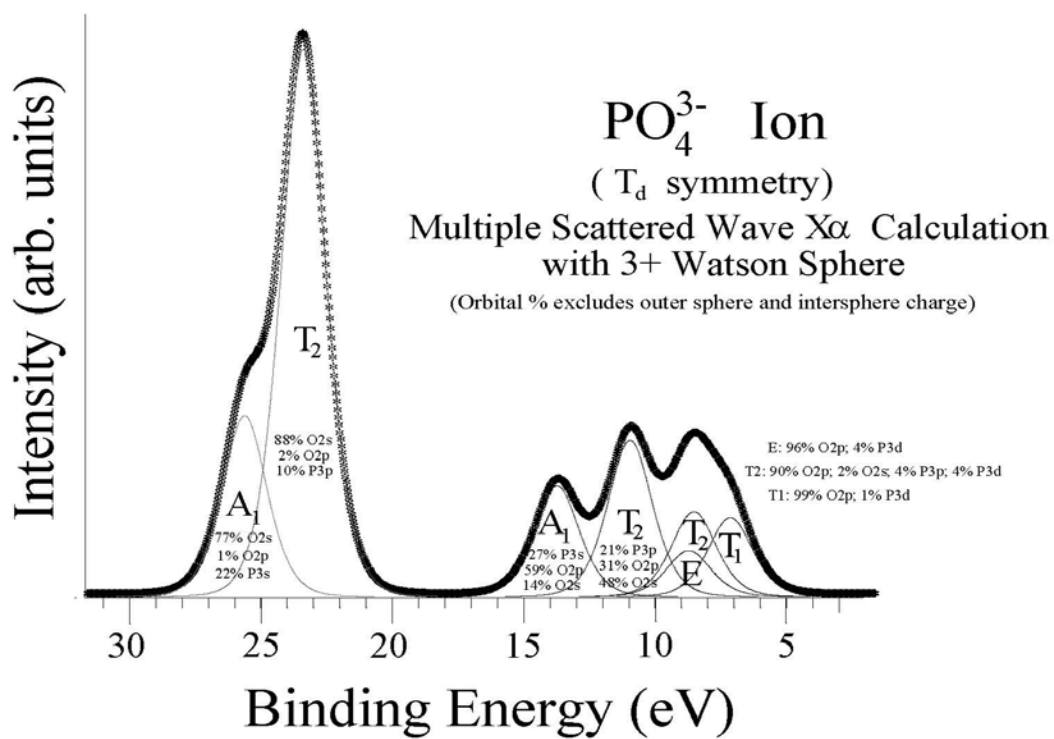


Figure 7.9 Comparison of metaphosphate features and orthophosphate features. A valence band spectrum of chromium tripolyphosphate generated from a band structure calculation is shown in (a), while the orthophosphate CrPO_4 is shown in an experimental VBXPS spectrum (b) and a calculated valence band of the PO_4^{3-} ion generated from multiple scattered wave X-alpha calculations is shown in (c).

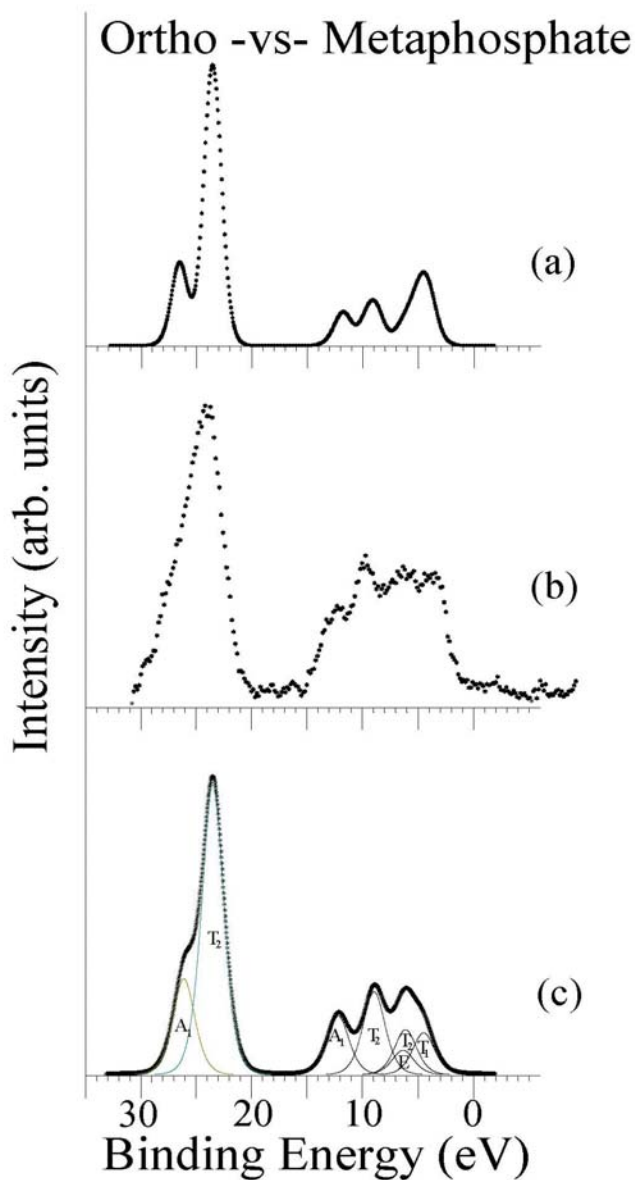


Figure 7.10 Overlay of condensed phosphate band structure calculations on VBXPS spectrum of CPB sample. Generated spectra of (a) $\text{Cr}_7(\text{PO}_4)_6$, (b) $\text{Cr}_3(\text{PO}_4)_2$ and (c) $\text{Cr}_6(\text{P}_2\text{O}_7)_4$.

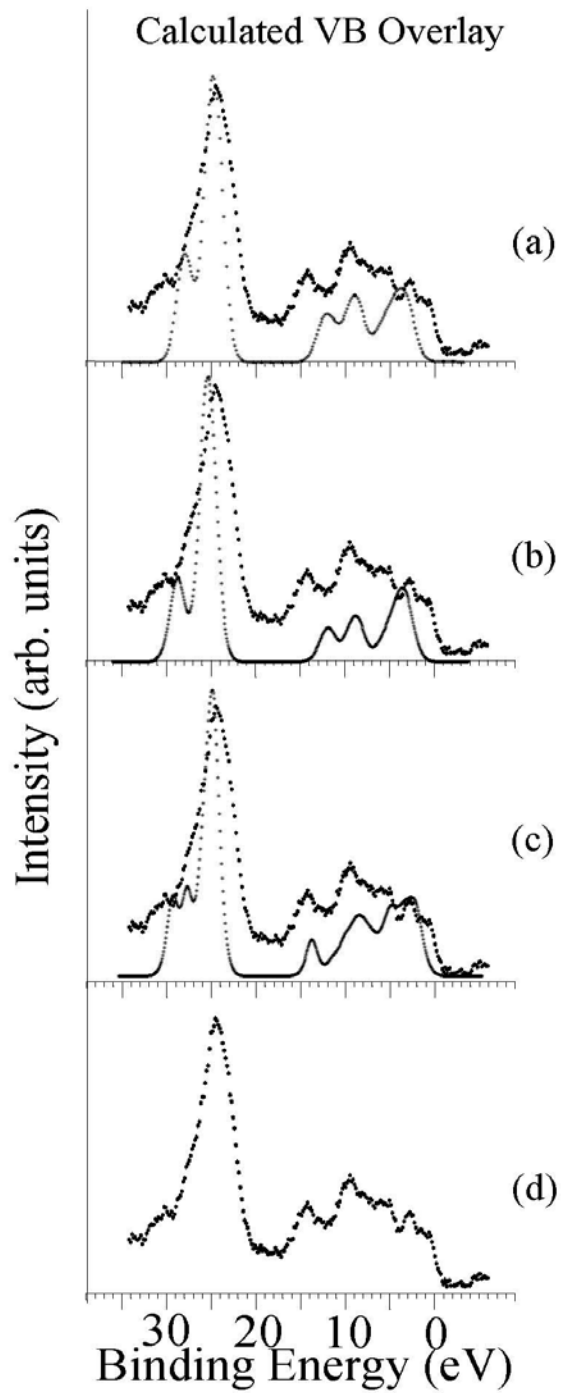


Figure 7.11 Topographical comparison of XPS valence band spectrum of the CPB sample below the predicted dichromium(II) tetrachromium tetrakis(diphosphate) $[\text{Cr}_6(\text{P}_2\text{O}_7)_4]$ spectrum generated from band structure calculations.

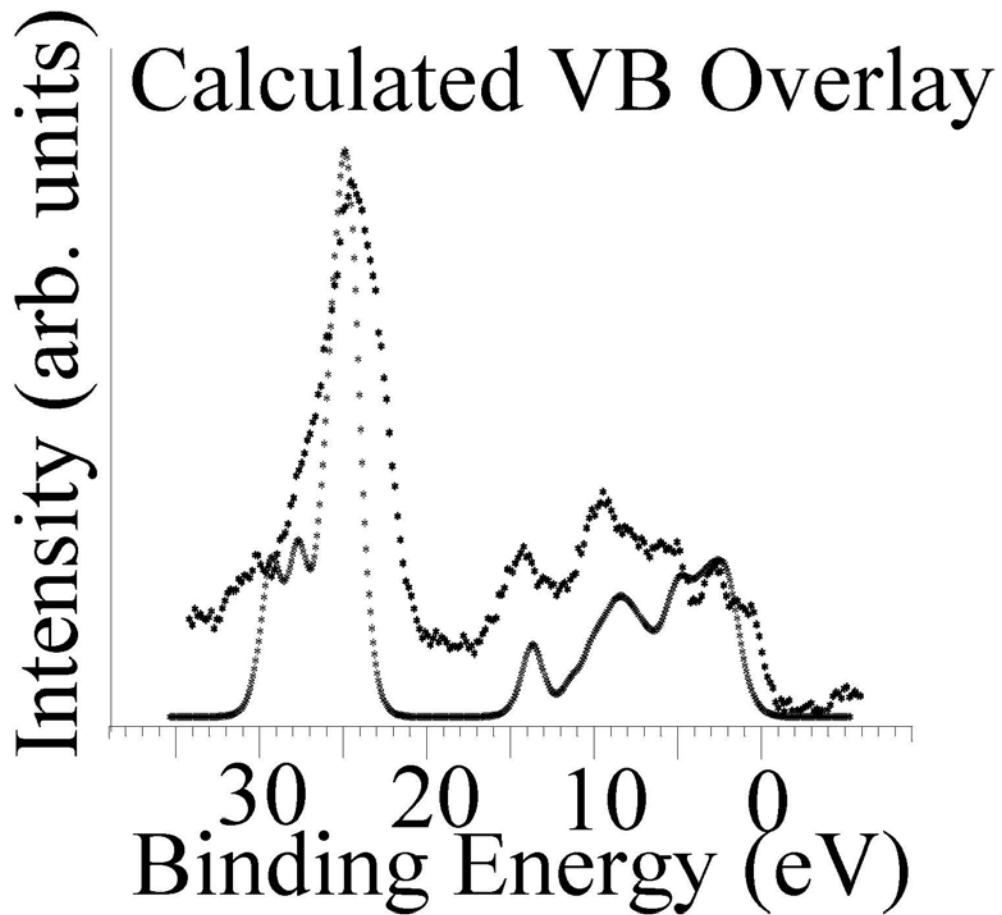


Figure 7.12 Valence Band XPS spectra of (a) chromium foil exposed to 4-D H₂O in the anaerobic cell for 10 min., (b) polished chromium foil and (c) chromium foil treated with 5M o-H₃PO₄ in the anaerobic cell for 1 hour.

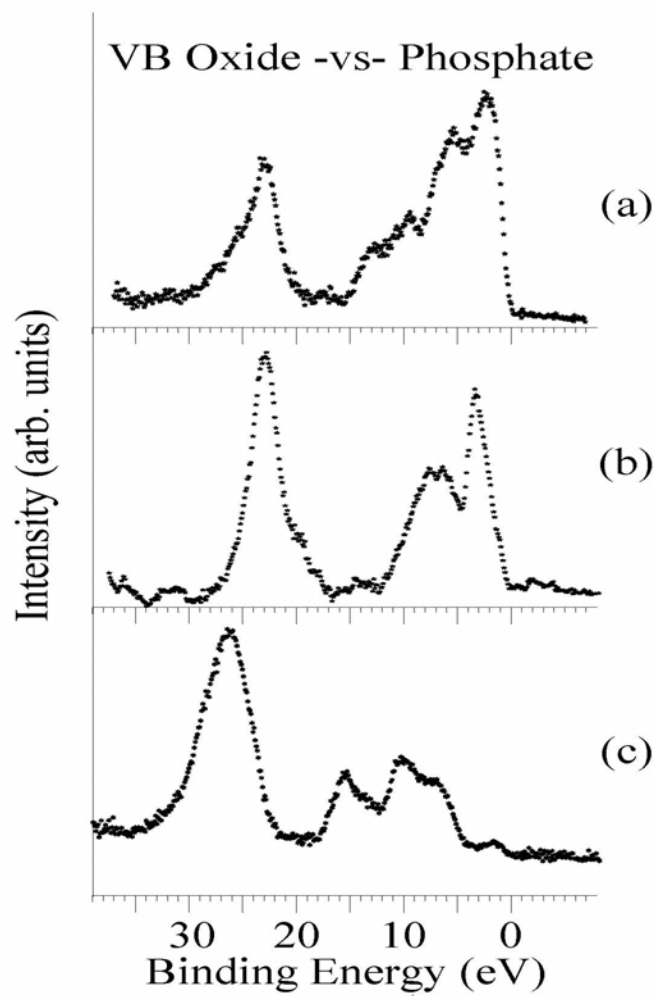


Figure 7.13 X-ray photoelectron valence band spectra of O 1s curve fitted peaks of CPA1H at normal angle and surface sensitive angle shown one on top of the other.

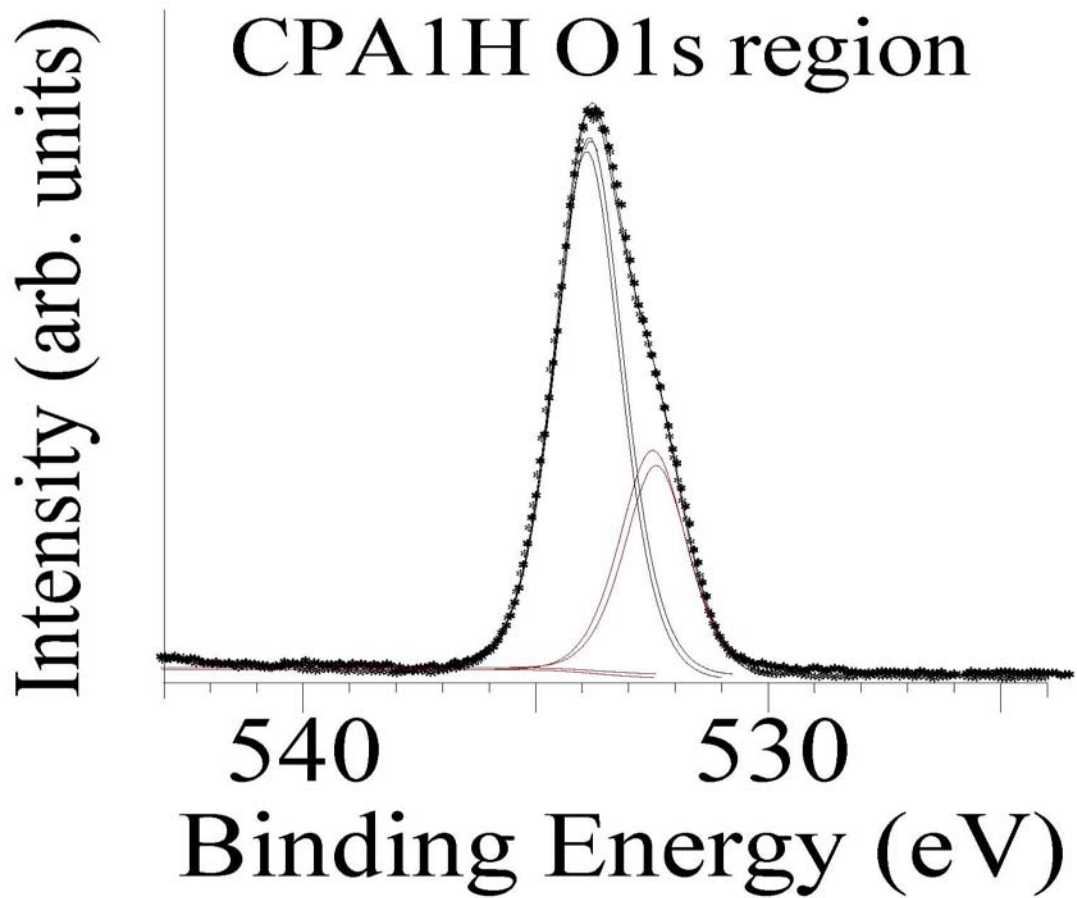


Figure 7.14 Comparison of CPA1H sample (a) to the valence band spectra generated from band structure calculations of (b) dichromium(II) tetrachromium tetrakis(diphosphate) $[\text{Cr}_6(\text{P}_2\text{O}_7)_4]$ and (c) tripolyphosphate $[\text{Cr}_3(\text{PO}_4)_2]$.

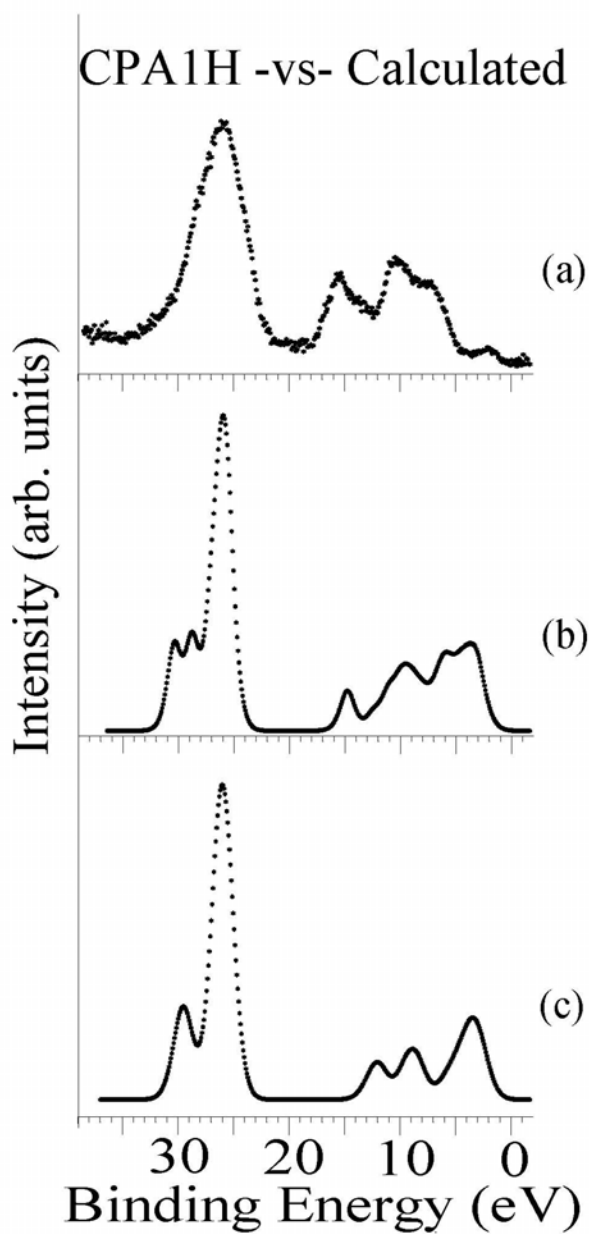


Figure 7.15 Topographical comparison of XPS valence band spectrum of the CPA1H sample beneath the predicted valence band spectrum of chromium cyclo-hexaphosphate $[\text{Cr}_2\text{P}_6\text{O}_{18}]$ spectrum generated from band structure calculations.

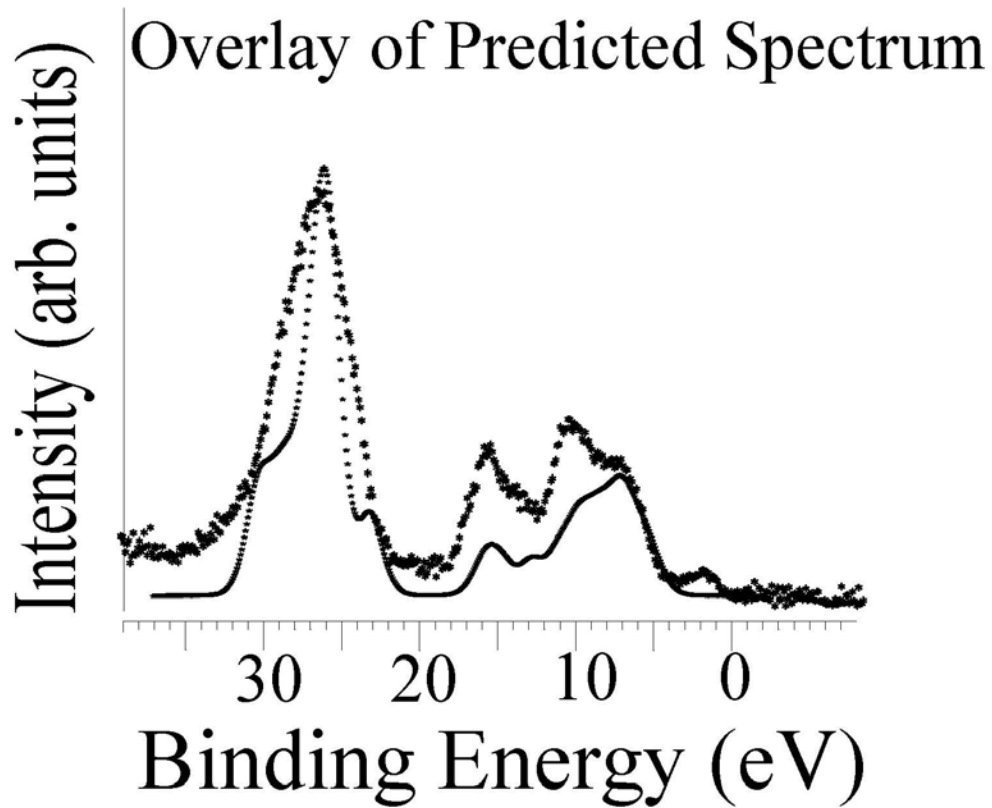
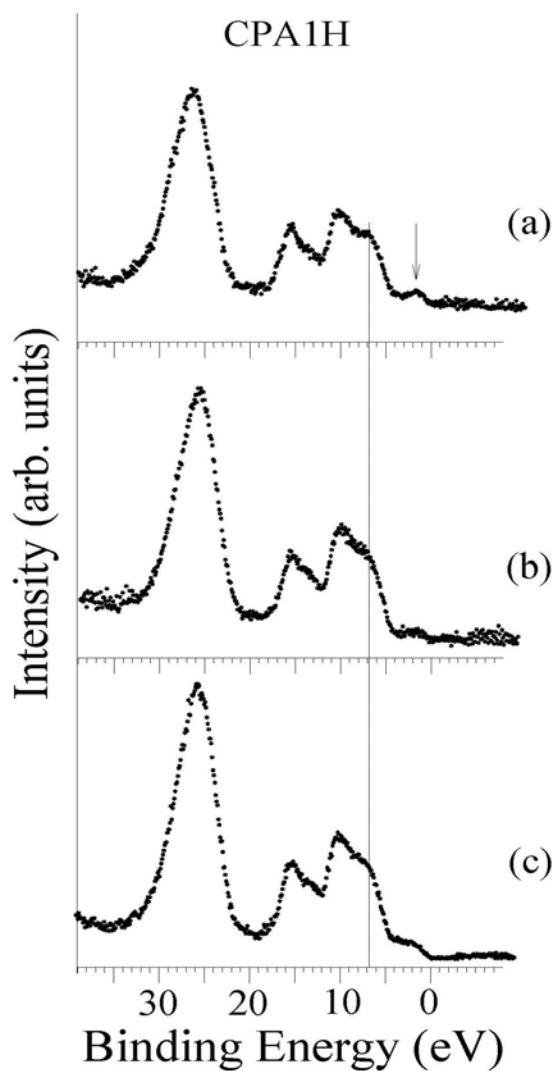


Figure 7.16 Experimental Valence Band XPS spectra of (a) CPA1H, (b) CPA1H recorded at a surface sensitive angle and (c) the same sample after exposure to ambient air for one week.



7.10 Tables

Table 7.1 Summary of Experiments

Experiment	Surface	Treatment Method
CPBno	Polished Cr	11 min Immersion No Treatment
CPB	Polished 10 min	Bench top 5 min abrasion/5 min rest in 5 M H ₃ PO ₄
CPA10	Ar ⁺ Etched	Anaerobic Cell 10 min in 5M H ₃ PO ₄
CPA1H	Ar ⁺ Etched	Anaerobic Cell 1 hour in 5M H ₃ PO ₄
CPAa	Ar+ Etched	Anaerobic Cell 1 hour in 5M H ₃ PO ₄ Exposed to air 1 week
CPAaw	Ar+ Etched	Anaerobic Cell 1 hour in 5M H ₃ PO ₄ Exposed to air 3 weeks Immersed in water 24 hours

Table 7.2 Core level peaks widths at half maximum (FWHM) and atomic ratios listed by sample.

Sample	O 1s FWHM	P 2p FWHM	O:Cr	P:Cr
CPBno	3.6	1.7	1.11	0.02
CPB	2.9	2.1	4.68	2.10
CPA10	3.6	1.8	1.00	0.10
CPA1H	2.4	1.8	18.5	5.4
CrPO ₄	N/A	2.0	N/A	1.0

Table 7.3 Data for Chromium Foil Atomic Ratio Calculations

Sample	Core Region	Normalized Area	O/Cr Ratio	P/Cr Ratio
CPBno	Cr2p	4350	1.14	0.02
	O1s	2025		
	P2p	24		
CPA10	Cr2p	19705	1.00	0.10
	O1s	8025		
	P2p	795		
CPA1H	Cr2p	174	18.5	5.40
	P2p	261		
CPA1H 60° angle	Cr2p	324	11.4	2.98
	O1s	1499		
	P2p	268		
CPAa	Cr2p	602	9.46	5.22
	O1s	2319		
	P2p	873		
CPAaw	Cr2p	2034	5.53	0.98
	O1s	4576		
	P2p	555		
CPB	Cr2p	1244		
	O1s	2368		
	P2p	726		

Table 7.4 Binding energy (eV) for Cr 2p (left) and O 1s (right) core level regions. *PO₄³⁻ peak in CrPO₄ O 1s at 534.1 BE

Sample	Chromium				Oxygen		
	2p _{3/2} met	2p _{3/2} ox	2p _{1/2} met	2p _{1/2} ox	H ₂ O	OH ⁻	O ²⁻
Cr Acetate	577.7	-	587.5	-	533.2	532.0	530.4
Cr ₂ O ₃	576.7	-	586.6	-	532.4	530.4	529.8
CrO ₂	575.2	576.9	586.6	585.2	532.4	530.4	529.0
CrO ₃	577.9	579.6	587.3	589.2	532.8	530.9	529.2
Cr + H ₂ O	574.7	577.5	584.8	587.8	533.2	531.8	530.1
Cr Etched	574.5	-	584.8	-	533.9	532.0	530.8
Cr Polish	574.3	576.9	574.3	586.5	-	531.8	530.5
CrPO ₄	-	578.0	-	587.8	533.0	531.6	*

Table 7.5 Crystal structure data for calculated chromium phosphate compounds.

Compound	International Gp. #	Space Gp.	Symmetry
α CrPO ₄ Chromium phosphate	74	Imma	B.C.Orthorhombic
Cr(PO ₃) ₃ Chromium(II) tris(metaphosphate)	9	C1c1	Cent. Monoclinic
Cr ₇ (PO ₄) ₆ Trichromium(II) tetrachromium hexaphosphate	2	P1	Triclinic
Cr ₆ (P ₂ O ₇) ₄ Dichromium(II) tetrachromium tetrakis (diphosphate)	2	P1	Triclinic
Cr ₃ (PO ₄) ₂ Trichromium(II) bis(phosphonate(V))	19	P 21 21 21	Orthorhombic(disph)
Cr ₂ P ₆ O ₁₈ Chromium cyclo- hexametaphosphate	14	P 1 21/a 1	Simple Monoclinic
Cr ₂ P ₄ O ₁₃ Chromium tetrapolyphosphate	14	P 1 21/c 1	Simple Monoclinic

CHAPTER 8 - Formation of Ultra Thin Oxide-free Protective Coatings on Chromium and 316 L Stainless Steel from 3M Etidronic Acid.

8.1 Abstract

This chapter reports a study of phosphate films formed directly on the surface of metallic chromium and 316 L stainless steel via treatment in 3 molar (M) etidronic acid. Two unique methods were used in formation of these films, both taking place in an anaerobic environment, resulting in the phosphate layer forming directly on the metal surface without the presence of an oxide layer. One method of treatment utilized an anaerobic cell that enabled the etched metal surface to remain in an isolated anaerobic environment during the exposure of the metal to deaerated etidronic acid. The second method utilized is a bench top treatment developed previously by this research group.¹ Core level and valence band XPS were used to study the films formed on the clean sample surfaces. Compositional variations were interpreted through the use of band structure and X-alpha calculations. Valence band photoemission spectra interpreted in this manner were found to be effective in understanding subtle differences in the resulting surface chemistry as well as in identification of the various phosphate structures.

The chromium foil experimental results indicate that the etidronate broke up and formed a phosphide on the surface. The anaerobic cell treatment of the chromium foil produced an extremely thin layer consisting of a phosphate that appears characteristic of chromium orthophosphate indicating that, again, the etidronate molecule did not remain intact. Polished 316L stainless steel treated in 3 M deaerated etidronic acid showed no reaction with the organic phosphonic acid, but formed an oxide film identical to the as-received 316L stainless steel sample. The anaerobic cell treatment readily produced an etidronic film directly bonded to the stainless steel surface.

Evaluation of the core level XPS spectra alone was not effective in determining the nature of the surface films generated in the two treatment methods, but valence band XPS spectra provided details which were specific to the "fingerprint" region of the phosphate species as previously determined by this research group.²⁻⁷

8.2 Introduction

Our group has found that it is possible to form ultra thin oxide-free phosphate films onto clean metal surfaces from orthophosphoric acid introduced to the metal surface in a specially designed anaerobic cell and also via bench top treatment.^{1,2} A number of metals - aluminum, iron, copper, and titanium, among others- formed a phosphate layer less than 100 Angstroms (Å) thick when exposed to deoxygenated orthophosphoric acid. Initial formation occurred as a metaphosphate structure which converted to an orthophosphate upon exposure to ambient atmosphere. The resulting films are stable for indefinite periods under atmospheric conditions.

The evaluation of the surface changes relies on distinguishing between the various possible metal oxides, hydroxides, phosphates and metaphosphate compounds. Diffraction methods of characterization are not effective with the samples due to their ultra thin and amorphous nature. Chemical shifts are present in the core level spectra, but tend to be somewhat ambiguous when trying to discern between subtle differences in oxide and phosphate shifts in the metal regions. The O 1s region does not clearly elucidate the differences between oxygen in a phosphate, oxygen in an oxide, or oxygen in adsorbed water. However the outer valence band region shows significant differences in binding energy between different oxides and phosphates, as shown in previous chapters. Valence band XPS also enables the researcher to distinguish between the high symmetry orthophosphate ion and the lower symmetry metaphosphate and condensed phosphates. Spectral features are easily explained when using a predictive model such as band structure calculations or X-alpha calculations which reveal differences in energy occurring as a result of the pronounced atomic character within the molecular orbitals involved in the chemical bonds.

Etidronic acid (hydroxyethylidene diphosphonic acid) is widely used in industry as a corrosion inhibitor, in paints, boiler water treatments, and coatings and has been widely investigated in its corrosion inhibition effects on iron and steel. Earlier work within our group has investigated the effect of etidronate on iron surfaces and mild steel, as well as characterization of etidronic acid and its salts through the use of valence band XPS.^{7,8} Initial studies found an etidronate-rich film which could be removed by argon ion etching revealing increasing amounts of iron oxides. Further study concluded that the etidronate ion interacted with the native oxide film on the iron and mild steel metal.

Chromium is a major component of stainless steels and is employed in the manufacture of steel because of its particular ability to lend corrosion resistant properties to the alloy. The 316L stainless steel employed in this experiment contains 18% chromium and is the most widely utilized material in the manufacturing of implant materials. A serious problem has occurred whereby older implants have eroded the bone in which they reside causing catastrophic failure of the implant. One treatment is the inhibition of osteoclastic bone resorption, which is the cause for the implant failing, by the use of an administered bisphosphonate drug.⁹ Recent studies have been undertaken with the focus on developing a method of applying the bisphosphonate drug directly to the area via applying the drug directly to the implant material to attain direct local delivery of the drug to the site.¹⁰ A continuous layer of calcium etidronate has been successfully applied to titanium by electrolytic deposition, but the technique produced globular, rather thick films (3.7 μm thick).¹¹

The purpose of this research is to study the results of exposing 316L stainless steel and chromium metal surfaces, which have had the native oxide layer removed, to etidronic acid utilizing both anaerobic treatment methods. This approach facilitates reaction of a clean, oxide-free metal surface directly with the deaerated aqueous organic acid producing an ultrathin (<100 \AA) potentially protective surface film. An oxide-free metal surface is required for the formation of ultra thin phosphate films. The anaerobic cell allows the metal surface to be monitored during the etching process as well as after the surface chemistry has been altered without ever exposing the experiment to ambient oxygen or contaminants until the resulting chemical system has been characterized.

Examination of the results reveal formation of a novel surface which is revealed by valence band XPS and interpreted by spectra generated from calculations as well as a compound powder standards. There is a subtle difference in the phosphate films formed on the two metals as well as differences in the films formed via the two anaerobic treatment methods.

8.3 Experimental

8.3.1 Instrumentation

XPS measurements with a VSW HA150 spectrometer (150 mm hemispherical analyzer), equipped with a 16 plate multichannel detector system and aluminum K_{α} X-radiation (240 W) produced from a 32 quartz crystal via study among broader providing an X-ray line width less than 0.2 eV. A constant pass energy of 50 eV for survey and valence band scans and 20 eV for core level data was maintained. Spectrometer energy scales were calibrated using copper and silver with all spectra referenced against the C1s peak for adventitious hydrocarbon at 284.6 eV or the Fermi edge at 0.0 eV where a distinct metal edge was observed in the valence band data.¹⁵ The specially designed anaerobic cell consists of an ultra high vacuum (UHV)-capable chamber separated from the analysis chamber by a gate valve. This allows for the solid liquid interface formed under an inert atmosphere to be studied.¹⁶ The base pressure of the system is better than 10^{-9} Torr. When appropriate, sample charging was offset by use of a low energy flood gun operated at 280eV and 2.2 mA

8.3.2 Materials and Preparation

Chromium foil and 316 L stainless steel (18%Cr, 10%Ni, 3%Mo) was obtained from Goodfellow. Chromium phosphate powder [Cr PO_4] was obtained from Aldrich Chemicals. Calcium etidronate (1:1) was synthesized from materials obtained from Aldrich Chemicals following the procedure outlined by Browning and Fogler.¹¹ Orthophosphoric acid was obtained from Fischer Scientific and etidronic acid from Sigma-Aldrich and TG National.

Samples of 99.99% chromium foil and 316L stainless steel foil each measuring 0.5 cm x 2.0 cm were polished with 600 grit emery paper manufactured by 3M Corp., blown clean with compressed argon and degreased with acetone before being placed in the anaerobic environment.

All solutions were deaerated to drive dissolved oxygen from the solution. The solutions, and also the emery paper in the case of the bench top treatment, were deaerated by bubbling nitrogen or argon gas through the solution for four hours immediately prior to the chemical treatment.

The native oxide on the metals was removed by argon ion etching for 80 minutes for chromium and 45 minutes for 316L stainless steel until the presence of oxide as monitored in the Cr2p core region was not detected. Ultra high purity (UHP 99.999%) argon from Matheson was used with an Ion Tech B21 saddle-field ion etcher operated at 2 mA and 5 kV, the argon pressure being less than 10^{-3} Torr. The etch rate is estimated to be in the range of 2-5 Angstroms minute^{-1} .

8.3.2.1 Anaerobic Cell Procedure

Chemistry performed in the anaerobic cell is done under a positive pressure (above 1 atm or >760 Torr) to prevent any ambient air or contaminants from entering the chamber during the procedure. Once etching has removed the native oxide and surface adsorbants the anaerobic cell was isolated from the vacuum chamber by a gate valve. The cell is filled with UHP argon (to a positive pressure) to create an inert atmosphere around the experiment. Deaerated 3M etidronic acid is introduced into the cell and the sample is submerged in the acid for the duration of the reaction time. Once the reaction is complete the acid is drained, quadruply distilled water is introduced and the sample rinsed. The water is drained out of the cell, the reaction vessel is removed and the sample is returned to ultra high vacuum. Once UHV has been achieved surface analysis is performed via XPS.

8.3.2.2 Bench top Procedure

The bench top method of treatment has been previously reported.¹ The native oxide on the metal is removed simultaneously with exposure to the phosphoric or etidronic acid. The polished metal is submerged in the deaerated acid solution and abraded with the waterproof, 600 grit emery paper exposing the metal surface to the phosphate-containing solution. The metal is abraded for five minutes then allowed to remain in the acid solution for an additional five minutes in order for the surface metal to completely react with the acid. The metal is then removed and rinsed with deaerated, quadruply distilled water for 5 minutes. The excess water is removed from the sample surface by placing a Kem Wipe against the sides of the sample. The treated sample is dried overnight in vacuum before being transferred to the XPS instrument in air.

8.3.2.3 Calculations

Data obtained from Valence Band XPS was interpreted by comparison to spectra derived from either band structure or cluster model calculations. Band structure calculations were done using an extended version of CRYSTAL^{17,18}. Calculated spectra generated from band structure calculations via adjusting the density of states for each orbital type by the appropriate cross-section as given by Scofield.¹⁹ The adjusted density of states is convoluted with a mixed Gaussian-Lorentzian (50%) product function with a full width at half-maximum of 1 eV. The energy scale is contracted by 1.3.

8.4 Results and discussion

The scheme used in Chapter 7 will also be used for the sake of brevity and is outlined in Table 8.1. The two methods of treatment employed in this study as described above are again represented with the letters "B", referring to the *bench top* approach, and "A" which refers to the *anaerobic cell* process. Both methods are used with 3M *etidronic acid*, and so the letter E will precede the method reference letter. The sample substrate reference is the first portion of the experiment name and will be "C" for the *chromium* foil and 316L refers to the *316L stainless steel* foil. Following this logic the chromium foil treated in 3M *etidronic acid* via the *bench top* method is abbreviated as "CEB", and the *anaerobic cell* treatment becomes "CPA". The need for further designation references treatment times involved are not necessary with this experiment. The *bench top* method was utilized with the ten-minute exposure time only, as was the *anaerobic cell* method. The reaction in the *anaerobic cell* process exposing the sample to acid solution for ten minutes was found to produce results sufficient to evaluate the chemistry involved in the chromium and 316L steel / *etidronate* systems. Additional designators are necessary in this study as film stability was explored in more detail. Samples were exposed to ambient laboratory *atmosphere* for one week and re-examined in the spectrometer. This experiment is denoted by use of the lower case "a" after the treatment method designator. The samples further examined by immersion into 1M sodium chloride (*NaCl*) solution for two hours have the lower case "n" used after the treatment method designator. Note that even though the sole letter "n" is used the sample has been exposed to *atmosphere* for one week and then re-examined in the spectrometer. The *NaCl* solution was not deaerated and the experiment was performed at STP on the lab bench.

"CEAn" would therefore refer to the 99.99% chromium foil sample treated in the anaerobic cell for ten minutes, exposed to atmosphere for one week, followed by immersion in 1M NaCl solution for two hours.

8.4.1 Discussion of Chromium and Stainless Steel States.

Band structure calculations have been performed on both chromium and iron, which is the largest component in the 316L stainless steel alloy. The outer valence band region of the etched metal samples is shown in Figure 8.1 along with the spectra generated from the band structure calculations. Even though Fe 3d has a cross section which is over two times that of chromium (0.1944 units, compared to 0.0748 units for Cr 3d), the 3d peak for iron is much narrower than that for chromium. There is very good agreement between the calculated spectra and the argon ion etched metal foil samples.

Both metal foils were degreased with acetone prior to placing in UHV. The foils were placed on a copper sample holder and secured using double-sided carbon tape. The as-received samples showed very thick oxide and contaminant films on the foil, as illustrated in Figure 8.2. The 316L steel sample had a visible metal edge, but essentially the only other features were in the O 2s, O 2p and C 3s regions. The chromium foil had a complicated spectra as a result of the surface contamination. The valence band spectra of the sample which had been polished with 600 grit silicon carbide emery paper showed more definition in the features in the outer valence band below 15 eV. The chromium foil had a broad peak of medium intensity in the O 2p region which was typical for chromium oxide, Cr₂O₃, which is the oxide of Cr^(III). The O 2s region in the chromium sample is high in intensity, but very narrow. The same region in the iron sample is less than half the intensity of the same region for the as-received sample. The iron also has a reduction in intensity in the O 2p region, and appears as a sloping higher binding energy shoulder on the very intense Fe 3d peak. The etched samples both show very intense metal edges and peaks corresponding to the Ar 3s at 22 eV, Ar 3p at 9 eV and a carbide peak at 12 eV. This carbide formation is the result of the etching process and is an unavoidable reaction, and so must be accounted for in the baseline spectra.

The valence band XPS spectra of 316L stainless steel and 99.9% iron foil are shown in Figure 8.3(a) and (b), respectively. It is clear that the generalization of using iron to predict

spectral results is valid when using 316L stainless steel (316L) as the valence band spectra for the two foils is nearly identical. While chromium is a major component of 316L it does not impact the valence band region due to the lower cross-section of chromium combined with the fact that 316L is only 18% chromium.

8.4.2 The Etidronate Ion

Etidronic acid (1-hydroxyethylidene-1, 1-diphosphonic acid (HEDP)) is a nontoxic analogue of diphosphoric acid. The bridging P-O-P linkage in the condensed phosphate is instead a P-C-P sequence in the organophosphorous acid joining the two phosphate tetrahedra in the trans- arrangement on the carbon atom. The other two functional groups on the central carbon atom are $-\text{CH}_3$ and $-\text{OH}$, as illustrated in Figure 8.4.⁷ Etidronic acid $[\text{C}_2\text{P}_2\text{O}_7\text{H}_8]$ is a colorless to pale yellow viscous solution that is stable under most chemical conditions but decompose at relatively low temperatures ($<200^\circ\text{C}$).¹³ The etidronic acid (HEDP) becomes bidentate upon dissociation of the four H atoms on the two phosphate tetrahedra. At 25°C the pK_a of the first hydrogen (pK_1) is below 1 and the remaining acidity constants for HEDP are: $\text{pK}_2 = 2.54$, $\text{pK}_3 = 6.97$ and $\text{pK}_4 = 11.41$. This bidentate nature of the etidronate ion allows it to readily react with divalent ions.

Earlier work in this research group focused on the reaction of iron and mild steel with calcium etidronate which established that an etidronate-rich film was formed on the surface of both metal samples. In order to establish that the film was etidronate in nature and not phosphate spectra were recorded of iron(II) phosphate $[\text{Fe}_3(\text{PO}_4)_2]$ for comparison purposes.¹² Outer valence band spectra from this study for iron etidronate and iron phosphate are shown in Figure 8.5. There is a difference in topography and in location of the phosphate peaks between the two iron phosphorous-containing compounds.

Prior spectra of the etidronate ion in the form of calcium etidronate were recorded using Mg $K\alpha$ X-ray light and contain satellite features which would not be present in current investigations which use monochromatic Al $K\alpha$ X-rays. An appropriate valence band spectrum of an etidronate-containing compound recorded using monochromatic Al $K\alpha$ light was required to use as a reference when evaluating the efficacy of the on-hand etidronic acid, which had been

stored in the lab since 1989 (aged), as well as in interpretation of the valence band XPS spectra of the films generated in this experiment.

Etidronate compounds are not commercially available so calcium etidronate was synthesized in the lab as this compound was successfully used in the research performed earlier in this group.^{7, 12} The precipitation reaction described by Browning and Fogler¹¹ was used to synthesize two forms of calcium etidronate. One precipitate was a 2:1 molar ratio and the other was a 1:1 ratio. In addition to the procedure referenced the resulting precipitate was crushed into very fine powders and rinsed four times with quadruply distilled water to remove residual excess sodium. Both precipitates were white powders with the 2:1 calcium etidronate resulting in needle-like powder crystals while the 1:1 precipitate was a very fine white powder after crushing.

Both powder samples were mounted on double-sided carbon tape and XPS spectra were recorded using the monochromatic Al K α X-radiation produced in the HA150 X-ray spectrometer. The valence band spectra of the two powders are shown in Figure 8.6(c) and (d) with the achromatic valence band spectrum of calcium etidronate (a), the multiple scattered wave X- α calculation of calcium etidronate and the experimental valence band spectrum of 99.99% chromium foil treated using the bench top method (CEB) with the aged etidronic acid (e). The 1:1 molar ratio calcium etidronate yielded a valence band XPS spectrum nearly identical to the previously recorded achromatic spectrum for calcium etidronate. The monochromatic spectrum has greater resolution and shows fine detail not present in the achromatic spectrum due to the presence of satellites in the spectrum of the latter. The valence band spectrum of the CPB sample treated in the aged etidronic acid clearly indicates that degradation of the etidronic acid had occurred and a fresh supply was obtained from Sigma-Aldrich.

8.4.3 Chromium Treatment

Experimental results of the chromium samples CEB and CEA are shown in Figure 8.7(a) and (b) respectively. The P 2p and O 1s regions have been curve fitted in order to extract more information from the core level spectra. Pronounced differences in the experimental results of the two treatment methods reveal that the CEB sample produced a chromium phosphide which

appears most prominently in the P 2p spectrum at a binding energy of 129 eV, or about 4 eV lower binding energy than the phosphate peak at 133 eV.

8.4.3.1 Core Level Spectra

The curve fitted O 1s core level spectrum indicates three forms of O-bonding are present in the sample. The dominant peak at 532 eV and the higher binding energy peak at around 533 eV are produced by the terminal oxygens and the bridging oxygens, respectively. The very small peak appearing at 531 eV results from the presence of an –OH group on the carbon atom in the etidronate ion. All of the O 1s peaks in the chromium foil phosphate film series reported in this dissertation have a peak at around 533 eV which is not present on any etched, as-received or polished sample nor does it show on any of the chromium oxide standards having no carbon. It is logical to assign the peak at 533 eV to the bridging oxygens based on this observation as well as the observation of the relative peak areas in the curve fitted O 1s spectra roughly corresponding to the relative percentages of terminal oxygen to bridging oxygens present in the phosphate.

The P 2p spectra show more than two forms of phosphorous environments are present. The CEB sample has a prominent phosphide while the CEA10 sample shows only faint phosphide formation, if any at all. The only indications of the phosphide formation in the CEA sample is the very small peak required to fit the P 2p peak appearing at about 132.5 eV and the very faint possible phosphide peak in the background at about 4 eV lower binding energy from the dominant peak. The intensity of the P 2p region is low and results in poor statistics. An in depth study of the chromium phosphide system was done and concluded that there were P-P interactions in the compound.¹⁴ The P-P intensity was approximately one half that of the Cr-P intensity in the study which could account for the doublet in the phosphide portion of the P 2p peak.

The Cr 2p regions have been curve fitted as well and are shown in Figure 8.8(d) and (e) alongside an example of raw data prior to curve fitting (a). Also shown in Figure 8.8 is the curve fitted spectrum of the as-received sample (b) and Figure 8.8(c) is the curve fitted spectrum for the argon ion etched 99.99% chromium foil. The curve fitted Cr 2p core level XPS spectra support the theory that there are four different chemical environments in the CEB sample. The highest binding energy peak in either the Cr 2p_{3/2} or Cr 2p_{1/2} would correspond to a Cr-O

environment which is present in phosphates in the Cr-O octahedral coordination environment found in phosphates. In the Cr 2p_{3/2} peak this appears at 577.5 eV indicating that the chromium is in the Cr^(III) state. The peak at 576.2 eV appears in both samples and corresponds to the phosphate coordination with the metal. A peak at 575.5 eV in the CEB sample is not present in the CEA sample, or in any previous chromium phosphate or oxide samples. This peak must result from the Cr-P bonding in the chromium phosphide (CrP). The very intense narrow peak at 574.3 eV is the chromium metal peak.

8.4.3.2 Valence band XPS results

Both samples resulted in very thin films as evidenced by the valence band spectra being dominated by the Cr 3d peak at 1 eV with a very sharp metal edge visible in the results of both samples shown in Figure 8.9(a) and (b). The bench top method valence band XPS spectrum has a very prominent symmetrical O 2s region peak at 23 eV and another oxygen feature around 5 eV. Even though there are prominent oxygen features this does not necessarily imply the film is not oxide free. There is a great deal of oxygen in the etidronate ion in the form of P-O and C-OH. The carbon in the etidronate ion shows near 17 eV. The low intensity peaks at 13.4 eV and 9.6 eV are characteristic of phosphates with the exception that most phosphates also have a peak midway between the two and indeed there is a small but distinct peak at 11.2 eV. The peak appearing as a shoulder on the high binding energy side of the chromium is mostly O 2p in character and is actually two peaks very close together in energy and intensity at 6.3 eV and 5.2 eV supporting the conclusion that there are two different oxygen environments as previously stated. Given the large difference in the phosphate peaks the phosphide feature most likely resides in the 13 eV region. There are several observations which support the conclusion that the film is directly bonded to the chromium surface. In the core level XPS spectra the information is ambiguous in the Cr 2p region, but the P 2p and O 1s peaks have the same phosphate peak present as is found in the other chromium phosphate core level spectra. If there were an oxide present it would certainly show in the O 1s region around 529 eV and the O 1s spectra for both samples are lacking any feature in this region. Additionally, the outer valence band region would have a much larger O 2p region, both in peak width and peak intensity, around 5-6 eV as was shown in Chapter 6.

The CEB valence band spectra shown in Figure 8.10(a) has the outer valence band XPS spectrum of calcium etidronate superimposed underneath the corresponding region of the sample. It is difficult to tell the amount of etidronate present in the film as the Cr 3d peak is so prominent due to the film being so thin. It appears that there could be some etidronate in the film, but the feature around 9 eV is of much lower intensity than the same peak in the calcium etidronate. This could result from the etidronate being broken down in the formation of the clearly evident phosphide. That being the case, it is logical to say the surface film is composed of a mixed phosphate and phosphide bonded directly to the oxide-free chromium surface.

The valence band XPS spectrum of the CEA sample is quite different from the sample prepared in the bench top treatment method. The feature around 4 eV is much broader and increased in intensity than the same region in the CEB sample, encompassing the features that were present in the previous sample around 5-6 eV. The O 2s feature is of relatively lower intensity and has become asymmetrical. The three phosphate features have been reduced in intensity so as to seem non-existent. When the CEA sample is compared to the spectrum below it in Figure 8.9 it is evident that the features present in the CEA sample are the same in location and relative intensity as those present in the etched chromium foil which have been previously addressed in Chapter 6.

The Ar 3s peak in the etched sample is still somewhat visible in the CEA sample but has an obvious increase in width and intensity. The features from the carbide and Ar 3p in the outer valence band region have likewise become less distinct, broader and more intense. These changes from the etched chromium foil spectrum are due to the formation of a very thin film on the surface. An oxygen component has appeared around 25 eV and between 5-6 eV. There is an increase in intensity and decrease in definition at the beginning of the outer valence band region which indicates the presence of a phosphorous compound, although there is not enough detail to facilitate identification of the form of phosphate. A very small feature has appeared at 18 eV from C 2s. The only thing that can be concluded is that an extremely thin film has formed on the etched chromium surface which is likely a phosphate bonded directly to the metal. For the sake of comparison the outer valence band spectrum of calcium etidronate is superimposed over the likewise region in the CEA results in Figure 8.10(b).

The core region spectra indicate that there is phosphorous present and the same three peaks identified in the O 1s region of the CEB sample are present in the O 1s region of the CEA

core level spectrum. The Cr 2p region also indicates a film present but no further information can be extracted from the core level data.

Figure 8.11(b) shows the valence band spectral results of a corrosion study done on the anaerobic cell prepared chromium foil sample. Exposing the film to ambient lab atmosphere succeeded in burying the thin film in an oxide. The most obvious indicator of the presence of an oxide is the very broad peak centered around 7 eV. The spectrum of the polished chromium foil in Figure 8.2(b) emphasizes this feature in the chromium oxide film remaining on the substrate after polishing.

Exposure to 1M NaCl solution for two hours under ambient temperature and pressure eroded the oxide film somewhat producing the results shown in Figure 8.11(c). This is an excellent example of the stability of the oxide layer formed on chromium and illustrates why chromium is so desirable in the fabrication of materials which require resistance to corrosion, such as stainless steel.

When the experimental results for the treatment of chromium in etidronic acid are compared to the CPA sample results shown in Figure 8.12(a) it is evident that chromium does not easily react with etidronate, which is not surprising considering the bidentate nature of the etidronate ion which easily reacts with divalent cations such as Ca^{2+} .

8.4.4 316L Stainless Steel Treatment

Polished 316L stainless steel foil samples were prepared as described above. The 316L stainless steel was argon ion etched for 45 minutes, as determined by monitoring the Cr 2p region since this component of the steel alloy reacts almost instantly with oxygen. The two treatment methods for producing oxide-free surface films described previously were used in this study as well. The exposure time for both methods was ten minutes. The bench top method exposure time was kept the same for uniformity, while the exposure time of ten minutes in the anaerobic cell was used for an initial assessment of the degree of reaction between the acid solution and the foil substrate. It was found that the ten minute exposure period produced results sufficient for evaluation and characterization of the generated film.

8.4.4.1 Core level XPS results

The core level XPS spectra are shown in Figure 8.13. As in the chromium foil results for treatment with etidronic acid the 316L steel shows dramatically different results between the bench top and anaerobic cell procedures. The Fe 2p region of the CEB sample has prominent features at 3.8 eV higher binding energy from the metal 2p_{3/2} peak and 4.0 eV higher than the metal 2p_{1/2} peak. The metal component of the spin orbit split components is readily visible indicating the film is sufficiently thin that the metal substrate is still available for sampling and detection (<100Å). The CEA sample has a very low shift appearing about 1 eV higher in binding energy than the iron metal peak, which appears at a slightly lower intensity.

The Cr 2p region of the CEB sample also indicates a substantial oxide or phosphate presence as the chemically shifted portion is nearly five times higher in intensity than the chromium metal 2p feature and 3.2 eV higher in binding energy than the metallic portion of the peak. Table 8.2 addresses the atomic ratios for the five forms of 316L steel as well as chromium foil studied in the etidronic acid research. Table 8.3 shows the normalized peak areas and Table 8.4 the experimental binding energies. The 316LEB (etidronic acid, bench top method) calculations reveal a preponderance of oxygen and carbon with a very low amount of phosphorous. The CEA sample also shows a chemically shifted peak at a slightly wider separation of 4.2 eV. This sample shows the ration of intensities between the two features to be much closer to being equal than the Cr 2p core level peak of the CEB sample.

As with previous P 2p peaks there are two peaks in the curve fitted spectrum, but in the 316LEB sample the lower binding energy peak is half the size of the higher binding energy component indicating P-O-P linkage in this sample is lower than in the other treated samples. Otherwise the P 2p core level peak information does not contribute any significant information to use in the interpretation of the spectra of this sample. The P 2p peak of the sample treated in the anaerobic cell (CEA) is unremarkable except to note that it is centered at a higher binding energy of 134 eV, a 1.5 eV shift from the P 2p core level peak of the CEB sample.

Each of the samples shown in Figure 8.13 has different component peaks in the curve fitted spectra for the O 1s core level. The O 1s core level spectrum of the CEB sample indicates a large component at 532 eV which is associated with either water or the P-O bond, or both. The two smaller peaks on either side at 533.9 eV and 530.5 also appear in all the treated samples and

correspond to the presence of the P-O-P bridging oxygen and the –OH present in the etidronate ion as a functional group on the bridging carbon atom.

There is no corresponding peak in the O 1s core level spectrum of the CEA sample. The comparison of the O 1s core level XPS spectra of the 316L steel etidronate samples and calcium etidronate are shown in Figure 8.14. Note the absence of the peak at 530 eV in the calcium etidronate sample.

8.4.4.2 Valence Band XPS Spectra

Valence band spectra of the two 316L steel samples treated in etidronic acid and the polished 316L steel sample. Figure 8.15(a) of the valence band XPS spectrum of the 316EB sample shows a two main features corresponding to the metal 3d region. This peak is much broader than the same region in the spectrum of the 316L polished steel sample. The other prominent feature in the 316EB valence band spectrum is the broad medium intensity peak at 24 eV in the O 2s region. There are other low intensity features at 18 eV and 6 eV which are mostly C 2s and C 2p in character and three peaks at 15.4, 11.8 and 9.3 eV which indicate an underlying phosphate structure. Given the high oxygen and carbon-to-metal ratios and the similarity in spectral topography to that of the polished 316L steel sample there is some form of contamination covering the phosphate film formed on the steel surface. The 316EB valence band spectrum is shown in Figure 8.16(a) with the etidronic acid outer valence band underneath the corresponding region of the sample. The separation between each of the three phosphate peaks is 3.6 eV between the two higher binding peaks and 2.5 eV between the peaks at 11.8 and 9.3 eV in the 316EB sample. These separation distances are inconsistent with the etidronate phosphate region which has 4.5 eV between the two higher binding energy peaks at 14.7 and 10.2 eV, and 4.1 eV between the two phosphate peaks at 10.1 and 6.0 eV. It is reasonable to assert that the etidronate ion broke up during the reaction sequence. It is difficult to say that the surface is oxide-free, though there is high probability that it is true because if not the oxide features discussed earlier would dominate the region where the low intensity phosphate-related peaks are seen.

The valence band of the 316EB sample is clearly indicative of a phosphate film on the stainless steel surface. The O 2s peak is the most prominent feature, appearing at 26 eV. There

is definite contribution from the two carbon atoms in the etidronate molecule which occur at 18.7 eV which is mostly from the C 2s contribution and the C 2p interaction shows up at 6.5 eV mixed with the O 2p component. P 3s is found in both the 14.6 eV peak and somewhat in the O 2s region where it appears as a low intensity peak at the high binding energy side of the O 2s peak. The feature at 1.3 eV is a mixture of the Cr and Fe 3d metal peaks. The metal edge shows clearly indicating the surface film is thin enough to allow the metal substrate to be detected (<100Å thick).

The spectra of the 316EA sample and the outer valence band of calcium etidronate are shown for comparison in Figure 8.16(b). There is very strong agreement between the topography and binding energies of the outer valence band region below 15 eV as well as the position and intensity agreement of the C 2s peak at 18 eV. The precise binding energies of the peaks in the 316EA sample valence band spectrum are 25.94, 18.71, 14.62, 9.67, 6.16, 5.03 and 1.26 eV. The valence band spectral binding energies are 26.12, 18.91, 14.67, 10.15 and 6.52 eV. The etidronate ion stayed intact and formed a thin surface film on the stainless steel substrate. There is no oxide present in the 316EA sample as there are no features characteristic of an oxide in the O 2s peak, which is relatively narrow, or in the mostly O 2p region around 7-8 eV which would show up as a broad feature with intensity at least half that of the O 2s peak.

The treatment of 316L stainless steel in the anaerobic cell with deaerated etidronic acid produced a metal substrate which is directly bonded to an etidronate film. A corrosion study was done to assess the stability of the resulting etidronate film. Figure 8.17(b) shows the changes resulting from allowing the film coated sample to remain in ambient lab atmosphere for about one week. There is a reduction in intensity of the peak at 5.03 eV which is mostly metallic 3d mixed with O 2p character. The metal edge is also reduced in intensity as a result of the outermost layer of the film becomes exposed to oxide and other contaminants present in the lab. The underlying etidronic film remained intact as demonstrated by the peak binding energies remaining consistent between the two samples.

Immersion of the 316EA sample in 1M NaCl solution produced a degradation of the etidronate film shown in Figure 8.18(c) which is further compared with the chromium phosphate valence band XPS spectrum. It would appear that the phosphate film remaining changed into the orthophosphate.

8.5 Conclusion

Samples of 99.99% chromium foil and 99.9 % 316L stainless steel were treated in 3 M etidronic acid using the previously described methods developed in this research group. The chromium samples did not form substantial films with etidronic acid. This is not surprising as the natural state of chromium is most often in the $\text{Cr}^{\text{(III)}}$ state and etidronic acid reacts well with divalent cations due to its bidentate nature. The thermodynamics of the reactions are evidently insufficient to promote a change in valency in the chromium from $\text{Cr}^{\text{(III)}}$ to $\text{Cr}^{\text{(II)}}$ which would be the preferred state for complexation with the etidronic acid.

Iron is the major component in 316L stainless steel alloy and exists in both the $\text{Fe}^{\text{(III)}}$ and $\text{Fe}^{\text{(II)}}$ states in nature. Initial atomic ratio calculations indicate a chromium-to-iron ratio of roughly 1:1. The actual surface of the stainless steel is most likely an outer layer comparatively rich in chromium as this metal readily diffuses through the alloy matrix to the less constrained surface layers. When etched the surface of the 316L alloy is altered due to both mechanical rearrangement by the argon ions as well as a result of the thermodynamic conditions which exist in the etching environment. Additionally, both iron and chromium form carbides during the etching process which causes a further reconstruction of the surface layers.

The reconstruction is conducive to the formation of an oxide-free etidronate film which was bonded directly to the steel surface upon treatment in the anaerobic cell. This film proves to be stable in air but was degraded by the exposure to 1 M NaCl solution. This does not necessarily preclude the use of this film on stainless steel surgical implants in as much as the biochemical conditions within the physiological environment are far less saline. Possibly this could prove to be sufficiently non-reactive to allow this method of treating implants to inhibit corrosion as well as directly deliver bisphosphonate drugs which are known to inhibit osteolysis, the cause of catastrophic implant failure.

The chromium foil samples produced films which have features consistent with phosphates, however the films were of insufficient thickness to characterize further. Likewise, the 316L stainless steel foil treated via the bench top method was too thin to evaluate other than noting very small phosphate features between 8 eV and 14 eV.

8.6 References

1. Y-Q Wang and P.M.A. Sherwood, *J. Vac. Sci. Technol. A*, **21**, 11 (2003).
2. J. Rotole and P. Sherwood, U.S. Patent No. 6,066,403, (23 May 2000).
3. J. Rotole, K.Gaskell, A. Comte and Peter M.A. Sherwood, *J. Vac. Sci. Technol. A*, **19**, 1176, (2001).
4. John A. Rotole and Peter M.A. Sherwood, *Surf. Sci.Spectra*, **5**, 67, (1998).
5. A. L. Asunskis, K.J. Gaskell, D.J. Asunskis and P.M.A. Sherwood, *J Vac. Sci. and Technol. A*, **21**, 1126-1132, (2003).
6. D. J. Asunskis and P.M.A. Sherwood, *J. Vac. Sci. Tech. A*, **21**, 1133-1138, (2003).
7. I.D. Welsh and P.M.A. Sherwood, *Proceedings Electrochemical Society*, **89-13** (Advances in Corrosion Protection by Organic Coatings: Edited by D. Scantlebury and M. Kendig), 417, (1989).
8. P.M.A. Sherwood, I.Welsh and D.M. Hercules, *Applied Spectroscopy*, **42**, 658, (1988).
9. T. M. Wright and S. B. Goodman, editors, Implant Wear in Total Joint Replacement: Clinical and Biological Issues, Material and Design Considerations, *Am. Orthopaed. Surg.*, 3, (2001).
10. K. Duan, Y. Fan and R. Wang, *J. Biomed.Mater. Res. Part B: Appl. Biomater.* **72B**, 43, (2005).
11. F. H. Browning and H. S. Fogler, *Langmuir*, **11**, 4143, (1995).
12. I.D. Welsh and P.M.A. Sherwood, *Chem. Mater.*, **4**, 133, (1992).
13. H. Fleisch, Bisphosphonates in Bone Disease: From the Laboratory to the Patient, 4th ed., Academic Press, San Diego, (2000).
14. A. P. Grosvenor, S. D. Wik, R. G. Cavell and A. Mar, *Inorg. Chem.*, **44**, 8988, (2005).
15. 25.ASTM, E902-93, (1994), 1994 Annual book of ASTM Standards, Vol. 09.06. American Society for Testing and Materials, Philadelphia.
16. J. Rotole and P. Sherwood, U.S. Patent No. 6,066,403, (23 May 2000).
17. V. Saunders, et al., CRYSTAL 98 User's Manual. University of Torino: Turin, Italy. (1998).
18. C. Pisani, R. Dovesi and C. Roetti, Hartree-Fock ab Initio Treatment of Crystalline

- Systems: Lecture Notes in Chemistry, 48. Springer: Berlin. (1988).
19. J. Scofield, Electron Spectr. Relat. Phenom., **8**, 129, (1976).

8.7 Figures

Figure 8.1 Outer valence band XPS results for 99.99% chromium foil and 99.9% iron foil. Experimental VBXPS results (a) and outer valence band of spectra generated from band structure calculations (b) of the metals are shown.

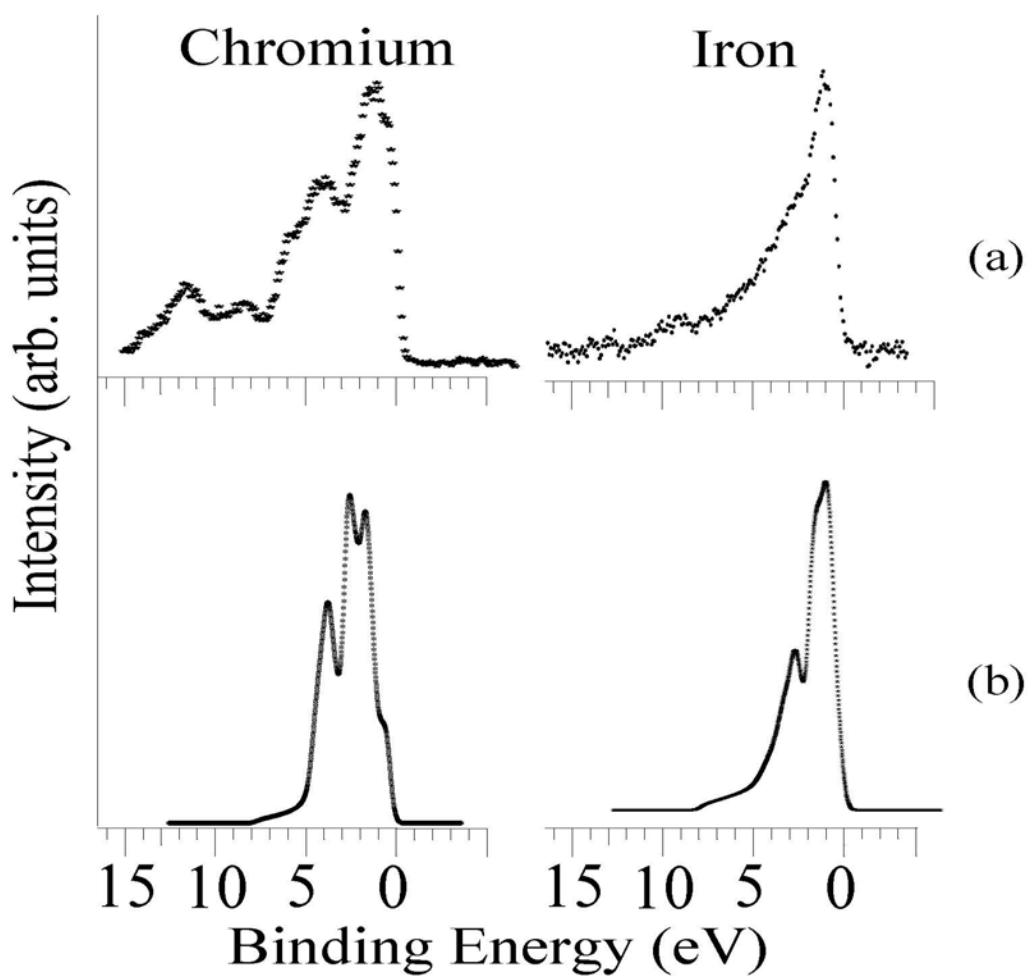


Figure 8.2 Valence band XPS results of 99.99% chromium foil and 99.9% 316L stainless steel foil in the (a) as-received state, (b) polished with 600 grit silicon carbide emery paper and (c) 99.999% argon ion etched.

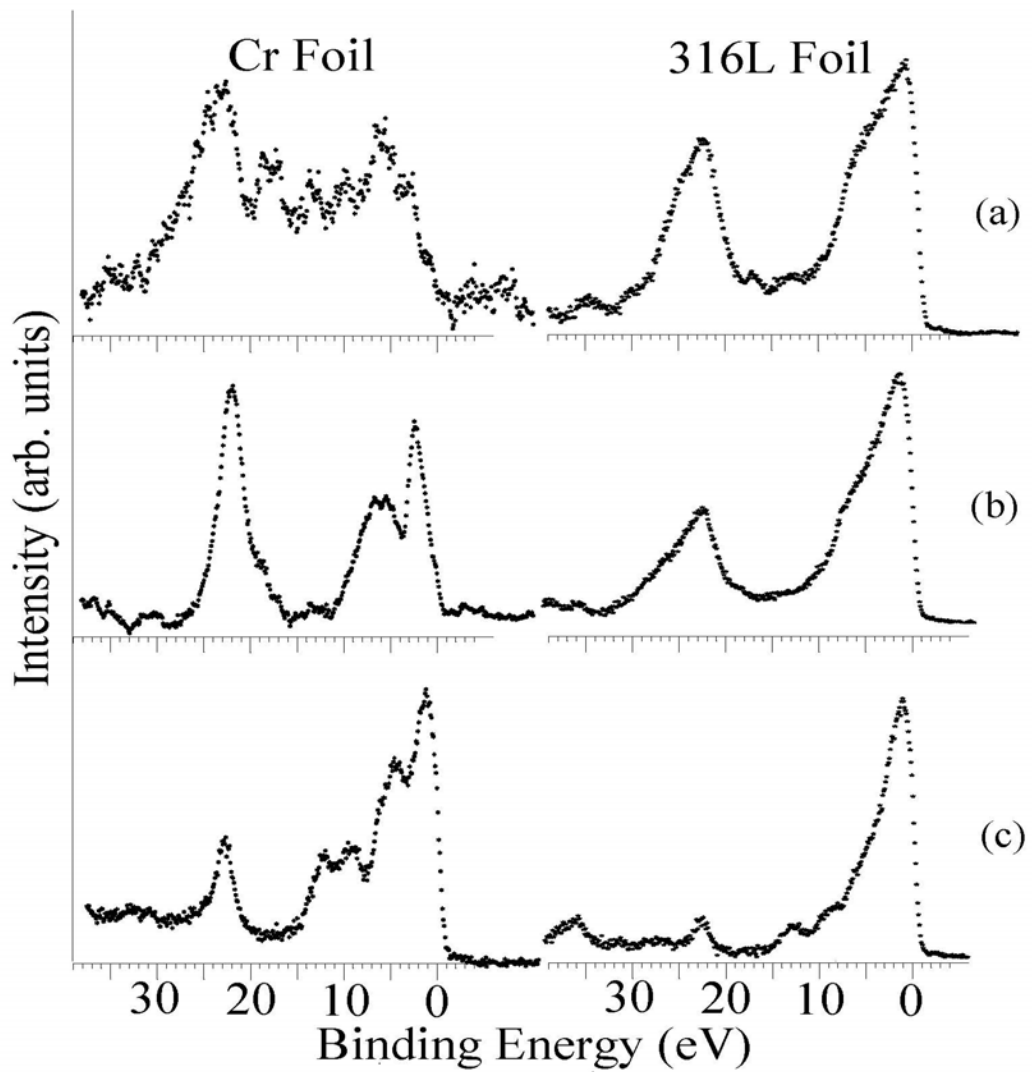


Figure 8.3 Valence band XPS spectra of argon ion etched (a) 99.9% 316L stainless steel foil and (b) 99.9% iron foil.

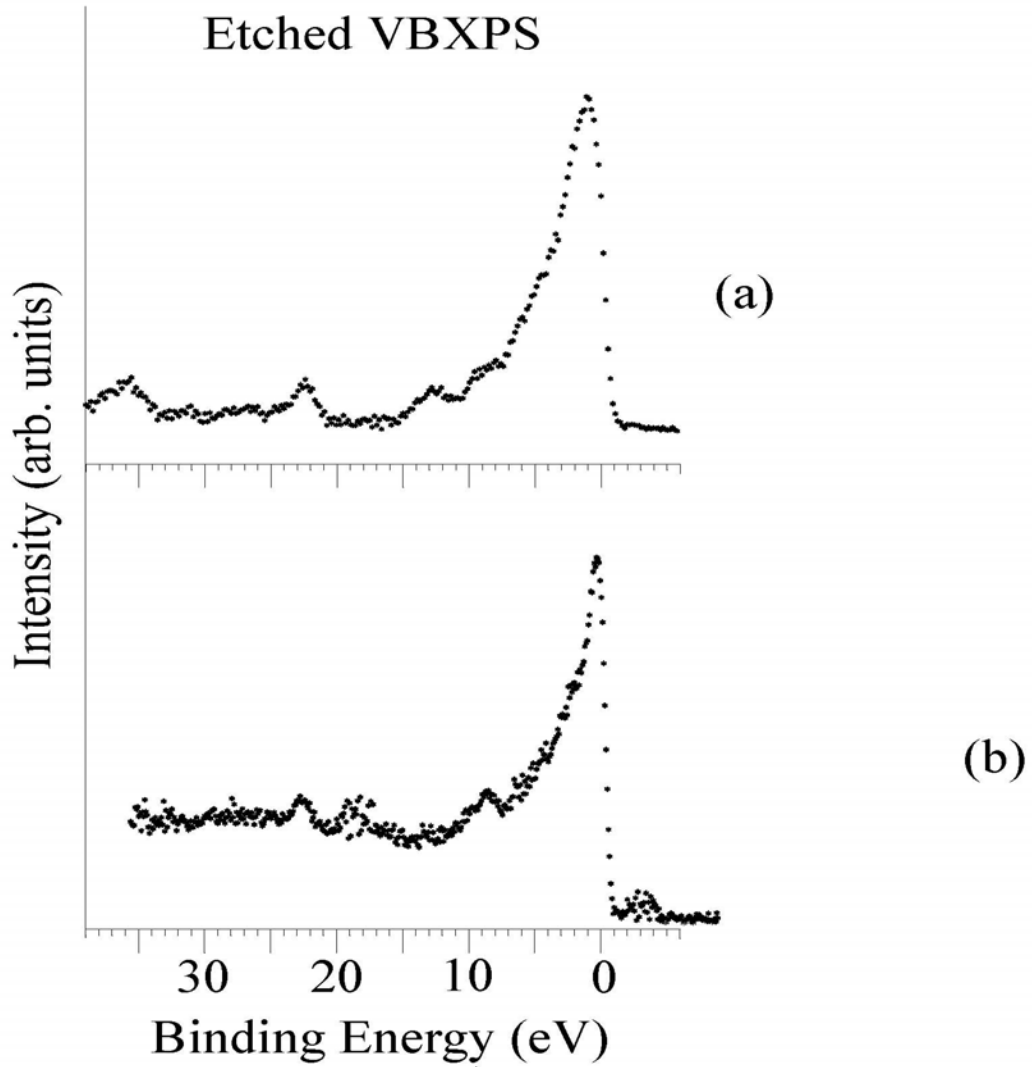


Figure 8.4 Atomic configuration within the idealized etidronate ion.

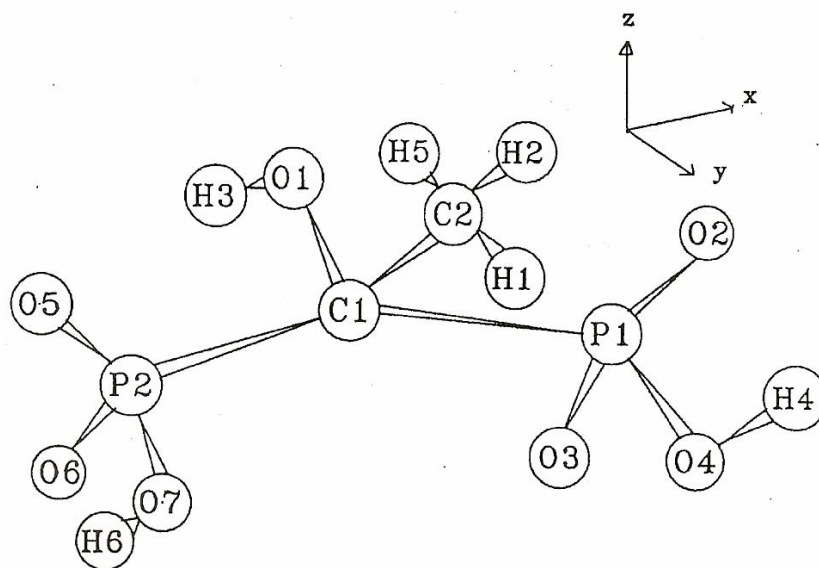


Figure 8.5 Experimental outer valence band region XPS spectra for the iron-phosphorous containing compounds (a) iron etidronate and (b) iron phosphate.

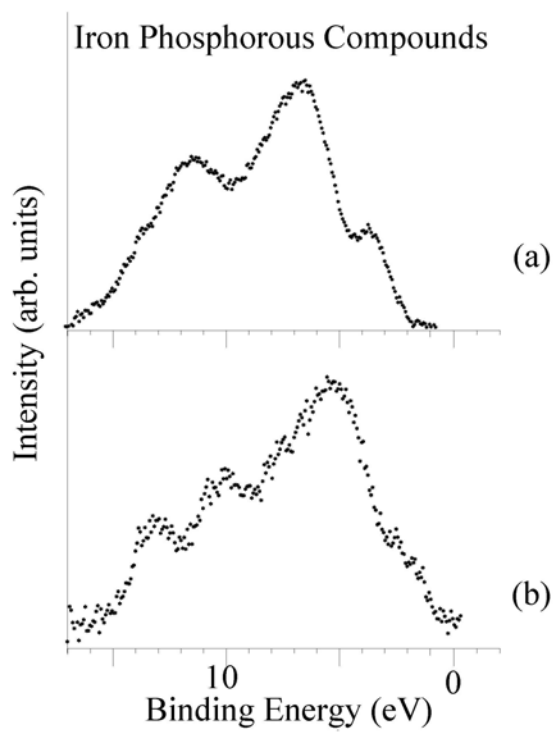


Figure 8.6 X-ray photoelectron spectroscopy valence band spectra of (a) calcium etidronate (achromatic), (b) multiple scattered wave X-alpha calculation of etidronate ion, (c) lab prep calcium etidronate (2:1 molar ratio), (d) lab prep calcium etidronate (1:1 molar ratio) and (e) aged etidronic acid on 99.99% chromium foil.

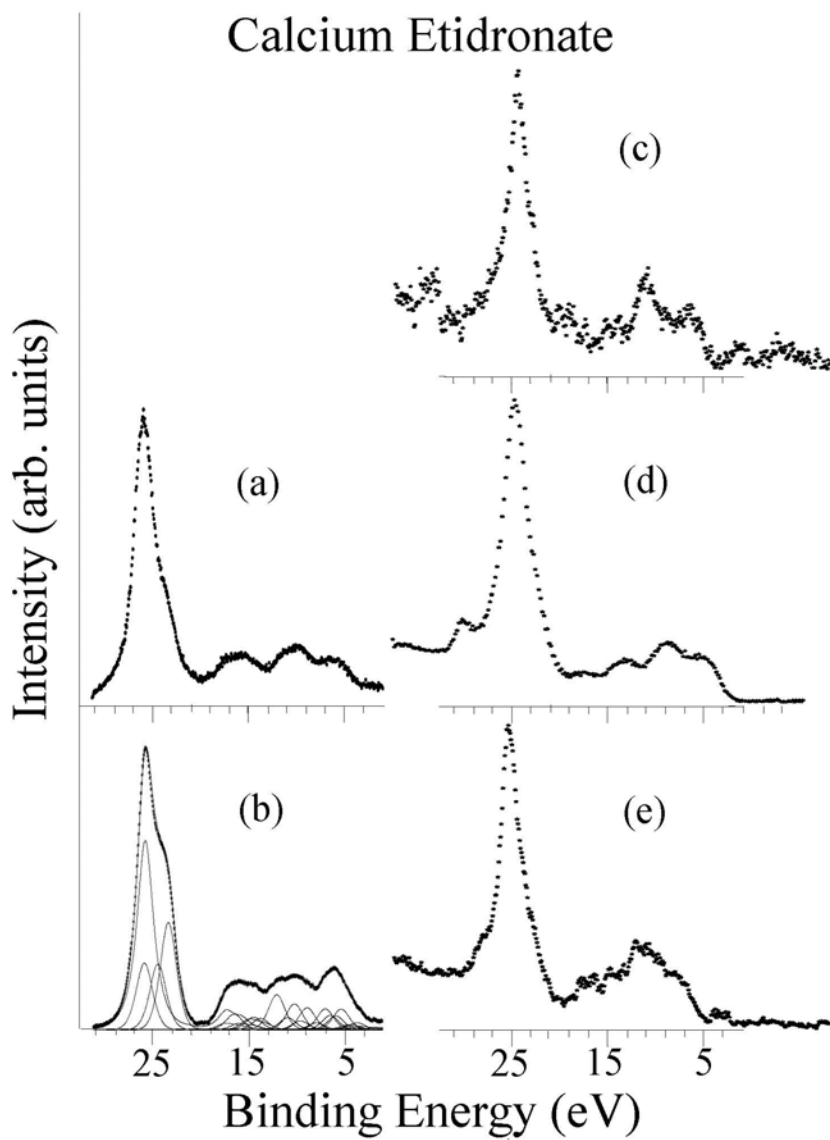


Figure 8.7 Core level X-ray photoelectron spectroscopy spectra for (a) CEB sample, 99.99% chromium foil treated using bench top method, (b) CEA sample, 99.99% chromium foil treated using the anaerobic cell method and (c) argon ion etched 99.99% chromium foil.

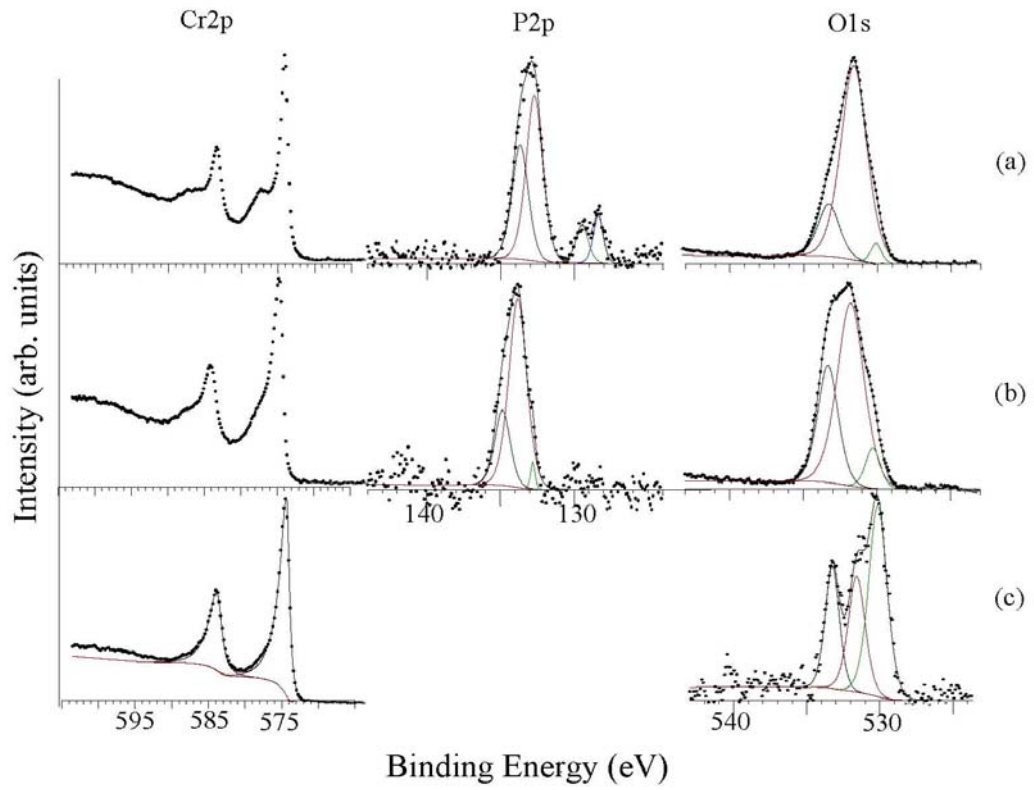


Figure 8.8 Core level x-ray photoelectron spectroscopy spectra for (a) curve fitted spectra of as-received chromium foil, (b) curve fitted spectra argon ion etched 99.99% chromium foil, (c) chromium foil treated in etidronic acid using bench top method and (d) using anaerobic cell method.

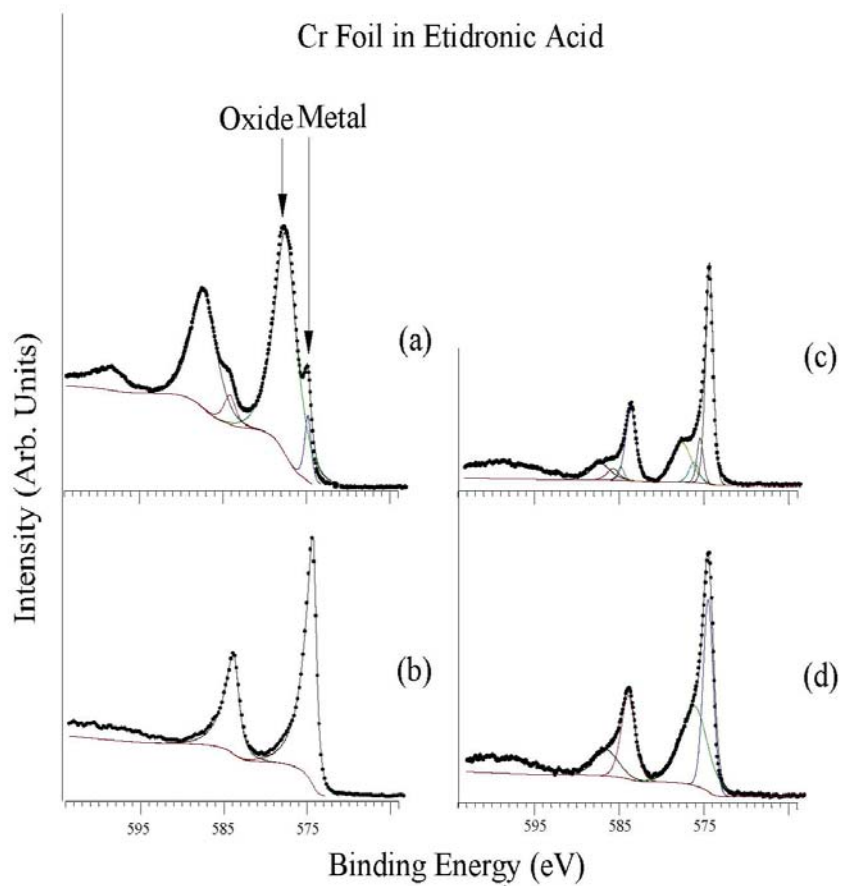


Figure 8.9 Valence band X-ray photoelectron spectra for (a) CEB sample, (b) CEA sample and (c) argon ion etched chromium foil.

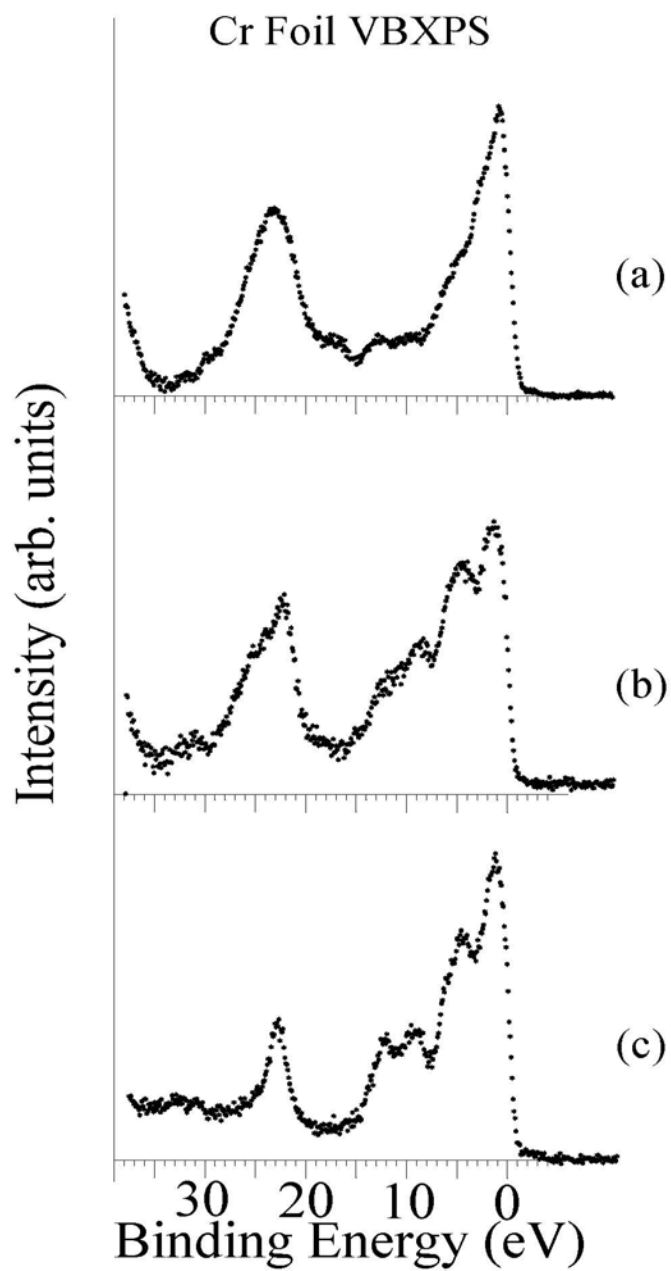


Figure 8.10 Comparison of VBXPS of outer valence band of calcium etidronate (lower overlain spectra) to VBXPS spectra of (a) CEB sample and (b) CEA sample.

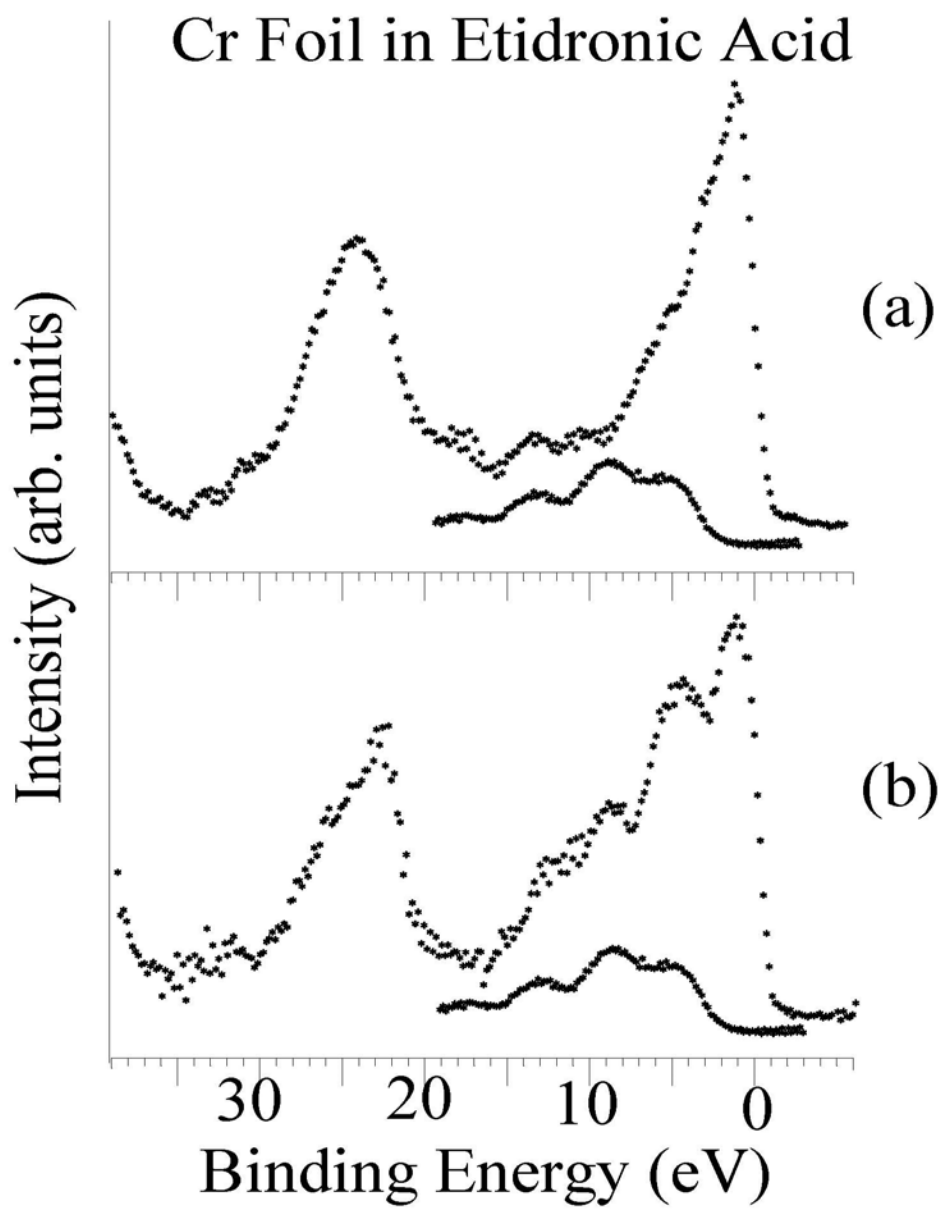


Figure 8.11 Corrosion study of CEA sample results. VBXPS spectra of (a) chromium foil treated using bench top method (CEA), (b) same sample after exposure to ambient air for one week and (c) same as for (b) after two hour immersion in 1M NaCl solution.

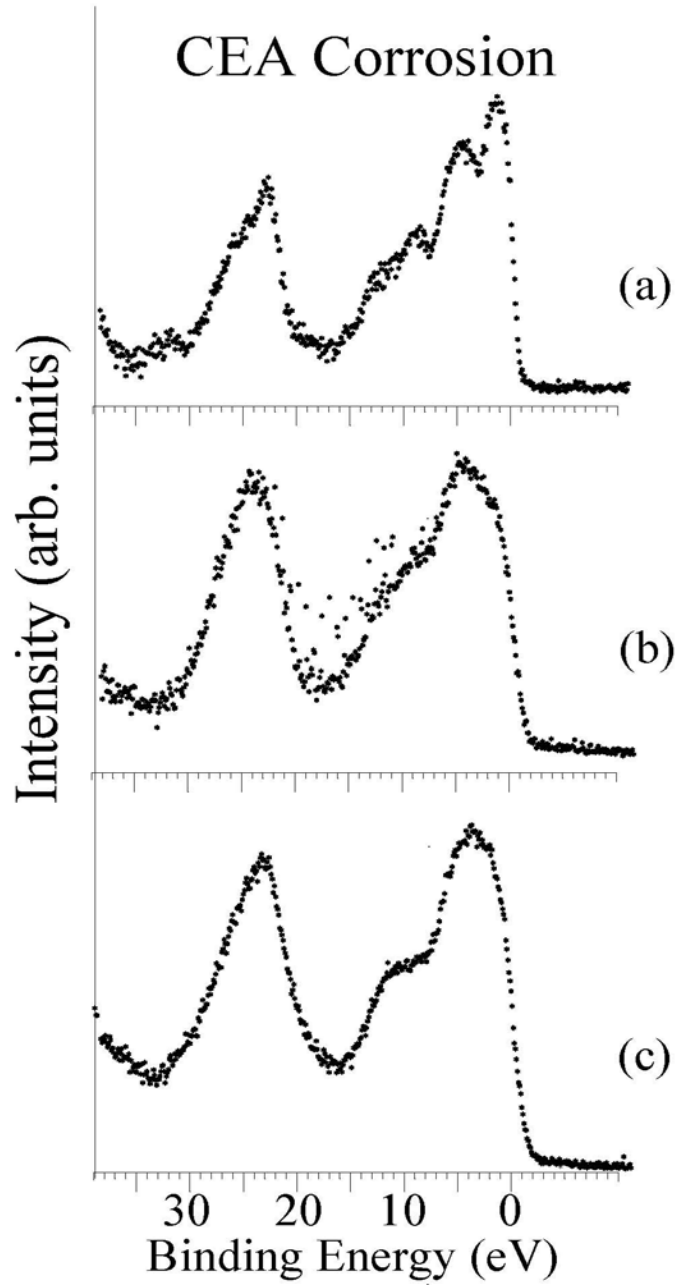


Figure 8.12 Valence band XPS spectra for (a) polished chromium foil immersed in 5 M H_3PO_4 11 min. with no treatment, (b) chromium in 3 M etidronic acid using bench top method, (c) chromium foil treated in anaerobic cell with 3 M etidronic acid and (d) etched chromium foil.

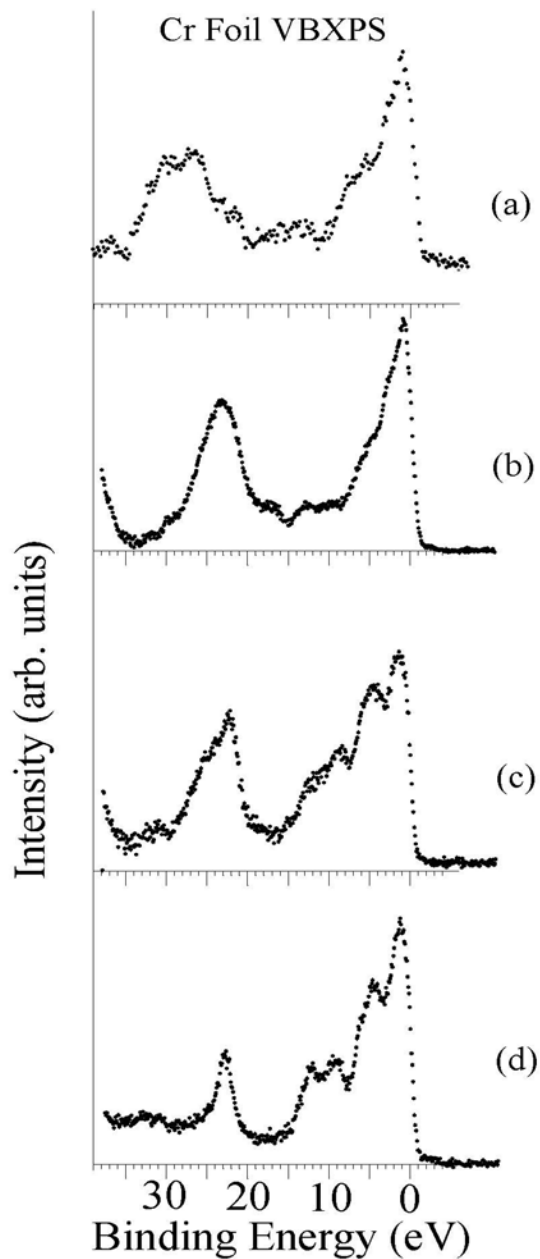


Figure 8.13 Core level XPS spectra of (a) 316L stainless steel treated using bench top method (316EB), (b) 316L stainless steel treated using anaerobic cell method (316EA) and argon ion etched of 99.99% 316L stainless steel.

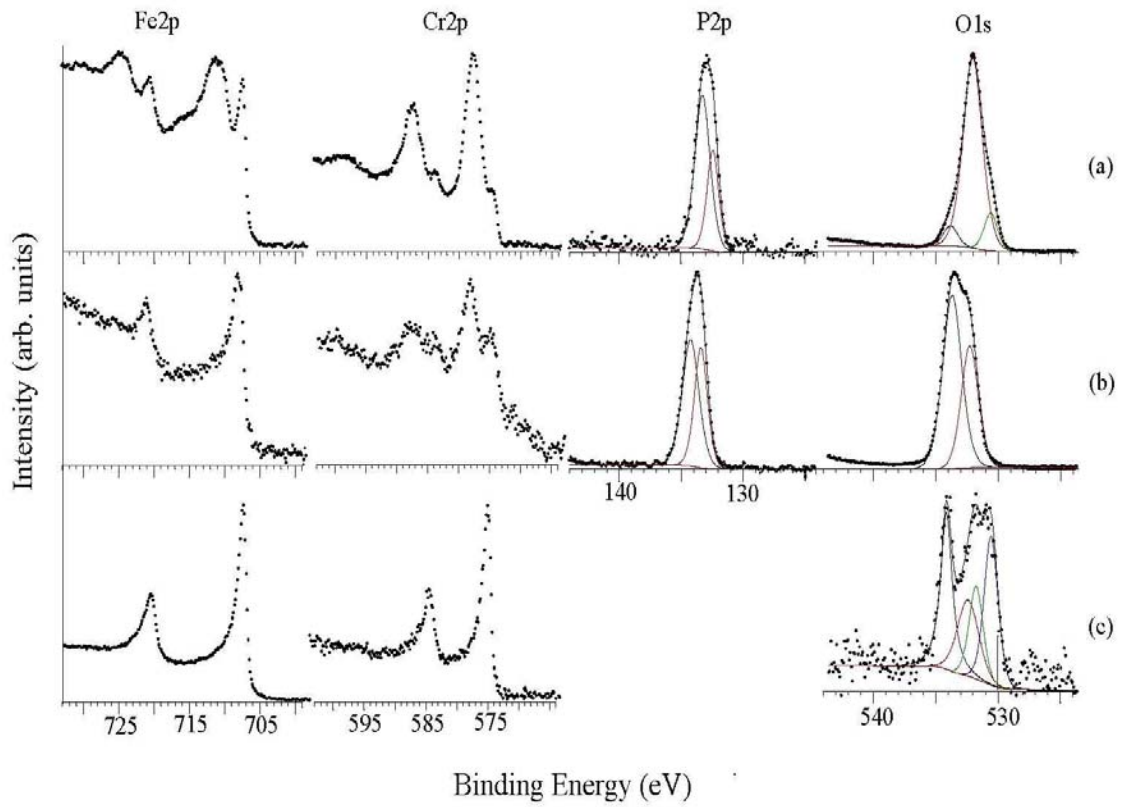


Figure 8.14 Core level XPS curve fitted spectra of the O 1s region of (a) 316EB, (b) 316EA and (c) calcium etidronate.

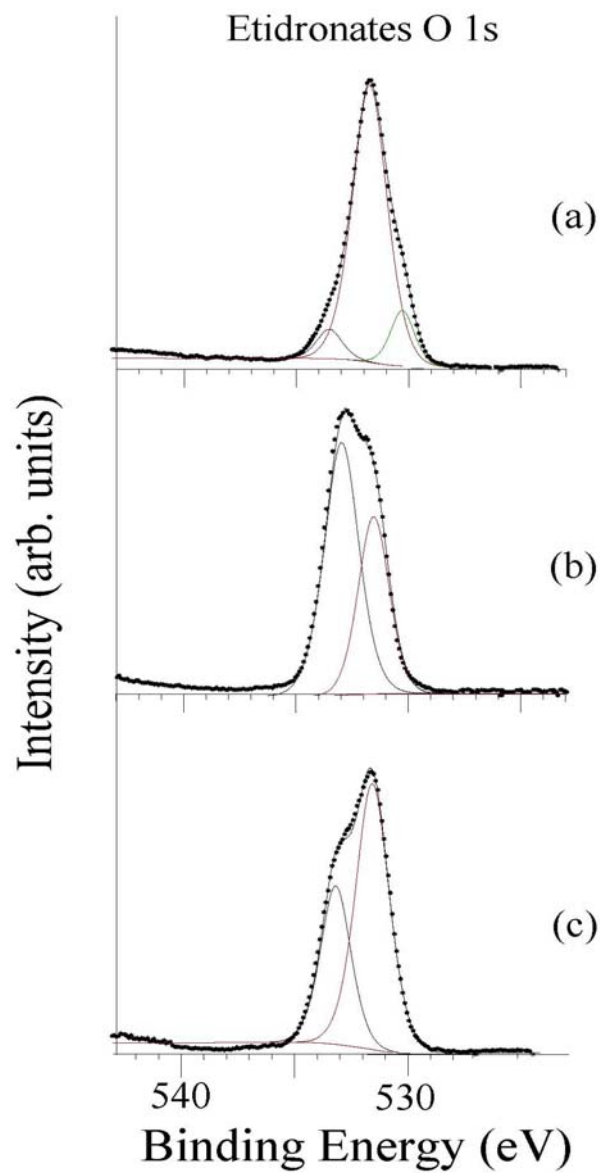


Figure 8.15 Valence band XPS results for 316L stainless steel: 316EB sample (a), 316EA sample and (c) 99.99% 316L stainless steel polished with 600 grit silicon carbide emery paper.

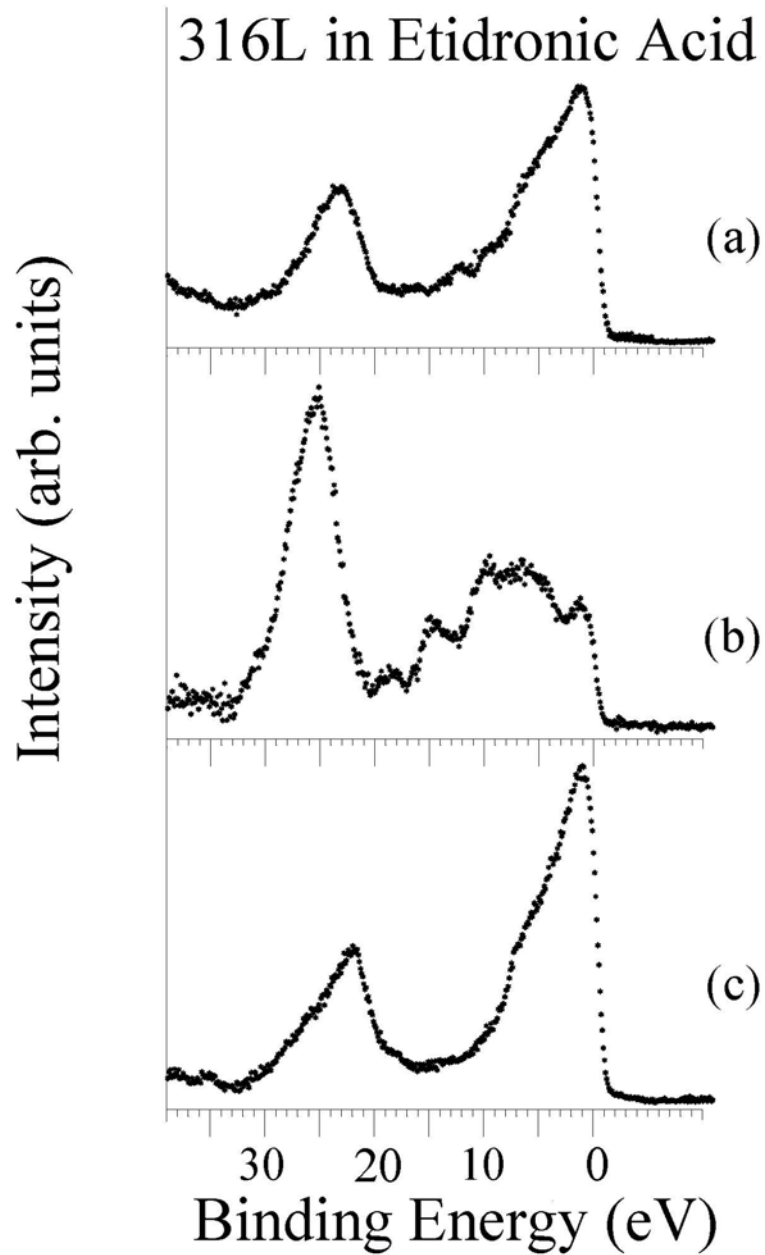


Figure 8.16 Comparison of VBXPS of outer valence band of calcium etidronate (lower overlain spectra) to VBXPS spectra of (a) 316EB sample and (b) 316EA sample.

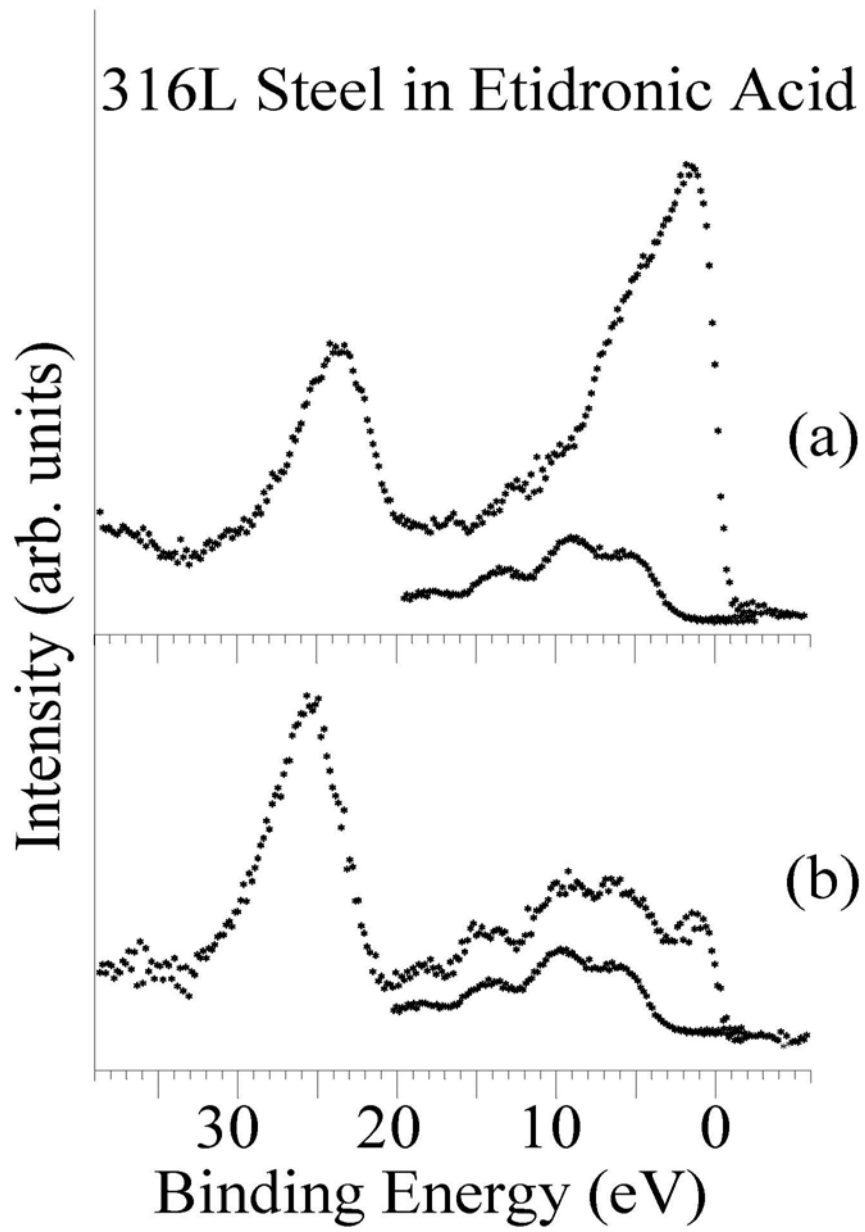


Figure 8.17 Corrosion study of 316EA sample results. VBXPS spectra of (a) chromium foil treated using the anaerobic cell method (316EA), (b) same sample after exposure to ambient air for one week and (c) same as for (b) after two hour immersion in 1M NaCl solution.

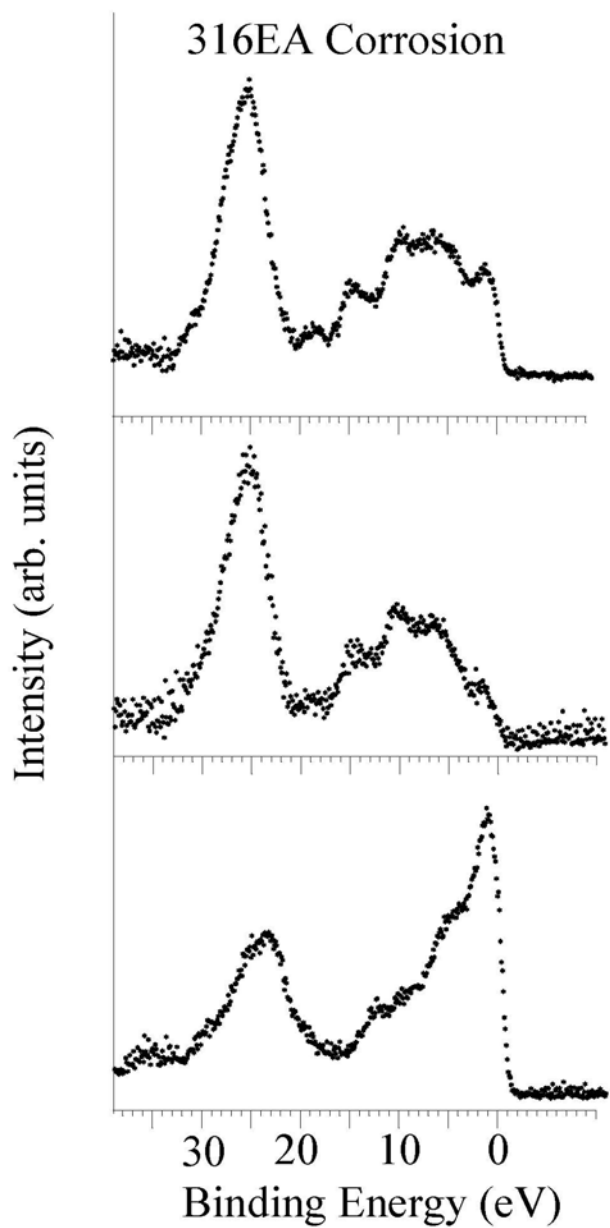
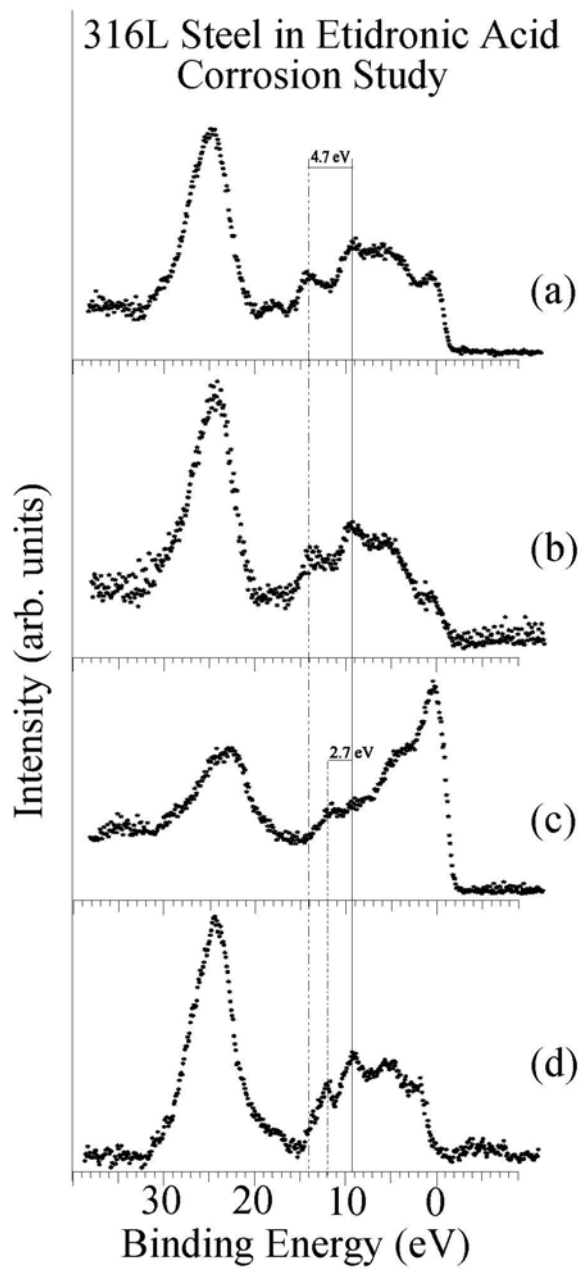


Figure 8.18 Valence band XPS spectra for 316EA sample (a) treated in anaerobic cell, (b) sample in (a) after being exposed to air for one week, (c) same as in (a) and (b) after immersion in 1 M NaCl solution for two hours compared with chromium phosphate powder (d).



8.8 Tables

Table 8.1 Summary of Experiments

Experiment	Surface	Treatment Method	Reactant
316EB	Polished 316L Steel	Bench top	3M Etidronic Acid
316EA	Polished 316L Steel	Anaerobic Cell	3M Etidronic Acid
316EAa	Etidronic Acid Film on 316L Steel (An. Cell)	Exposure	Ambient Air
316EAn	Etidronic Acid Film on 316L Steel (An. Cell)	2 Hour Immersion	1M NaCl

Table 8.2 Core level atomic ratios per sample

Sample	Fe2p/Cr2p	O1s/Cr2p	C1s/Cr2p	P2p/Cr2p
316LAR	0.94	7.90	8.12	--
316LPol	0.95	6.44	6.60	--
316Letch	0.15	0.86	3.29	--
316LEA	0.55	4.09	9.33	3.64
316LEB	1.14	2.79	5.03	0.95
CrAR	--	9.03	12.45	--
CrPol	--	0.86	0.37	--
CrEtch	--	0.24	5.21	--
CrEA	--	1.57	3.85	0.34
CrEB	--	1.83	2.61	0.48

Table 8.3 Normalized Peak Areas (counts*step size) eV

Sample	Cr2p	Fe2p	O1s	C1s	P2p
316L As Received	1412.5	2025.3	2725.1	851.3	
316L Polished	2533.0	3667.3	3992.2	1249.9	
316L Etched	3740.0	25698.7	736.7	1445.0	
316EA	2443.0	1185.7	15543.7	4828.3	2582.0
316EB	2451.7	4299.1	1670.8	916.5	194.4
Cr Foil As Received	794.5		1752.7	734.9	
Cr Foil Polished	4469.2		942.3	498.8	
Cr Foil Etched	3302.1		362.6	1094.8	
CEA	5622.4		1435.3	1074.3	107.3
CEB	6590.9		2956.7	1278.5	256.2

Table 8.4 Experimental Binding Energies

Experiment	Fe2p _{3/2}		Cr2p _{3/2}		O1s	P2p
	oxide	metal	oxide	metal		
(a) 316B	711.4	707.65	577.7	574.54	531.88	132.53
(b) 316EA	707.6	707.69	578.0	575.24	532.80	133.08
(c) CEB		--	577.37	574.23	532.25	132.35
(d) CEA		--	577.87	574.72	532.71	134.18

CHAPTER 9 - Concluding Remarks

9.1 Conclusion

The work published in this dissertation is a continuation of an ongoing investigation into the complex chemistry occurring within metal/phosphate systems with the objective of developing a greater understanding of corrosion inhibition processes. Previous work within this research group has probed the metal/phosphate interface and characterized the surface films generated from phosphorous-containing acids such as orthophosphoric and etidronic acid.

This study focuses on producing oxide-free films generated from orthophosphoric and etidronic acids on clean chromium and Type 316L stainless steel foils.

It has been found that it is possible to create novel surface films utilizing an anaerobic cell which enables the generation of an oxide-free film directly bonded to a clean metal surface.¹ The resulting phosphate and oxide films vary in composition but are found to be stable in ambient air for extended periods of time. Characterization of these films has been facilitated by creating an in-house database of core and valence band XPS spectra along with corresponding band structure and multiple scattered wave $X\text{-}\alpha$ calculations of a series of phosphate standards. Members of this group have successfully formed oxide-free phosphate films on Ti, Cu, V, Fe and Al.²⁻⁵

Chromium presents a unique opportunity in the ongoing study within this research group because of its durability and corrosion inhibiting properties. Chromium reacts almost instantly with oxygen to form a very thin protective oxide film that is self-healing if compromised. Chromium is a major alloying component in stainless steel because of these desirable properties.

In this investigation oxide-free chromium foil was used to study the oxide which forms on the clean metal surface in the presence of quadruply distilled water, a condition attainable through the use of the anaerobic cell. Prior studies of the chromium oxidation process have studied oxide films formed on the native chromium oxide interface. A second method of generating oxide-free films developed in this group⁷ was also employed in film formation on clean chromium and 316L stainless steel foils. XPS studies were done to distinguish between chromium oxide species and a set of standards consisting of four chromium compounds of differing chromium valencies was created.

Two methods of forming oxide-free films were used to generate phosphate films on chromium from deaerated orthophosphoric acid. A baseline of chromium's reactivity toward

o-phosphoric acid was established by placing polished chromium foil into the deaerated acid for 10 minutes, rinsing with quadruply distilled water and drying under a vacuum prior to executing an XPS characterization of the surface film on the foil. Results indicate a trace amount of phosphorous was in the film; however the film was formed atop an oxide/hydroxide interface. The films formed during this study in an anaerobic environment produced oxide-free metaphosphates bonded directly to the chromium.

Etidronic acid, an organophosphonic acid in the bisphosphonate group, has been used to generate an oxide free etidronate film on chromium and 316L stainless steel foils in this work. Oxide-free films formed on chromium foil, but were assembled into phosphate films as a result of the etidronate breaking down during the reaction. The 316L steel produced an oxide-free phosphate film in the bench top treatment method using etidronic acid. The anaerobic cell approach successfully generated an oxide-free etidronic film on the 316L stainless steel.

Stainless steel is the most widely used metal in the biomedical industry. When incorporated into the physiological environment pitting corrosion can occur leading to implant failure. Recent investigations into utilization of a calcium etidronate film as a corrosion inhibitor *and* a method of direct delivery of bisphosphonate drugs, which currently are administered orally or intravenously, produced a substantial, thick and amorphous coating on a titanium substrate.⁶

Etidronic acid, an organophosphonic acid in the bisphosphonate group, has been used in this investigation to generate a thin oxide free etidronate film less than 100 Å thick on 316L stainless steel in this work. The potential for application of oxide-free phosphate and etidronate films in implant fabrication is significant.

9.2 References

1. J. Rotole and P. Sherwood, U.S. Patent No. 6,066,403, (23 May 2000).
2. John A. Rotole, Karen Gaskell, Alex Comte and Peter M.A. Sherwood, *J.Vac. Sci. Technol. A*, **19**, 1176, (2001).
3. J.A. Rotole and Peter M.A. Sherwood, *J.Vac. Sci. Technol. A*, **18**, 1066, (2000).
4. John A. Rotole and Peter M.A. Sherwood, *Chem. Mater.*, **13**, 3933, (2001).
5. D. J. Asunskis and P. M. A. Sherwood, *J. Vac. Sci. Technol. A*, **21**, 1133, (2003).
6. K. Duan, Y. Fan and R. Wang, *J. Biomed. Mater. Res. Part B: Appl. Biomater.*, **72B**, 43, (2005).
7. Y-Q Wang and P.M.A. Sherwood, *J. Vac. Sci. Technol. A*, **21**, 11 (2003).